

ABSTRACT

KOLANJIYIL, ARUN VARGHESE. Whole-Lung Airflow and Particle Transport/Deposition Modeling. (Under the direction of Dr. Clement Kleinstreuer).

Prediction of aerosol transport and deposition in the human respiratory tract can assist in predicting health effects of inhaled toxic particles or in developing new drug-aerosols. However, the sheer complexity of the human lung, featuring a total of 16 million complex tubular airways, prohibits full-scale computer simulations of the fluid-particle dynamics for the entire respiratory system. Hence, three different modeling approaches have been developed to predict particle transport and deposition during breathing. Starting with the *whole-lung airway model I (WLAM I)*, the actual lung geometry was radically reduced by lumping all airways together into an exponentially expanding one-dimensional conduit which looks like a trumpet. With *whole-lung airway model II (WLAM II)*, an attempt has been made to realistically and accurately represent actual transient airflow as well as inhaled particle dynamics, representing the impact of all respiratory-tract airways, i.e., from nose/mouth to generation 23. Finally, focusing on the O₂-CO₂ gas exchange region, the *alveolar model* consists of *triple bifurcation units (TBUs)* with attached spherical alveoli. The expanding and contracting motion of the alveoli during inhalation and exhalation is then accommodated in WLAM I and WLAM II.

In WLAM I the respiratory tract geometry is first represented by a 3-D mouth-to-trachea configuration and then all subsequent airways are lumped together into an exponentially expanding 1-D conduit. The diameter for each generation of the 1-D extension was obtained on a subject-specific basis from the calculated total volume which represents each generation of the individual. The alveolar volume was added based on the approximate

number of alveoli per generation. A wall-displacement boundary condition was applied at the bottom surface of the first-generation WLAM, so that any breathing pattern due to the negative alveolar pressure can be reproduced. Specifically, different inhalation/exhalation scenarios (rest, exercise, etc.) were implemented by controlling the wall/mesh displacements to simulate realistic breathing cycles in the WLAM I.

In WLAM II, a more realistic approximation of the human lung was achieved by using geometric data sets for subject-specific *human upper airways*, typically from nose/mouth to generation three, *with* TBUs attached to capture a few additional generations. Specifically, the model geometry consists of subject-specific upper airways in 3-D, which are connected to geometrically and flow-rate adjusted TBUs plus the alveolar model in series and parallel - all based on morphometric measurements of human lung casts. So, the TBUs are used to extend the geometry from the 3-D upper airways to simulate the local airflow and hence capture the influence of the bifurcating geometry (carinal ridge) on particle deposition. In this new whole-lung model, the alveolar movement was applied on the alveoli surface to control any given inhalation and exhalation waveform, and hence physiological lung breathing mechanism was captured.

The objective of this study was to develop three-dimensional whole lung models which can effectively be used to predict micron- and nano-particle deposition in human lungs during breathing. The airflow and particle transport through the lung airways were successfully simulated and analyzed, using computational fluid-particle dynamics. Total and regional particle depositions were calculated and validated with experimental lung deposition data. These model results provide critical insight into aerosol transport and deposition in lung airways. The results indicate that large amounts of particles are being filtered out by the

extra-thoracic and the upper tracheo-bronchial airways. For example, aerosol inhalation devices have typically high air-particle flow rates, thereby wasting large amounts of drugs in the upper respiratory tracts. Hence, in order to achieve drug-aerosol delivery to, say, the alveolar region, slow and deep inhalation is recommended; implying that commercial inhalers have to be modified. Specifically, applying the new methodology for direct drug-delivery in the current modeling approach, targeted delivery can be achieved. Additionally, it has been shown that increased aerosol deposition in specific lung regions can be achieved by changing the aerosol diameter. In summary, the models can be used for: (i) analyzing the toxicological effects of exposure to particulate matter, (ii) estimating pharmacological effects of administered pulmonary drugs, and (iii) providing inhaler-design guidelines for improved drug-aerosol targeting.

© Copyright 2017 by Arun Varghese Kolanjiyil

All Rights Reserved

Whole-Lung Airflow and Particle Transport/Deposition Modeling

by
Arun Varghese Kolanjiyil

A dissertation submitted to the Graduate Faculty of
North Carolina State University
in partial fulfillment of the
requirements for the Degree of
Doctor of Philosophy

Mechanical Engineering

Raleigh, North Carolina

2017

APPROVED BY:

Dr. Clement Kleinstreuer
Committee Chair

Dr. Tarek Echehki

Dr. Yun Jing

Dr. Mette Olufsen

DEDICATION

To my Family

BIOGRAPHY

Arun Varghese Kolanjiyil was born in Kerala, India. He attended Mahatma Gandhi University, Kerala, India, for his undergraduate studies and earned Bachelor's degree in Mechanical Engineering. Upon completion of his undergraduate study, he decided to go abroad for higher education and joined North Carolina State University, Raleigh, NC. He completed Master's in Mechanical Engineering from the Department of Mechanical and Aerospace Engineering in spring 2013. During his Master's program he had the opportunity to work under the direction of Professor Clement Kleinstreuer in the area of lung fluid-particle dynamics. After receiving his Master's degree he continued his research while enrolling for a doctoral degree in the same department.

ACKNOWLEDGMENTS

First and foremost, I would like to express my deep gratitude to my advisor, Dr. Clement Kleinstreuer, for his encouragement, guidance, and support throughout my graduate study. This work has been possible only due to the enormous support and patience provided by him.

I would also like to express my gratitude to Dr. Tarek Echehki, Dr. Yun Jing and Dr. Mette Olufsen for taking time from their schedule to be a part of my dissertation committee.

I would like to take this opportunity to thank the people who have helped me in various ways during my research. First of all I would like to thank my lab mates Luke, and Sriram for all the help and support. I am very thankful to my friends who have been very supportive and accommodating.

I would like to thank my family for all their support throughout my education, with special thanks to my beloved wife and parents.

I thank the ALMIGHTY for having bestowed the blessings on me.

TABLE OF CONTENTS

LIST OF TABLES	ix
LIST OF FIGURES	x
ABBREVIATIONS AND SYMBOLS.....	xvi
CHAPTER 1	
Introduction.....	1
1.1 Need for lung modeling	2
1.2 Anatomy and morphometry of the human respiratory tract	3
1.3 Lung morphometric models.....	7
1.4 Lung diseases and pulmonary drug delivery.....	10
1.5 Research objectives and novel contributions	12
1.6 Organization.....	14
CHAPTER 2	
Introduction to Computational Modeling of Lung-Aerosol Dynamics.....	15
2.1 Background information on computational multiscale lung models	16
2.2 Background information on computational lung-aerosol dynamics.....	20
2.3 Math modeling equations	24
CHAPTER 3	
Whole Lung Airway Model I	30
3.1 Theory and model development	31
3.1.1 Introduction.....	31
3.1.2 Model geometry.....	36

3.1.3	Governing Equations	38
3.1.4	Numerical method.....	41
3.1.5	Results and discussion	43
3.1.5.1	Airflow	43
3.1.5.2	Particle transport	49
3.1.5.3	Comparison of regional deposition.....	54
3.1.5.4	Three-compartment segmental deposition	58
3.1.6	Model limitations and future work	61
3.1.7	Conclusions.....	63
3.2	Dry-powder inhalation	65
3.2.1	Introduction.....	65
3.2.2	Theory	69
3.2.3	Model validations	74
3.2.4	Results and Discussion.....	76
3.2.4.1	Curcumin-particle deposition in a whole-lung model	77
3.2.4.2	Improvement in drug-aerosol delivery and local deposition	78
3.2.5	Polydisperse vs. monodisperse particle distributions	80
3.2.6	Considerations for targeted drug-delivery	81
3.2.7	Model Limitations and Future Work.....	84
3.2.8	Conclusions.....	85
 CHAPTER 4		
	Regional Alveolar Model.....	87
4.1	Single alveolus model.....	88

4.1.1	Introduction.....	88
4.1.2	Model geometry.....	92
4.1.3	Wall motion and boundary condition	97
4.1.4	Numerical methods	98
4.1.5	Results and discussion	100
4.1.5.1	Alveolar flow pattern.....	100
4.1.5.2	Particle transport and deposition	104
4.1.5.3	Effect of gravity.....	109
4.1.5.4	Periodically alveolated and multi-alveolated duct.....	112
4.1.6	Conclusion	114
4.2	Human acinar model	116
4.2.1	Introduction.....	116
4.2.2	Model geometry.....	117
4.2.3	Wall motion and boundary condition	122
4.2.4	Numerical method.....	126
4.2.5	Results and discussion	128
4.2.5.1	Alveolar flow pattern.....	128
4.2.5.2	Particle transport and deposition	138
4.2.5.3	Total alveolar deposition	143
4.2.6	Conclusions.....	144
 CHAPTER 5		
	Whole Lung Airway Model II.....	146
5.1	Single-path and two-path models	147

5.1.1	Introduction.....	147
5.1.2	Model geometry.....	150
5.1.3	Wall deformation and boundary conditions	157
5.1.4	Numerical methods	157
5.1.5	Experimental data set	159
5.1.6	Results and discussion	160
5.1.6.1	Air flow	161
5.1.6.2	Whole lung particle transport and deposition.....	165
5.1.6.3	Segmental lung deposition results	169
5.1.7	Why alveolar sac model and why transient over steady state?	176
5.1.8	Limitations of the current model.....	178
5.1.9	Future work.....	178
5.1.10	Conclusion	180
 Chapter 6		
	Summary.....	182
6.1	General conclusions	183
6.2	Comparison of total lung deposition by WLAM I and WLAM II	186
6.3	Computational resource requirement for WLAM I and WLAM II.....	188
 Chapter 7		
	References	189
	Appendix.....	224

LIST OF TABLES

Table 1.1. Model dimensions for generations 0 to 23. (based on Weibel [2]).....	9
Table 3.1. Model dimensions for generations 0 to 23.....	37
Table 4.1.1. Geometric model parameters	94
Table 4.2.1. Comparison of alveolar TBU model dimensions for generation 16-18 with morphometric measurements reported in literature	119
Table 4.2.2. Comparison of alveolar TBU model dimensions for generation 19-21 with morphometric measurements reported in literature	120
Table 4.2.3. Number of alveoli and alveolar volume fraction in the TBU	125
Table 5.1. Experimental deposition results from Heyder [119] for mouth breathing condition at 15 L/min (LPM)	160
Table 6.1. Run time comparison between WLAM I and WLAM II.....	188

LIST OF FIGURES

Fig. 1.1. Anatomy of the human respiratory tract.....	4
Fig. 1.2. Schematic representation of variation of airway wall structure down the airway tree (adapted from [5] with permission from Elsevier)	6
Fig. 1.3. Schematics of the human airway tract (from [12]).....	8
Fig. 2.1. Section through Visible Human Male - thorax, including heart, lungs, spinal column, major vessels, musculature (from Thorax subset) from the Visible Human Project at U.S. National Library of Medicine [32].....	17
Fig.3.1.1: Schematic of whole lung airway model (WLAM I).....	38
Fig.3.1.2. Breathing profiles depicted in terms of the changes in lung volume and the corresponding mass flow rates: (a) inhalation flow rate 15 LPM and tidal volume 500 cm ³ ; and (b) inhalation flow rate 30 LPM and tidal volume 1000 cm ³	44
Fig. 3.1.3: Velocity contours and secondary velocity vectors in the mid-plane of the idealized oral-upper airway geometry at steady inhalation flow rates: (a) 15 LPM; (b) 30 LPM; and (c) 60 LPM.	46
Fig. 3.1.4: Velocity contours and representative secondary velocity vectors in the mid-plane of the idealized oral-upper airway geometry during transient breathing with a flow rate of 30 LPM: (a) peak inhalation; (b) start of exhalation; and (c) peak exhalation.	48
Fig. 3.1.5. Comparison of particle deposition in the idealized mouth-throat geometry with experimental results from Cheng et al. [120].....	50
Fig. 3.1.6. Comparison of particle deposition in the idealized upper airway model with experimental results from Cheng et al. [120].....	51

Fig. 3.1.7. Comparison of particle deposition in the WLAM I with experimental results (Experimental 1 denotes results from Heyder et al [119] and Experimental 2 denotes results from Kim and Hu [127] for (a) inhalation flow rate 15 LPM and tidal volume 500 cm³; (b) inhalation flow rate 15 LPM and tidal volume 1000 cm³; (c) inhalation flow rate 15 LPM and tidal volume 1500 cm³; (d) inhalation flow rate 30 LPM and tidal volume 1000 cm³; (e) inhalation flow rate 45 LPM and tidal volume 1500 cm³..... 53

Fig. 3.1.8. Comparison of particle deposition in the extra-thoracic airway with experimental results. (Experiment a denotes results from [129]; Experiment b denotes results from [130]; Experiment c denotes results from [125]; Experiment d denotes results from [128]; Experiment e denotes results from [126]; Experiment f denotes results from [131]). Experimental results are reported in [126]..... 55

Fig. 3.1.9. Comparison of rapidly cleared thoracic deposition with experimental results (Experiment a denotes results from [129]; Experiment c denotes results from [125]; Experiment d denotes results from [128]; Experiment e denotes results from [126]). Experimental results are reported in [126]..... 57

Fig. 3.1.10. Comparison of slowly cleared thoracic deposition with experimental results (Experiment a denotes results from [129]; Experiment b denotes results from [130]; Experiment c denotes results from [125]; Experiment d denotes results from [128]; Experiment e denotes results from [126]). Experimental results are reported in [126]..... 58

Fig. 3.1.11. Superimposed three-compartment deposition curves for each of the breathing patterns: (a) 15 LPM with tidal volume 500 cm³; (b) 15 LPM with tidal volume 1000 cm³; (c) 15 LPM with tidal volume 1500 cm³; (d) 30 LPM with tidal volume 1000 cm³; and (e) 45 LPM with tidal volume 1500 cm³..... 60

Fig. 3.2.1. (a) Novolizer DPI (adapted from [148] with permission of Springer); and (b) WLAM I with attached dry powder inhaler mouthpiece	70
Fig. 3.2.2. Lung volume change with respect to time when using the Novolizer DPI.	72
Fig. 3.2.3. Particle diameter distributions of budesonide and curcumin emitted from a DPI. 74	
Fig. 3.2.4. Comparison of the budesonide DPI drug deposition results with experimental results for an inhalation profile with PIFRs of 54, 65, and 99 LPM (Experimental results from [147]).....	76
Fig. 3.2.5. Curcumin dry powder deposition results when using a commercial DPI	78
Fig. 3.2.6. Velocity distribution in the oropharyngeal airway for different injection angles: (a) horizontal; and (b) positive angle	79
Fig. 3.2.7. Curcumin dry powder deposition result when the DPI injection angle is $+10^\circ$	80
Fig. 3.2.8. Comparison of curcumin powder deposition for an inhalation PIFR of 65 LPM, considering both polydisperse and monodisperse curcumin dry powder	81
Fig. 3.2.9. Direct drug-aerosol delivery: (a) Particle release maps generated at the oral inlet for a breathing profile with inhalation PIFR 65 LPM; and (b) Comparison of curcumin deposition in the lung airways with and without targeting	83
Figure 4.1.1. Schematic representation of a single alveolated duct and (b) shows 3-D representation.....	94
Fig. 4. 1.2. (a) periodically alveolated and (b) multi-alveolated ducts.	95
Fig. 4.1.3 . Flow through an alveolated duct	99
Fig. 4. 1.4. Alveolus flow pattern in generation (a) 18 (rigid alveoli) (b) generation 18 (c) generation 22.....	101

Fig 4. 1.5. Alveolus flow pattern under (a) rest (15 LPM), (b) exercise (30 LPM) and (c) 45 LPM) inhalation flow rates	103
Fig. 4. 1.6. Comparison of particles deposition in generation 18 and generation 22	105
Fig. 4.1.7. comparison of alveolus particle deposition trend for a rigid and flexible alveolus	106
Fig.4.1 8. Trajectories of a 2 μm particle in a single alveolated duct representing generation22 under (a) rest (15 LPM), (b) exercise (30 LPM) and (c) 45 LPM) inhalation flow rates.....	108
Fig. 4.1. 9. Aerosol deposition in a single alveolated duct representing generation 22 for an inhalation flow rate of 30 LPM.....	110
Fig. 4.1.10. Alveolar particle transport highlighting influence of gravity orientation.....	111
Fig. 4. 1.11. Particle trajectory in a periodically alveolated duct model for inhalation period (a) 1s (b) 2s	112
Fig. 4. 1.12. Particle trajectory in a multi-alveolated duct model with flexible wall (left) and rigid wall (right) for inhalation period (a) 1s, (b) 2s (simulations were conducted without the gravitational force).....	114
Fig. 4.2.1. (a) A representative TBU model with alveoli for generation 16-18. (b) Image of a terminal conducting airway from a lung cast (Weibel [223]).....	118
Fig. 4.2.2. (a) A representative TBU model with alveoli for generation 19-21(b) Image of an alveolar airway from a lung cast (Weibel [223]).....	119
Fig. 4.2.3. A representative Double Bifurcation Unit (DBU) model with alveoli for generation 22-23	121
Fig. 4.2.4. Final assembled full alveolar model.....	122

Fig. 4.2.5. Breathing profiles depicted in terms of the changes in lung volume and the corresponding mass flow rates: inhalation flow rate 15 LPM and tidal volume 500 cm³ 127

Fig. 4.2.6. Enlarged view of the flow stream lines and velocity vectors inside TBU 16-18 130

Fig.4.2.7. Enlarged view of the flow stream lines and velocity vectors inside TBU 19-21 . 132

Fig.4.2.8. Enlarged view of the flow stream lines and velocity vectors inside DBU 22-23. 133

Fig.4.2.9. Enlarged view of the flow stream lines and velocity vectors inside TBU 16-18. 135

Fig.4.2.10. Enlarged view of the flow stream lines and velocity vectors inside TBU 19-21 136

Fig.4.2.11. Enlarged view of the flow stream lines and velocity vectors inside DBU 16-18 137

Fig.4.2.12. Particle deposition results for (a) 3 μm and (b) 5 μm case during inhalation phase
..... 139

Fig.4.2.13. Location of the deposited particles (3 μm) in the full alveolar model during inhalation phase with a tidal volume of 1000ml..... 140

Fig.4.2.14. Particle deposition results for (a) 3 μm and (b) 5 μm case during exhalation phase
..... 142

Fig. 4.2.15. Total acinar particle deposition results during a full breathing cycle..... 143

Fig. 5.1. Schematic representation of scaled Triple Bifurcation Unit (TBU) models connected in series and parallel (TBUs are scaled down to match the outlet diameter with the inlet diameter of the successive TBU) 151

Fig. 5.2. (a) Human nasal-oral upper airway model, (b) representative TBU 152

Fig. 5.3. (a) TBU model with alveoli for generation 16-18, (b) TBU model with alveoli for generation 19-21 153

Fig. 5.4. Alveolar sac model for generation 22-23 154

Fig. 5.5. Single-path whole lung model..... 155

Fig. 5.6. Dual-path whole lung model	156
Fig. 5.7. Flow stream lines through the oral-upper airway model for an inhalation flow rate of 15 L/min.....	162
Fig. 5.8. Flow stream lines through the TBUs of the dual-path WLAM for an inhalation flow rate of 15 L/min	164
Fig. 5.9. Total and segmental particle deposition results in (a) single- and (b) dual-path whole lung models for an inhalation tidal volume 500ml	166
Fig. 5.10. Total and segmental particle deposition results in (a) single- and (b) dual-path whole lung models for an inhalation tidal volume 1000ml	168
Fig. 5.11. Regional deposition results during the inhalation phase in (a) single- and (b) dual-path whole lung models	170
Fig. 5.12. Regional deposition results during the exhalation phase in (a) single- and (b) dual-path whole lung models	172
Fig. 5.13. Regional deposition results during the inhalation phase in (a) single- and (b) dual-path whole lung models	174
Fig. 5.14. Regional deposition results during the exhalation phase in (a) single- and (b) dual-path whole lung models	175
Fig. 5.15. Particle transport in alveolar DBU model at t= 2s, 3s, 4s	177
Fig. 5.16. WLAM III (multi-path whole lung model)	179
Fig. 6.1 Comparison of total lung deposition prediction by WLAM I and WLAM II with experimental results for (a) TV 500ml and (b) TV 1000ml.....	187

ABBREVIATIONS AND SYMBOLS

1-D	One-dimensional
3-D	Three-dimensional
ρ	Density
ω	Pseudo-vorticity
ν	Kinetic viscosity
μ	Dynamic viscosity
σ_ν	Turbulent Schmidt number
ARDS	Acute Respiratory Distress Syndrome
ALI	Acute Lung Injury
C_{lim}	Clip factor
CAD	Computer Aided Design
CFD	Computational Fluid Dynamics
CF-PD	Computational Fluid-Particle Dynamics
CNT	Carbon Nano Tube
CT	Computerized Tomography
d	Distance from the field point to the nearest wall
d_p	Particle diameter
DBU	Double Bifurcation Unit
DE	Deposition Efficiency
DF	Deposition fraction

DPI	Dry Powder Inhaler
FSI	Fluid Structure Interaction
ICRP	International Commission on Radiological Protection
k	Turbulence kinetic energy
LRN	Low Reynolds number
NP	Nanoparticles
P	Pressure
pMDI	pressurized Metered-Dose Inhaler
RANS	Reynolds-Averaged Navier-Stokes
SST	Shear Stress Transport
t	Time
TB	Tracheobronchial region
TBU	Triple Bifurcation Unit
TKE	Turbulent Kinetic Energy
u	Velocity
\bar{u}_i	Time-averaged velocity
u_i	Velocity vector (same for u_j)
WLAM	Whole Lung Airway Model

CHAPTER 1

Introduction

1.1 Need for lung modeling

Inhaled materials into the human lung airways include gases/vapors, liquid droplets and soluble/insoluble particulate matter, which can be toxic or therapeutic (or both). For example, drug aerosols, as part of pulmonary medicine, are now being used as drug carriers for passive and active targeting of solid tumors and inflamed tissue. However, natural and especially manmade aerosols can also be harmful, such as carbon nanotubes (CNTs), asbestos fibers, automobile combustion engine emissions, cigarette smoke particle and ambient toxic pollutants. In fact, ultrafine particles have been found to pose a higher toxicity impact than larger particles made of the same material, mainly due to the more uniform deposition patterns in lung airways and easier migration across several barriers into the systemic system. Investigations related to the deposition and removal of inhaled particles are of great importance because accumulation and retention of toxic particles can result in serious lung diseases, including, chronic bronchitis, lung fibrosis, silicosis, asbestosis, lung cancer, etc. At the same time, respiratory drug delivery is becoming an increasingly popular way of administering medicine. It is efficient in treating both pulmonary and systemic pathogenic conditions. Hence, mathematical models and associated computer simulations, which can predict realistic particulate lung burden for specific parameters of exposure conditions, can offer valuable assistance in developing new preventive strategies. Additionally, optimal drug-aerosol targeting requires suitable physical drug-particle characteristics, appropriately controlled delivery to a pre-determined site, and an accurate assessment of the deposited medicine. The objective of the current study includes providing computational models to

predict realistic particulate lung burden and critical insight into particle deposition in lung airways.

1.2 Anatomy and morphometry of the human respiratory tract

The anatomy of a human lung can be compared to a tree. Similar to the bark, branches and leaves of the tree, the lung airways consist of trachea, bronchi, and bronchioles and the air-sacs or alveoli. Like the tree, the airway branches of the lung have thick walls, and the alveoli have thin walls and thickness of the airways gets thinner and thinner as they approach the alveoli. As the number of airway branches increases, the surface area increases. The total surface area of the upper branching system is small compared to that in the gas exchange region [1]. Air enters through the mouth or nose, then passes through the pharynx (the throat), the larynx (the voice box), and the trachea (the wind pipe). The trachea splits into two bronchi each of which feed air to one of the lungs. Each bronchi split to form bronchioles, which, in turn, split to form smaller bronchioles, and so on (see Fig. 1.1). Bronchioles extend to about 16 levels of branching before reaching the terminal bronchioles [2]. After the terminal bronchioles the airways have small projections attached to the airway duct, called the alveoli. These alveolated airways are called the respiratory bronchioles which branches again to end in an alveolar sac (see Fig. 1.3). The whole alveolated airway region is collectively known as the acinus. Acinus is the region where gas exchange occurs. The inner surfaces of the airways other than that in the acinus have a mucous layer over the ciliated epithelium tissue. Mucus layer helps in the cleaning process of the lung surfaces. It has two layers of liquid with varying viscosity. The bottom layer has a low viscous gel (hypo-phase)

and the top layer has high a viscous gel. The cilia beat in the bottom layer which pushes the top layer to move upwards against the gravity. Alveoli are the smallest unit in the lung and there are approximately 300 million of them in each lung [3]. Eventhough alveoli are tiny structures, they have a very large surface area in total ($\sim 100 \text{ m}^2$) for performing efficient gas exchange. The acinar region of the lungs is supplied with large number of pulmonary arteries to efficiently exchange gas through the large surface area of the alveoli. The blood barrier between the alveolar space and the pulmonary capillaries is a very thin membrane which easily allows rapid gas exchange. Oxygen diffuses through the alveolar tissue into the blood circulatory system during inspiration and carbon dioxide diffuses in the opposite direction during expiration.

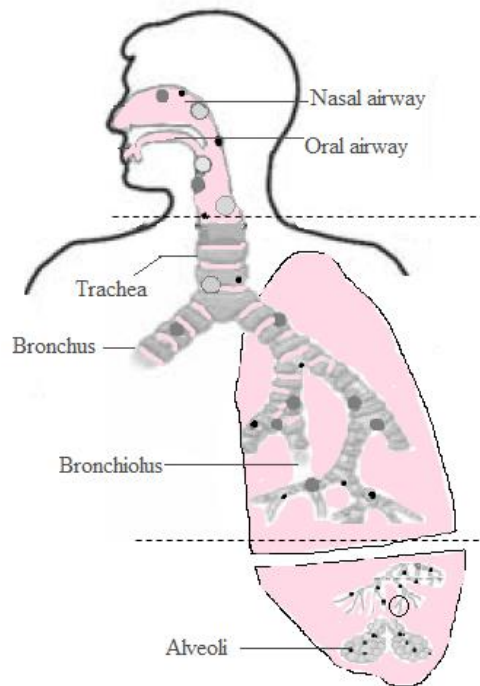


Fig. 1.1. Anatomy of the human respiratory tract.

Respiration is the outcome of contraction and relaxation of the respiratory muscles. Respiratory muscles must overcome the mechanical resistance put forward by the elastic recoil of the lung tissue and the flow resistance of the airways in order to produce inspiratory flow. The gas exchange region known as acinus has thin tissue structures which help in gas diffusion to the pulmonary blood vessels. The main objective of the upper airways and tracheo-bronchial airways is to distribute the inhaled air to the acinus.

The variation of the airway tissue composition with distance along the lung airway tree suits the specific purpose of each airway. For example, the tracheo-bronchiolar airways support the lung, connect the lower alveolar region to the upper extra-thoracic airways, and distribute the inhaled air to the gas exchange region. Hence, these airways are stiffer compared to the deeper airways. Although the trachea is considered to be the stiffest of all airways, it may undergo significant deformation due to intra-thoracic pressure during breathing. The trachea is a fibro-elastic tube composed of 15-20 C-shaped cartilaginous rings along its tube. These rings are connected by a muscular membrane. The mechanical properties of the tracheal cartilage structure affect the airflow. Changes in wall mechanical properties have been associated with obstructive lung diseases. Deterioration of the cartilaginous tissue, due to infection, which leads to loss of wall rigidity, is one of the prominent tracheal diseases [4].

The tissue structure of a bronchial airway is different from that of a tracheal airway. The stiffness of the airway decreases down the airway tree which can be attributed to the decrease in the cartilage content [5]. The schematic representation of variation of airway wall structure down the airway tree is depicted in Fig. 1.2. The surface of the airway is covered with epithelial cells which hold the cilia. The epithelial layer is anchored to the sub-epithelial

collagen layer by a basement membrane. These three layers are considered to compose the mucosa. Outside the mucosa is the sub-mucosa, which contains mainly proteoglycans which consists of long carbohydrate chains. Smooth muscle layers can be noticed on the outer regions of the sub-mucosa. The outer layer adventitia tethers the airways to the lung parenchyma. The sub-epithelial collagen layer, sub-mucosa and the smooth-muscle layer are considered to mainly contribute to airway rigidity.

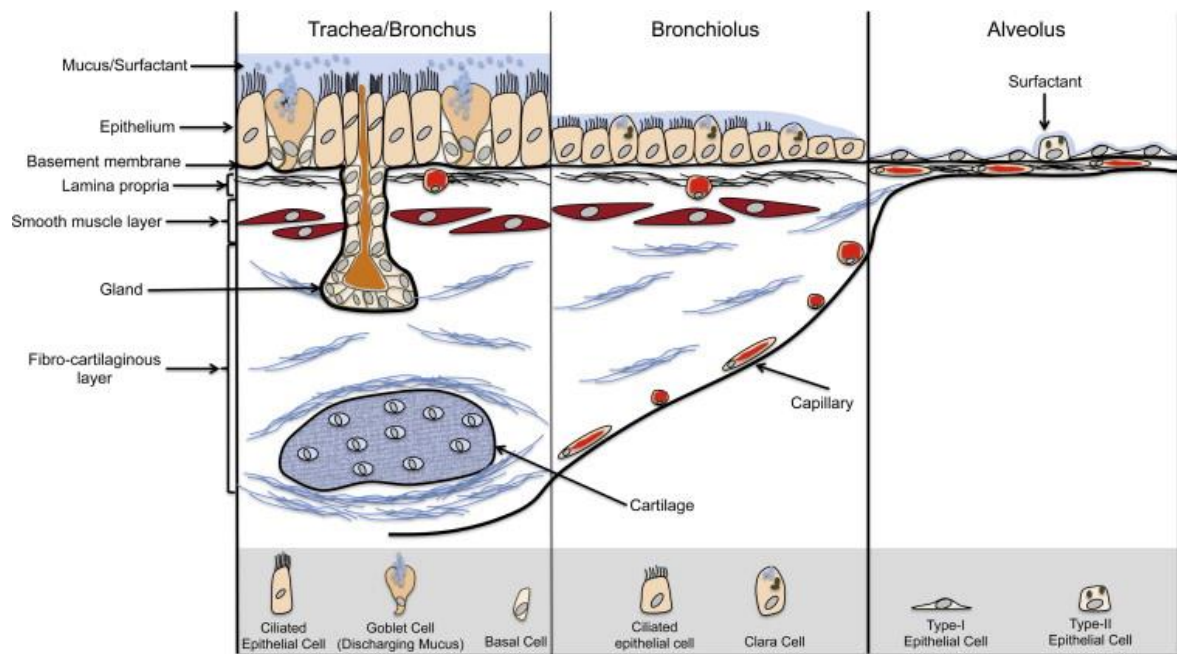


Fig. 1.2. Schematic representation of variation of airway wall structure down the airway tree (adapted from [5] with permission from Elsevier)

1.3 Lung morphometric models

Measurements of the lung flow and pressure are required for identifying and providing treatment options for many of the lung diseases. However, direct measurements of these parameters are difficult to obtain especially in the smaller airways. Hence, mathematical models were developed to estimate these parameters in the respiratory lung airways. Most of these models assumed a morphometric model for the lung. Among the different models the symmetrical lung model published by Weibel [2] is the most commonly used. The symmetrical dichotomic structured lung model reported by Weibel [2], features all 23 lung generations of which the first 16 are conducting airways and the remaining are alveolated ducts (see Fig. 1.3 and refer Table 1.1). Apart from the alveolar duct volume, the volume of alveoli in generations 17 to 23 has been added based on the approximate number of alveoli per generation [6]. Weibel obtained airway measurements of a resin casted human lung up to the 5th generation and partially to the 10th generation. Microscopic analysis of lung tissue samples from conventional histological techniques and scaling laws were then applied to estimate the measurements for the very small airways. Alternative lung-configurations have been proposed in references as well [7-11].

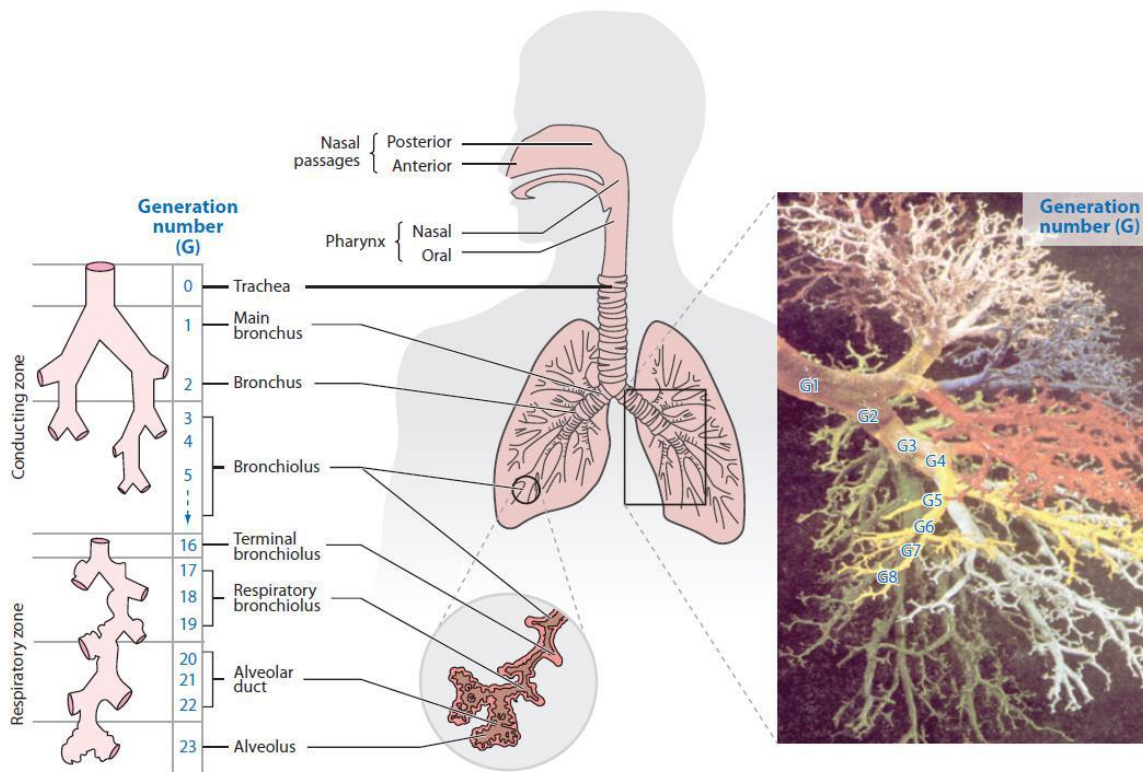


Fig. 1.3. Schematics of the human airway tract (from [12])

Table 1.1. Model dimensions for generations 0 to 23. (based on Weibel [2])

Generation number	No: of airways	Length (cm)	Diameter (cm)	Total Surface area (cm ²)	Accumulated volume (cm ³)
0	1	10.26	1.539	19.07	19.07
1	2	4.07	1.043	6.95	26.027
2	4	1.624	0.71	2.57	28.598
3	8	0.65	0.479	0.93	29.53
4	16	1.086	0.385	2.02	31.55
5	32	0.915	0.299	2.05	33.61
6	64	0.769	0.239	2.206	35.81
7	128	0.65	0.197	2.53	38.35
8	256	0.547	0.159	2.77	41.13
9	512	0.462	0.132	3.23	44.36
10	1024	0.393	0.111	3.89	48.25
11	2048	0.333	0.093	4.630	52.88
12	4096	0.282	0.081	5.949	58.839
13	8192	0.231	0.07	7.27	66.11
14	16384	0.197	0.063	10.05	76.17
15	32768	0.171	0.056	13.79	89.96
16	65536	0.141	0.051	18.86	108.835
17	131072	0.121	0.046	26.34	139.31
18	262144	0.1	0.043	38.04	190.6
19	524288	0.085	0.04	55.97	288.16
20	1048576	0.071	0.038	84.39	512.94
21	2097152	0.06	0.037	135.224	925.04
22	4194304	0.05	0.035	201.667	1694.16
23	8388608	0.043	0.035	346.867	3000

1.4 Lung diseases and pulmonary drug delivery

Unlike other major causes of death, such as cardiovascular disease and cancer, the incidence of lung disease and lung disease-associated death are increasing. Lung diseases can be generally classified as obstructive or restrictive lung diseases. Patients with obstructive lung diseases have shortness of breath due to difficulty in exhaling the air out of the lung. The main reason for this disease is the damage to the lungs or narrowing of the lung airways leading to obstruction to the exhaled flow. Restrictive lung disease most often results from a condition causing stiffness in the lungs themselves. Major lung diseases include:

Asthma: It is an inflammatory disease that may lead to obstruction of the bronchial airways. It is a major health problem affecting millions of people worldwide. For example, in 2012, 26 million (thirteen percent) of the U.S adult population had been diagnosed with asthma, and 16 million (8%) still have asthma [13]. More than 10 million U.S. children under age 18 (14%) have been diagnosed with asthma of which 6.8 million children still have asthma (9%) [14]. More than 10 % of adults and 35 % of children worldwide are affected by asthma [15]. About \$56 billion are spent on asthma treatment every year. In spite of this, there is increasing evidence, indicating that the current treatment options are not effective in controlling asthma. Despite having recent advancements in aerosol drug formulations and delivery devices, disease control using current therapies is not achieved in large proportion of patients with asthma and this leads to long term consequences such as respiratory impairment and even permanent airway alterations [15-17].

Chronic Obstructive Pulmonary Disease (COPD): It refers to chronic obstructive bronchitis and emphysema that are characterized by obstruction of normal airflow and it is

usually associated with an abnormal inflammatory response of the lung airway tissue. COPD is the fourth leading cause of death in America. Patients with chronic obstructive bronchitis have inflammation in the bronchial airways which leads to excess production of mucus and tissue scarring. Emphysema is caused by the structural collapse of the alveolar sacs within the lungs which leads to shortness of breath and reduced surface area for gas exchange.

Cystic Fibrosis: It is a genetic condition that results in unusually thick mucus. This thick mucus will not be easily cleared out of the airway vessels and hence it may accumulate leading to coughing and frequent lung infections.

Acute Respiratory Distress Syndrome (ARDS) and Acute Lung Injury (ALI): It involves respiratory failure resulting from various diseases or injuries to the lungs. It is a severe respiratory ailment that is a major cause of mortality for patients in the Intensive Care Unit.

Treatment options for lung diseases primarily involve administration of pulmonary drugs to the affected lung sites. Respiratory drug delivery is becoming an increasingly popular way of administering systemic medicines as well. Pulmonary route of drug administration has many key advantages compared to other non-invasive administration methods. Pulmonary drug delivery is efficient for treating both pulmonary and systemic pathogenic conditions [18]. In cases of pulmonary lung diseases respiratory drugs are the most effective treatment option for several reasons: (i) instantaneous onset of action; (ii) minimal side effects; (iii) maximal use of drugs at the affected area. The rapid absorption of the inhaled drug through the large surface area of the alveolar lung region into systemic circulation helps in quick bio-distribution to other vital organs. Depending on the

pathological condition, it may be required to control the drug delivery [19]. In cases of localized lung tumors, it may be ideal to have perfect delivery to tumor tissues and there by avoid healthy tissue damage and other side effects. Optimal delivery of drug depends on delivery devices, aerosol characteristics, inhalation conditions and lung airway configurations. The delivery devices helps in generating drug aerosols of sufficient size and mass to be delivered to the distal lung regions along with the inhaled air/carrier gas. Over the last few years, several design modifications have helped to increase the drug delivery efficiency and optimize drug delivery to localized lung regions using inhalers [12]. The development of such drug delivery methodologies and subsequently, device prototyping require analysis of complex transport phenomena. While *in vivo* lung deposition measurements are the most ideal way to study the efficacy of the delivery device and formulation, safe and efficient clinical studies for inhaled drug products are very difficult to conduct with animals and humans. Recently, several new modeling techniques incorporating Computational Fluid-Particle Dynamics (CF-PD) tools to simulate inhalation/deposition of therapeutic drug products in lungs have introduced which can provide detailed lung deposition measurements. [1, 12, 20-30].

1.5 Research objectives and novel contributions

This research aims to address the current research needs in therapeutic drug delivery to treat lung diseases, considering intersubject variability and different inhalation scenarios. Inhaled drug therapy has become a common treatment option for most lung diseases, such as asthma

and COPD. It is timely and important to address the issues related to inhaled drug therapy and obtain pragmatic solutions, because unlike other major causes of death such as cardiovascular disease and cancer, the incidence of lung disease and lung disease-associated death are increasing. Even though, CFPD has been shown to be prudent tool for estimating particle deposition in lung airways, the lack of a detailed Whole Lung Airway Model (WLAM) limits its extensive utilization. Hence, the primary objective of the current study is to develop computational WLAMs which are physiologically accurate and computationally efficient. Two WLAMs were created during the course of this project. A *whole lung airway model I (WLAM I)*, in which actual lung geometry was radically reduced by lumping all airways together into an exponentially expanding one-dimensional conduit which looks like a trumpet. A *whole-lung airway model II (WLAM II)*, an attempt has been made to realistically and accurately represent actual transient airflow as well as inhaled particle dynamics, representing the impact of all respiratory-tract airways, i.e., from nose/mouth to generation 23.

The novel contributions of this study include development of the two whole lung-airway models which can predict segmental and total particle depositions in the human lung. The presented WLAMs are physiologically accurate reconstruction of a human lung. These models are validated against in vivo lung deposition results. These models are time-and-resources efficient tools which can be used to analyze toxicological effects of inhaled particles as well as the pharmacological impact of drugs.

Using WLAM I, proof of concept of a new methodology of delivering drug-aerosols directly from currently marketed inhaler devices to the diseased site was demonstrated, with the goal

of greatly reducing medical cost as well as side-effects. The presented WLAM II is the first whole lung model which can simulate the mass transport through the entire lung generations using CF-PD under physiological breathing conditions.

1.6 Organization

The dissertation is organized in to four chapters. The following chapter gives background information on computational lung mechanics and introduces the specifics of the computational model used in all of the simulations discussed in this work. Chapter three is divided in to two sections. First section introduces WLAM I and the models results are validated against experimental in vivo lung deposition results, while second section discusses one of the application of WLAM I in predicting the drug deposition in lung airways when inhaled from a Dry Powder Inhaler (DPI). Chapter four is also divided in to two sections. First section introduces computation modeling approach to predict the alveolar flow and particle transport using single alveolus model, while the second section provides alveolar flow and particle transport simulation results in elaborate models to cover the entire acinar region. In chapter six, WLAM II is introduced and particle deposition results are provided for different breathing conditions. The final chapter in this work consists of a summary of general conclusions.

CHAPTER 2

Introduction to Computational Modeling of Lung-Aerosol Dynamics

2.1 Background information on computational multiscale lung models

Lung-airway wall distensibility may influence the transport and deposition of particulate matter into the lung. Furthermore, wall tissue structure and its mechanical behavior are directly related to severe health problems such as asthma, emphysema, and other obstructive pulmonary diseases. Specifically, wall displacement depends on the transient net air pressure, surface stress as well as tissue structure and properties of the airways which vary greatly over the lung generations. Due to the complexity and inaccessibility of wall tissue, a complete understanding of the airway wall biomechanics has not yet been achieved. Hence, mathematical lung models were developed to study airway wall mechanics. Apart from the models developed from the morphometric measurements of lung casts, recently lung models were developed from CT or MRI scanned images. Some researchers have focused on generating anatomically accurate geometric models using bifurcation algorithms. For example, Tawhai et al., [31] generated a lung model (1-D centerline tree) of the conducting airways using a volume-filling branching algorithm (see Fig. 2.2). The limiting volume configuration for the branching algorithm was obtained using magnetic resonance imaging of the lung and the scanned images (see Fig. 2.1) from the Visible Human Project [32]. The geometric characteristics of the model mainly length, branching angle, and diameter ratios were in good agreement with previous morphometric measurements.



Fig. 2.1. Section through Visible Human Male - thorax, including heart, lungs, spinal column, major vessels, musculature (from Thorax subset) from the Visible Human Project at U.S. National Library of Medicine [32].

Tawhai et al. [33] developed a soft tissue mechanics model for large strain elastic deformation of the lung tissue. They linked the volume filling airway model to the soft tissue mechanics model so that the local volume change of the peripheral lung parenchymal tissue can be used for setting flow and pressure boundary conditions in the volume filling airway model. It was assumed in the model that each terminal bronchioles of the volume filling conducting airway model are associated with a specific region of tissue, representing the pulmonary acinus. The large deformation of the lung tissue was modeled using a nonlinear stress-strain relationship assuming incompressible, isotropic, homogeneous tissue. Lin et al. [34] suggested a method to convert the 1-D centerline airway tree to 2-D surface mesh and hence generate 3-D volume meshes of the specified section. The advantage of this technique is that the 3-D meshed geometry can be coupled with 1-D centerline tree to apply realistic

boundary conditions. Also, they proposed a multi-scale framework that can be utilized to couple 3-D airway geometries developed from CT images with 1-D centerline tree and lung parenchyma and hence provide physiologically realistic boundary conditions. Yin et al., [35] also calculated subject specific boundary conditions by registering differences between CT images at two points of the respiratory cycle. They acquired two CT datasets at different levels of lung inflation in the same scanning session and using a mesh preserving image registration algorithm [36, 37], they estimated the regional ventilation (local air volume difference). The CFD simulation results with the subject-specific boundary condition were physiologically consistent with the regional distribution of flow compared to uniform velocity and pressure boundary conditions. Yin et al., [38] further extended the model by using three CT datasets at different levels of lung inflation. Instead of using FSI simulations, Yin et al., [39] proposed a dynamical lung geometrical model in which the lung airway displacements were obtained from lung images acquired (B-spline-based hybrid registration framework) during breathing process.

Wu et al., [40, 41] proposed a novel registration algorithm to align different images of the lung during the breathing cycle. They also successfully combined different phase images to produce a super resolution image which can provide accurate anatomical details. These 4D-CT lung images can provide physiologically accurate boundary conditions and simulations. These images can be used by applying displacement boundary conditions on airway walls, which requires less computational resources when compared to Fluid Structure Interaction (FSI) simulations. However, the extraction of anatomical details is only possible in the upper airways, where wall distensibility is very less.

Wall and Rabczuk [42] modeled the FSI in a CT scanned airway geometry consisting trachea to generation 3, assuming linear elastic material property for the airway wall. They concluded that the influence of FSI is more pronounced in lower generations and in cases of acute lung diseases like COPD. The influence of surrounding tissue on airway wall deformation is mentioned in another paper Wall et al., [43, 44] , but detailed information is not provided. Recently, computational multi-scale lung models were used [44, 45] to couple large scale lung parenchymal tissue dynamics with small scale acinar tissue dynamics (called FE² strategy). This method helps in estimating realistic stress distribution on lung parenchyma and also provides physiologically consistent displacement boundary conditions for alveolar simulations. Yoshihara et al., [46] modeled the influence of mechanical properties of parenchymal tissue on airflow in a simple bifurcation model and hence showed the dependence of flow bifurcation on material property of downstream airway tissue. The lung parenchymal tissue was modeled as a nonlinear dynamic problem and the coupled micro scale alveolar level was modeled as a quasi-static problem.

Summary: The airway wall deformation is significant only in the lower lung airways, and the upper airways can be assumed to be rigid. Even though there are multi-scale models of lung, these models still lack the resolution in the lower alveolar region. Most of these models present lung geometry for the bronchiolar region and a tissue dynamics model for the distal lung regions. Hence these models cannot be used for simulating whole airflow-aerosol transport. To date, a realistic tissue dynamics model has not been developed, which can

generate physiological airflow through the entire lungs. Hence, in this modeling study, a fluid wall deformation boundary condition will be used to replicate the tissue dynamics.

2.2 Background information on computational lung-aerosol dynamics

Most of the initial lung aerosol deposition studies [47, 48] are based on micron-sized particles because they are more probable to deposit in the upper respiratory tract, whereas smaller particles are more probable to the most distal parts of the lung [49, 50]. Computational Multi-Physics Lab (CMPL) at N C State University is one of the pioneers in utilizing advanced CF-PD tools to study the deposition of inhaled particles in lung airways [51-54]. With the advancement in computational resources, improved lung airway geometrical models with multiple bifurcations [22, 51, 55], idealistic upper airway models [30, 50, 56-58], realistic oral and nasal cavity models [59-62] and subject-specific models [63, 64] were used. However, the sheer complexity of the human lung, featuring a total of 16 million complex airways, prohibits full-scale computer simulations of the fluid-particle dynamics for the entire respiratory system [20]. Additionally, realistic airway configurations are currently restricted to the few upper airway generations since lower airway configurations are not easy to reconstruct due to the limited resolution of the scanned images [29].

Modeling and simulating the fluid-particle dynamics in subject-specific respiratory tracts is quite a challenging task (see lung aerosol dynamics reviews [34, 65-68]). Major assumptions include rigid, geometrically simplified and shortened airways, steady laminar inhalation, and spherical, micron-size aerosols, i.e., solid spheres or droplets. For inhalation flow rates above 12L/min, airflow can be expected to be turbulent in the laryngeal region and a few

generations thereafter [23, 62, 64, 69]. Indeed, several numerical simulation studies have considered turbulent dispersion to capture particle transport and deposition in human lung airways especially in the first six generations [30, 70]. Modeling flow up to the first six generations requires high computational power, due to the large number of airways present, implying that simulations of the actual human respiratory tract is impossible because of the lack of detailed medical images and computer resources. Hence, simplified models by truncating some of the airway paths and by using appropriate boundary conditions have been typically employed. Use of constant pressure [71, 72] or constant mass flow rate boundary conditions [20, 60, 73] at truncated boundaries were found to produce reasonably accurate results. Nevertheless, use of other realistic boundary conditions like the impedance model (transmission line model) [74], 1-D truncated tree model [34, 75] and stochastic coupling model [76] have shown some improvements in lung airflow simulations.

Other examples of lung-airway model simplifications include the symmetrical dichotomic structured lung model which was reported by [2], featuring all 23 lung generations of which the first 16 are conducting airways and the remaining are alveolated ducts; alternative lung-configurations have been proposed by [7-11]. Popular approaches for simulating inhaled particle deposition in greatly simplified models are the semi-empirical models [28], ICRP model [77], “trumpet” model [78], deterministic single- and multiple-path models [79, 80], and stochastic multi-path lung models [81, 82]. Hofmann [68] recently reviewed the applicability of these models by comparing the deposition efficiencies of inhaled monodisperse particles predicted by these models with available experimental results. Major advantages of these simplified deposition models include easy implementation and lower

computational resource requirements. However, the deposition estimation is based on predetermined analytical correlations. Hence, these models do not predict realistically the drug inhalation conditions from, say, inhaler devices. Recently published simplified analytical modeling results by Katz et al. [83], did not provide successful comparisons with *in vivo* deposition results, due to the model's inability to successfully capture the complex secondary flow structures and resultant particle deposition in the extra-thoracic airways. As reported by the authors [83], the extra-thoracic airway has a significant influence on particle transport and deposition. Additionally, processes like drug-size changes due to evaporation/condensation and drug-wall interactions cannot be easily incorporated into these simplified models without additional corrections which again require experimental data. These limitations can be overcome by employing suitable CF-PD-modeling approaches in which the airflow and particle transport/deposition are simulated based on the solution of transport equations [84, 85]. Recently, several new modeling techniques have been introduced incorporating CF-PD tools to simulate inhalation/deposition of therapeutic drug products in lungs [1, 12, 21-30, 73, 86]. These models have been validated against experimental measurements and the results from these studies provide critical insight into device/formulation design modifications.

Only a few numerical studies have focused on modeling lung airflow in either the entire bronchiolar airways or the entire lung. Kleinstreuer and Zhang [22] and Zhang et al. [71] compared their computational results successfully with semi-empirical solutions of particle deposition, for both micron particles and nanoparticles, in lung airways up to generation 15 by using triple bifurcation unit models in parallel and in series. The results from these models

indicated that turbulent effects are prominent in the lung airways up to generation 5 (G5) and a fully developed flow assumption can be made for airflow past generation 12. Following the approach, we further improved the model by incorporating realistic extra-thoracic upper airway and alveolar airway models; hence, extending the model from mouth inlet to generation 23 [21]. Four different paths (by attaching triple bifurcating geometrical models at one of the truncated outlets) were modeled from generation 4 to generation 23. This validated, steady-state whole lung airway model provides accurate results of aerosol deposition in the conductive lung airways as well as the alveolar region.

Most of the previously reported extensive CF-PD models either considered steady-state inhalation conditions [21], or considered tracheobronchial airways only [29, 68, 71], or assumed the inhalation phase only [26]; thus, a very limited number of studies have focused on *whole lung modeling*. Multiscale modeling involving large scale models representing central airways and small scale/reduced scale modeling for peripheral airways is one the most feasible approaches to develop a representative whole lung model. Two research groups [38, 45, 87, 88] have proposed a multi-scale framework that can be utilized to couple 3-D airway geometries developed from CT images with 1-D centerline tree and lung parenchyma. There, a volume-filling algorithm was used to build the conducting airway structure. Even though the multiscale modeling approach can provide physiological lobar structures, they are still limited in resolving the asymmetrical nature of the bifurcating airways. Also, the model's efficiency is limited in estimating whole and regional particle deposition; although, large computational resources are required. Recently, we have shown that human whole lung-airways can be represented by using adjustable triple bifurcation units (i.e., in series and

parallel, in-plane and out-of-plane) which are attached to one of the truncated outlets. It effectively predicts total, segmental and regional lung depositions, utilizing limited computational resources. At the same time, it incorporates multiscale modeling, involving 3-D realistic lung-airway geometries of the extra-thoracic and upper lung airways and symmetrical conducting and alveolar airways [21]. Similar modeling approach [73, 86, 89, 90] utilizing continuous bifurcating models for the conducting airways have shown good agreement with in vivo results. However, these models [60] have several drawbacks including limited resolution for the alveolar region, lack of respiratory bronchioles, uncoupled bronchiolar and alveolar region, simulation of inhalation phase only, and artificial limitation on the particle injection timing.

Summary: Modeling aerosol transport through the lung airways is quite a challenging task. Turbulent models are required in the upper airways up to generation 6 and laminar flow can be assumed afterwards. Even though, CF-PD has been shown to be an efficient tool for estimating particle deposition in lung airways, the lack of a detailed Whole Lung Airway Model (WLAM) limits its extensive utilization.

2.3 Math modeling equations

Airflow: The Shear Stress Transport (SST) $k-\omega$ turbulence model was employed to simulate the laminar as well as turbulent flow regimes in the upper lung airways and a laminar model was used modeling airflow in other lung generations (ANSYS 15.0 CFX-Solver Modeling Guide [91]). The SST $k-\omega$ turbulence model is a conglomeration of the standard $k-\omega$ model in

the near-wall region and the standard $k-\varepsilon$ model in the far field region. The SST $k-\omega$ turbulence model has been found to accurately predict the transitional turbulence flows and particle transport in nasal and oral airway models and tracheobronchial airway bifurcations [23, 92].

The Reynolds-averaged Navier-Stokes equations (RANS) describing conservation of fluid mass and momentum for laminar-turbulent transitional flow of any incompressible Newtonian fluid with no body forces were solved numerically using Ansys CFX 15.0 (from ANSYS, Inc. (Canonsburg, PA)).

$$\frac{\partial \bar{u}_i}{\partial x_i} = 0 \quad (2.1)$$

$$\frac{\partial \bar{u}_i}{\partial t} + u_j \frac{\partial \bar{u}_i}{\partial x_j} = -\frac{1}{\rho} \frac{\partial p}{\partial x_i} + \frac{\partial}{\partial x_j} [(\nu + \nu_t) (\frac{\partial \bar{u}_i}{\partial x_j} + \frac{\partial \bar{u}_j}{\partial x_i})] \quad (2.2)$$

Where \bar{u}_i is the time-averaged velocity in three coordinate directions, i.e., $i = 1, 2,$ and 3 representing x, y, z directions in Cartesian co-ordinate system, P is the modified time-averaged pressure term, ρ is the fluid density, and ν is the kinematic viscosity and ν_t is the turbulent viscosity.

The transport equations governing the turbulent kinetic energy (k) and the specific dissipation rate (ω) are given by:

$$\rho \left[\frac{\partial k}{\partial t} + \bar{u}_j \frac{\partial k}{\partial x_j} \right] = P - \beta^* \rho \omega k + \frac{\partial}{\partial x_j} \left[(\mu + \sigma_k \mu_t) \frac{\partial k}{\partial x_j} \right] \quad (2.3)$$

$$\rho \left[\frac{\partial \omega}{\partial t} + \bar{u}_j \frac{\partial \omega}{\partial x_j} \right] = \frac{\gamma}{\nu_t} P - \beta \rho \omega^2 + \frac{\partial}{\partial x_j} \left[(\mu + \sigma_\omega \mu_t) \frac{\partial \omega}{\partial x_j} \right] + 2(1 - F_1) \frac{\rho \sigma_{\omega 2}}{\omega} \frac{\partial k}{\partial x_j} \frac{\partial \omega}{\partial x_j} \quad (2.4)$$

where

$$P = \tau_{ij} \frac{\partial \bar{u}_i}{\partial x_j} \quad (2.5)$$

$$\tau_{ij} = \mu_t \left(2S_{ij} - \frac{2}{3} \frac{\partial \bar{u}_k}{\partial x_k} \delta_{ij} \right) - \frac{2}{3} \rho k \delta_{ij} \quad (2.6)$$

$$S_{ij} = \frac{1}{2} \left(\frac{\partial \bar{u}_i}{\partial x_j} + \frac{\partial \bar{u}_j}{\partial x_i} \right) \quad (2.7)$$

and the turbulent eddy viscosity is defined using limiter and blending functions as shown below

$$\mu_t = \frac{\rho a_1 k}{\max(a_1 \omega, SF_2)} \quad (2.8)$$

Additional functions are given by:

$$F_1 = \tanh(\arg_1^4) \quad (2.9)$$

$$\arg_1 = \min \left[\max \left(\frac{\sqrt{k}}{\beta^* \omega d}, \frac{500\nu}{d^2 \omega} \right), \frac{4\rho\sigma_{\omega_2} k}{CD_{k\omega} d^2} \right] \quad (2.10)$$

$$CD_{k\omega} = \max \left(2\rho\sigma_{\omega_2} \frac{1}{\omega} \frac{\partial k}{\partial x_j} \frac{\partial \omega}{\partial x_j}, 10^{-20} \right) \quad (2.11)$$

$$F_2 = \tanh(\arg_2^2) \quad (2.12)$$

$$\arg_2 = \max \left(2 \frac{\sqrt{k}}{\beta^* \omega d}, \frac{500\nu}{d^2 \omega} \right) \quad (2.13)$$

Here, ρ is the density, $\nu_t = \mu_t / \rho$ is the turbulent kinematic viscosity, μ is the molecular dynamic viscosity, d is the distance from the field point to the nearest wall, and S is the vorticity magnitude.

Note that it is generally recommended to use a production limiter to avoid the excessive buildup of turbulent kinetic energy in the stagnation regions. For this, the term P in the k -equation is replaced by:

$$P = \min(P, C_{lim} \rho \varepsilon) \quad (2.14)$$

where C_{lim} is called clip factor and has a value of 10.

The model constants are:

$$\beta^* = 0.09, \quad a_1 = 0.31, \quad K = 0.41 \quad (2.15a-c)$$

The inner model coefficients are:

$$\sigma_{k1} = 0.85, \sigma_{\omega1} = 0.5, \beta_1 = 0.075, \gamma_1 = \frac{\beta_1}{\beta^*} - \frac{\sigma_{\omega1} K^2}{\sqrt{\beta^*}}, \quad (2.16a-d)$$

The outer model coefficients are:

$$\sigma_{k2} = 1, \sigma_{\omega2} = 0.856, \beta_2 = 0.0828, \gamma_2 = \frac{\beta_2}{\beta^*} - \frac{\sigma_{\omega2} K^2}{\sqrt{\beta^*}} \quad (2.17a-d)$$

The model coefficients (denoted with the symbol Φ) are defined by blending the coefficients of the original k - ω model, denoted as Φ_1 , with those of the transformed k - ε model, denoted as Φ_2 :

$$\phi = F_1 \phi_1 + (1 - F_1) \phi_2, \text{ where } \phi = \{\sigma k, \sigma \omega, \beta, \gamma\} \quad (2.18a,b)$$

Mesh deformation: The integral continuity and momentum equations governing the fluid flow when the domain mesh is deforming is modified using the Leibniz theorem (modified equations are given in equation 2.19 and 2.20). The displacement of the mesh nodes were controlled using displacement diffusion (ANSYS 15.0 CFX-Solver Modeling Guide [91]).

$$\int_{CS} (u_i - W_i) n_i dA = 0 \quad (2.19)$$

$$\rho \frac{d}{dt} \int_{CV(t)} u_i dV + \rho \int_{CS} (u_i - W_i) u_j n_i dA \quad (2.20)$$

$$= - \int_{CS} p n_i dA + \int_{CS} \mu \left(\frac{\partial u_i}{\partial x_j} + \frac{\partial u_j}{\partial x_i} \right) n_i dA + \int_{CV(t)} \rho g_i dV \quad (2.21)$$

$$\nabla \cdot (\Gamma_{disp} \nabla \delta) = 0$$

where W_i is the velocity of the control volume boundary and Γ_{disp} is the mesh stiffness and δ is the mesh displacement.

Particle transport: For dilute suspensions with a high density-ratio of particle-to-air is modeled using a Lagrangian approach:

$$m_p \frac{du_i^p}{dt} = \sum F_i + (m_p - m_f)g_i \quad (2.22)$$

The major point forces acting on each particle are the drag and gravity. Specifically,

$$F_i^D = \frac{\pi}{8} \rho_f d_p^2 C_D (u_i^f - u_i^p) |u_i^f - u_i^p| \quad (2.23)$$

where ρ_f is fluid density, d_p is particle diameter, u_i^f is fluid velocity where the particle center is, u_i^p is the particle velocity, and C_D is the Schiller-Naumann drag coefficient:

$$C_D = \frac{24}{\text{Re}_p} + 3.6 \text{Re}_p^{-0.313} \quad (2.24)$$

The regional deposition of micron particles in human airways can be quantified in terms of the deposition fraction (DF):

$$\text{DF} = \frac{\text{Number of deposited particles in a specific region}}{\text{Number of particles entering the mouth}} \quad (2.25)$$

Additional modifications for the governing equations made during current study are explained in each chapter.

CHAPTER 3

Whole Lung Airway Model I

3.1 Theory and model development

This chapter is a manuscript published in *Computers in Biology and Medicine* titled “Computationally Efficient Analysis of Particle Transport and Deposition in a Human Whole-Lung-Airway Model. Part I: Theory and Model Validation”. The authors of this manuscript are Arun V Kolanjiyil and Clement Kleinstreuer.

3.1.1 Introduction

Epidemiological and pathological studies have indicated that the majority of lung diseases are associated with occupational and environmental exposure to ambient aerosol pollutants [93-97]. In contrast, inhalation of drug-aerosol is a modern way of targeting lung tumors and combating systemic diseases [85, 98]. Clearly, simulating realistically and efficiently the lung-aerosol dynamics can provide critical insight into toxic particle deposition and associated pulmonary disease treatment [1, 98, 99].

However, in light of the current computational resources available, it is impossible to simulate the transient 3-D aerosol dynamics in all 23 lung generations. So, simplified configurations have to be considered which satisfy specific modeling requirements. For example, a symmetrical dichotomic structured lung model was reported by [2], featuring all 23 lung generations of which the first 16 are conducting airways and the remaining are alveolated ducts. Alternative lung-configurations have been proposed in references [7-11]. Popular approaches for simulating inhaled particle deposition are the semi-empirical models [28], ICRP model [77], “trumpet” model [78], deterministic single- and multiple-path

models [79, 80, 100], and stochastic multi-path lung models [81, 82]. Hofmann [68] recently reviewed the applicability of these models by comparing the predicted deposition efficiencies of inhaled monodisperse particles with available experimental results. The simplified deposition models are still popular because of their easy implementation and low requirements of computational resources. However, the computed deposition results are not predictive, being based on simple inlet conditions and semi-analytical correlations for the deposition mechanisms [68]. Hence, such models may not be able to predict realistically the drug inhalation conditions from inhaler devices, where inhaler mouth pieces, high momentum flow and dense drug-suspensions may significantly affect the air-particle flow to the lung. As an example, the modeling results by Katz et al. [83] did not provide successful comparison with *in vivo* deposition results, due to the model's inability to successfully capture the complex secondary flow structures and resultant particle deposition in the extra-thoracic airways. Additionally, processes like drug evaporation/condensation, agglomeration, aerosol atomization and drug-wall interactions cannot be easily incorporated into these simplified models without additional corrections which again require experimental data. While a few reduced whole-lung models have focused on these topics, these models may not be suitable for predicting complex particle dynamics when inhalers are used [101-105]. These limitations can be overcome by employing computational fluid-particle dynamics (CF-PD) techniques, i.e., a modeling approach in which the laminar/turbulent airflow and particle transport/deposition are simulated based on the solution of suitable transport equations [84, 85]. However, the sheer complexity of the human lung, featuring a total of 16 million complex airways, prohibits full-scale computer simulations of the fluid-particle dynamics for

the entire respiratory system [98]. Additionally, realistic airway configurations are currently restricted to the few upper airway generations since lower airway configurations are not easy to reconstruct due to the limited resolution of the scanned images [29]. Nevertheless, even CF-PD simulations covering only mouth/nose to generation 4 are computationally taxing and time consuming. Examples of multiscale hybrid modeling have been provided by several research teams [34, 74, 88, 106]. However, their focus was on applying appropriate boundary conditions, while detailed particle dynamics modeling was not conducted. Huang et al. [107] also employed a hybrid modeling approach where the inspiratory flow was simulated using a moving boundary condition. From their simulation results they concluded that the expanding wall motion significantly influences the flow characteristics. Additionally, most of the previously reported extensive CF-PD lung models either considered steady-state inhalation conditions [98] or focused on the tracheobronchial airways only [29, 68, 71], or assumed inhalation-phase alone [26]. Hence, in this study a whole-lung model is introduced which combines the advantages of the CF-PD technique with a simplified modeling approach for the bifurcating airway geometry and associated fluid-particle dynamics. Also, the present model has the ability to incorporate any inhalation-exhalation waveform via realistic lung-wall and air-flow interactions, rather than air being blown into or out of the lung-airway model as done so far.

In lumping the connected airways together, the resulting cross sectional area increases dramatically, which forms geometrically a trumpet-like shape. For example, Paiva [108, 109] used a trumpet model, based on the morphometric data of Weibel, to analyze the transport of gas in lung airways. Later Paiva and Engel [110, 111] employed trumpet models to analyze the dependency of intrapulmonary gas distribution on parallel geometrical

inhomogeneity and diffusivity of gas. Their study indicated that more diffusive gases can penetrate and get trapped in poor ventilated lung regions. In contrast, Taulbee and Yu [78] calculated the deposition of inhaled aerosols in lung airways using a trumpet model. Specifically, the concentration of particles was tracked using a convection-diffusion equation and the deposition was calculated with a mass balance equation containing loss terms due to diffusion, sedimentation, and impaction, assuming steady, fully-developed (parabolic) flow in cylindrical tubes. They found general agreement for simulated results of total lung deposition of particles and washin-washout particle concentration curves with experimental results. Using the same model, Yu [112] analyzed the effects of inter-subject variation of breathing pattern on total and regional lung aerosol deposition. In order to account for the asymmetry of the lung airways, improvements in trumpet model geometry have been made using published lung morphometric measurements. Darquenne and Paiva [113] simulated aerosol transport and deposition in lung airways using a trumpet model and compared the results with those in an asymmetrical multi-branch point model as well as *in vivo* experimental data. Their results suggest that symmetrical models can predict similar deposition results as those found in asymmetrical models. Also they suggested the use of multi-dimensional aerosol transport models for better accuracy. Choi and Kim [100] extended the trumped-like geometry by including new morphology for alveolar ducts and alveoli. They theoretically derived alveolar deposition considering the particle flux from alveolar duct to the alveoli during inhalation and reverse particle flux during exhalation. From these studies it is evident that the trumpet model is suitable for calculating the lung deposition of inhaled particles under transient breathing conditions.

Now, in reality the secondary flow structures created due to the bronchial bifurcation as well as the curvature of the geometry causes a radial shift in the particle trajectory which brings the particle closer to the airway walls and cause deposition [114, 115]. In addition, diffusion, sedimentation and impaction deposition mechanisms must be accounted for. It should be noted that the use of an “apparent diffusion term” in previous trumpet-model studies to account for particle dispersion has been challenged [116]. Hence, in the present study a new modeling methodology is introduced, extending the work of Mayank and Kleinstreuer [117]. Specifically, a radial force term in the Lagrangian particle transport equation is introduced, so that the 1-D conduit model can realistically predict particle deposition in actual lung airways. In summary, a first-generation whole-lung-airway model (WLAM I) is presented where the respiratory tract geometry is first represented by a 3-D mouth-to-trachea configuration and then all subsequent airways are lumped together into an exponentially expanding 1-D conduit. The extra-thoracic airway has a significant influence on particle transport and deposition in the lung airways; hence, it is not advisable to reduce the extra thoracic airway geometry to simplified shapes, as done in previous simplified modeling approaches. So, adding a representative (or subject-specific) 3-D oropharyngeal airway model improves the accuracy of whole-lung simulations. The model dimensions were calculated based on the morphometric data reported in Weibel [2]. Similar to the expansion and contraction of the thoracic cavity, the WLAM-volume expands and contracts producing pressure differences resulting in realistic inward and outward flow waveforms. The volume of airways in a particular generation was summed up to find the resultant total volume of the generation. The diameter per generation of the WLAM I was calculated from the total

volume of each generation. The particle deposition results were compared with *in vivo* data sets reported in the literature.

3.1.2 Model geometry

As an example, the standard human upper lung-airway model of [50, 70] was selected as part of the WLAM I plus all volume additions to accommodate the remaining generations. Specifically, the volume of airways in a particular generation (from generation 2 onwards) was summed up to find the resultant total volume of each generation. The diameter for each generation of the model was obtained from the calculated total volume. The remaining generations were created based on the calculated diameter. This modeling approach helps to maintain a detailed mesh for the actual upper respiratory tract where complex flow characteristics occur and a coarse mesh for the remaining part. The geometric data for all 23 generations are listed in Table 1. Apart from the alveolar duct volume, the volume of alveoli in generations 17 to 23 has been added based on the approximate number of alveoli per generation [6]. The total volume was taken to be 3000 cm^3 , which is the average human lung volume. Noticing that the 23rd airway generation of the WLAM I has a diameter of 39.8 cm and only 0.071cm in thickness, it is inappropriate to generate a mesh with this dimension. Hence, the 22nd and 23rd airway-generation diameters were changed to be the 21st airway-generation diameter and the length of the airway was calculated keeping the volume constant. Figure 3.1.1 depicts the WLAM I.

Table 3.1. Model dimensions for generations 0 to 23.

Generation	Length (cm)	Volume per generation (cm ³)	WLAM I radius (cm)
0	10.26	19.07	0.76
1	4.07	6.95	0.70
2	1.62	2.57	0.71
3	0.65	0.93	0.63
4	1.09	2.02	0.89
5	0.92	2.05	0.79
6	0.77	2.20	1.10
7	0.65	2.53	1.12
8	0.55	2.77	1.41
9	0.46	3.23	1.56
10	0.39	3.89	1.97
11	0.33	4.63	2.23
12	0.28	5.94	2.93
13	0.23	7.27	3.39
14	0.2	10.05	4.64
15	0.17	13.79	5.48
16	0.14	18.86	7.51
17	0.12	30.47	10.32
18	0.10	51.29	15.09
19	0.08	97.56	22.88
20	0.07	224.78	39.86
21	0.06	412.10	53.35
22*	0.23	769.12	53.35
23*		1305.84	
Total	23.45	3000	

***Note:** If generations 22 and 23 are considered with a diameter of 53.35 cm (i.e., equivalent to a generation 21 diameter), the length calculated for the equivalent volume is $L = 0.23$ cm

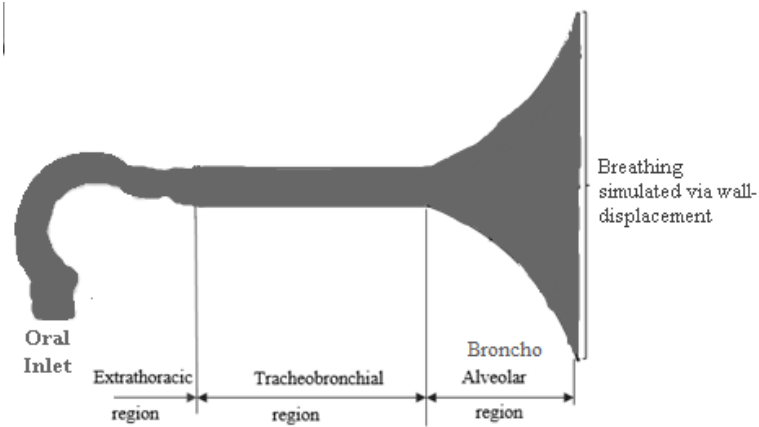


Fig.3.1.1: Schematic of whole lung airway model (WLAM I)

3.1.3 Governing Equations

Airflow: The Shear Stress Transport (SST) $k-\omega$ turbulence model was employed to simulate the laminar, transitional and fully turbulent flow regimes. The SST $k-\omega$ turbulence model is a conglomeration of the standard $k-\omega$ model in the near-wall region and the standard $k-\epsilon$ model in the far field region. The SST $k-\omega$ turbulence model has been found to accurately predict the transitional turbulence flows and particle transport in nasal and oral airway models and tracheobronchial airway bifurcations ([23, 92]).

The Reynolds-averaged Navier-Stokes equations (RANS) are commonly used to describe conservation of mass and the momentum for laminar-turbulent flow in this case:

$$\frac{\partial \bar{u}_i}{\partial x_i} = 0 \quad (3.1)$$

$$\frac{\partial \bar{u}_i}{\partial t} + \bar{u}_j \frac{\partial \bar{u}_i}{\partial x_j} = -\frac{1}{\rho} \frac{\partial P}{\partial x_i} + \frac{\partial}{\partial x_j} [(v + \nu_t) (\frac{\partial \bar{u}_i}{\partial x_j} + \frac{\partial \bar{u}_j}{\partial x_i})] \quad (3.2)$$

Where \bar{u}_i is the time-averaged velocity in three coordinate directions, i.e., $i=1, 2,$ and $3,$ P is the modified time-averaged pressure term, ρ is the fluid density, and ν is the kinematic viscosity and ν_t is the turbulent viscosity.

The transport equations governing turbulent kinetic energy (k), specific dissipation rate (ω) and other sub models with additional functions for the SST $k-\omega$ turbulence model are given in chapter 2 [23, 92].

Particle transport: Particle transport for dilute suspensions with a high density-ratio of particle-to-air is modeled using a Lagrangian approach:

$$m_p \frac{du_i^p}{dt} = \sum F_i + (m_p - m_f) g_i \quad (3.3)$$

The major point forces acting on each particle are the drag, gravity, and a radial force to compensate for the absence of airway bifurcations in the simplified model. Specifically,

$$F_i^D = \frac{\pi}{8} \rho_f d_p^2 C_D (u_i^f - u_i^p) |u_i^f - u_i^p| \quad (3.4)$$

where ρ_f is fluid density, d_p is particle diameter, u_i^f is fluid velocity where the particle center is, u_i^p is the particle velocity, and C_D is the Schiller-Naumann drag coefficient:

$$C_D = \frac{24}{\text{Re}_p} + 3.6 \text{Re}_p^{-0.313} \quad (3.5)$$

Clearly, the secondary flow in the airway bifurcations as well as the wall curvature cause a radial shift in the particle trajectories, which may lead to particle deposition. This effect is

captured in the WLAM I by incorporating a radial force acting on the particles. *In vitro* and *in vivo* deposition studies revealed that, in addition to the individual lung-airway geometry, particle deposition largely depends on the inhalation flow rate, the particle diameter, and the inhalation tidal volume. Based on a comprehensive comparison with experimental results [118], the following expression for the radial force term was developed, which predicts particle deposition in lung airways under a wide range of inlet conditions:

$$F_{\text{radial}} \hat{i} = T_{\text{ratio}}^{0.5} Q_{\text{ratio}}^{0.5} 2.7(10^{-15})(10d_p)^{2.4} \cdot \vec{r} \quad (3.6)$$

where d_p is the aerodynamic particle diameter in micron and \vec{r} is the unit vector in radial direction. The other parameters are defined as follows:

$$T_{\text{ratio}} = \frac{\text{tidal volume in ml}}{500\text{ml}} \quad (3.7)$$

and

$$Q_{\text{ratio}} = \frac{\text{average inspiratory flow rate in L/min}}{15 \text{ L/min}} \quad (3.8)$$

The radial force is activated in the particle transport equation when a particle reaches the first lung airway generation. As a base case, the coefficients of the radial force were estimated by comparing the particle deposition results with measured *total* lung deposition results, reported by Heyder et al., [119] for a flow rate of 15 L/min (LPM) and a tidal volume of 500 ml.

The regional deposition of micron particles in human airways can be quantified in terms of the deposition fraction (DF):

$$DF = \frac{\text{Number of deposited particles in a specific region}}{\text{Number of particles entering the mouth}} \quad (3.9)$$

3.1.4 Numerical method

The governing equations for airflow and particle transport were solved with a user-enhanced commercial CF-PD package (i.e., CFX, Version 15 from ANSYS, Inc. (Canonsburg, PA)). Steady state simulations were conducted using the 3-D upper airway model (up to trachea) and transient simulations were conducted using the WLAM I. The airflow characteristics in the 3-D upper airway model with the steady state assumption and the respective approximated boundary condition were compared with transient inhalation-exhalation waveforms for the WLAM I. It is postulated that a steady state assumption can capture the airflow characteristics at the peak mass flow rate conditions (see Zhang et al. [53]), however, transient simulation are required to account for the intrinsic flow behavior during flow reversal. The run time for a transient whole-lung simulation on an engineering workstation (Dell computer with 32 GB RAM and four 3.0-GHz Intel Xeon processors) was 7 hours for completing 1sec of inhalation with 60,000 particles. That is 10 times less than that for steady fluid-particle dynamics simulations with an idealized whole-lung geometry reported in [98].

Mesh: The geometrical models were meshed using ICEM from ANSYS, Inc. (Canonsburg, PA). The oral-upper airway domain (up to generation 3) of the WLAM I consists of tetrahedral elements with five prism layers and the bronchoalveolar domain of the WLAM I consists of tetrahedral elements with two prism layers. A mesh convergence study by comparing the velocities at different cross sections as well as regional particle depositions

was performed to ensure grid independency of the results. Increasing the number of elements by a factor of 1.5 showed less than 1% of difference in these results. The final mesh for the oral-upper airway model had 1.5 million elements and the idealized broncho-alveolar model had 2.8 million elements.

Boundary conditions: For the steady-state simulations in the 3-D oral-upper airway model, a uniform zero gauge pressure condition was applied at the outlets and mass flow rate boundary conditions (i.e., $Q= 15 \text{ LPM}$, 30 LPM , 45 LPM and 60 LPM) were applied at the oral inlet. The no-slip boundary condition was applied on the airway walls.

For the transient simulations using WLAM I, the breathing mechanism due to the negative alveolar pressure was simulated by applying wall movement boundary conditions at the bottom surface of the model. By controlling the displacement of the bottom wall, the required negative alveolar pressure and hence the mass flow rate was created. A similar approach has been used by Huang et al. [107], in which the inspiratory flow was modeled using a moving boundary condition. They attached a bell-mouthed tube to the oropharynx geometry, so that the mesh motion of the bell-mouth tube replicates the negative alveolar pressure. The displacement of the moving wall boundary was determined from the airflow rate and the area of the moving-wall surface. For the simulations, uniform zero gauge pressure condition was applied at the oral inlet. Again, the no-slip boundary condition was applied on the airway walls. Particles were distributed uniformly at the oral inlet with an initial velocity being the same as the inlet-air velocity. 15, 000 particles per second per diameter were injected at the oral inlet and particles were assumed to deposit on the walls on contact.

The realistic 3-D oral-upper airway model was connected to the 1-D geometric expansion using the domain interface coupling method. This interface modeling helps to reduce the

mesh generation effort. Clearly, the extra-thoracic airway model needs a fine mesh to simulate all the secondary flow structures, while the 1-D model requires only a relatively course mesh. A fluid-fluid interface algorithm maps the results from the boundary of one domain to the other domain [91].

3.1.5 Results and discussion

3.1.5.1 Airflow

The WLAM I was used to simulate different breathing conditions. Figure 3.1.2a depicts a synthetic breathing profile during light activities, where a mass flow rate of 15 LPM was assumed. Figure 3.1.2b shows the breathing profile during a heavy activity, resulting in a mass flow rate of 30 LPM. The simple breathing waveforms shown here were selected in order to compare the model predictions with experimental data sets in which subjects inhaled and exhaled with constant mass flow rates. Clearly, by controlling the end-wall displacement, any inhalation wave forms can be simulated, which implies that the WLAM I is capable of simulating actual breathing patterns.

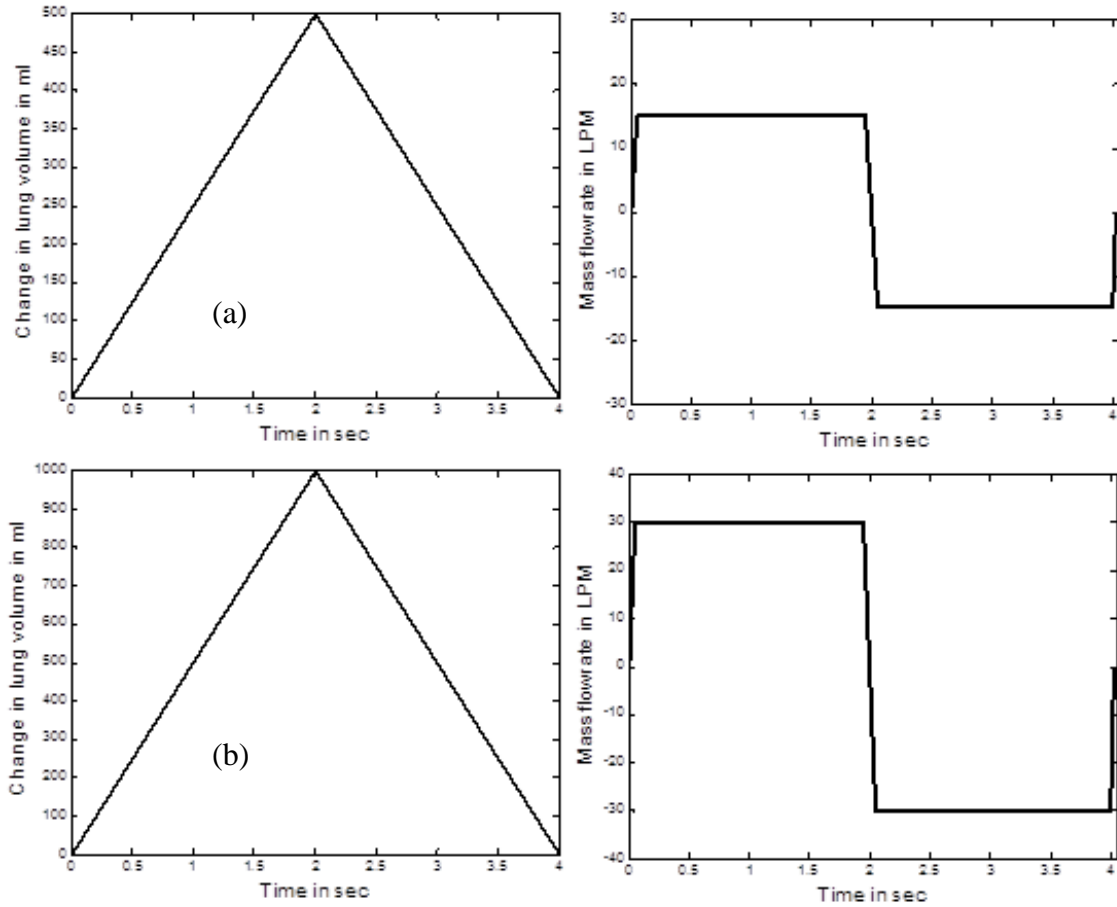


Fig.3.1.2. Breathing profiles depicted in terms of the changes in lung volume and the corresponding mass flow rates: (a) inhalation flow rate 15 LPM and tidal volume 500 cm³; and (b) inhalation flow rate 30 LPM and tidal volume 1000 cm³

Figure 3.1.3 illustrates the mean velocity contours and representative velocity vectors in the mid-plane of the 3-D oral-upper airway geometry for different inhalation flow rates. At all inhalation flow rates an asymmetric laryngeal jet is prominent after the oropharynx due to the sudden geometric constriction at the glottis. The velocity of the laryngeal jet increases as the flow rate is elevated from light activity to exercise condition. The pressure gradient induced

by the centrifugal force, generated at the curvilinear cross-section of oropharynx, causes secondary flows (cross section A-A1 and B-B1). Due to this sudden change in flow direction at the oropharynx, several recirculation zones can be observed. Also, secondary flow structures caused by the laryngeal jet appear in the trachea. At the end of the trachea, the flow becomes blunt (maximum velocity zones is seen near the anterior wall in cross section D-D1) due to the redistribution of the flow kinetic energy.

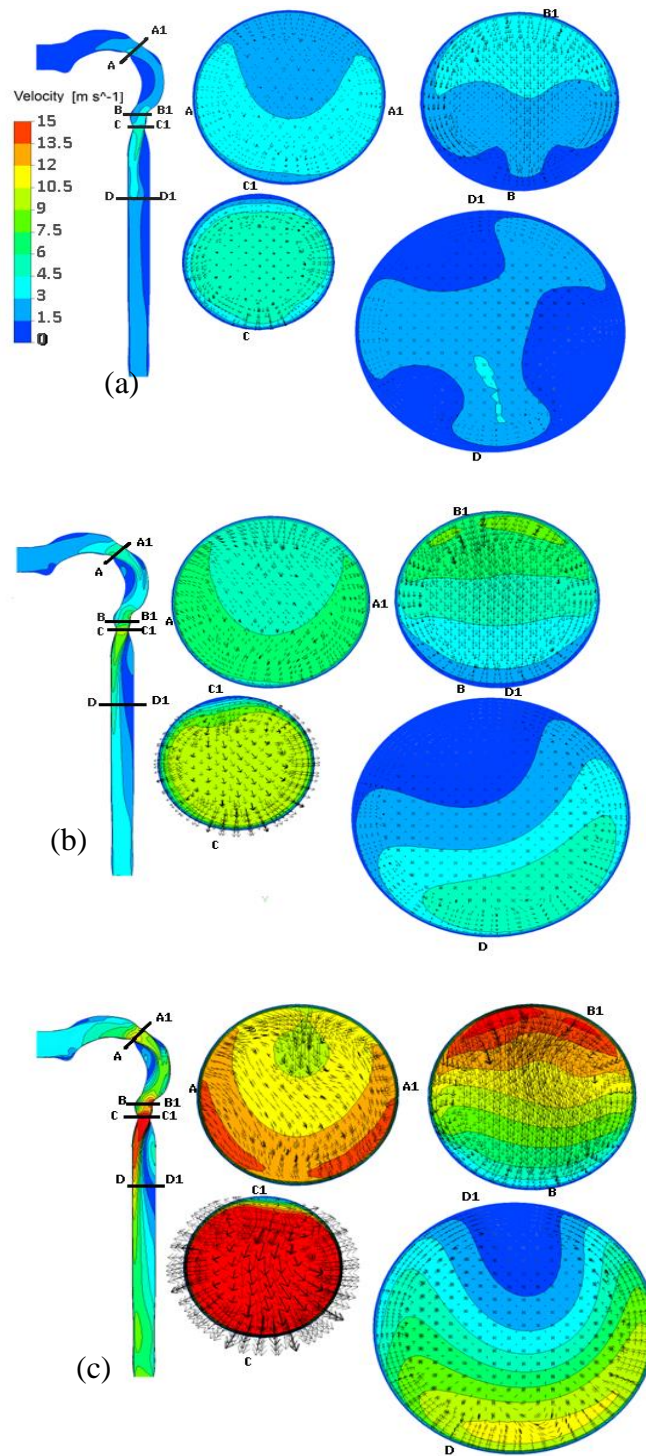


Fig. 3.1.3: Velocity contours and secondary velocity vectors in the mid-plane of the idealized oral-upper airway geometry at steady inhalation flow rates: (a) 15 LPM; (b) 30 LPM; and (c) 60 LPM.

Figure 3.1.4 shows the velocity contours and representative secondary velocity vectors in the mid-plane of the WLAM I upper airway geometry during transient breathing with a peak flow rate of 30 LPM (see breathing profile in Fig. 3.1.2). As postulated, the velocity profiles obtained under transient breathing conditions match the simulation results for steady inhalation (Fig. 3.1.4a). When the flow is in the inhalation phase, the negative pressure gradient produced by the bottom wall displacement drives the air into the lung. The opening boundary condition applied at the oral inlet ensures that the velocity profile at the inlet was calculated from the regional airflow field. Several secondary vortices were created when the breathing phase changed from inhalation to exhalation (see Fig. 3.1.4b). Due to the flow reversal, the maximum velocity zone is shifted to the posterior wall from the anterior wall, which created a secondary flow from the anterior wall to the posterior wall. These secondary vortices were damped out once the airflow reached steady exhalation. During peak exhalation, the flow is tubular in the upper airways before it reaches the glottis. A laryngeal jet towards the upper mouth palate is created due to the glottis. The majority of the exhaled air passes through the middle to upper portion of the oral cavity which results in a blunt velocity profile in the oral cavity (see Fig. 3.1.4c).

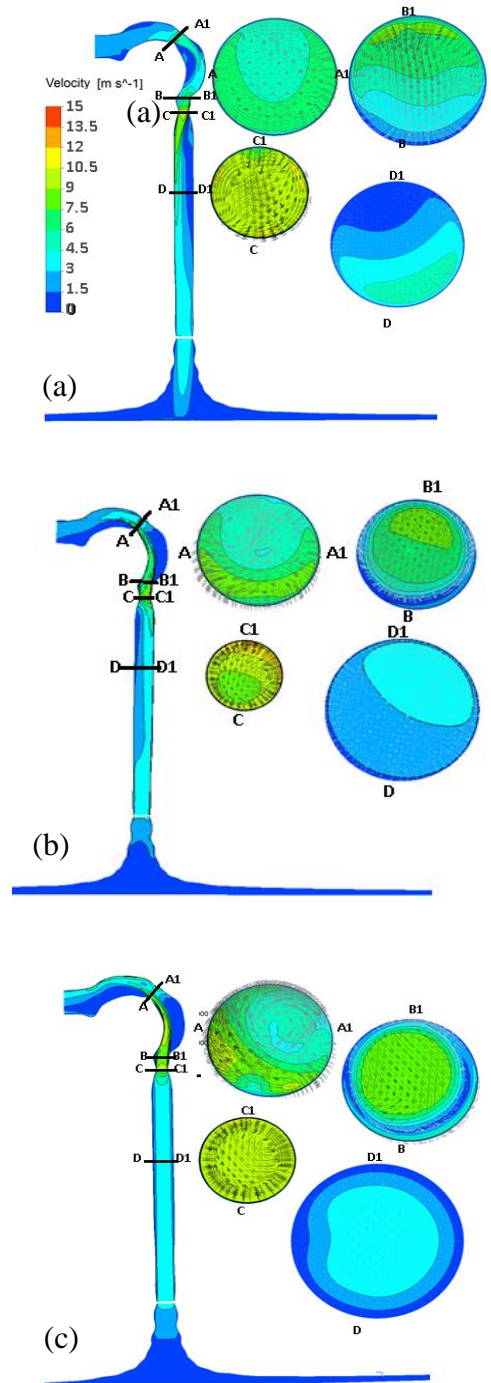


Fig. 3.1.4: Velocity contours and representative secondary velocity vectors in the mid-plane of the idealized oral-upper airway geometry during transient breathing with a flow rate of 30 LPM: (a) peak inhalation; (b) start of exhalation; and (c) peak exhalation.

3.1.5.2 Particle transport

Steady-state simulation results for the oral-tracheobronchial airways: Particle depositions were first analyzed under steady-state conditions for oropharyngeal and tracheobronchial regions separately, and then in Fig. 3.1.5 compared to experimental data from Cheng et al. [120]. Particle transport and deposition were simulated for inhalation flow rates of 15, 30 and 60 LPM and particle diameters of 0.93, 1.79, 2.79, 4.0, 6.07, 9.8, 16, 23.8 and 30 μm . The results are plotted in terms of Stokes number, defined as $St = \rho_p d_p^2 U / 9\mu D_h$, where ρ_p is the particle density, d_p is the particle diameter, U is the mean inlet velocity based on the mean inlet cross-sectional area, and D_h is the minimum hydraulic diameter. The predicted results show a good agreement with the experimental observations, following the well-known ‘S’-curve. Deposition results in the oropharyngeal region have been compared with several other experimental studies (see Section 3.1.5.3). The steady-state deposition results in the oral/lung casts from recent studies (see [121-124]) have been successfully compared with published results (Cheng et al. [120], Chan and Lippmann [125], Stahlhofen et al., [126]; among others).

Also insightful is Fig. 3.1.6, indicating the degree of deposition in the idealized tracheobronchial airways as a function of particle diameter, where the 16 μm particle appears to be an outlier in Cheng et al. [120]. The deposition trend is similar for different inhalation flow rates. Deposition peaks around 10 μm . The peak shifts to the left side as the inhalation flow rate increases. For particle diameters below 15 μm the deposition is a maximum at the lowest inhalation flow rate. Less particles reach the lower airways for particle diameters

above $15 \mu m$, as larger diameter particles tend to deposit in the oropharyngeal cavity due to inertial impaction. When the inhalation flow rate increases, the trachea-bronchial deposition decreases because more particles are deposited in the oropharyngeal area, again, due to inertial impaction. The results indicate that the current modeling methodology accurately predicts total as well as segmentally averaged particle depositions in human lung airways. Similar to the deposition study for the oral airway cast, recent experiments, using tracheobronchial lung casts (see [122-124]), have shown comparable results published results (Chan and Lippmann [125] and Cheng et al. [120]).

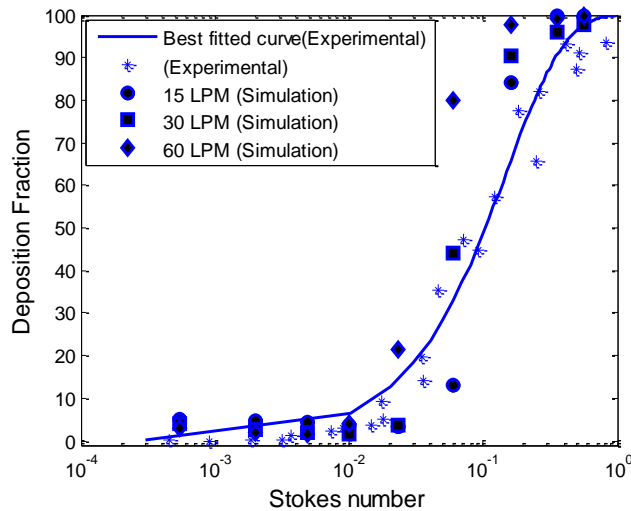


Fig. 3.1.5. Comparison of particle deposition in the idealized mouth-throat geometry with experimental results from Cheng et al. [120]

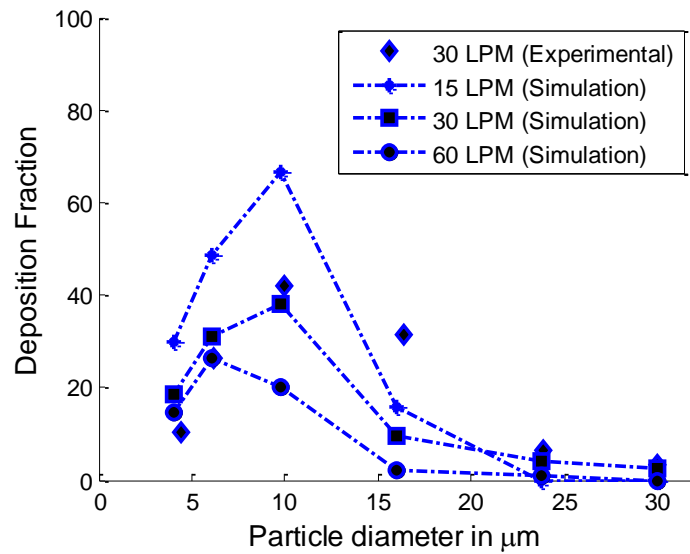


Fig. 3.1.6. Comparison of particle deposition in the idealized upper airway model with experimental results from Cheng et al. [120]

Transient simulation in WLAM I: The WLAM I is able to capture the transient airflow and particle behavior under realistic breathing conditions, providing total as well as regional particle deposition results. By assuming a closed geometry, the model is replicating the human lung action while breathing. The total and regional particle deposition results under transient conditions were compared with measured *in vivo* deposition results reported by Heyder et al. [119] and Kim and Hu [127]. All simulations were performed with a lung model having a functional residual capacity of 3L and the mean experimental values are compared with the simulation results. Particle deposition was studied for inhalation/exhalation flow rates of 15 LPM with tidal volume 500 cm^3 , 15 LPM with tidal volume 1000 cm^3 , 15 LPM with tidal volume 1500 cm^3 , 30 LPM with tidal volume 1000 cm^3

and 45 LPM with tidal volume 1500 cm³ and particle sizes 0.4 μm to 15 μm were considered. For example, Fig. 3.1.7a shows the comparison of particle deposition in the WLAM I with experimental results from [119, 127] for inhalation flow rate 15 LPM and tidal volume 500 cm³. The scenario simulated is similar to a breathing pattern at rest (i.e., 15 breaths per minute). The predicted particle deposition agrees with the experimental data, except a slight over-prediction for particles > 5 μm.

To examine the effect of tidal volume on particle deposition, two other breathing patterns were considered; shallow (15 LPM with tidal volume 1000 cm³) and deep breathing (15 LPM with tidal volume 1500 cm³). Figure 3.1.7b and 3.1.7c show the comparison of particle deposition with experimental results from [119, 127] for these two conditions. In the case of slow but deep breathing (see Fig. 3.1.7c), whole lung deposition already occurs for smaller particles. This may be due to the increase in the particle residence time, i.e., more particles tend to reach the alveolar region.

The influence of the inhalation flow rate was examined by simulating the particle deposition under exercise breathing conditions. Figure 3.1.7d and 3.1.7e show the comparison of particle deposition with experimental results from [119, 127] for 30 LPM with tidal volume 1000 cm³ and 45 LPM with tidal volume 1500 cm³, respectively. The deposition trends reveal that the shape of the deposition curves is maintained even though the curve shifts up and down depending on the inhalation flow rate. The slope of the curve is steeper when the inhalation flow rate is high, indicating that more particles are deposited in the respiratory tract due to inertial impaction. In summary, the current modeling methodology accurately predicts total particle deposition in whole-lung airways.

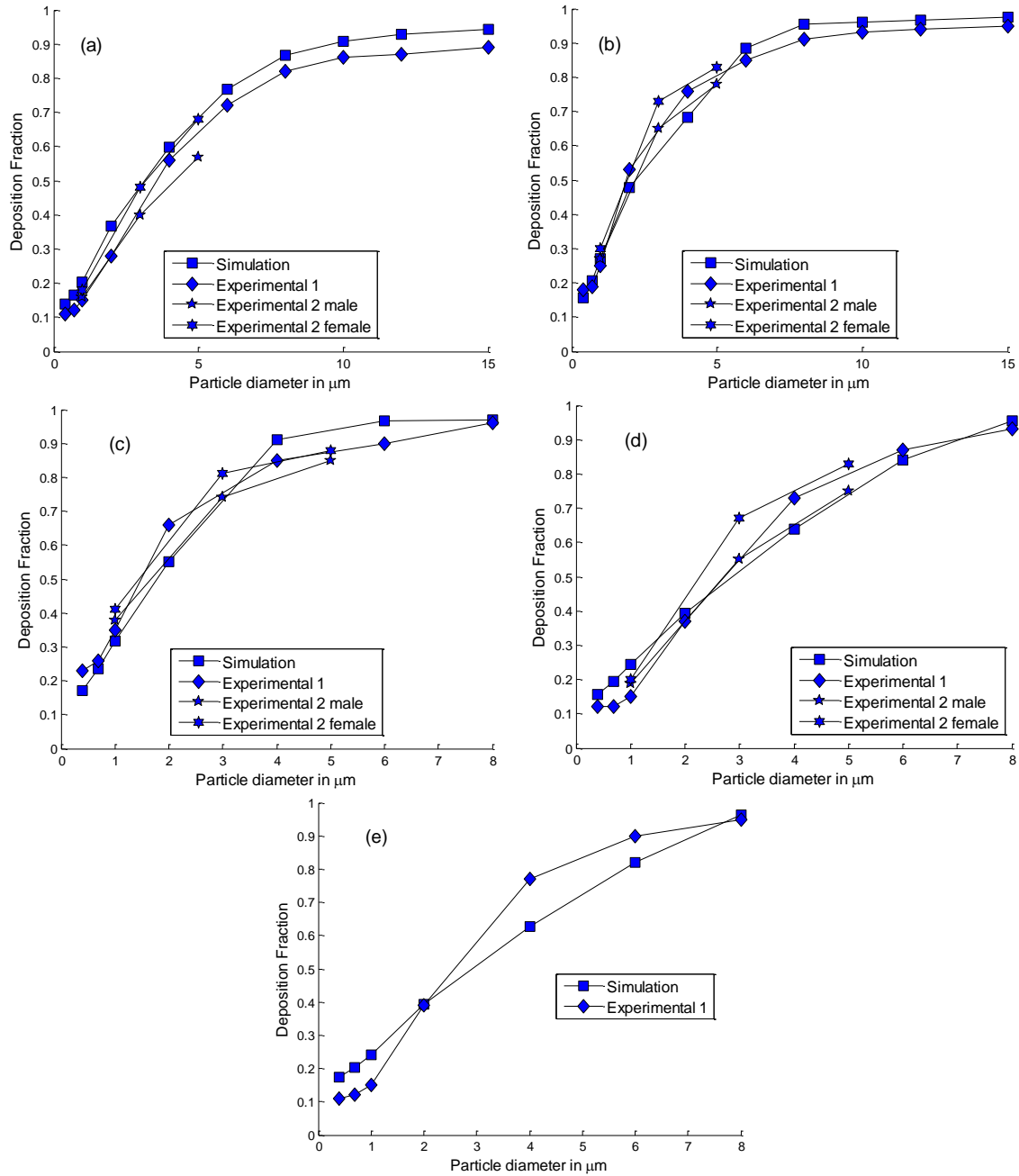


Fig. 3.1.7. Comparison of particle deposition in the WLAM I with experimental results (Experimental 1 denotes results from Heyder et al [119] and Experimental 2 denotes results from Kim and Hu [127] for (a) inhalation flow rate 15 LPM and tidal volume 500 cm^3 ; (b) inhalation flow rate 15 LPM and tidal volume 1000 cm^3 ; (c) inhalation flow rate 15 LPM and tidal volume 1500 cm^3 ; (d) inhalation flow rate 30 LPM and tidal volume 1000 cm^3 ; (e) inhalation flow rate 45 LPM and tidal volume 1500 cm^3 .

3.1.5.3 Comparison of regional deposition

The *regional* particle deposition results are highly desirable for toxicological studies as well as for impact analyses of administered drug-aerosols. Experimental deposition results for the extra-thoracic region indicated both fast and slow cleared thoracic regions, with the slow clearance process being dominant in the bronchiolar and alveolar airways [126]. So, the tracheobronchial model prediction was compared with experimental data for rapidly cleared thoracic deposition, while the broncho-alveolar model prediction was compared with measured evidence for slowly cleared deposition. Figure 3.1.8 shows the comparison of particle deposition in the extra-thoracic airway with experimental results. As already shown in Fig. 3.1.5, the extra-thoracic deposition increases exponentially for particles with diameters greater than $3\mu m$. Overall, the predicted deposition-curves for different particle diameters follow the experimental data sets. As reported by Stahlhofen et al. [126], the experimental data points are scattered, indicating some discrepancies due to experimental uncertainty and intersubject variability. Nevertheless, the simulation results are within the standard deviation values of the experimental observations. It should be kept in mind that the WLAM I results were plotted for different inhalation conditions with flow rates varying from 15 LPM to 45 LPM. However, most of the experimental results were conducted at 30 LPM, except the data from Emmett et al. [128].

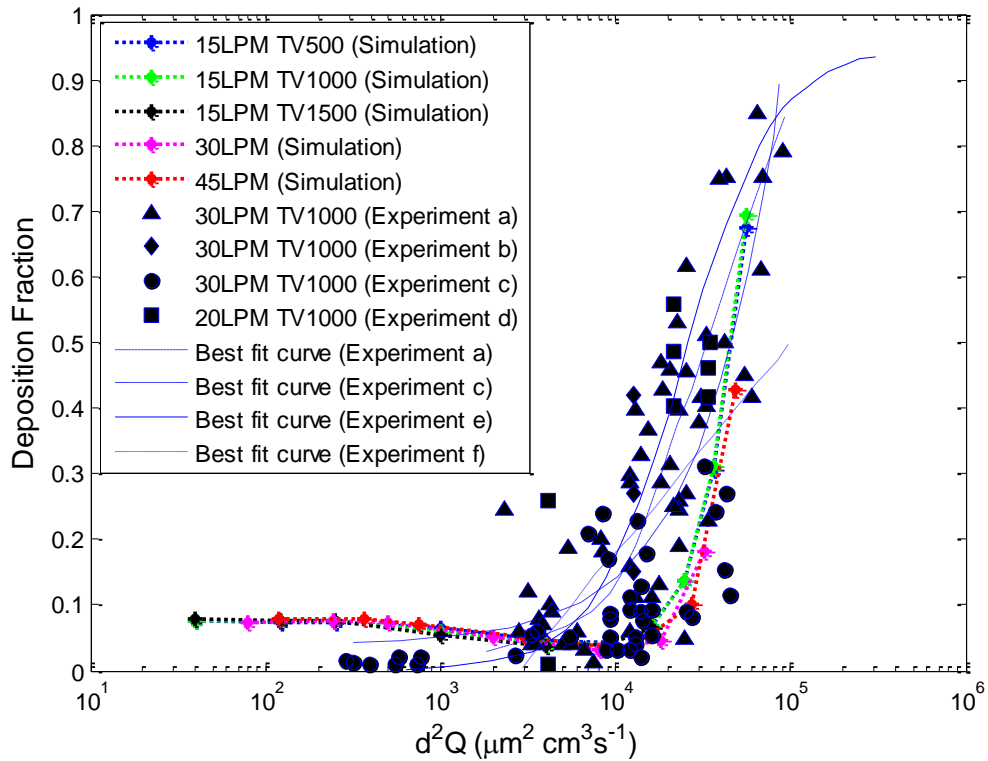


Fig. 3.1.8. Comparison of particle deposition in the extra-thoracic airway with experimental results. (Experiment a denotes results from [129]; Experiment b denotes results from [130]; Experiment c denotes results from [125]; Experiment d denotes results from [128]; Experiment e denotes results from [126]; Experiment f denotes results from [131]). Experimental results are reported in [126]

Figure 3.1.9 shows the comparison of particle deposition in the rapidly cleared thoracic airways, i.e., tracheobronchial airways up to generation 12. Most of the experimental results were obtained from measuring retained /removed radio-activity in the thoracic region after inhalation of labeled particles. As reported in Stahlhofen et al. [126], a direct comparison of different experimental results is difficult due to the differences in experimental techniques, subjects' airway geometry and breathing pattern, evaluation method, and way of presentation. Again, reasonable agreement can be observed for the results predicted by the

new model. The deposition trends show that the shape of the deposition curve is maintained even though the curve shifts up and down depending on the actual inhalation flow rate. The tracheobronchial deposition peaks around $10\ \mu m$, and the deposition decreases on both sides of the peak. This may be due to the higher deposition in the extra-thoracic airways for larger diameter particles and decreased total lung deposition for smaller diameter particles. The deposition peak shifts to the left with increasing flow rate. Additionally, the peak deposition value increases with increasing tidal volume. However, the peak deposition does not increase much with an increase in inhalation flow rate. This may be the result from the increased inertial deposition in the extra-thoracic airway and the balance between diffusional deposition and inertial impaction. This indicates that in order to achieve a higher tracheobronchial dosage, deep inhalation is required.

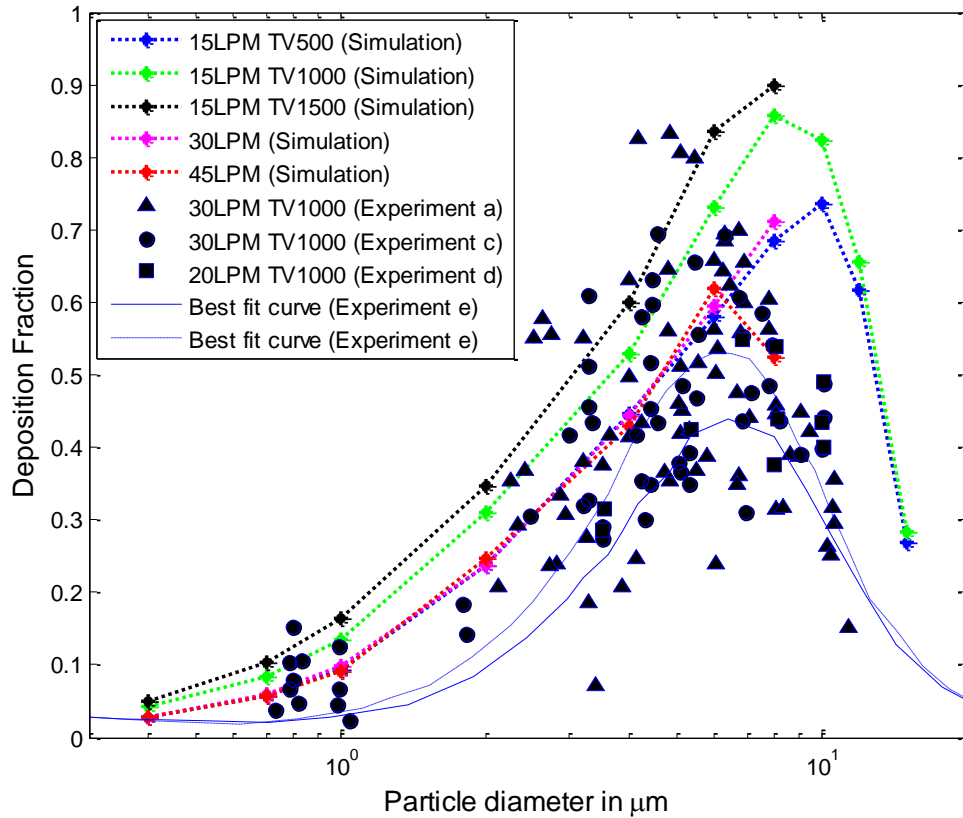


Fig. 3.1.9. Comparison of rapidly cleared thoracic deposition with experimental results (Experiment a denotes results from [129]; Experiment c denotes results from [125]; Experiment d denotes results from [128]; Experiment e denotes results from [126]). Experimental results are reported in [126]

Figure 3.1.10 provides a comparison of particle deposition in the slowly cleared thoracic airway, i.e., alveolar trumpet airway which includes generations 13 to 23. Good agreement was obtained for the WLAM I predictions when compared to experimental deposition data. The peak broncho-alveolar deposition is noticed for particle diameters around $5 \mu m$. The peak deposition fraction does not increase with an increase in inhalation flow rate; instead, it increases with higher tidal volume. Again, if a large drug-dosage in the alveolar region is desired, deep inhalation is required. The shape of the deposition curve is

maintained even though the curve shifts up and down depending on the inhalation tidal volume, while the deposition curve shifts from right to left with an increase in inhalation flow rate.

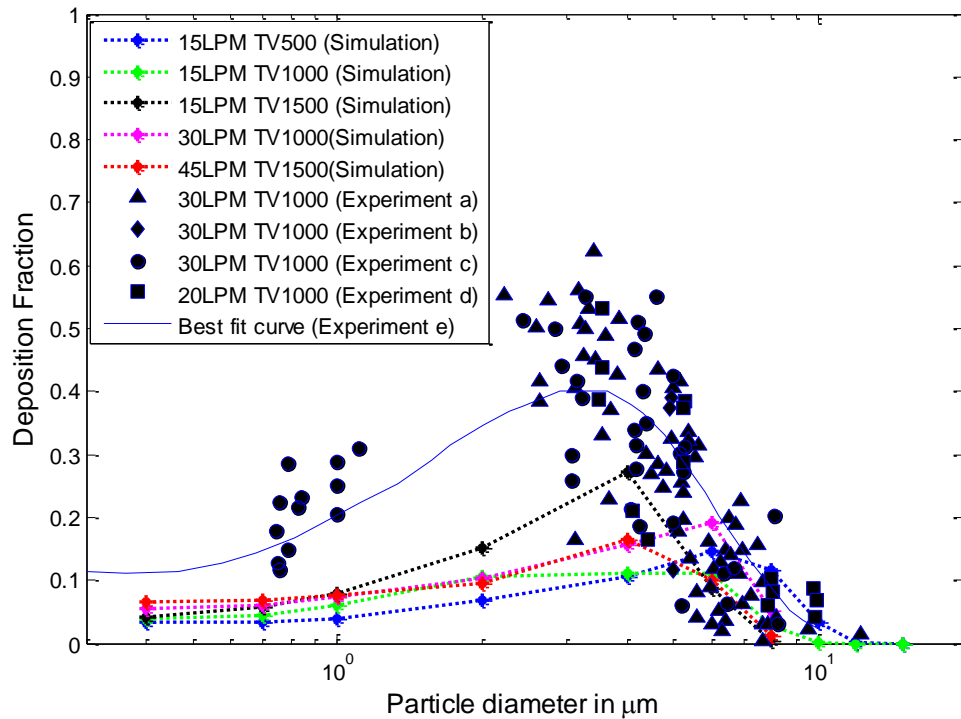


Fig. 3.1.10. Comparison of slowly cleared thoracic deposition with experimental results (Experiment a denotes results from [129]; Experiment b denotes results from [130]; Experiment c denotes results from [125]; Experiment d denotes results from [128]; Experiment e denotes results from [126]).

Experimental results are reported in [126]

3.1.5.4 Three-compartment segmental deposition

Figure 3.1.11 depicts the superimposed three-compartment deposition curves for each of the breathing patterns, i.e., 15 LPM with tidal volume 500 cm^3 , 15 LPM with tidal volume 1000

cm^3 , 15 LPM with tidal volume 1500 cm^3 , 30 LPM with tidal volume 1000 cm^3 , and 45 LPM with tidal volume 1500 cm^3 . It is noticed that the shape of the deposition curve for each flow rate is somewhat maintained. However, at higher flow rates the extra-thoracic deposition increases due to larger particle momentum, leading to stronger inertial deposition. The superimposed graphs provide valuable inferences regarding the influence of particle size on human respiratory tract deposition. The extra-thoracic deposition is high for any particle having a diameter above $10 \mu\text{m}$. The trachea-bronchial deposition is elevated for particle size around $10 \mu\text{m}$ and the alveolar deposition is high for particle size around $5 \mu\text{m}$. The alveolar deposition peak shifts to the left when the tidal volume is increased, and it shifts to the right when the inhalation flow rate is increased. For targeted drug-aerosol delivery it can be concluded that the size of the drugs needs to be controlled for efficient transfer from the inhaler-exit to desired lung regions (see Part II). Clearly, maximum deposition of drugs in the upper tracheobronchial airways can be ensured by keeping the drug-size around $10 \mu\text{m}$ and maximum deposition of drugs in the alveolar airways can be ensured by keeping the drug-size around $5 \mu\text{m}$

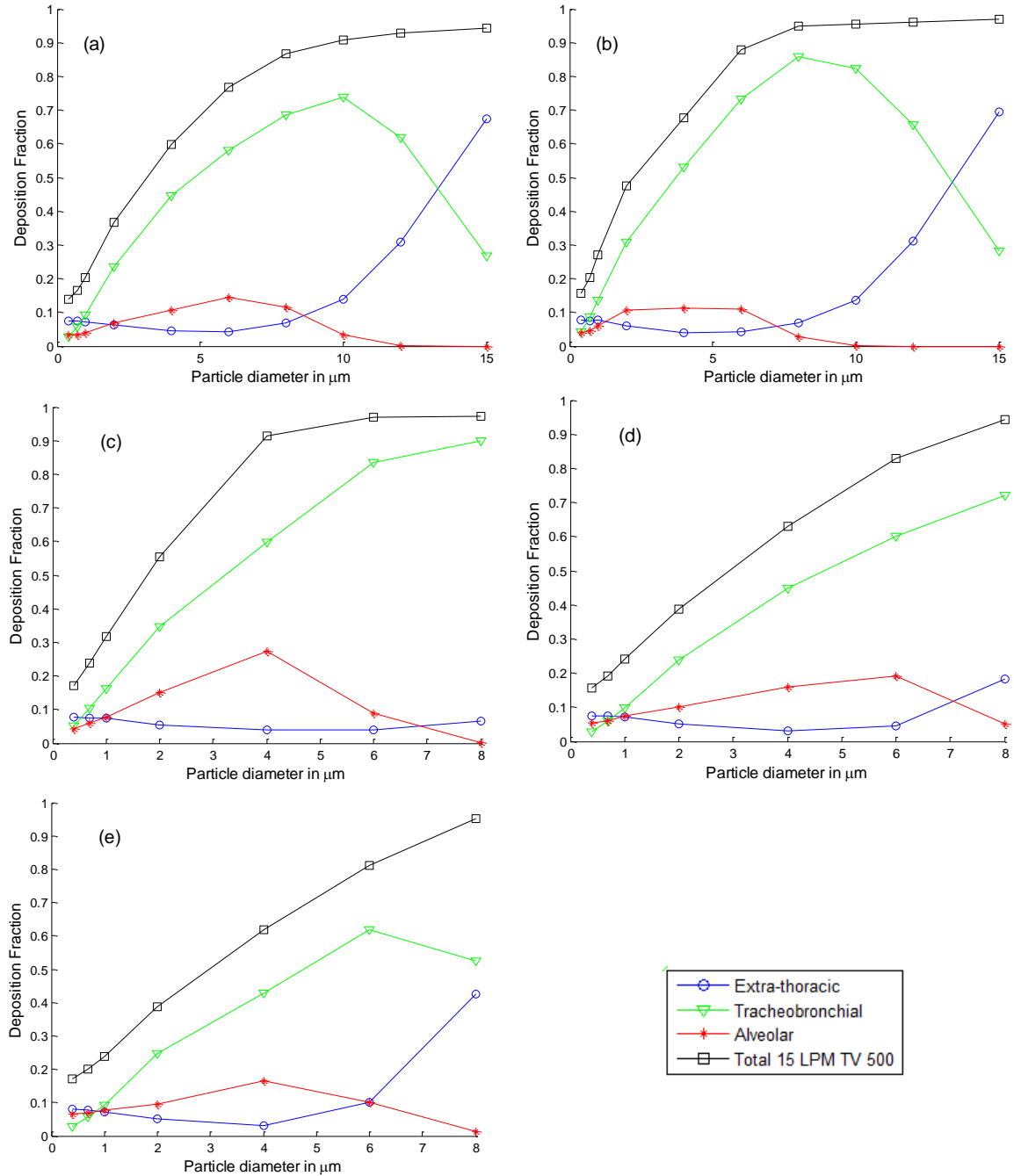


Fig. 3.1.11. Superimposed three-compartment deposition curves for each of the breathing patterns: (a) 15 LPM with tidal volume 500 cm^3 ; (b) 15 LPM with tidal volume 1000 cm^3 ; (c) 15 LPM with tidal volume 1500 cm^3 ; (d) 30 LPM with tidal volume 1000 cm^3 ; and (e) 45 LPM with tidal volume 1500 cm^3

3.1.6 Model limitations and future work

One of the limitations of the current modeling approach is that the model can predict local deposition inhomogeneity only in the extra-thoracic airways, while from then on deposited particle concentrations are segmentally averaged. Another limitation of the model is that inter-subject variability in lung morphometric measurements has not been considered yet. However, the current WLAM I can be readily varied by incorporating different lung data to represent subject variability. Presently, WLAM I can predict deposition in lung airways for particle sizes higher than 400 nm. For nanodrugs, typically below 100 nm, additional modeling will be required to include the Brownian diffusion effect. Another limitation is that the asymmetrical nature of human lung airways is not considered. It is possible to update the current model by incorporating realistic upper tracheobronchial airways as previously reported in [110]. The particle transport is affected by the asymmetrical flow structures mainly in the upper tracheobronchial airways. Hence, the updated model will improve the current modeling accuracy, but at the expense of computational time and resources.

Recent publications have pointed out the importance of accurate modeling requirements in the extra-thoracic airway region [83], especially when drug inhalers are used. Additionally, it should be noted that similar models were used to address intersubject variability in lung deposition studies [132]. Future work will focus on evaluating the impact of different 3-D extra-thoracic models attached to 1-D conduits with varying lung morphometries [132]. Future work will include further verification of the model prediction considering wide ranges of inhalation conditions and particle diameters. Also, particle

transport and deposition in the WLAM I considering nasal inhalation can be explored. Additional model validations will be performed via comparisons to more detailed *in vivo* lung-deposition measurements using a combination of gamma scintigraphy image of radio-labelled aerosols with CT scan images of the same subject to obtain accurate deposition values at different sites [133, 134].

Drug inhalation conditions differ for inhaler devices, where the inhaler mouth piece, high momentum flux and dense suspensions of drug aerosols significantly affect the subsequent fluid-particle dynamics (see Part II). Additionally, processes like drug evaporation/condensation, agglomeration, aerosol atomization and drug-wall interactions, and non-spherical particle dynamics have a significant impact on aerosol deposition in human lung airways. These processes cannot be easily incorporated into simplified models without additional modifications which again require experimental data sets. While a few reduced whole-lung models have focused on these topics [101-105], these models may not be suitable for predicting complex particle dynamics when inhalers are used. However, some of these transport phenomena have been previously incorporated in CF-PD simulations [84, 135-137] and could be included in the current model.

An application of the WLAM I for the prediction of drug-aerosol deposition in human lung airways when inhaled from a commercial dry power inhaler is discussed in Part II of the current study.

3.1.7 Conclusions

A first-generation whole-lung-airway model (WLAM I) is presented where the respiratory tract geometry is first represented by a 3-D mouth-to-trachea configuration and then all subsequent airways are lumped together into an exponentially expanding 1-D conduit. This new whole-lung model combines the advantages of segmental particle-deposition predictions at moderate computational cost. Similar to the expansion and contraction of the thoracic cavity, the WLAM-volume expands and contracts, thereby producing pressure differences resulting in realistic inhalation and exhalation flow waveforms. Total and regional particle deposition results under transient conditions in the WLAM I were compared with experimental data sets reported in the open literature. Reasonably accurate agreements are shown for the model predictions when compared to experimental deposition results. Thus, the particle deposition in the lung airways obtained with the new WLAM I provides critical insight into lung-aerosol dynamics. Specifically, the deposition fraction in the extra-thoracic airway is more than 90%, when the inhaled particle diameter is larger than $10\mu m$. Additionally, the deposition trend increases exponentially for smaller particles. Peak deposition can be observed in the tracheobronchial airways for a particle size of around $10\mu m$ and in the broncho-alveolar airways for a particle diameter of around $5\mu m$. Also, the peak deposition increased with an increase in tidal volume but not with the inhalation flow rate. Hence, in order to target drug-aerosols to these specific lung regions, the drugs should be kept near-uniformly at these corresponding peak diameters, while the dosage to these sites can be increased with deep breathing patterns. The WLAM I is time efficient and requires less computational resources, even when compared to CF-PD simulations under steady-state

assumptions [98] or CF-PD models considering the tracheobronchial region only [22, 26]. For example, the run time for a transient whole-lung simulation on an engineering workstation (Dell computer with 32 GB RAM and four 3.0-GHz Intel Xeon processors) was 7 hours for completing 1sec of inhalation with 60,000 particles. That is 10 times less than that for steady fluid-particle dynamics simulations with an idealized whole-lung geometry reported in [98]. In summary, the successful comparison of regional and total particle deposition results in WLAM I demonstrates that the current model is a time-and-resources efficient tool to analyze toxicological effects due to exposure to particulate matter or to estimate the pharmacological impact of pulmonary drugs.

3.2 Dry-powder inhalation

This chapter is a manuscript accepted for publication in *Computers in Biology and Medicine* titled “Computationally Efficient Analysis of Particle Transport and Deposition in a Human Whole-Lung-Airway Model. Part II: Dry Powder Inhaler Application”. The authors of this manuscript are Arun V Kolanjiyil, Clement Kleinstreuer and Ruxana T Sadikot.

3.2.1 Introduction

Respiratory drug delivery is becoming an increasingly popular way of administering medicine. It is efficient for treating both pulmonary and systemic pathogenic conditions as discussed in [85, 138, 139]. This route of drug delivery has many advantages when compared to other non-invasive administration methods. In cases of pulmonary lung diseases like asthma, chronic obstructive pulmonary disease (COPD), cystic fibrosis, acute respiratory distress syndrome (ARDS), and lung fibrosis, respiratory drugs may be very effective treatment options for several reasons: (i) instantaneous onset of action; (ii) minimal side effects; and (iii) maximal use of drugs at the affected area [12]. Also, the rapid absorption of the inhaled drug-aerosols, especially nanodrugs, through the large surface area of the alveolar lung region into systemic circulation results in rapid bio-distribution when targeting diseased organs [99].

Respiratory drugs are administered to the lungs with the inhaled air using an inhaler device, as discussed in [140-143]. The dosage of administered drugs to different regions of the lungs depends on the drug formulation and inhaler-device characteristics. The dry powder inhaler

(DPI) is a frequently used device because of the greater drug stability and minimally required patient coordination, as pointed out by [144, 145]. In a DPI, the aerosols are generated by deagglomeration of the powdered drug particles via the shear forces generated by the inhaled airflow [142, 146]. Hence, the amount of drug delivered to lung regions from a DPI inhaler depends on the patient's inspiratory capacity [147]. Currently, there are more than 30 different DPIs on the market. Among the different DPIs available, the Novolizer from Meda Pharmaceuticals (Somerset, NJ) is a multidose breath-actuated DPI, approved for delivery of budesonide and salbutamol [148]. In this DPI, the drug is stored as a powder blended with lactose-carrying particles. The patient's inspiratory flow actuates the Novolizer valve, and when the inspiratory flow is above a threshold value (usually peak inspiratory flowrate (PIFR) of 30–50 LPM), a predetermined drug dose is released into the inhalation chamber [149, 150]. The design of the flow channel, mouth piece and the cyclone-base help in generating aerosols of clinically effective fine particle fractions [148]. The inspiratory air with the drug aerosols exit the mouth piece through a 6mm-diameter opening, forming a fluid-particle jet at the mouth-inlet.

Scientific measurements to predict the lung dosage and device function are required for new inhaler devices. New or generic drugs have to be bio-equivalent before approval for clinical application. The most common way of measuring the amount of drugs deposited in the lung airways are *in vitro* tests using idealized oral cavity models and assuming that the particles exiting the oral cavity deposit in the lung airways [150-152]. Clearly, these measurements cannot provide detailed total and regional lung deposition/dosage measurements. Alternatively, *in vivo* experiments using radio-nuclide imaging (via gamma scintigraphy and

positron emission tomography) and/or pharmacokinetic studies were used [147, 153, 154]. For radio-nuclide imaging the active therapeutic agents are labelled with a radionuclide before inhalation by the subject. After administration of the radio-labelled drug formulation using the device, the different views of the lung are captured using a gamma camera [147, 155, 156]. In pharmacokinetic measurements, the amount of drugs deposited in the lungs is estimated based on the amount of drugs measured in blood and urinary samples, collected from the subjects after administration of the drugs [153, 157, 158]. There are many limitations for these two measurement techniques; both techniques need human subjects and these techniques involve either inhalation of radioactive materials or requiring blood and urinary samples during intervals of time. The radio-nuclide image measurement method is further complicated due to the limited ability to radiolabel drug formulations without varying the aerodynamic properties. However, the gamma scintigraphy image can provide direct image visualization and an approximate whole-lung and regional deposition measurements [138, 154, 159, 160]. In case of the pharmacokinetic measurement method, only an approximate estimate of total lung deposition is possible; thus, without any information regarding the deposition sites. Recently, there has been an effort to combine single-photon-emission-computed-tomography (SPECT) image of deposited radio-labelled drugs with high resolution computed-tomography (CT) scan images of the same subject to accurately estimate the deposition sites [133, 134, 161]. However, due to the limited resolution of airway imaging via CT and SPECT, associated with long processing times, detailed lung anatomical mapping is not possible except for few upper bronchial airways. Considering all these limitations of the experimental and *in vivo* measurement methods, computational

analysis has significant advantages as it is safe as well as time and cost efficient [26, 67, 98, 149, 162-164]. Once validated, computer simulations can provide detailed total and regional particle-deposition results which are of interest to toxicologists, health-care providers and inhaler-manufacturers alike [165-167].

The efficiency of respiratory drug administration is highly dependent on the type of delivery device [141]. Most of the currently used inhalers have low lung deposition efficiencies because high amounts of drugs are deposited in the oral cavity [168]. Efficient delivery of drugs to the deeper lung regions requires proper coordination between modified inhaler-device, its actuation, and breathing pattern [85]. Hence, direct drug-delivery to the required lung sites, e.g., optimal lung-tumor targeting, has become an active research area. For example, Kleinstreuer et al. [12] introduced and validated a new methodology to achieve direct drug-particle delivery from the injection point to the desired lung site, using an optimal particle-release map to generate a unique air-particle stream. The optimal particle-release positions can be predicted on a subject-specific basis with computer simulations of drug-aerosol transport and deposition [85].

In recent years, there have been several medical applications of curcumin for treating critical organ diseases, as discussed in [169-173]. Curcumin is a polyphenol compound present in *Curcuma longa* plant (commonly known as turmeric) which is largely cultivated in subtropical Asian countries. Recent investigations have shown that curcumin possess high therapeutic potential as an antioxidant, anti-inflammatory and anti-cancer agent [173, 174]. More recent studies have reported that curcumin has the therapeutic potential to inhibit lung inflammatory reactions and additionally, curcumin has shown to possess potential to reverse

steroid resistance in patients with asthma and COPD [174-176]. Corticosteroid resistance is a major barrier to adequate disease control for asthma and COPD patients and curcumin may be an alternative medicine to these pathological conditions [175, 177]. However, efficacy of treatments with curcumin is limited because of the low bioavailability of curcumin when ingested [178]. Hence, delivering curcumin via inhalation to specific lung sites has been suggested. However, this type of treatment is limited because of the unstable nature of the colloidal formulation, e.g., particle-aggregation may occur. Further investigations are required to improve both drug formulation and delivery to lung airways using inhaler devices.

In Chapter 3.1, the WLAM I is employed to analyze particle transport and deposition in a human respiratory tract model when a drug-aerosol is inhaled via a commercial DPI. The DPI assumed for the current study is the powder inhaler Novolizer (Meda Pharmaceuticals, Somerset NJ) which has shown reproducible dosing capabilities. Additionally, to validate the current computational modeling methodology, accurate *in vivo* lung deposition measurements for the Novolizer DPI were used [147]. With our validated model much needed information has been obtained concerning the efficacy of delivering curcumin dry powders to lung airways, when using a DPI.

3.2.2 Theory

The background information for the development of the first-generation WLAM I, i.e., the 3-D plus 1-D model geometries (see Fig. 3.2.1), governing equations plus boundary

conditions for the fluid-particle dynamics analysis, and the numerical solution method are described in Part I. Inhalation waveforms emanating from the DPI are discussed next.

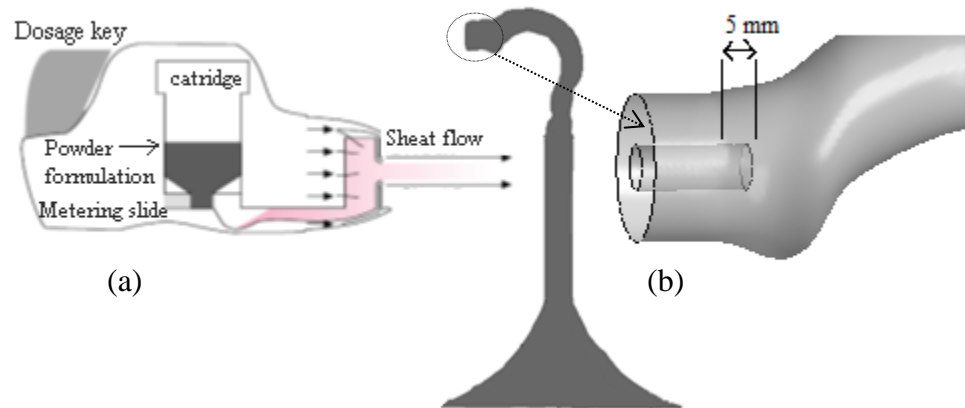


Fig. 3.2.1. (a) Novolizer DPI (adapted from [148] with permission of Springer); and (b) WLAM I with attached dry powder inhaler mouthpiece

The Novolizer DPI uses the patient's inspiratory airflow to generate drug aerosols by de-agglomeration of the powdered drug particles. When the inspiratory flow is above a critical threshold, i.e., the peak inspiratory flowrate (PIFR) of 50–100 LPM), a predetermined drug dose is released into the inhalation chamber. Hence, the inhaler is inherently breath actuated. Depending on the inhaler type, appropriate breathing style is required for efficient drug delivery. Recent studies by [150, 179, 180] have reported measured inhalation waveforms during DPI use. For example, Delvadia et al. [150] reported representative inhalation profiles (quick and deep inhalation profiles) while conducting *in vitro* experiments with budesonide drug emitted from a Novolizer DPI. They estimated the oropharyngeal,

tracheobronchial and lung depositions, using a basic mouth-throat model. The validity of these breathing profiles has been verified by comparing *in vitro* deposition results with *in vivo* lung deposition results from Newman et al. [147]. Newman et al. [147] had measured very similar lung depositions using radio-labeled budesonide in human subjects, administered with the Novolizer DPI. They reported the inhalation conditions in terms of PIFR and tidal volume. The subjects inhaled at PIFR 54 ± 7 , 65 ± 3 and 99 ± 13 LPM with tidal volumes 2.77 ± 0.97 , 2.96 ± 0.83 and 3.13 ± 1.01 L respectively. Depending on the peak inspiratory flow rate and tidal volume in Newman et al. [147], the inhalation profile was adjusted according to Equations (1-3) as given below [150]. Specifically, Equation (1) describes the quick inhalation where the flow rate accelerates to the required PIFR. The required PIFR is achieved within the inhalation time of $t_{\max}=0.45$ s. Equation (2) indicates deep inhalation where the inhalation flow rate reduces from PIFR to zero. The value of t_{total} was calculated in order to achieve the tidal volume as reported in [147]. The *in vitro* experimental study did not consider the exhalation phase. However in the present study, the exhalation phase has been included by simulating the contraction of lungs to functional residual capacity within a time period of 2s, assuring that the exhaled volume is the same as the inhaled volume (see Equations (1) to (4)). The *in vivo* experiment included a breath-holding pause which was not considered in the computational study. Figure 3.2.2 shows the inhaled lung volume changes with respect to time when using the DPI. Thus the volumetric flow rates can be described as:

$$Q(t) = PIFR \sin\left(\frac{\pi}{2} \frac{t}{t_{\max}}\right) \quad \text{for } 0 < t < t_{\max} \quad (3.2.1)$$

$$Q(t) = PIFR \quad \text{for } t_{\max} < t < 0.6s \quad (3.2.2)$$

$$Q(t) = PIFR \cos\left(\frac{\pi}{2} \frac{t - (t_{\max} + 0.15)}{t_{\text{total}} - (t_{\max} + 0.15)}\right) \quad \text{for } t > 0.6s \quad (3.2.3)$$

$$V = \int_0^{t_{\text{total}}} Q(t) dt \quad (3.2.4)$$

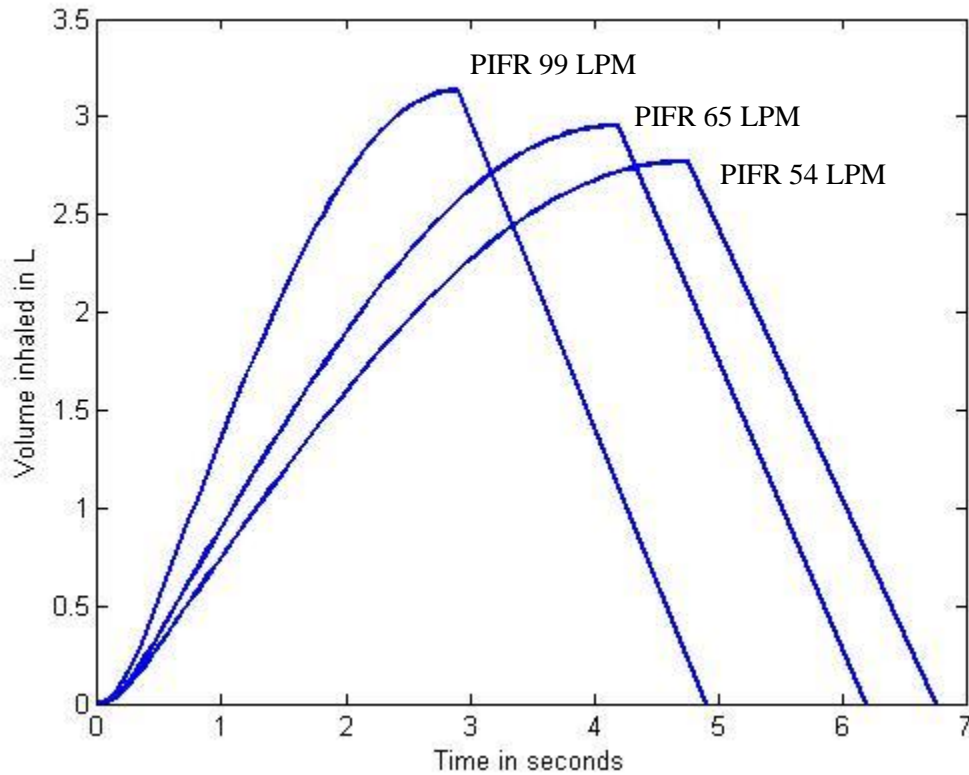


Fig. 3.2.2. Lung volume change with respect to time when using the Novolizer DPI.

Particle release time: DPIs are designed to utilize the shear stresses from the inhaled flow field to generate aerosols. Hence, the dry powder is de-aggregated and aerosols emitted during the first part of the inhalation, when the flow accelerates to PIFR. Experiments have shown that the drug aerosols are discharged from the DP-inhaler within the first 0.5s [26, 149]; thus, in the present simulation study particles were released during that time frame.

Aerosol size distribution: The amount of drug delivered to the lung from a DPI depends on the patient's inspiratory effort and capacity. Hence, the particle diameter distribution of the aerosols emitted from a DPI may vary depending on the inhalation conditions. For the current computational study it was assumed that the measured particle-size distribution under the given inhalation condition serves as a representative distribution for all inhalation conditions considered. Additionally, it was assumed that the particles exiting the DPI-mouth piece do not change in size.

The fine particle fractions of the budesonide drug from the Novolizer DPI were reported in Newman et al., [147], but not the particle-size distribution. Hence, the different aerodynamic particle diameter distributions of budesonide aerosols, emitted from a DPI, were taken from Tian et al., [26]. Aerodynamic particle size of curcumin powder were measured by Hu et al., [169] (see Fig. 3.2.3). The diameters shown are the midpoint cut-off diameters of the Next Generation Impactor stages and the maximum diameter was chosen to be the pre-separator cut-off diameter.

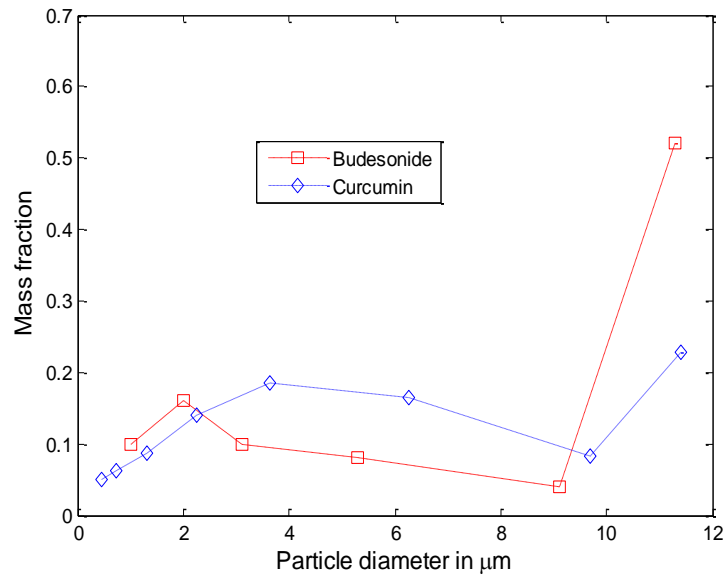


Fig. 3.2.3. Particle diameter distributions of budesonide and curcumin emitted from a DPI

3.2.3 Model validations

Drug-aerosol deposition: The results of the drug deposition in lung airways were compared with experimental deposition results reported in [147]. For the DPI-drug inhalation simulation, a mouthpiece with inlet diameter of 6mm (Fig. 3.2.1) was attached to the oral inlet (insertion depth is 5 mm). Particles (unit density) were distributed uniformly at the oral inlet and injected according to the mass fraction with an initial velocity being the same as the inlet-air velocity. Considering dilute particle suspensions, one-way coupling was assumed between the fluid and particle phases. 50,000 particles per second were injected at the mouth and particles were assumed to deposit on the walls on contact. Increasing the number of

particles by a factor of 1.5 showed less than 2% difference in the results. The comparison of the budesonide deposition results with experimental data sets for inhalation profiles with PIFRs of 54, 65 and 99 LPM are shown in Fig. 3.2.4. Good agreements were obtained, indicating that the WLAM I can adequately predict drug-deposition from commercial DPIs. Specifically, the WLAM I predicted for the three PIFR-values that 59.2%, 62.2% and 69% of the inhaled drug deposit in the oropharynx, while the experimental observations had mean value of 60.9 %, 61.6 % and 57 %, where the last measurement is being inconsistent with the expected trend. Figure 4 also shows inhaled drug deposition results for the tracheobronchial and broncho-alveolar airways in comparison with experimental data, representing the central, intermediate and peripheral lung regions. Reasons for some differences may be due to the approximated lung-airway geometry and inhalation waveforms as well as the assumed particle diameter distributions and due to the limitations of radionuclide imaging.

It can be inferred from the results that when using DPI, majority of the inhaled drugs deposit in the oropharyngeal and upper respiratory tract regions. Thus, drug-aerosol inlet modifications are necessary if one wants to achieve direct delivery to predetermined lung sites or regions.

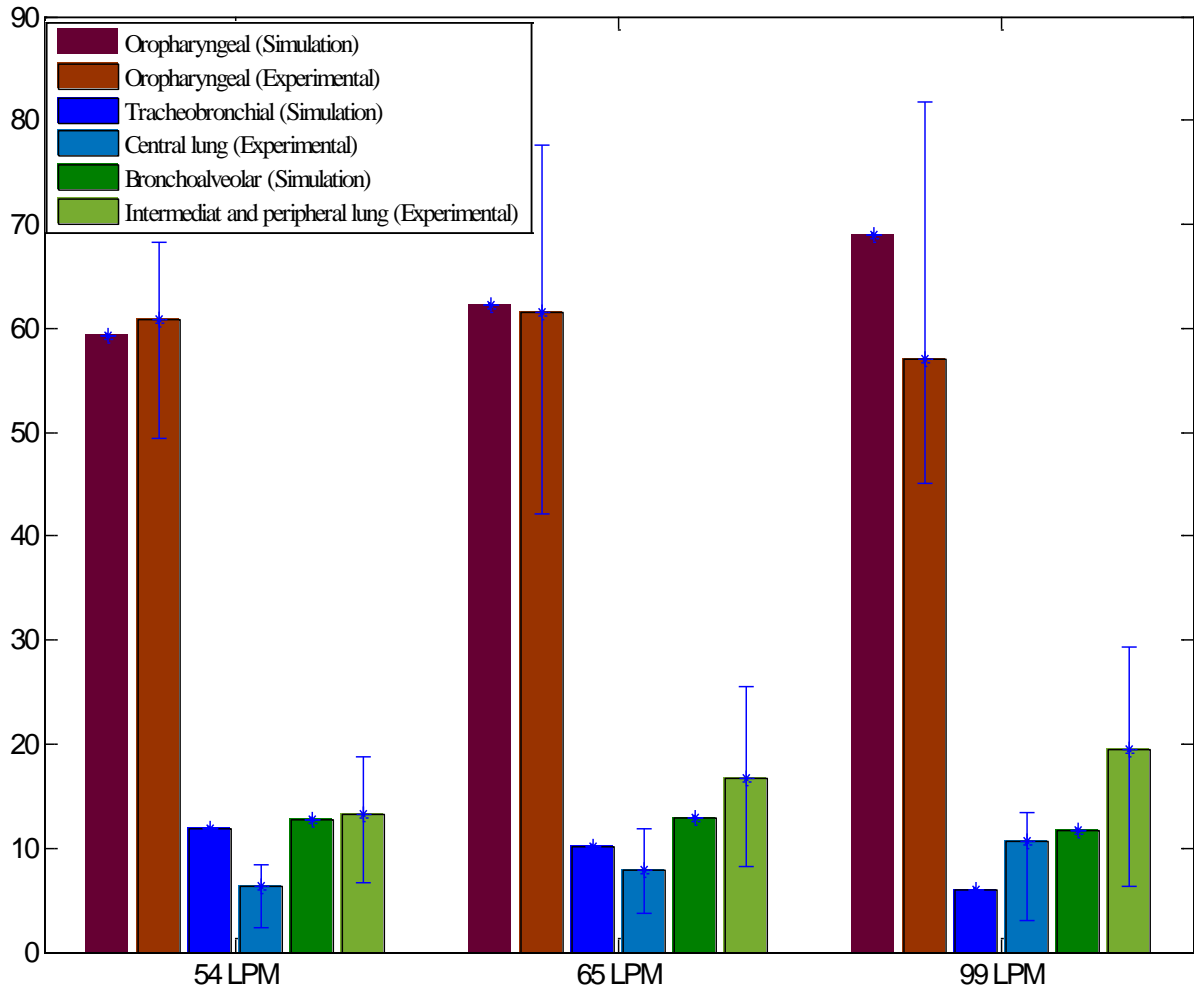


Fig. 3.2.4. Comparison of the budesonide DPI drug deposition results with experimental results for an inhalation profile with PIFRs of 54, 65, and 99 LPM (Experimental results from [147])

3.2.4 Results and Discussion

The validated WLAM I was used to study the efficacy of delivering curcumin dry powder to lung airways using the Novolizer DPI for realistic mouth-inlet conditions. As the respiratory aerodynamic diameter range of budesonide dry powder is somewhat similar to curcumin,

only deposition results for curcumin dry powder are reported. Once the base-case deposition results were established, *the drug-air stream angle and the effective aerosol release area were changed to reduce excessive deposition in the oropharyngeal region.*

3.2.4.1 Curcumin-particle deposition in a whole-lung model

Using the WLAM I subject to three breathing conditions, the transport and deposition of curcumin-powder inhaled from the DPI has been analyzed and the results are depicted in Fig. 3.2.5. Similar to budesonide (see Fig. 3.2.4), curcumin deposits more in the oropharyngeal region than in the lower lung airways. However, when compared to budesonide the curcumin-dosage to the oropharyngeal region is lower by 10% because of the high number of respirable curcumin aerosols. With higher PIFR-values the amount of curcumin deposited in the oropharyngeal region increases, indicating that impaction plays a leading role in aerosol deposition for the given curcumin-size range. Even though the total lung deposition remains a constant for different PIFR-values, with higher PIFRs deposition to the oropharyngeal region increased while the dosage to the lung airways decreased.

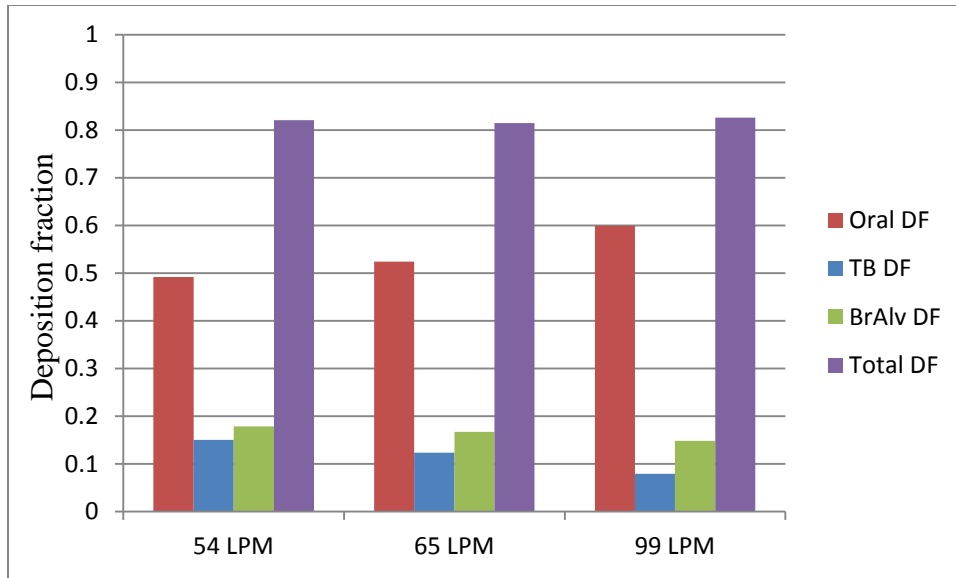


Fig. 3.2.5. Curcumin dry powder deposition results when using a commercial DPI

3.2.4.2 Improvement in drug-aerosol delivery and local deposition

The curcumin-deposition results indicate that much of the inhaled drug-particles deposits in the oropharyngeal region, and hence expensive drugs are wasted. Among the different parameters that control drug deposition, the radial position of the particle-release nozzle and the angle of injection have a significant influence [181, 182]. Limited by the design of the DPI, first only the effect of a change in the angle of the inhaler mouth-piece was investigated. Specifically, the DPI was placed into the oral inlet with a positive angle of 10° relative to the horizontal axis.

For a horizontal insertion angle the air-jet interacts more with the tongue, while for a positively angled mouth-piece the jet evolves more in the oral cavity (Fig. 3.2.6). These

strong airflow jets create secondary vortical structures and recirculation zones which may enhance or reduce drug-aerosol deposition in the oropharyngeal region, depending on the insertion angle.

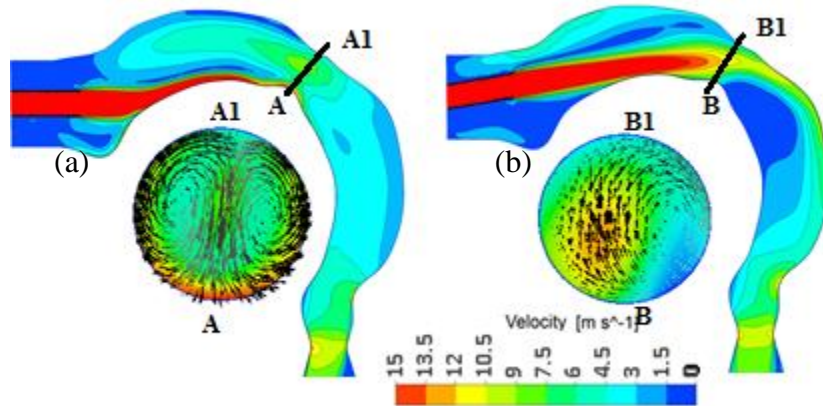


Fig. 3.2.6. Velocity distribution in the oropharyngeal airway for different injection angles: (a) horizontal; and (b) positive angle

In contrast to horizontal drug-aerosol injection (see Fig. 3.2.5), employing a DPI-tube angle of $+10^\circ$ (Fig. 3.2.7) results in higher particle deposition in the broncho-alveolar region (at least for the lower PIFR-values). With higher PIFR-values, however, similar to the horizontal insertion angle, the amount of curcumin deposited in the oropharyngeal region increased and the amount deposited in the tracheobronchial and broncho-alveolar regions decreased.

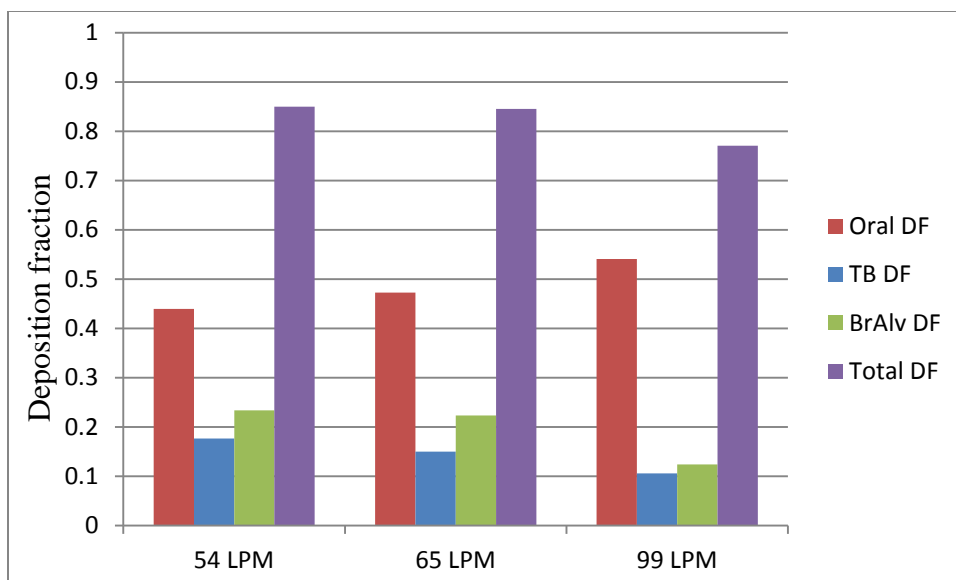


Fig. 3.2.7. Curcumin dry powder deposition result when the DPI injection angle is $+10^\circ$

3.2.5 Polydisperse vs. monodisperse particle distributions

The aerosols generated by DPIs are generally polydisperse with a high mass fraction in the upper respirable micron-particle range. A comparison study using polydisperse and monodisperse curcumin dry powder with Mass Median Aerodynamic Diameter (MMAD) was done to analyze the influence of polydispersity on curcumin aerosol deposition in lung airways for an inhalation PIFR of 65 LPM (Fig. 3.2.8). The MMAD was estimated to be $3.15 \mu m$ with geometric standard deviation of 2.08, based on the amount of curcumin deposited in stages 1 to 7. The results indicate high oropharyngeal deposition for polydisperse drug-aerosols due to the high mass fraction of large micron particles. In contrast, using monodisperse curcumin dry powder with particle diameters in the respirable

range resulted in low oropharyngeal deposition and high tracheobronchial and bronchi-alveolar deposition. Clearly, the efficiency of DPIs can be increased by fine-tuning the aerosol generation process to produce aerosols in the respirable range.

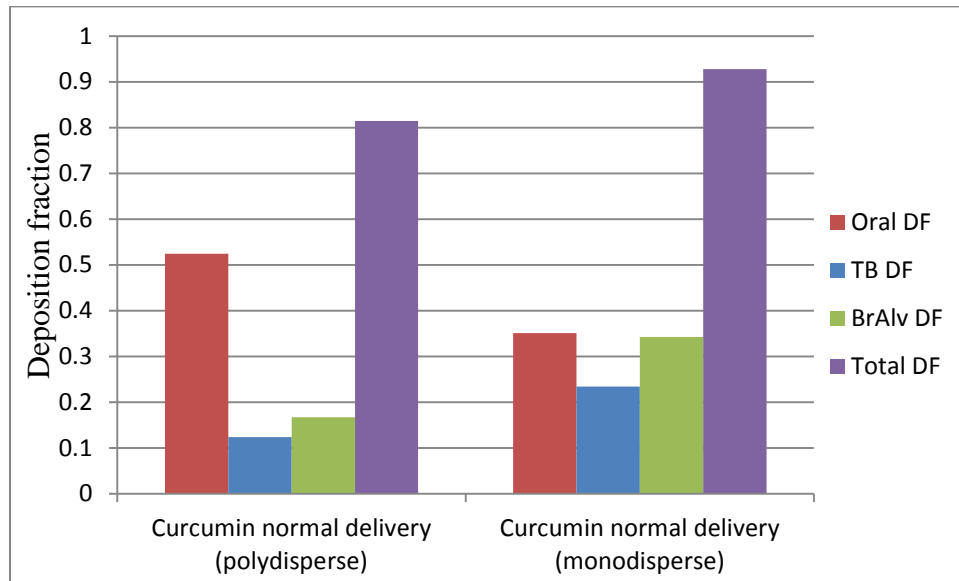


Fig. 3.2.8. Comparison of curcumin powder deposition for an inhalation PIFR of 65 LPM, considering both polydisperse and monodisperse curcumin dry powder

3.2.6 Considerations for targeted drug-delivery

It has been demonstrated that the efficiency of deep-lung deposition for DPIs is very low because a high amount of drugs is wasted in the oropharyngeal region. Even monodisperse curcumin powder with aerosol sizes in the respirable range cannot penetrate deep into the lung airways. However, it is desirable that most of the inhaled drugs, like curcumin, deposit into the smaller airways to combat severe inflammation or even into the alveolar region for

rapid mass transfer. As outlined in a series of publications [12, 67, 85] direct drug-aerosol delivery from the inhalation point to the desired lung site can be achieved. Specifically, via inhaled aerosol backtracking an optimal drug-release point can be computationally determined on a subject-specific basis. Using the WLAM I, which can approximately simulate aerosol deposition in three lung regions (i.e., extra-thoracic, tracheobronchial, and alveolar), first a particle-release map (PRM) is generated (Fig. 3.2.9a). Being just a simple conceptual example, the particle release map was created without considering the inhaler and the injection time. The PRM serves as a guide for the selection of suitable location (optimal drug-release point) from which the drug aerosols can be released in order to target a particular lung region. The PRM in Fig. 3.2.9a shows the apparent locations where the particles may deposit if injected/released from these radial positions. The red color indicates that if released from these zones, the particles will deposit in the oral cavity, blue in the tracheobronchial airways, and green in the broncho-alveolar airways. The results shown in Fig. 3.2.9b indicate that oropharyngeal and total deposition is high when polydisperse curcumin dry powder is delivered from the basic DPI. The oropharyngeal deposition decreases and total deposition increases when monodisperse curcumin powder is being administered. By selecting the circular drug-aerosol release area (adjusting the inhaler so that the inhaler mouthpiece is located at this area) as a conceptual example (see Fig. 3.2.9a), a larger amount of curcumin powder deposits in the broncho-alveolar region (see third histogram in Fig. 3.2.9b).

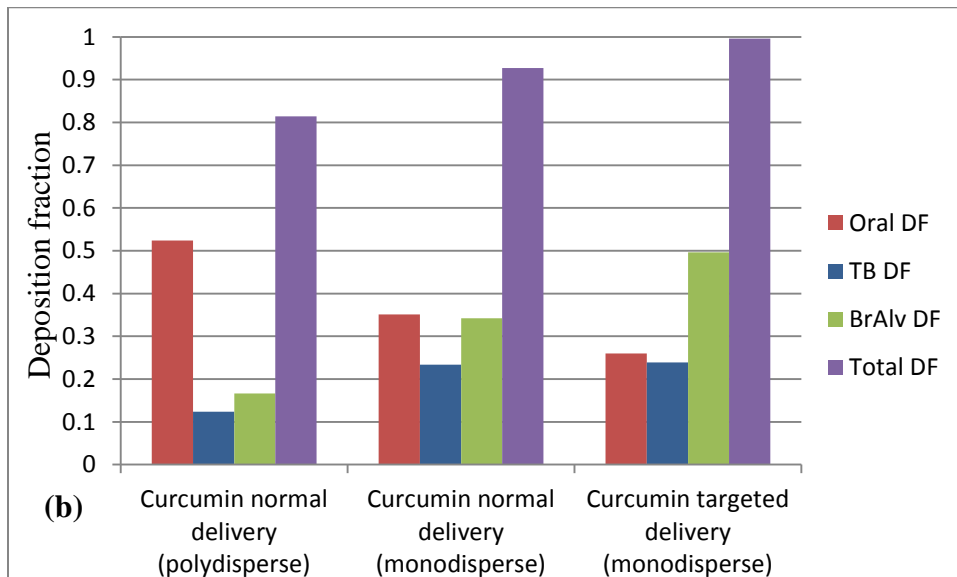
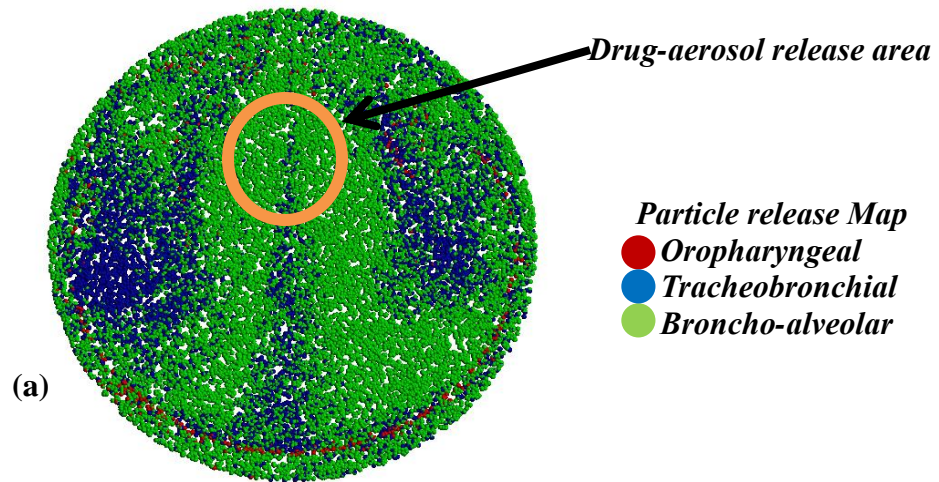


Fig. 3.2.9. Direct drug-aerosol delivery: (a) Particle release maps generated at the oral inlet for a breathing profile with inhalation PIFR 65 LPM; and (b) Comparison of curcumin deposition in the lung airways with and without targeting

With the new methodology of direct drug-delivery, the radial aerosol-release position is shifted and as a result the oropharyngeal deposition decreases, the broncho-alveolar deposition increases to 50%, and the total deposition increases significantly. This implies that higher amounts of curcumin reach the peripheral lung airways. It is evident, even when considering such an elementary set-up that targeted delivery can improve drug-delivery to deeper lung regions.

3.2.7 Model Limitations and Future Work

For the current study it was assumed that the polydisperse aerosols were injected into the respiratory tract and the particle-size distribution of the aerosols was obtained from *in vitro* experiments. The particle-diameter distribution of the aerosols emitted from a DPI may vary depending on the inhalation conditions, and it is difficult to evaluate particle-size changes for each flow rate. Clearly, more accurate computational results could be obtained if the particle size distributions used were measured for each inhalation PIFR considered. The presently employed flow waveforms were proven to be accurate for DPIs by *in vitro* and computational analyses [26, 149, 150]. The current computational study did not include aerosol deposition during breath-hold, possibly due to sedimentation of micron particles greater than $5\mu m$. In section I of this study it was shown that at higher inhalation flow rates, particle deposition in the oropharyngeal and upper airways increases exponentially with particle diameter. Hence, it is assumed that the smaller diameter particles reaching the lower lung airways during the inhalation phase stay in the inhaled air during breath-hold, and may deposit during the forced exhalation phase.

It is important to emphasize the preliminary nature of this study. The WLAM I can be further used to analyze the effects of inhalation waveforms, inhaler actuation, particle size distribution, and inhalation-PIFRs when employing the Novolizer DPI or other inhaler devices. Additionally, the model prediction can be expanded by incorporating phenomena such as drug-droplet evaporation/condensation, agglomeration, aerosol atomization and drug-wall interactions. These modeling strategies have been previously incorporated into CF-PD modeling [84, 135-137] and hence could be considered for broadening the capabilities of the WLAM I.

3.2.8 Conclusions

A first-generation whole lung-airway model (WLAM I) was developed and used to analyze particle transport and deposition in a human respiratory tract configuration when an anti-inflammatory drug was inhaled from a commercial DPI. The computational model was validated with measured *in vivo* data sets of Newman et al. [147]. They recorded deposition of radio-labeled budesonide, administered from a Novolizer DPI using gamma scintigraphy. Reasonably accurate agreement was observed for the WLAM I predictions when compared to the experimental deposition results. Then, the efficacy of the DPI to administer curcumin dry powder to lung airways was evaluated in terms of total and regional lung-deposition efficiencies. The model results provide critical insights regarding drug aerosol transport and deposition in lung airways, where the observations can be used to improve inhaler device design and drug formulation in terms of best physical properties. The results from this study indicate that under conventional inhalation conditions more than 60 % of the inhaled

budesonide and more than 50 % of curcumin deposit in the oral cavity. The corticosteroid drug budesonide is intended to deposit mostly in the tracheobronchial and bronchiolar airways while, curcumin is intended mostly to deposit in the alveolar region. Improved drug-delivery can be achieved by using a new targeting methodology as demonstrated in the current study. Specifically, for targeted monodisperse curcumin delivery a 50% reduction of (wasted) drug-deposition in the oropharynx was achieved when compared to traditional polydisperse drug delivery.

CHAPTER 4

Regional Alveolar Model

4.1 Single alveolus model

4.1.1 Introduction

The gas exchange region, also known as the acinar or the alveolar region, is the most vital part of the lung. The alveolar region encompasses millions of alveoli specifically designed to allow efficient gas diffusion during the normal breathing process [3]. Flow behavior and particle deposition in the alveolar region are not yet fully understood because of the complex geometrical structure of alveoli [183, 184]. Understanding the flow and particle behavior in the alveolar region carries utmost importance because inhaled aerosols depositing in the alveoli can lead to potential lung diseases [185, 186]. Additionally, understanding gas flow and particle behavior in alveolar region is pivotal in the treatment of pulmonary diseases including asthma, Adult Respiratory Distress Syndrome (ARDS), Acute Lung Injury (ALI), Chronic Obstructive Pulmonary Disease (COPD), pulmonary fibrosis and cystic fibrosis, bronchitis and emphysema etc. using therapeutic drug targeting [85, 187].

Even though the acinar region is the most vital region of the lung, only limited information is available regarding its geometry, due to its inaccessibility. Current limitations in obtaining detailed scanned images of submicron structures also restrict a detailed study [188, 189]. Similar to the conducting region, the acinar region is composed of repeating bifurcating alveolar ducts with alveoli arranged around the alveolar ducts [2, 190]. Each alveolus can be considered as a spherical shaped cup, tightly packed around the alveolar ducts in order to optimize the alveolar surface area, with only one opening to the ducts [190]. These alveoli are separated by a thin tissue layer called septa which contain multitude of blood vessels [2].

Several studies have used lung casts to analyze the geometrical structure of acinus and the reported alveoli topology varies with the study [2, 3, 9, 189-191]. Early lung cast study by Weibel [2] compared the shape of these structures to honeycomb or soap bubbles pattern. Due to the complexity and variability of the alveoli shape, Weibel [2] suggested simplified topologies which include partial spheroids, toroids, wedges of a hollow cylinder, elliptic cone. A similar study by Hansen [9] verified that among the different shapes, the most frequently observed alveoli shape in a human lung is partial spheroids. Recently, polygonal space filling structure of the alveoli has also been suggested by several studies [90, 185, 192, 193]. However, with these models, it is difficult to assess the bifurcation characteristics of the alveolar ducts.

Recent developments in imaging techniques have provided detailed information on rodent lung acinar morphometry [194, 195]. Micro X-ray computed tomography (micro- CT) has been used to study morphology and geometric structure of rodent acinar lung airways [191]. The 3-D volumetric reconstruction of acinar airways from high resolution-CT images shows the irregular nature of the alveolar topology but closely resembles the spheroidal topology assumption [189].

Traditionally it has been thought that the low Reynolds number flow in the alveolar region is completely reversible. However, this assumption was reanalyzed after the bolus inhalation experiments by Heyder et al., [196] in which they showed that the alveolar flow mixes irreversibly, leading to the deposition of inhaled particles deep inside the lung. In spite of the evidence showing convective mixing of acinar airflows, these in vivo experiments could not provide detailed information regarding trajectories and deposition of particles in

submillimeter alveolar structures. As an alternative, several investigators have used numerical methodology to shed light on alveolar mechanics and particle transport and deposition in these alveoli. Most of the initial numerical analysis was based on simplified 2-D alveolar structures. Tsuda et al., [197] conducted numerical analysis of alveolar flow and reported chaotic mixing of flow in the alveolar region. The model developed by Tsuda et al., [197] consists of an axisymmetric 2D straight tube with a torus attached on the outer surface representing an alveolus. The model wall was displaced using rhythmic expansion and contraction to represent alveolar wall movement. Tsuda et al., [198] used flow visualization technique to demonstrate alveolar flow recirculation in a rhythmically ventilated rat lung. They verified their previous numerical results demonstrating chaotic irreversible alveolar flow characterized by stagnation saddle points associated with alveolar vortices. Haber and Tsuda [199] numerically analyzed the particle deposition pattern in a rhythmically expanding alveolus. The alveolus and alveolar duct were modeled as a spherical cap attached at its rim to a circular opening in an expanding plane. The results showed that the particle deposition pattern considerably varies with the alveolar wall motion. Later Haber et al., [200] analyzed the effects of gravity and alveolar wall movement on deposition of particles with size ranging from $0.5 \mu\text{m}$ to $2.5 \mu\text{m}$. They found that the submicron particles are significantly influenced by the alveolar flow patterns compared to the micron sized particles. Henry et al., [201] obtained similar results using numerical analysis alveolar flow pattern and particle deposition in a 9-cell alveolated duct model.

Darquenne and Paiva [202] used a simplified model of the alveolated duct using sections of an annular ring around a central channel. They showed that the radial alveolar walls are

important sites of particle deposition. Expanding on this model, using similar geometrical representation to generate three-dimensional multi-bifurcation model of acinar tree. Harrington et al., [203] and Darquenne et al., [204] established the significance of alveolar airway bifurcation and alveolar wall motion on particle trajectory. Darquenne [205, 206] developed symmetric two-dimensional six-generation structure of the human acinus to study the extent of heterogeneity in alveolar airway particle deposition characteristics during normal breathing. Their results indicated that the particle deposition could be heterogeneous and particles may deposit in hot spots. Snitzman et al., [207] analyzed alveolar flow pattern using a three-dimensional expanding alveolus attached to a straight tube. The dimensions of the alveolar duct and alveolus were changed according to the lung dimensions reported by Weibel [2]. They noticed recirculation in proximal acinar generations, but no recirculation was noticed in the final generations. In the deeper acinar generations, flows become largely radial due to rhythmic wall motion and increasing alveolar dimensions. Oakes et al., [208] conducted experimental study on the terminal alveolar sac made of hyper elastic material under normal breathing conditions. The experimental results showed no recirculation zones for both healthy idealized terminal alveolar sac and emphysemic terminal alveolar sac models. Similar results were observed by Harding and Robinson [189] using a terminal alveolar sac model with 13 alveoli with expanding alveolar walls. Their analysis, using rhythmic inlet breathing profile, showed significant convective motion due to expanding alveolar wall. Berg et al., [209] observed flow in a hollow compliant model of a terminal air sac, with geometry from an actual human lung cast, under conditions of normal breathing using particle image velocimetry (PIV). This study demonstrated that the two generations

immediately proximal to the terminal alveolar sacs do not have recirculating eddies which supports the previous findings [189, 208]. Recently three-dimensional space filling alveolar models have been used to improve the geometric accuracy and produce realistic lung simulations [90, 185, 192, 193]. Sznitman et al., [186, 192, 193, 210] used 14-hedron-shaped alveoli, whereas Kumar et al., [211, 212] used truncated octahedron-shaped alveoli. In both cases, radial flow was reported for normal breathing conditions, assuming a sinusoidal breathing profile. Ma and Darquenne [213] used multigenerational three-dimensional models of alveolated airways with arbitrary bifurcation angles and spherical alveolar shape to predict the deposition of $1\mu\text{m}$ and $3\mu\text{m}$ aerosol particles in models of human alveolar sac and terminal acinar bifurcation under rhythmic wall motion. Flow recirculation was noticed only during transition between inspiration and expiration and accounted for no more than 1% of the whole cycle. Recently, microfluidic labs on chip models of the acinar generations were developed to study the rhythmic motion of the alveoli and its impact alveolar flow pattern and particle transport [214-217]. The initial results from these models have shown streamline crossing of particles; however, in order to estimate realistic lung particle deposition, further improvements are required.

The objective of this study was to develop human alveolar airway models and identify the significant forces affecting the particle transport through these airways.

4.1.2 Model geometry

In order to analyze the influence of the expanding and contracting motion of the alveoli on particle transport and deposition, a simplified model with a single alveolus (three fourth of

spheroid) with a neck attached to an alveolar duct (cylindrical shell) was considered. The spherical shape of alveoli was selected based on observations of Hansen [9]. A cylindrical projection (neck) from the lumen was used to anchor the spherical alveolus to the duct. The partial spheroid with the neck was arbitrarily assembled on the surface of the duct so that the alveolar neck opens to the duct. The alveoli attached TBU units were developed using computer aided design software Solid Works. A single alveolus can be described using four parameters: alveolus radius (AR), neck radius (NR), alveolus depth (D) and the duct diameter (DD). The current geometrical assumption has been verified by the morphometric study using human lung casts and images (refer Harding and Robinson [189]). Figure 4.1.1a shows the schematic representation of a single alveolus attached to a duct and Fig. 4.1.1b shows the 3-D representation. The dimensions of the alveolus are based on the morphometric measurements of human lung casts. Even though the lung cast studies indicate that the scale of the alveoli varies with in a subject (increase in scale with increase in lung generation number) the size of the alveoli has been considered constant in this study. However, the variation in duct diameter with lung generation number was considered. The alveolus radius and alveolus depth change with time depending on the inhalation conditions. However, for the current study the alveolar neck and the duct are assumed to be rigid. The initial dimensions (at time $t=0$) of the alveoli are given in Table 4.1.1.

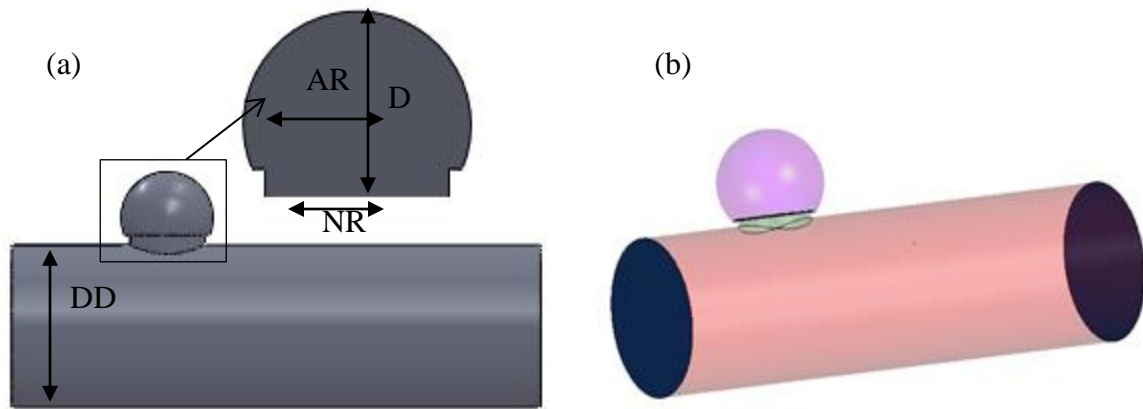


Figure 4.1.1. Schematic representation of a single alveolated duct and (b) shows 3-D representation

Table 4.1.1. Geometric model parameters

		Literature comparison	Reference
alveolus radius (AR)	0.1mm	0.11-0.14mm	Weibel [2] Harding and Robinson [189]
neck radius (NR)	0.085mm	0.085mm	Harding and Robinson [189]
alveolus depth (D)	0.2-0.22 mm	0.23	Weibel [2] Harding and Robinson [189]
D/NR ratio	1.17-1.3	0.48-1.44	Harding and Robinson [189]

To investigate the effects of multiple alveoli on a single duct, three alveoli were attached in series to a duct (periodically alveolated duct) as shown in Fig. 4.1.2. At very low Reynolds number flows (Stokes flow) the repeating alveolated units might not influence the flow pattern. However, the expanding and contracting motion of the repeated alveoli may influence the particle trajectory especially if the particles are released close to the alveolar mouth. Additionally, a multi-alveolated model^(a) with alveolus assembled periodically on four sides of the duct was also developed in order to study the effects of the rhythmic motion of the alveoli in a fully alveolated duct. Figure 4.1.2a and 4.1.2b show the schematic representation of the periodically alveolated and multi-alveolated ducts.

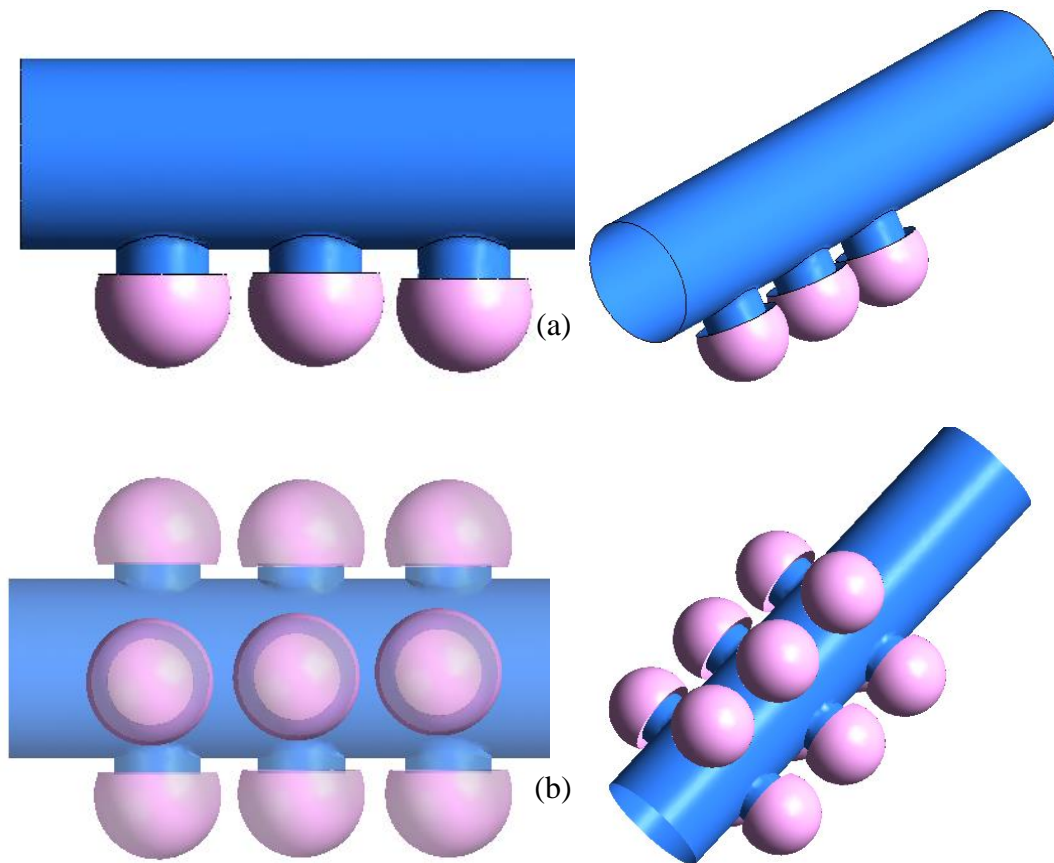


Fig. 4. 1.2. (a) periodically alveolated and (b) multi-alveolated ducts.

To study the variation of alveolar flow pattern and particle deposition with lung generation, two lung generations (generation 18 and 22) were considered. The duct diameter for each models were assumed based on the reported scaled Weibel's symmetrical lung model (Table 4.1.2).

Table 4.1.2. Lung morphometric measurements at functional residual capacity (3000ml)
(Weibel [2])

Generation number	Number of airways = 2^n	Length (cm)	Diameter (cm)	Number of alveoli	Volume per generation (cm^3)	Fractional alveolar volume
17	131072	0.121	0.046	5	30.47	0.01
18	262144	0.1	0.043	8	51.29	0.02
19	524288	0.085	0.04	12	97.56	0.03
20	1048576	0.071	0.038	20	224.78	0.08
21	2097152	0.06	0.037	20	412.1	0.14
22	4194304	0.05	0.035	14	769.12	0.27
23	8388608	0.043	0.035	sac	1305.84	0.45
Total					2891.16	1

4.1.3 Wall motion and boundary condition

The alveoli are assumed to deform and the deformation rate determines the inhalation and exhalation flow rate. The duct and alveolar neck are assumed to be rigid. The increase or decrease in volume of the alveoli produces a differential pressure, which brings in or out air. Depending on the volume flow rate, a deformation vector for the alveoli was estimated to produce the required volume change. The increase in volume from the initial functional residual capacity (FRC) (assuming three fourth of spheroid) can be represented using the following equations.

$$V_{FRC} = \pi r^3 \quad (1)$$

$$V_{FRC} + dV = \pi (r + dr)^3 = \pi (r^3 + dr^3 + 3r dr (r + dr)) \quad (2)$$

$$dV = \pi (dr^3 + 3r dr (r + dr)) \quad (3)$$

Where V_{FRC} is the alveolus volume at FRC and dV is the increase in volume due to the radial expansion dr .

Assuming symmetric dichotomous branching structure of the lung, the inhalation flow rate through any generation will be flow rate measured at the oral inlet divided by the number of airways in that generation. Also, it is assumed that the airflow rate due to the alveolar deformation varies with the generation. The alveoli in each generation deform in order to produce fraction of the oral inhalation volume flow rate which is equal to the total flow rate times the alveolar volume fraction (Table 2). Additionally, the individual alveolus wall deformation can be estimated by dividing the fractional volume flow rate per generation with the number of alveoli in that generation. The volume flow rate $\frac{dV}{dt}$ in a particular lung

generation for any given inhalation condition can be predetermined and hence the corresponding alveolar deformation can be estimated by solving equation (3) for $\frac{dr}{dt}$.

As suggested by previous studies [207], the rhythmic expansion and contraction of the lung is assumed to be geometrically self-similar in nature (self-similarity means the quality or state of having an appearance that is invariant upon being scaled larger or smaller (from Meriam-Webster dictionary)), indicating that the deformation is similar in all alveoli. The presence of surfactant also helps the alveoli to expand and contract at the same rate. In human lung, the deformation of the alveoli depends on the inhalation volume flow rate and the period of inhalation and the deformation is limited after a certain period of inhalation (once the maximum radial deformation is reached). The surface tension of the surfactants and nonlinear elasticity of the lung tissue prohibits expansion of alveoli beyond a specific radius. In order to replicate the physiological breathing motion of the alveoli, the deformation of the alveoli was restricted after a specified increase in alveolar radius. This final radius was estimated based on the self-similarity assumption. For an average human adult with FRC of 3000ml and total lung capacity of 6000ml, the maximum lung deformation possible is 3000ml. Based on the self-similarity rule, the maximum increase in alveolar radius possible is estimated to be 0.26 times the initial radius.

4.1.4 Numerical methods

An opening boundary condition was applied at the duct inlet and a mass flow rate condition was applied at the outlet. The outlet mass flow rate Q_D and mass flow rate due to the alveolar

wall motion Q_A together results in the inlet mass flow rate Q_G per generation. As shown in Fig. 4.1.3. , the resultant mass flow rate Q_G is the sum of alveolar mass flow rate Q_A and outlet mass flow rate Q_D which is the result of alveolar deformation in the distal generations.

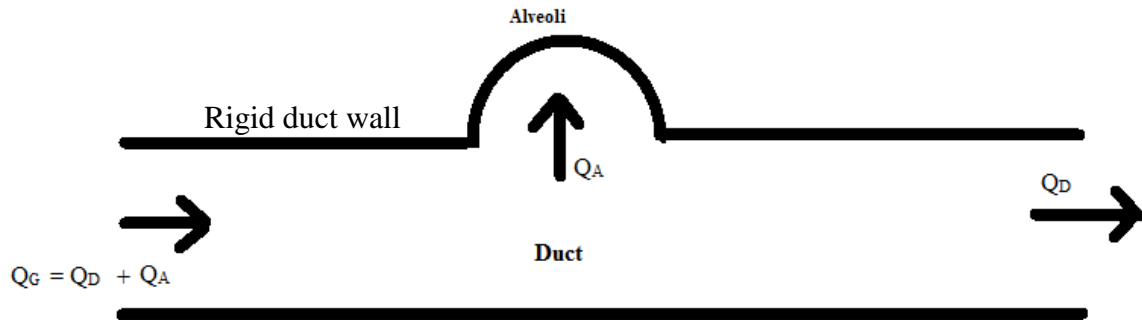


Fig. 4.1.3 . Flow through an alveolated duct

No slip boundary condition was applied at the wall boundaries (duct and alveoli) so that the fluid velocity matches with the wall velocity at the fluid wall interface. A user defined CEL (CFX Expression Language) functions was used to apply the wall deformation vector.

In order to study the effects of inhalation conditions on alveolar flow pattern, constant oral inhalation flow rates were assumed. Simulations were conducted for rest (15 LPM), exercise (30 LPM and 45 LPM) breathing conditions with inhalation period of 1s. Since the exhalation (contraction of the alveoli) have little influence on the deposition of particle sin the alveoli, only inhalation condition was simulated in this study. The transport equations for the continuous phase and the particles are described in chapter 2.

4.1.5 Results and discussion

4.1.5.1 Alveolar flow pattern

The airflow through an alveolated duct is highly influenced by the expanding and contracting motion of the alveolus. The alveolar flow Q_A primarily depends on the generation number (fractional alveolar volume in Table 4.1.2). The flow through a duct with rigid alveolus was first simulated and compared with air flow pattern when the alveolus is expanding (inhalation) (see Fig. 4.1.4). For this comparison, 15 LPM oral inhalation flow rate (Q_{oral}) was assumed. When the alveolus is rigid ($Q_A=0$), the convective flow exchange between the ductal flow with the alveolar flow is negligible. Instead, the alveolar flow pattern is dominated by a recirculating flow, filling the entire alveolus induced by the shear force generated by the ductal flow. Similar results have been noticed for alveolar flow simulations in generation 18. However, the recirculation region has been reduced and radial flow has started to dominate. This is due to the alveolar wall deformation which resulted in mixing of a small fraction of the ductal flow with the alveolus flow. At the distal generations, where the alveolar flow fraction is higher, the dominating radial flow into the alveolus from the duct was noticed. Due to this radial flow, the recirculating flow, which has been noticed in the upper generations, was diminished. This indicates the convective mixing of the ductal flow with the residual air in the alveolus. It is evident from the simulation results that the position of the alveolus (generation number) determines the alveolus wall deformation rate and the amount of convective mixing. Similar results have been reported previously by Sznitman et al., [207].

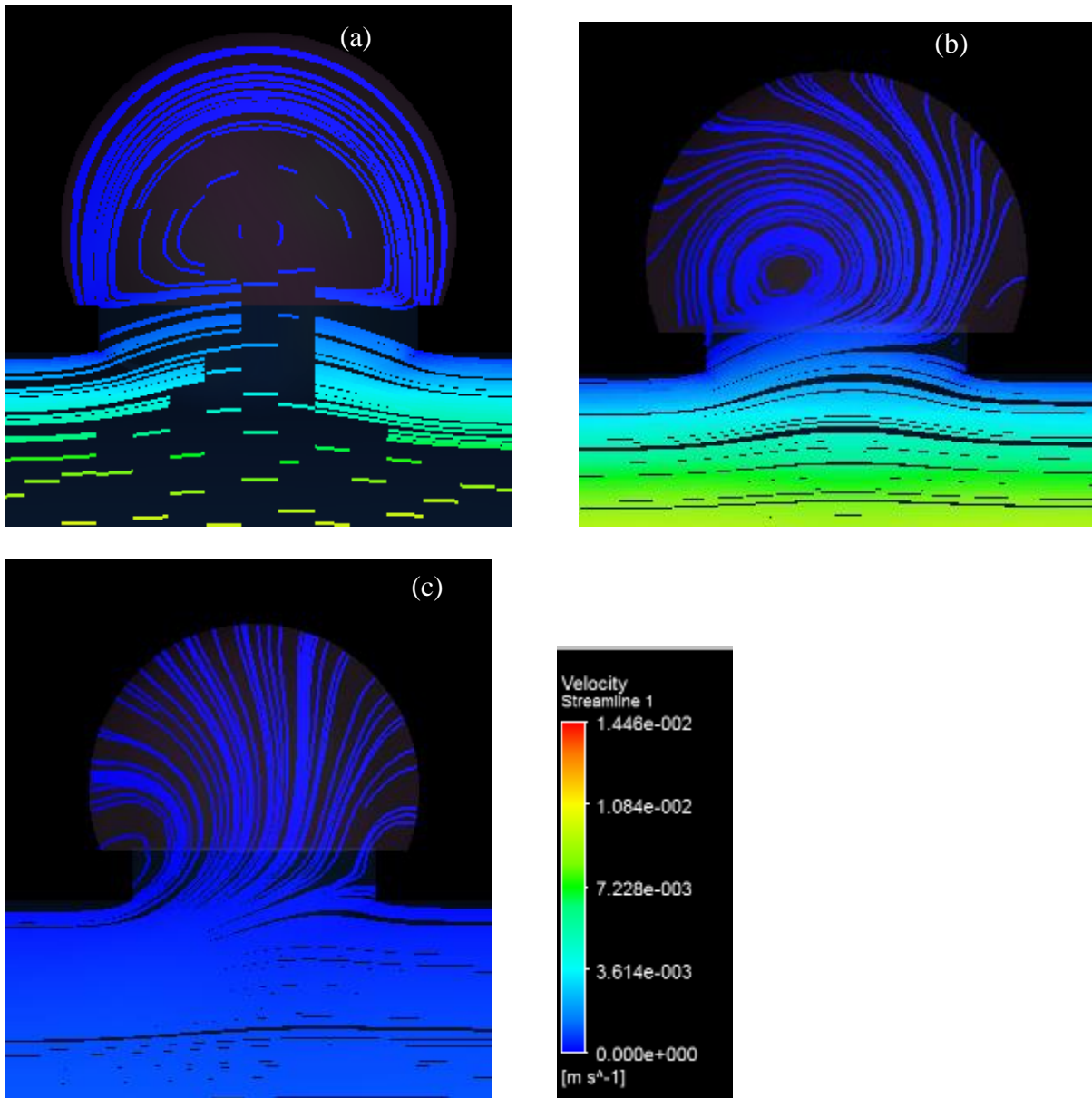


Fig. 4. 1.4. Alveolus flow pattern in generation (a) 18 (rigid alveoli) (b) generation 18 (c) generation

22

The air flow pattern in the alveolated ducts in generation 22 was analyzed at higher inhalation flow rates as well (rest (15 LPM), exercise (30 LPM and 45 LPM)) to study the

change in flow pattern with flow velocity. As shown in Fig. 4.1.5, as the inhalation flow rate increases, the alveolus deformation rate also increases which results in a higher radial flow to the alveolus. At 15 LPM inhalation flow rate, the radial flow velocity is low compared to the peak ductal flow velocity. The radial flow rate also increases, with the increase in inhalation flow rate. Hence, convective mixing of the duct flow with alveolar flow increases with increasing flow rate.

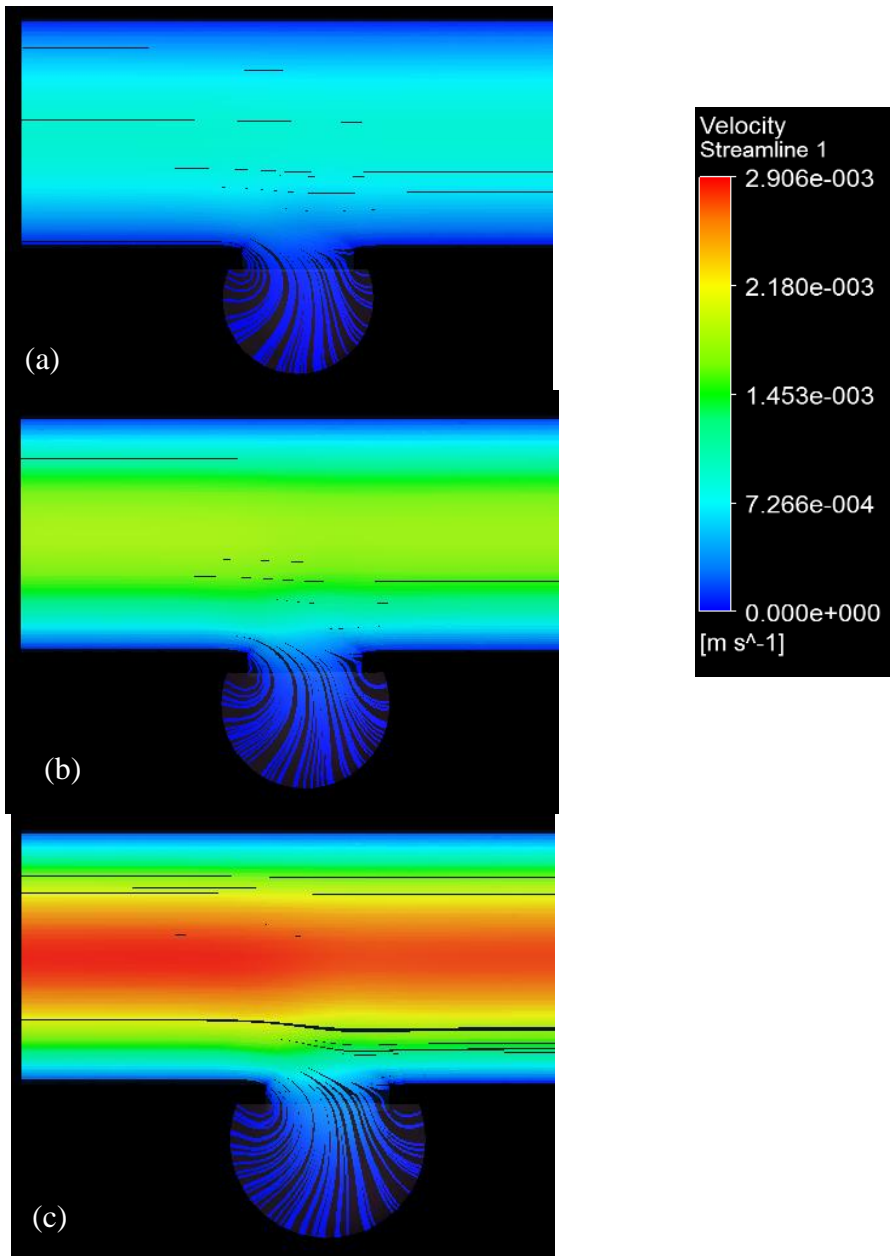


Fig 4. 1.5. Alveolus flow pattern under (a) rest (15 LPM), (b) exercise (30 LPM) and (c) 45 LPM inhalation flow rates

4.1.5.2 Particle transport and deposition

The particle transport and deposition of micron particles ($2\ \mu\text{m}$ to $10\ \mu\text{m}$) were investigated in single alveolated duct models in order to assess the influence of alveolar wall deformation, position of the alveoli and the orientation of the gravity vector on particle deposition. In this study, the key role of gravity on aerosol deposition in alveolated airways and the interplay between sedimentation and convection were mainly investigated and other forces like diffusion were assumed to have negligible influence on micron particle transport. This assumption has been verified by previous investigations in which the role of diffusion on micron particle in alveolated airways has been found to be negligible. The amount of particles deposited on the domain wall (duct and alveolar tissue) of single alveolated duct models representing generation 18 and generation 22 are compared in Fig. 4.1.6 (the gravity vector was assumed in the direction normal to the duct flow, towards the alveolar opening). The particle trajectory and deposition trend were similar to the particle transport in a horizontal pipe. Gravitational sedimentation was the dominant driving force for particle deposition. Most of the heavy particles (above $5\ \mu\text{m}$) deposited close to the duct inlet due to sedimentation. Diffusion dominated light micron particles closely followed the stream line, while heavy particles crossed stream lines to deposit at the bottom.

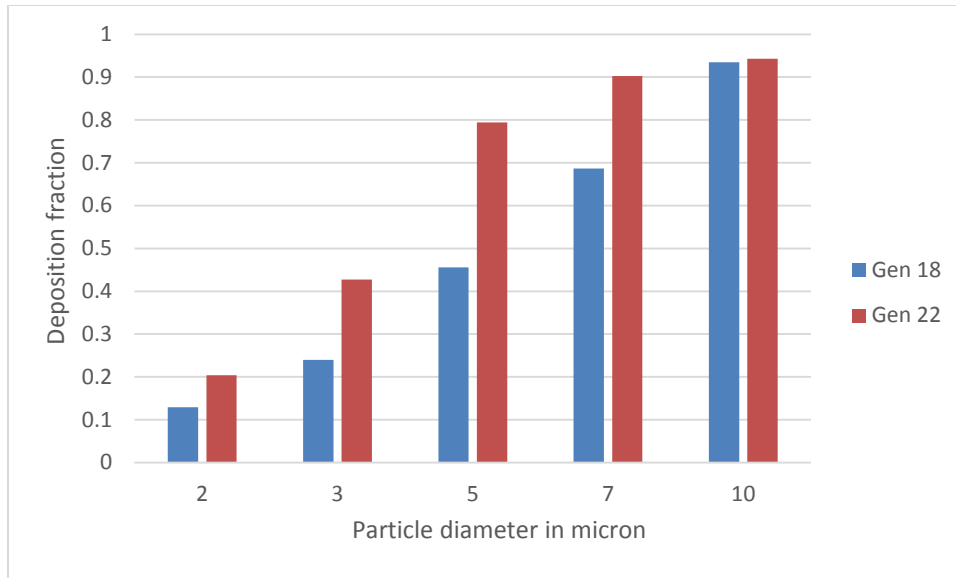


Fig. 4. 1.6. Comparison of particles deposition in generation 18 and generation 22

The results indicate that the particle deposition is high in the distal lung generations. This is because of the increased wall deformation, low flow Reynolds number and reduced duct dimensions. Many of the injected particles did not reach the outlet boundary due to the low inlet Reynolds number for the flow through generation 22. This indicates that the particle residence time is high in distal generations, which results in higher deposition due to sedimentation. The results also indicate that the position of the alveolated duct (generation number) may not have significant influence on deposition of heavy particles (above $7 \mu m$).

The trajectories of the particles were influenced by the presence of the deforming alveolus. The particle trajectory was also disturbed near the alveolus opening similar to the variation in the airflow pattern due to the presence of the expanding alveolus. This disturbance was higher when the particle size was lower. The comparison of alveolus particle deposition trend

for a rigid and flexible alveolus is shown in Fig. 4.1.7. It is to be noted that the plotted results are for a single alveolated duct in generation 18 at an inhalation flow rate of 15 LPM. The particle deposition is expected to be higher in the distal generation alveoli. Additionally, the particle deposition will be higher under physiological conditions where more alveoli are present and inhalation flow rate is high. The results indicates that the presence of deforming alveolus significantly influence particle deposition in alveolar airways.

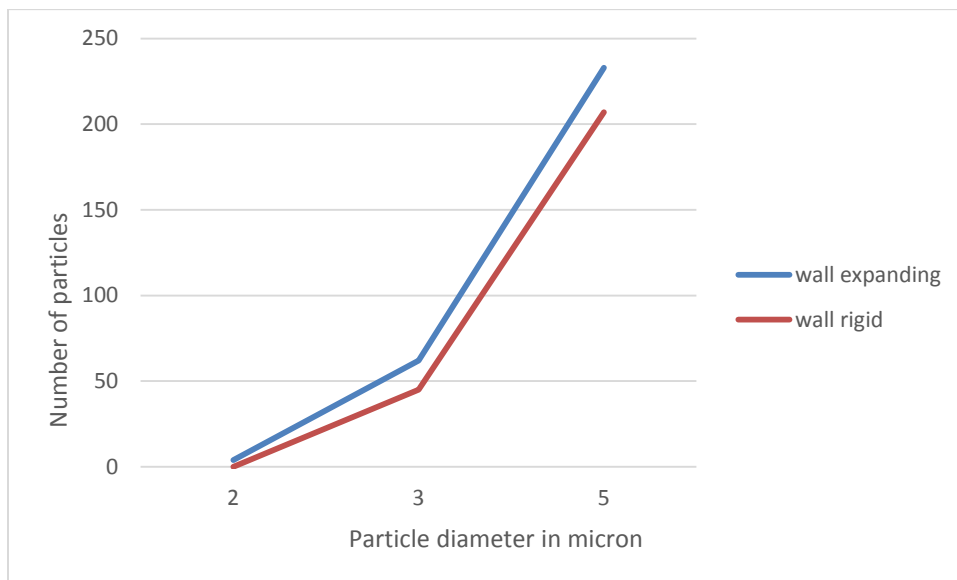


Fig. 4.1.7. comparison of alveolus particle deposition trend for a rigid and flexible alveolus

The influence of the inhalation flow rate on aerosol deposition in the alveolated lung airways was also assessed by simulating the particle trajectory using single alveolated duct models representing generation 22. The simulations were conducted for rest (15 LPM), exercise (30 LPM and 45 LPM) breathing conditions with an inhalation period of 1s. The trajectories of a

2 μm particle are shown in Fig.4.1.8. The results indicate that with the increase in inhalation flow rate, the alveolar flow rate increases, which results in increased transfer of inhaled particles into the alveoli. Due to the applied total simulation time of 1s and since the alveolar wall is expanding during this inhalation time, only limited number of the inhaled particles deposited in the alveolus. However, it is evident from the figure that with the increase in inhalation flow rate, more number of particles has entered the alveolus. These simulation results indicate that *even though with the increase in inhalation flow rate the particle residence time is reducing, the increase in the alveolar wall deformation rate is applying a higher pulling force on the particle which may eventually result in higher alveolar deposition.*

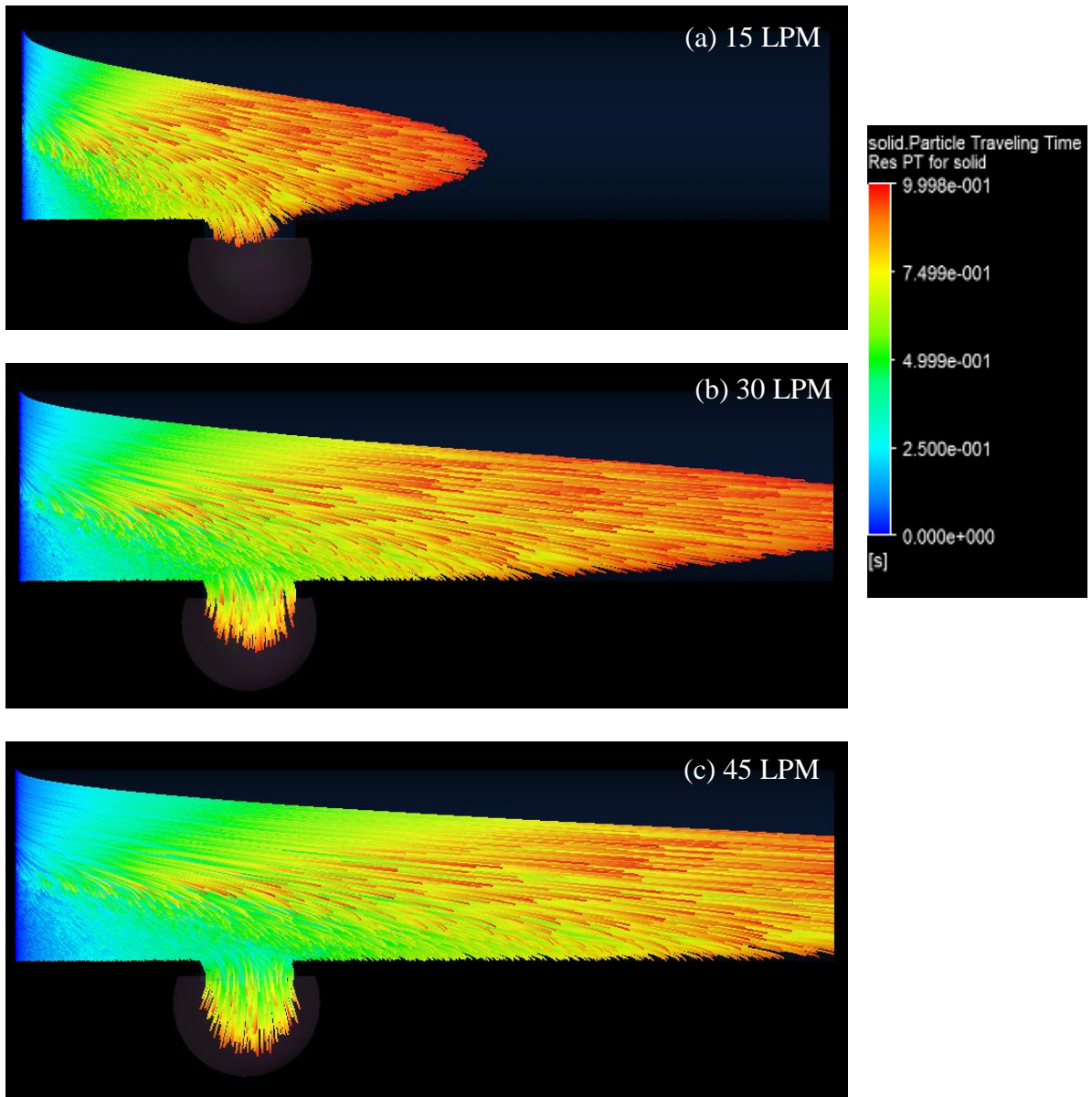


Fig.4.1 8. Trajectories of a $2 \mu m$ particle in a single alveolated duct representing generation22 under (a) rest (15 LPM), (b) exercise (30 LPM) and (c) 45 LPM inhalation flow rates

4.1.5.3 Effect of gravity

The influence of the orientation of the gravitational vector on aerosol deposition in the alveolated lung airways was also assessed by simulating the particle trajectory using single alveolated duct models (generation 22). Three cases were considered; case (i) gravity acts normal to the duct flow, towards the alveolus opening, case (ii) gravity acts normal to the duct flow, normal to the alveolus opening and case (iii) gravity acts in the direction of the duct flow. All the simulations were conducted for 30 LPM inhalation flow rate and an inhalation period of 1s. The results indicate that the sedimentation deposition is very high in the lower alveolar airway generations and the deposition is highly dependent on the orientation of the gravitational vector. Similar results were observed for case (i) and case (ii) where most of the micron particles were deposited on the alveolated duct. However, for case (iii) study, where the gravity is acting in the duct flow direction, significant reduction in particle deposition was noticed (see Fig. 4.1.9). Even though no specific alveolus deposition was noticed, it is evident that the alveolus wall deformation applies a pulling force on the particles even when an opposing gravitational force is present (see Fig. 4.1.10 where particle trajectory is influenced by alveolus expansion, when the gravity orientation is normal to the alveolus opening case (ii) and case (iii)).

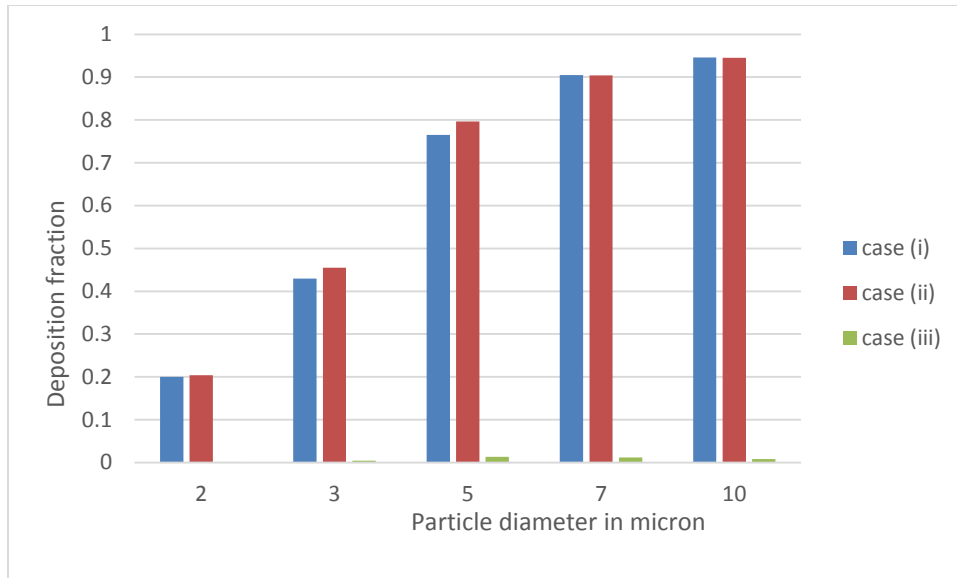


Fig. 4.1. 9. Aerosol deposition in a single alveolated duct representing generation 22 for an inhalation flow rate of 30 LPM

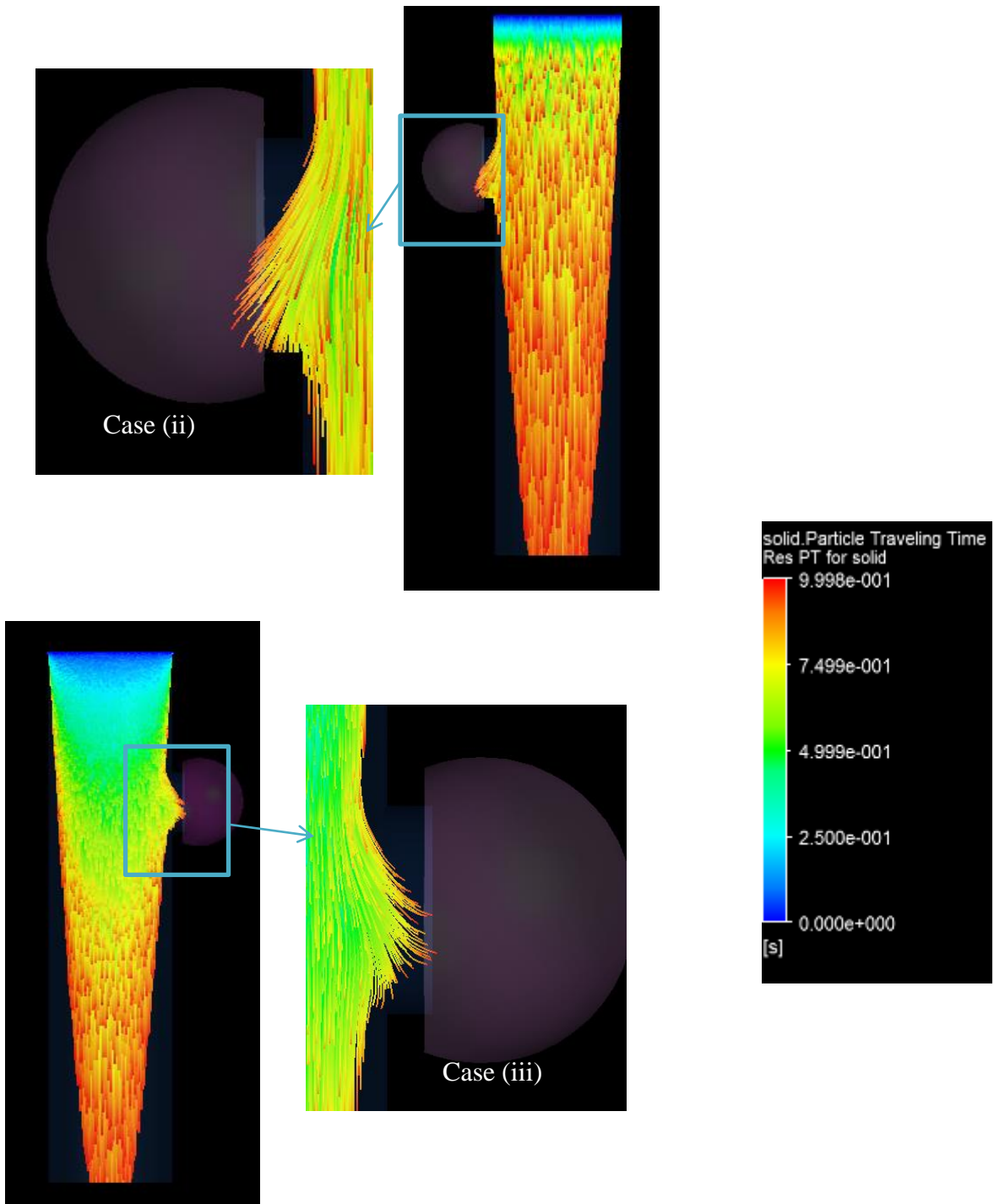


Fig. 4.1.10. Alveolar particle transport highlighting influence of gravity orientation

4.1.5.4 Periodically alveolated and multi-alveolated duct

To investigate the effects of multiple alveoli on particle trajectory, periodically alveolated duct and multi-alveolated duct models (representing generation 22) were used. The simulations were conducted for 30 LPM inhalation flow rate and an inhalation period of 2s. The particle deposition results in these models were similar to the deposition results in single alveolated duct. This is because the gravitational sedimentation force is dominating over other forces. However, it is interesting to notice that several of the particles were found to deposit in the alveoli over time. As shown in Fig. 4.1.11, increased deposition was noticed in the alveoli when the inhalation period was increased from 1s to 2s.

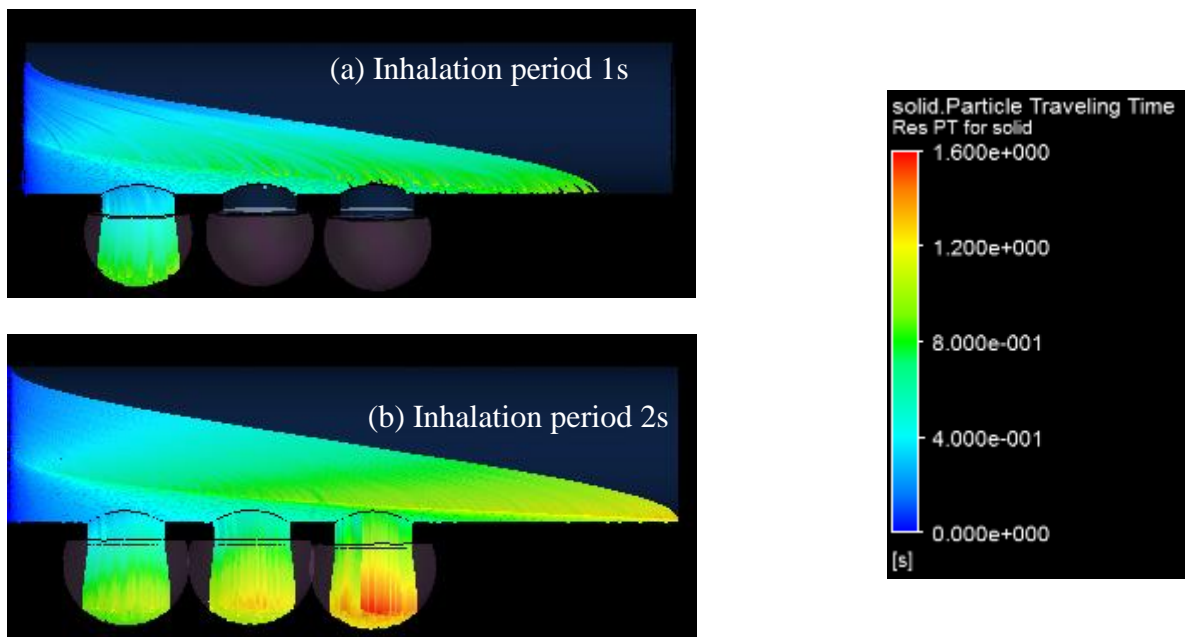


Fig. 4. 1.11. Particle trajectory in a periodically alveolated duct model for inhalation period (a) 1s (b)

2s

To better understand the extent to which the particle trajectory is influenced by the alveolar wall deformation, the multi-alveolated model was used. The number of alveoli in multi-alveolated model is 12 which is close to the number of alveoli in generation 22 as reported by Weibel. Hence the multi-alveolated model geometrically agrees well with a human lung airway generation. The simulation results are shown in Fig 4.1.12. In Fig. 4.1.12a and 4.1.12c, the simulations were conducted without the gravitational force but with an expanding alveoli. Figure 4b and 4c show the particle trajectory without the gravitational force and stationary alveoli. Clearly, the particles are pulled into the alveoli, when the alveolar wall is deforming. However, no particles entered the alveoli when the alveolar wall is stationary.

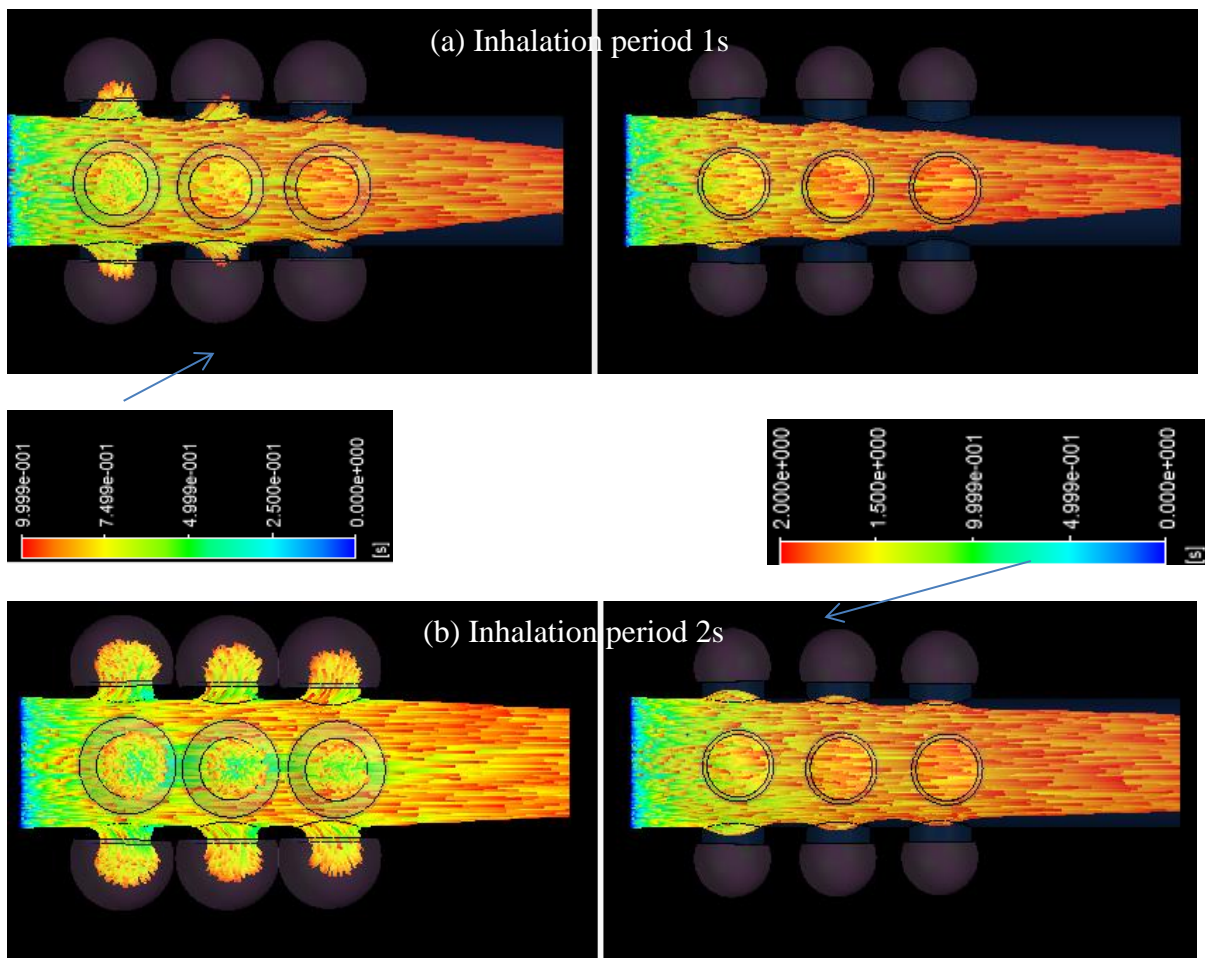


Fig. 4. 1.12. Particle trajectory in a multi-alveolated duct model with flexible wall (left) and rigid wall (right) for inhalation period (a) 1s, (b) 2s (simulations were conducted without the gravitational force)

4.1.6 Conclusion

In this study, three human alveolar airway models were developed and the significant forces affecting the particle transport through these airways were identified. It is evident from the simulation results that the position of the alveolus (generation number) determines the

alveolus wall deformation rate and the amount of convective mixing. The results clearly indicate the influence of alveolar wall deformation on air flow and particle deposition in these airways. *With increase in inhalation flow rate, the alveolar wall deformation rate increases, and results in a higher pulling force on the particle which may eventually result in higher alveolar deposition.* Hence, it can be concluded that for micron particles, even though the major deposition occurs due to gravitational sedimentation, the influence of alveolar deformation cannot be neglected.

4.2 Human acinar model

4.2.1 Introduction

Although several lung diseases are associated with toxic particle deposition in the alveolar airways, a detailed understanding of particle transport and deposition has not yet been fully analyzed [218]. In turn, for effective treatment a majority of pulmonary drugs are supposed to deposit in the alveolar region. The present study is limited because of the geometric complexity and inaccessibility of the alveolar region. To date, most of the available *in vivo* deposition results are obtained from high-resolution lung scans of sacrificed animals or from human autopsies. Available particle-deposition images of human lungs lack spatial resolution for identifying depositions in the acinar region ([186, 219, 220]).

These limitations can be overcome by computational study of the aerosol transport and deposition in lung airways [193]. The computational study of acinar flow and particle transport have mostly used single alveolus [221], single alveolated duct [184, 199, 213] and space filling polygonal model [90, 185, 192, 193]. The shape of the alveolus is one of the primary focus in these studies. Recently, investigations have been conducted using a polygonal space filling alveolar model [186, 192, 193, 210]. Even though the space filling model can accommodate multiple alveolated ducts, the model cannot account for the variation in airway bifurcation. Additionally, these models have not been shown to predict whole acinar lung deposition and hence these models have not been incorporated to study the deposition in a whole lung model except the work by Khajeh-Hosseini-Dalasm and Longest [222]. They used a space filling polygonal algorithm to study the deposition of drug aerosols

in human acinar models and the results from this study was incorporated into a whole lung model. However, their model did not account for the proximal partially alveolated lung airways and their modeling approach did not consider exhalation phase. Hence, there is an unmet need to develop a full acinar model which can predict realistically the particle transport and deposition.

The objective of this study is to develop a physiologically accurate whole acinar model. The developed model can efficiently simulate physiological breathing mechanism and predict alveolar particle deposition. The modeling approach, results, and conclusions from single alveolated duct study (See Chapter 4) have been utilized to develop the new human acinar model.

4.2.2 Model geometry

The alveolar region of the lung was modeled by attaching spherical alveoli to the TBU units. The attached alveoli did not intersect each other, but they were separated by a minimum distance to allow expansion. The alveoli attached TBU units were developed using computer aided design software. The spherical shape for alveoli was selected based on observations of Hansen [9]. A cylindrical projection from the lumen was used to anchor the spherical alveolus to the duct. The final alveolus has a $\frac{3}{4}$ spheroid shape. The dimensions of the TBU units and the alveolar cavities were based on the morphometric measurements of Weibel [2]. Table 4.2.1 shows the dimensions of an average TBU unit of generation 16-18 (Fig. 4.2.1). Weibel [2] reported that the alveolar region starts from the 17th generation with 5 alveoli and the 18th generation has 8 alveoli. The duct diameters were based on Weibel Type A

geometries Weibel [2] assuming a lung volume of 3 L. The diameter and depth of the alveoli in the 17th and the 18th generations were 0.021 cm and 0.02 cm respectively. Table 4.2.2 shows the dimensions of an average TBU unit of generation 19-21. Weibel [2] reported that the 19th generation has 12 alveoli, 20th generation has 20 alveoli and 21st generation has 20 alveoli. But due to space constriction, the developed model has 16 alveoli in 19th, 13 each in 20th and 21st generations (Fig. 4.2.2). Table 4.2.2 shows the dimensions of an average TBU unit of generation 19-21. Weibel [2] reported an average outlet diameter and depth of 0.018 cm and 0.0196 cm for an average total lung volume of 2.63L. It should be noticed that these dimensions were used to get a reference geometry. Each TBU units were again scaled to match the outlet diameters of the previous generations.

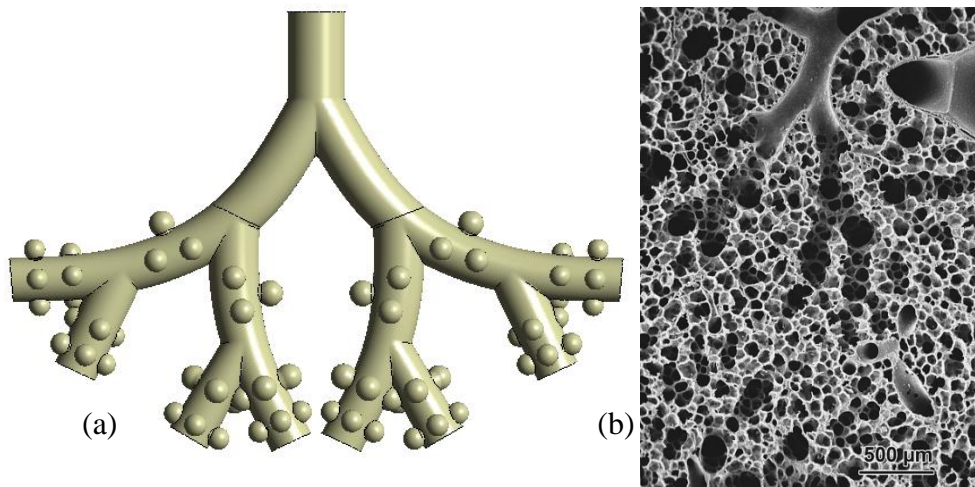


Fig. 4.2.1. (a) A representative TBU model with alveoli for generation 16-18. (b) Image of a terminal conducting airway from a lung cast (Weibel [223])

Table 4.2.1. Comparison of alveolar TBU model dimensions for generation 16-18 with morphometric measurements reported in literature

generation	Model			Scaled Weibel [2]		
	16	17	18	16	17	18
Number of alveoli	0	5	8	0	5	8
Duct diameter (cm)	0.051	0.046	0.043	0.051	0.046	0.043
Segment length (cm)	0.141	0.121	0.108	0.141	0.121	0.1

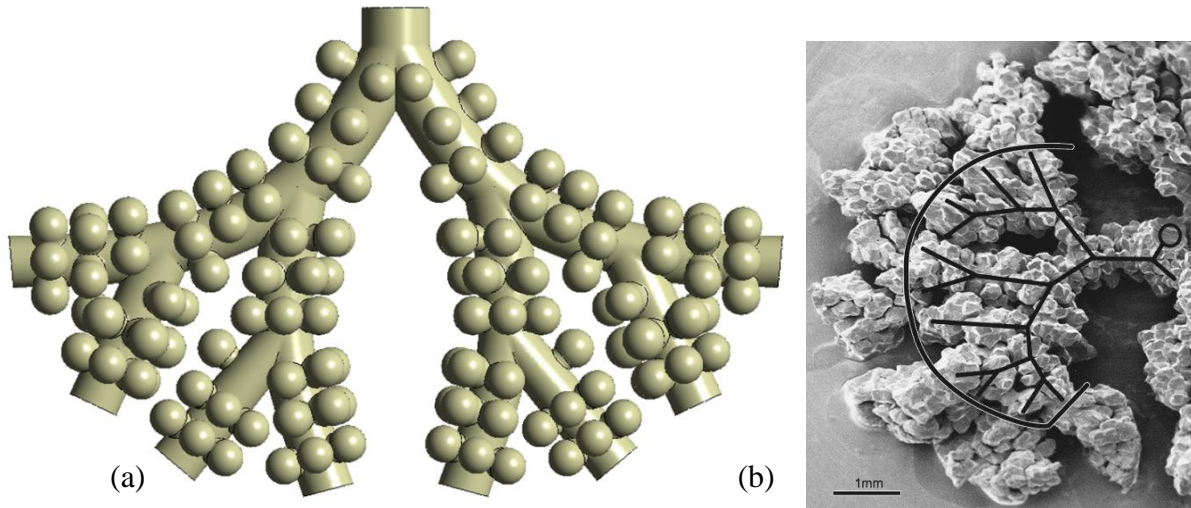


Fig. 4.2.2. (a) A representative TBU model with alveoli for generation 19-21(b) Image of an alveolar airway from a lung cast (Weibel [223])

Table 4.2.2. Comparison of alveolar TBU model dimensions for generation 19-21 with morphometric measurements reported in literature

generation	Model			Scaled Weibel [2]		
	19	20	21	19	20	21
Number of alveoli per generation	16	13	13	12	20	20
Total number of alveoli	42			42		
Duct diameter (cm)	0.04	0.037	0.033	0.04	0.038	0.037
Segment length (cm)	0.098	0.084	0.07	0.085	0.071	0.06

Figure 4.2.3 represents the TBU model of generation 22-23. As reported in literature, the final generation was modeled as a closed sac. The generation 22 has 14 alveoli attached to it duct. Instead of using separate alveoli, single spherical alveolus was used in generation 23. The total volume of 23rd generation was conserved in the model by creating the $\frac{3}{4}$ spheroid with the same total volume as generation 23. The total volume of generation 23 was calculated based on the reported number of alveoli, 17 in generation 23, and the duct diameter.

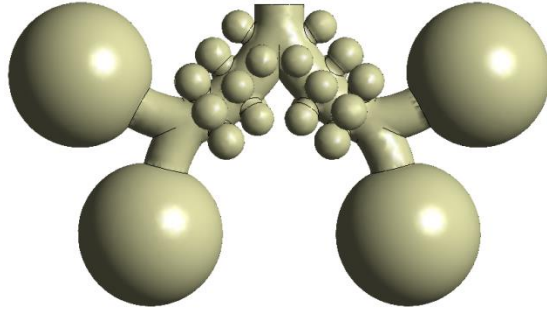


Fig. 4.2.3. A representative Double Bifurcation Unit (DBU) model with alveoli for generation 22-23

The final assembled full alveolar model is shown in Fig. 4.2.4. The surfaces marked with red are the alveoli and the surfaces marked with blue are the ducts. Only one TBU per generation was modeled and the TBU models for generation 19-21 and DBU model 22-23 were fitted to one of the outlets of the previous generation. This assumption has been proven to represent the whole alveolar generation provided that a symmetrical lung is assumed.

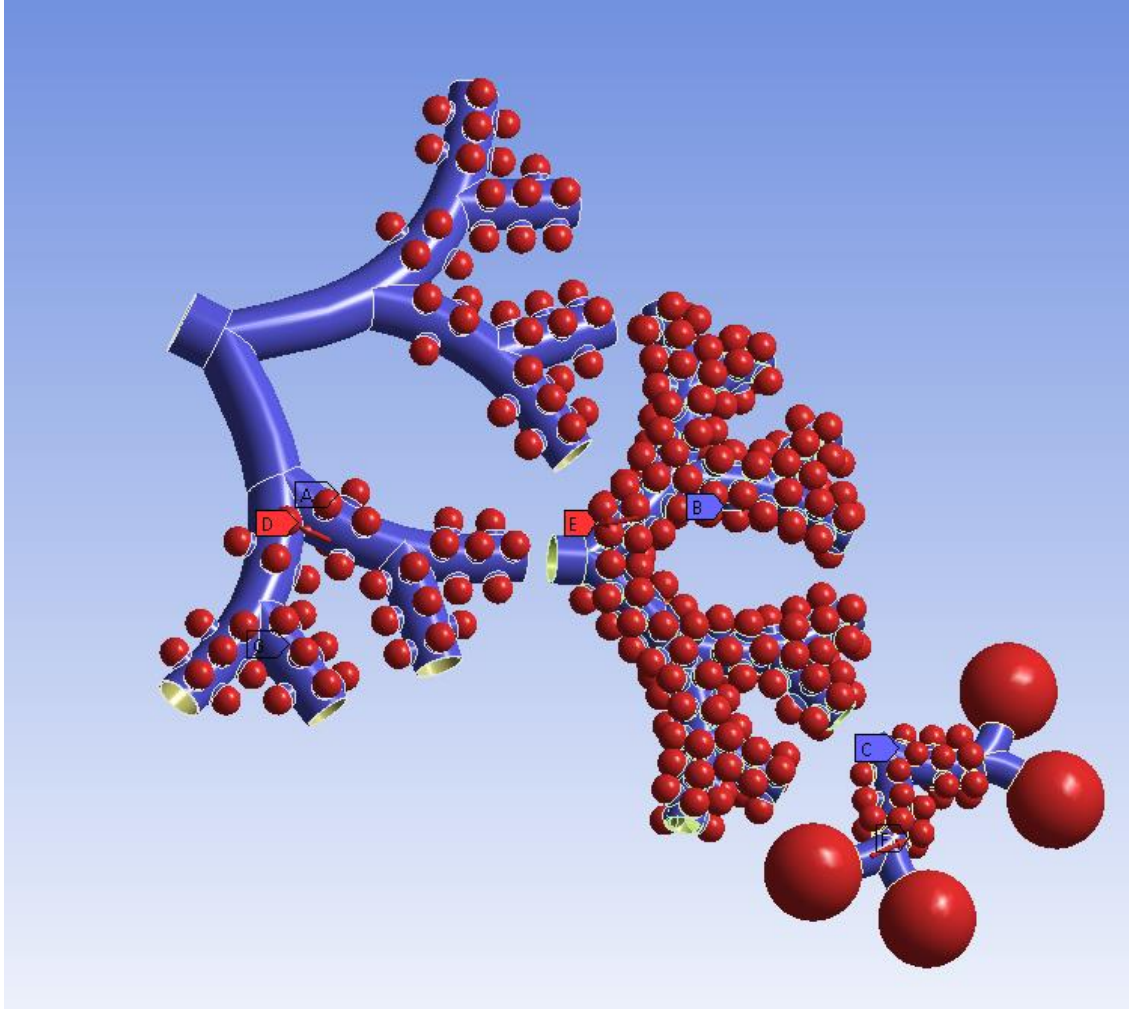


Fig. 4.2.4. Final assembled full alveolar model

4.2.3 Wall motion and boundary condition

The wall movement of the alveoli surface was modeled so that the breathing mechanism due to the negative alveolar pressure can be reproduced. The alveoli are assumed to deform and the deformation rate determines the inhalation and exhalation flow rate. The duct and alveolar neck are assumed to be rigid. The increase or decrease in volume of the alveoli

produces a differential pressure, which brings in or out air. Depending on the volume flow rate, a deformation vector for the alveoli was estimated to produce the required volume change. The increase in volume from the initial functional residual capacity (FRC) (assuming three-fourth of spheroid) can be represented using the following equations.

$$V_{FRC} = \pi r^3 \quad (4.21)$$

$$V_{FRC} + dV = \pi (r + dr)^3 = \pi (r^3 + dr^3 + 3r dr (r + dr)) \quad 4.2.2$$

$$dV = \pi (dr^3 + 3r dr (r + dr)) \quad (4.2.3)$$

Where V_{FRC} is the alveolus volume at FRC and dV is the increase in volume due to the radial expansion dr .

Assuming a symmetric dichotomous branching structure of the lung, the inhalation flow rate through any generation will be flow rate measured at the oral inlet divided by the number of airways in that generation. This can be mathematically represented using the following equations.

$$\dot{M}_g = \frac{\dot{M}_{inlet}}{2^g} \quad (4.2.4)$$

$$\dot{V}_g = \frac{\dot{V}_{inlet}}{2^g} \quad (4.2.5)$$

Where \dot{M}_{inlet} is the mass flow rate at the oral inlet, \dot{M}_g is the mass flow rate through the airway generation g , \dot{V}_{inlet} is the volume flow rate at oral inlet and \dot{V}_g is the volume flow rate through the airway generation g .

Also, it is assumed that the airflow rate is generated due to the alveolar deformation and the deformation rate varies with the TBU. The alveoli in each TBU deform in order to produce

fraction of the oral inhalation flow rate which is equal to the total flow rate times the alveolar volume fraction in the TBU (Table 4.2.3). This can be mathematically represented using

$$\dot{V}_{TBU}(t) = \dot{V}_{TBU}^{FRC} + \dot{V}_T \frac{\dot{V}_{TBU}^{FRC}}{\sum_{g=17}^{23} \dot{V}_g^{FRC}} \quad (4.2.6)$$

Where $\dot{V}_{TBU}(t)$ is the instantaneous volume of the TBU at any time t , \dot{V}_{TBU}^{FRC} is the volume of the TBU at FRC and \dot{V}_g^{FRC} is the volume of the airway generation g . The alveolar volume

fraction within a TBU is represented using

$$\frac{\dot{V}_{TBU}^{FRC}}{\sum_{g=17}^{23} \dot{V}_g^{FRC}}$$

The model describes how the inhaled fresh air is filled in the airways. The fresh inhaled air successively fills in the lung generations, starting from the most proximal airway first.

Additionally, the individual alveolus wall deformation can be estimated by dividing the fractional volume flow rate per TBU with the number of alveoli in that TBU. The volume

flow rate $\frac{dV}{dt}$ in a particular lung generation for any given inhalation condition can be predetermined and hence the corresponding alveolar deformation can be estimated by solving

equation (3) for $\frac{dr}{dt}$. The contraction of the alveoli was modeled by following a reverse path from the expanded volume to the original FRC volume at an identical deformation rate.

Table 4.2.3. Number of alveoli and alveolar volume fraction in the TBU

TBU	Number of alveoli	Alveolar volume fraction
16-18	84	0.03
19-21	182	0.25
22	25	0.27
23	4	0.45

As suggested by previous studies, the rhythmic expansion and contraction of the lung is assumed to be geometrically self-similar in nature, indicating that the deformation is similar in all alveoli. The presence of surfactant also helps the alveoli to expand and contract at the same rate. In human lung, the deformation of the alveoli depends on the inhalation volume flow rate and the period of inhalation and the deformation is limited after a certain period of inhalation. The surface tension of the surfactants and nonlinear elasticity of the lung tissue prohibits expansion of alveoli beyond a specific radius. In order to replicate the physiological breathing motion of the alveoli, the deformation of the alveoli was restricted after a specified increase in alveolar radius. This final radius was estimated based on the self-similar assumption. For an average human adult with FRC of 3000ml and total lung capacity of 6000ml, the maximum lung deformation possible is 3000ml. Based on the self-similarity rule, the maximum increase in alveolar radius possible is estimated to be 0.26 times the initial radius. Additionally, the nonlinear alveolar tissue dynamics and the presence of surfactants inside alveoli may limit the stretching of the alveolar walls after the initial

expansion. This effect was incorporated into the model by assuming that after 500 ml of tidal volume, the expansion rate was reduced to half. Once the alveoli reach its maximum deforming capacity, the deformation rates of the alveoli in distal generations are increased proportionally to satisfy the required oral inhalation volume flow rate.

4.2.4 Numerical method

In order to reduce the computational effort and resources required for simulating the full alveolar model, each individual TBU/DBU were simulated independently, At the inlet of these TBU/DBU, an opening boundary condition (entrainment) was applied. This boundary condition will ensure that the physiological breathing mechanism (air sucked in during inspirations and air pushed out during expiration) will be replicated. A wall deformation vector (depend on the TBU/DBU) was applied on the alveoli surface and rest of the airway wall was assumed to be rigid. At the outlet, a mass flow rate boundary condition was applied in such a way that the outlet mass flow rate Q_D and mass flow rate due to the alveolar wall motion Q_A together results in the inlet mass flow rate Q_G (mass flow rate per generation). For details regarding boundary conditions refer chapter 4.1.

No slip boundary condition was applied at the wall boundaries (duct and alveoli) so that the fluid velocity matches with the wall velocity at the fluid wall interface. A user defined CEL functions was used to apply the wall deformation vector.

In order to study the effects of inhalation conditions on alveolar flow pattern, constant oral inhalation flow rates were assumed. Simulations were conducted for rest (15 LPM), breathing conditions with inhalation period of 2s and 4s. Figure 4.2.5 depicts a synthetic

breathing profile during light activities, where a mass flow rate of 15 LPM was assumed. The simple breathing waveforms shown here were selected in order to compare the model predictions with experimental data sets in which subjects inhaled and exhaled with constant mass flow rates. Clearly, by controlling the alveolar-wall displacement, any inhalation wave forms can be simulated, which implies that the model is capable of simulating actual breathing patterns.

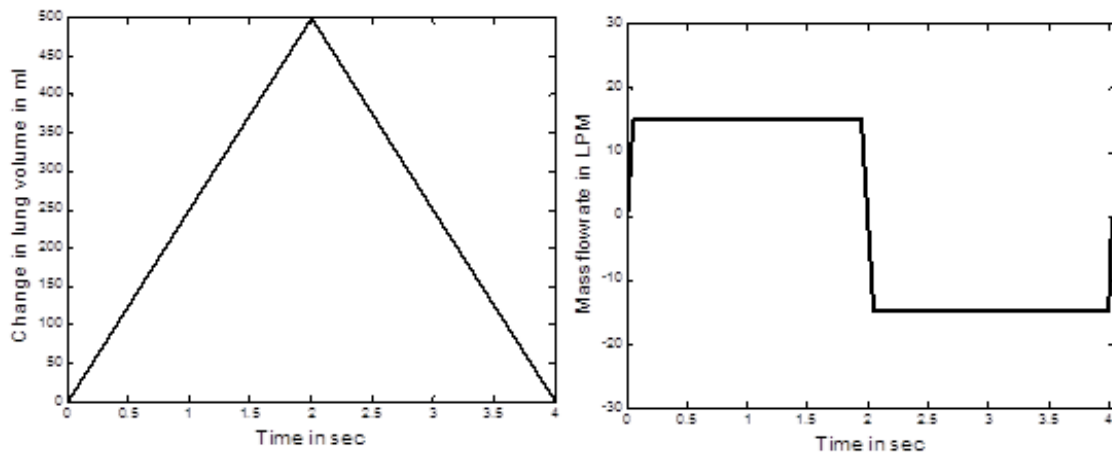


Fig. 4.2.5. Breathing profiles depicted in terms of the changes in lung volume and the corresponding mass flow rates: inhalation flow rate 15 LPM and tidal volume 500 cm^3

Assuming a dilute particle suspensions, one-way coupling was assumed between the fluid and particle phases. 20,000 particles per second were injected at the inlet of TBU 16-18 and particles were assumed to deposit on the walls on contact. Increasing the number of particles by a factor of 2 showed less than 2% difference in the results. Particles were distributed uniformly at the inlet with an initial velocity being the same as the inlet-air velocity. Since

the upstream particle distribution has a significant influence on the particle deposition in subsequent generations, the outlet measurements (particle distributions) from the upper TBU were exported at each time step to become the inlet conditions for the next generation TBUs and the process was continued for all TBUs attached later on.

4.2.5 Results and discussion

4.2.5.1 Alveolar flow pattern

In order to study the change in flow pattern in the acinar region, the inhalation and exhalation process was simulated using the full alveolar model. The airflow through an alveolated duct depends on the rhythmic expansion and contraction rate of the alveoli.

Inhalation 15 LPM: The flow pattern through different generations of the TBU 16-18 during inhalation with an inhalation flow rate of 15 LPM is shown in Fig. 4.2.6. Enlarged view of the flow streamlines and velocity vectors inside alveolus are also displayed. The results indicate that airflow in the alveolus of the proximal alveolar airways is highly recirculating. The flow in the airway duct induces a shear flow across the alveolar mouth, thus generating a recirculation region in the alveolar cavity. The presence of alveoli around the duct produces a deflection among a small portion of duct flow into the alveolar cavity. The size of the alveolar cavity is very less compared to the duct diameter. Hence the amount of duct air entering the alveoli is also less. However, within the TBU also variation in the intensity of the recirculation flow was noticed. As shown in Fig. 4.2.6, the velocity vectors inside alveolus in generation 17 shows rotating flow while the flow inside alveolus in

generation 18 has a mixed radial and recirculating flow. This is due to the decreased shear flow through the ducts. As the generation number increases the flow is divided by half which in turn reduces the shear flow through the duct and hence the recirculating alveolar flow and increase the radial flow into the alveolus.

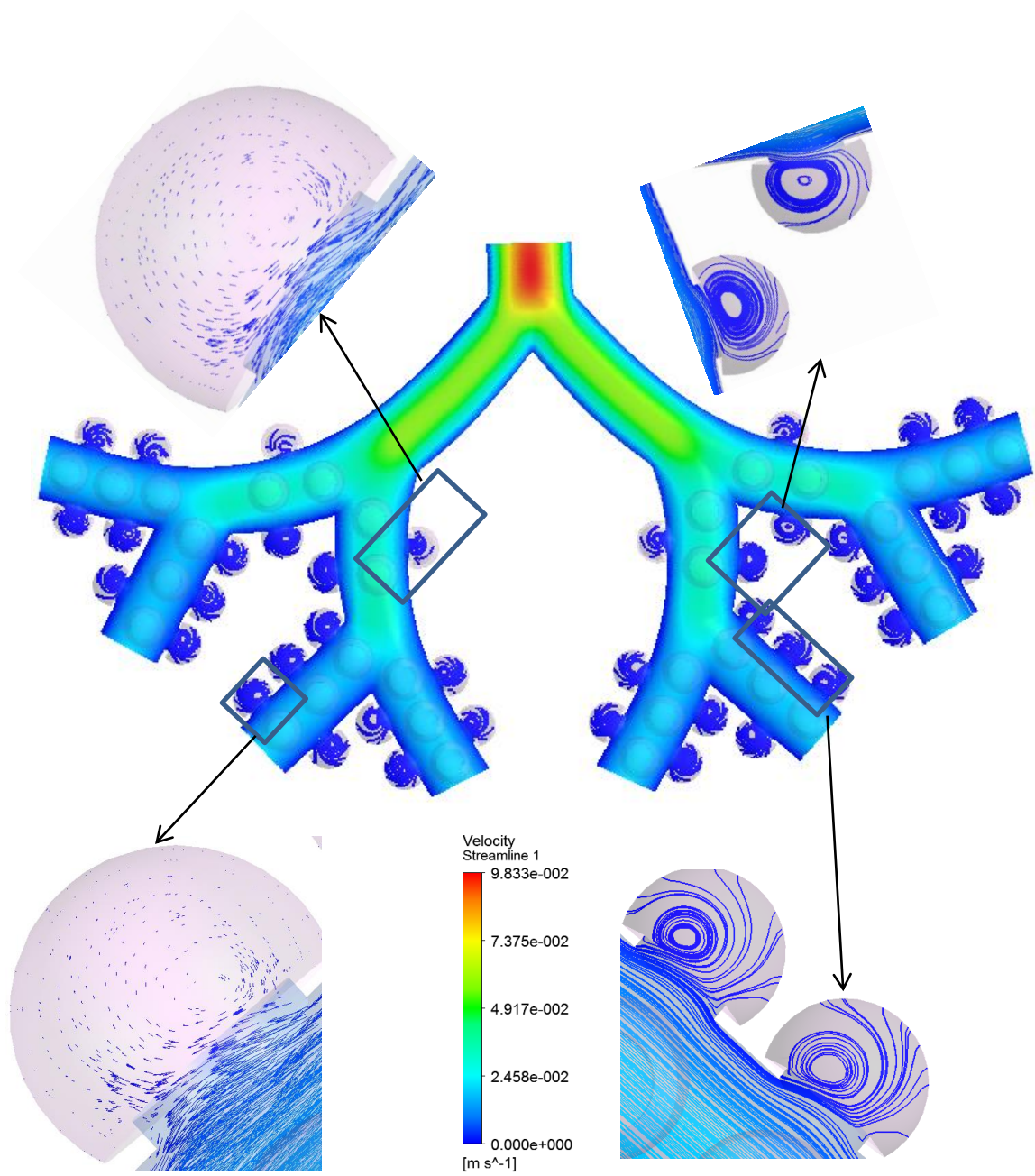


Fig. 4.2.6. Enlarged view of the flow stream lines and velocity vectors inside TBU 16-18

The flow pattern through different generations of the TBU 19-21 during inhalation with an inhalation flow rate of 15 LPM is shown in Fig. 4.2.7. An enlarged view of the flow streamlines and velocity vectors inside alveolus are also displayed. The results show that the intensity of the recirculating flow inside alveolus is decreasing while the radial flow is increasing. The flow inside an alveolus in generation 21 is mostly radial. Hence, it is expected that the mass transfer from the duct to the alveoli will increase in the distal lung generations.

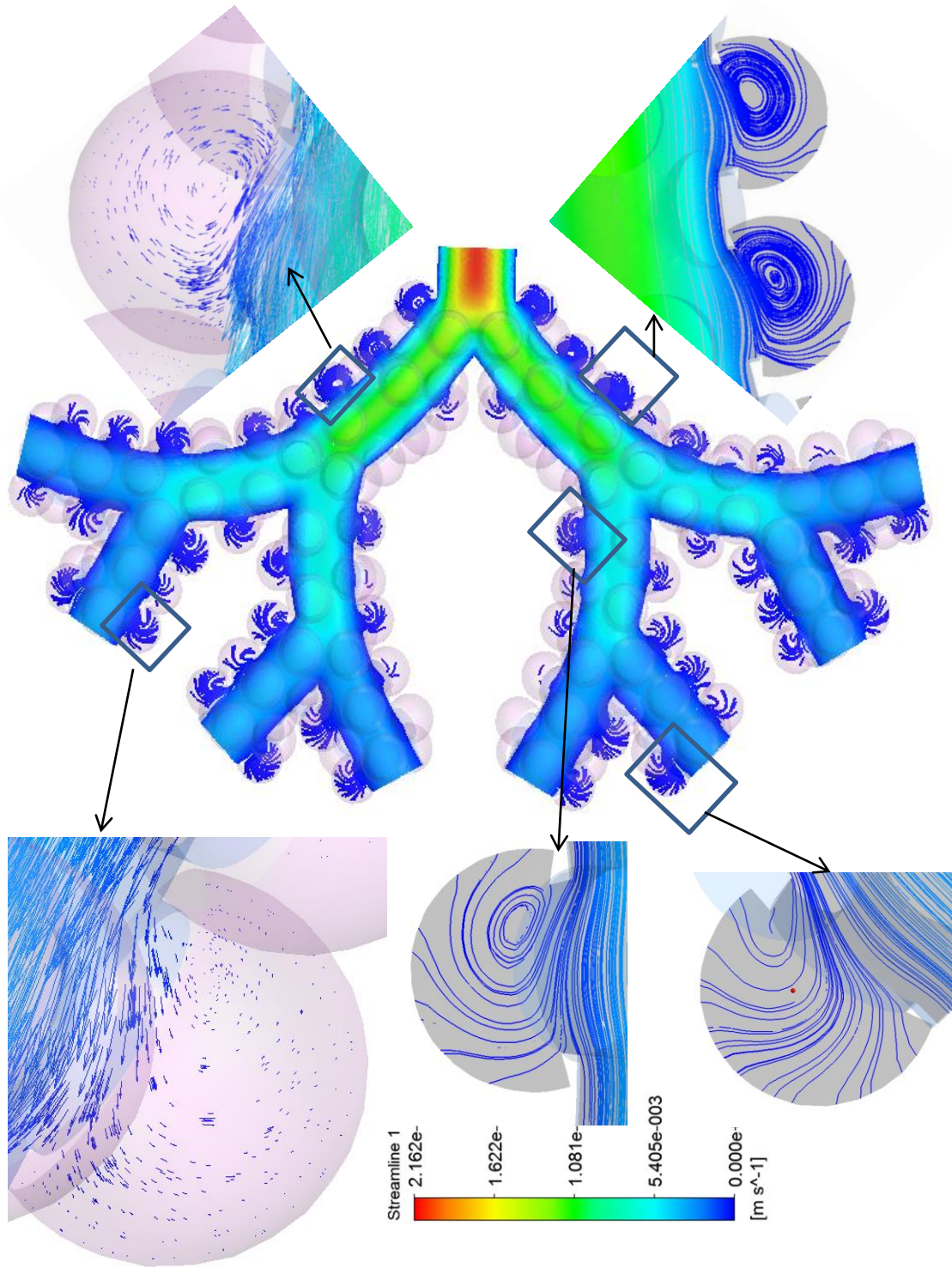


FIG.4.2.7. Enlarged view of the flow stream lines and velocity vectors inside TBU 19-21

The flow pattern through different generations of the DBU 22-23 during inhalation with an inhalation flow rate of 15 LPM is shown in Fig.4.2.8. Enlarged view of the flow stream lines and velocity vectors inside alveolus are also displayed. The flow pattern inside the alveolus is fully radial. The expansion of the alveolar sac model representing generation 23 generates most the inhalation flow rate. Hence the flow into the alveolar sac is fully radial. However, the flow in these distal lung regions under the assumed inhalation flow rate of 15 LPM exhibit low Reynolds number quasi-steady characteristics.

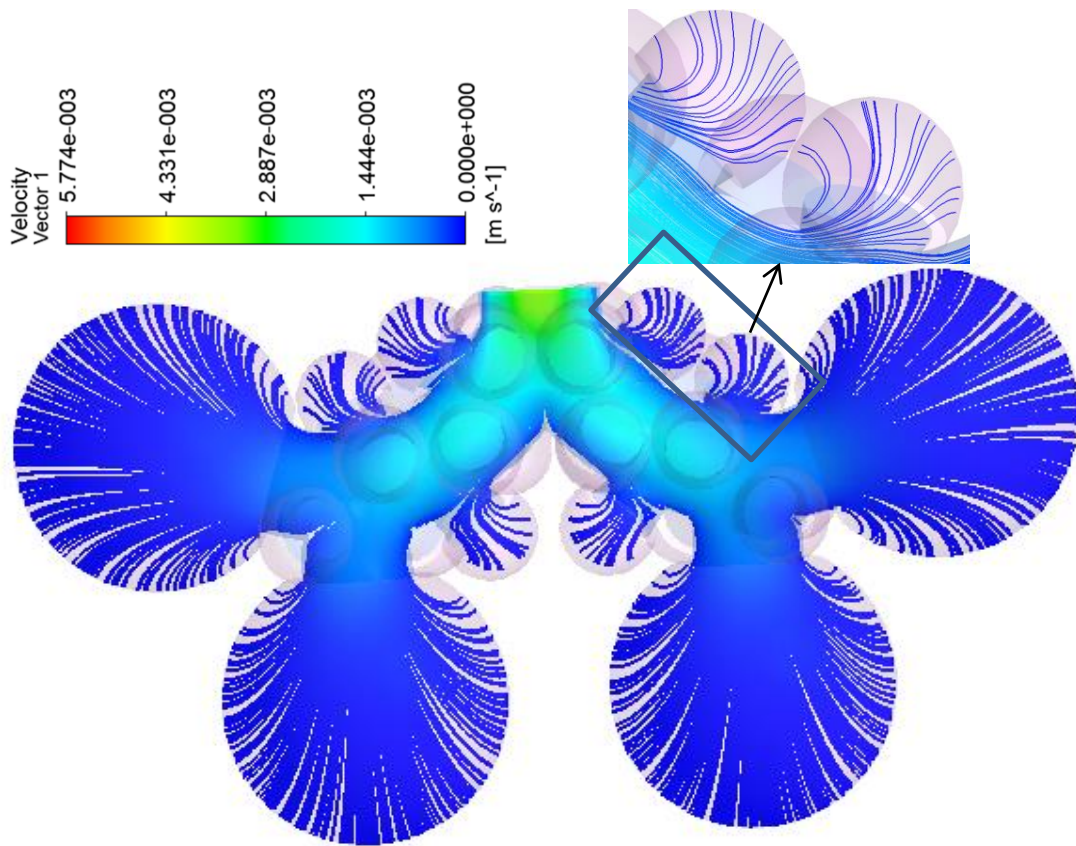


Fig.4.2.8. Enlarged view of the flow stream lines and velocity vectors inside DBU 22-23

Exhalation 15 LPM: The flow pattern during the exhalation phase is almost identical to the inhalation phase for all TBUs and DBU. However, the flow direction is causing the flow to exit the alveolus and merge to the duct flow. The flow pattern through different generations of the TBU 16-18, TBU 19-21 and DBU 22-23 during exhalation with an expiratory flow rate of 15 LPM is shown in Fig.4.2.9 to Fig.4.2.11.

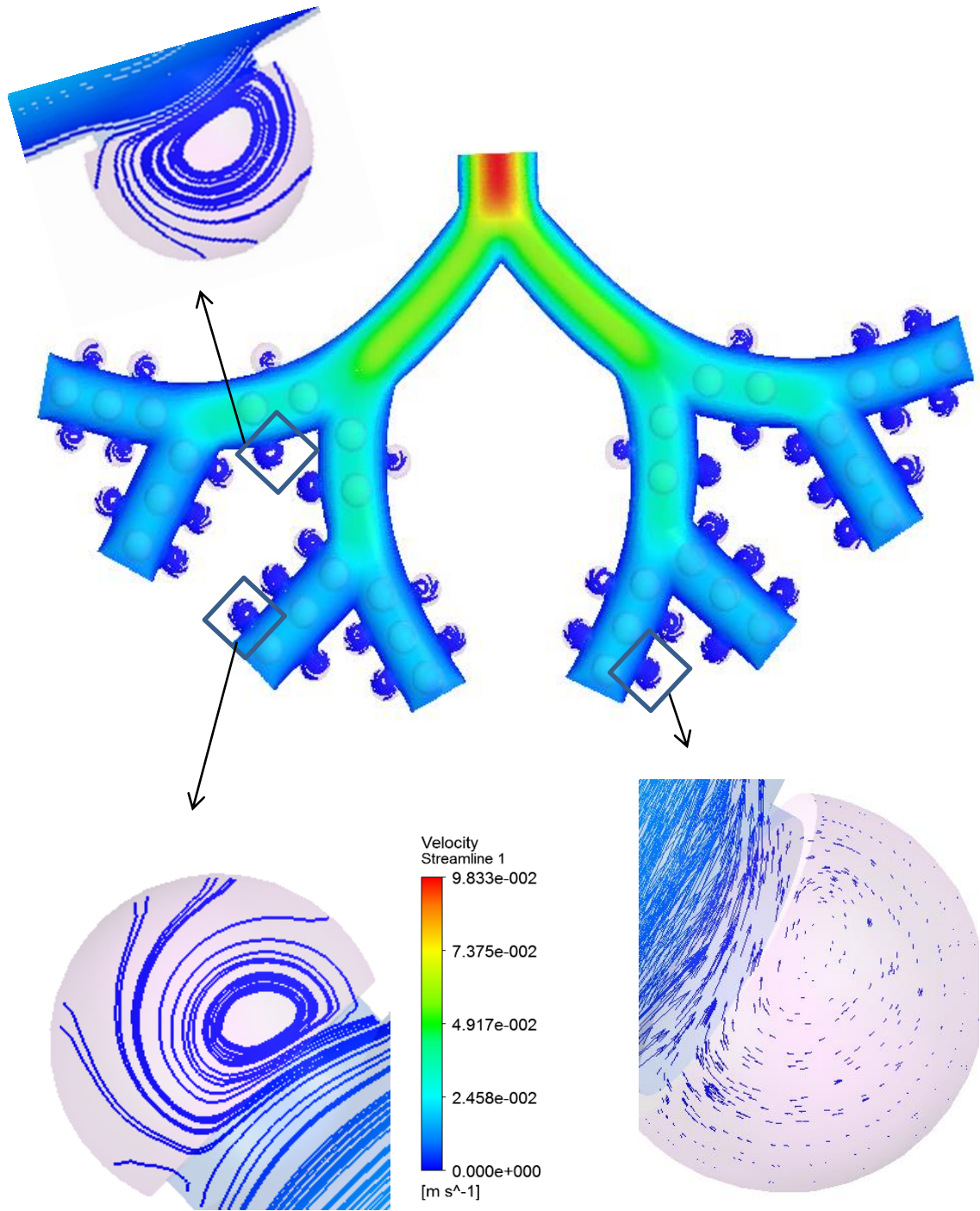


Fig.4.2.9. Enlarged view of the flow stream lines and velocity vectors inside TBU 16-18

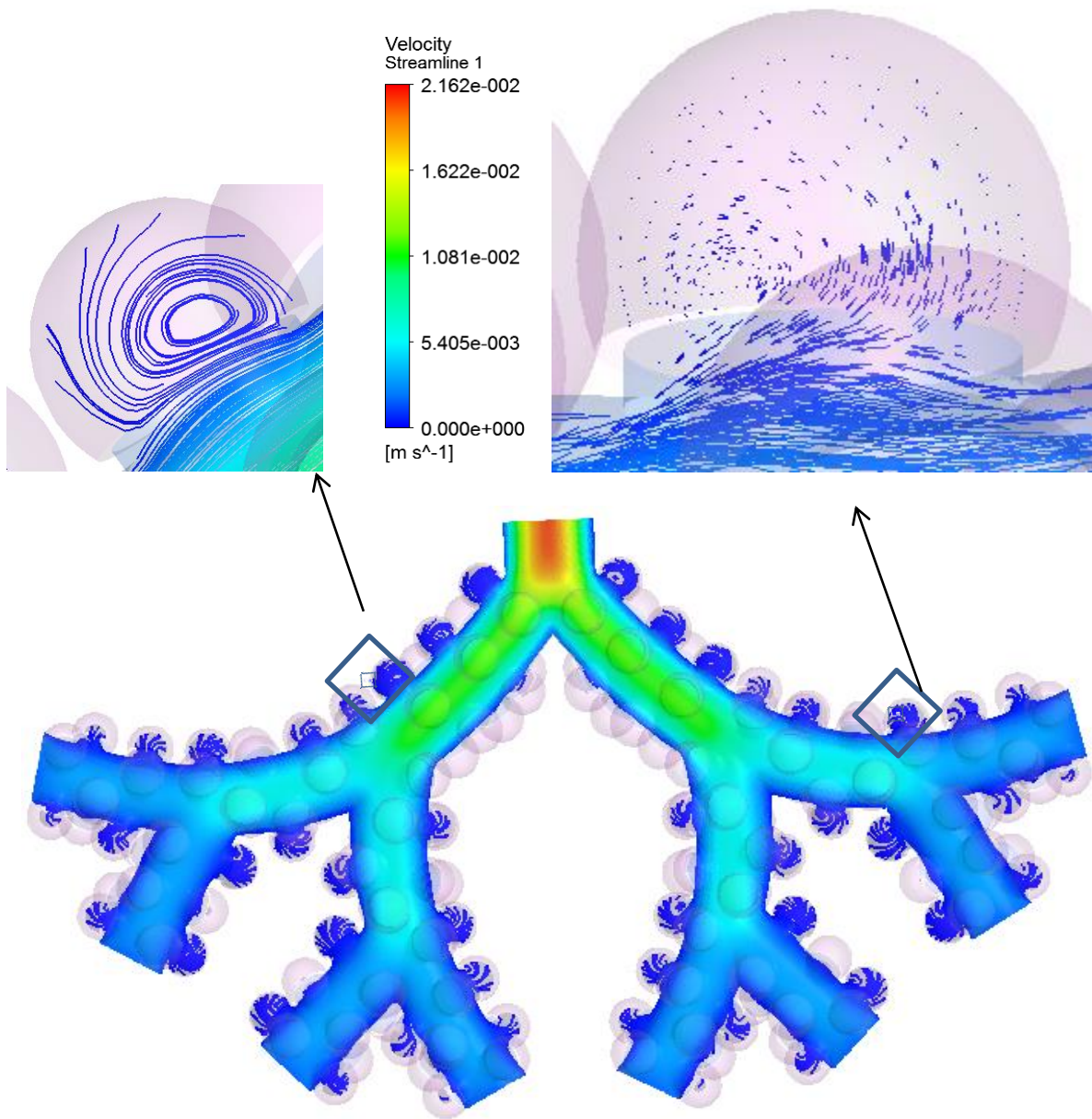


Fig.4.2.10. Enlarged view of the flow stream lines and velocity vectors inside TBU 19-21

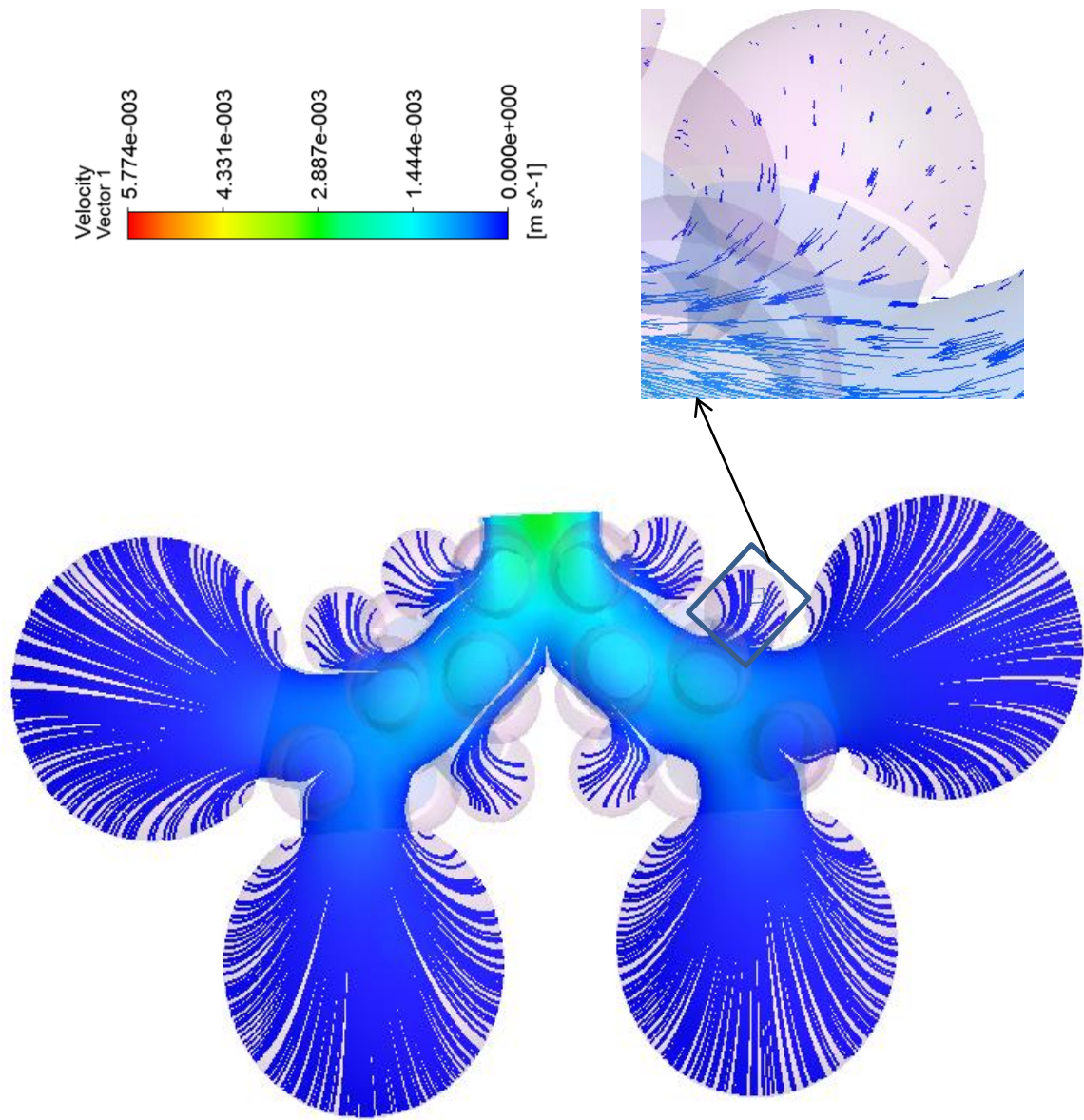


Fig.4.2.11. Enlarged view of the flow stream lines and velocity vectors inside DBU 16-18

4.2.5.2 Particle transport and deposition

The trajectories of the particle with diameter $3\ \mu\text{m}$ and $5\ \mu\text{m}$ were simulated using the full alveolar model. The simulations were conducted at an oral inhalation flow rate of 15 LPM with tidal volumes 500ml and 1000ml (inhalation period of 2s and 4s). The flow rate was assumed to be constant during inhalation and exhalation. The gravity was assumed to act in the negative z direction (the axis is shown in Fig.). This assumption will ensure that gravity is neither acting in the direction of flow nor normal to the flow. Both these cases will lead large bias in particle deposition due to the high influence of gravity on particle deposition in the alveolar airways. Hence, the current assumption will represent a generalized case in which an average of the both situations is represented.

Inhalation 15 LPM: The particle deposition results for $3\ \mu\text{m}$ and $5\ \mu\text{m}$ cases during inhalation phase are shown in Fig.4.2.12. The number of particles deposited is higher in the mid alveolar airways compared to other airway generations. The results show that as the inhalation tidal volume increases more number of particles are being pulled into the distal lung airways and hence the deposition in these distal lung regions increases. The deposition in the proximal alveolar region (generation 16 to 18) is constant for all the inhalation conditions. This is noticed for both $3\ \mu\text{m}$ and $5\ \mu\text{m}$ cases. However, increase in particle deposition in all lung generations was observed with an increase in the particle diameter. The results indicate that the increase in particle lung deposition with an increase in inhalation tidal volume is mostly due to the increased deposition in distal alveolar airways.

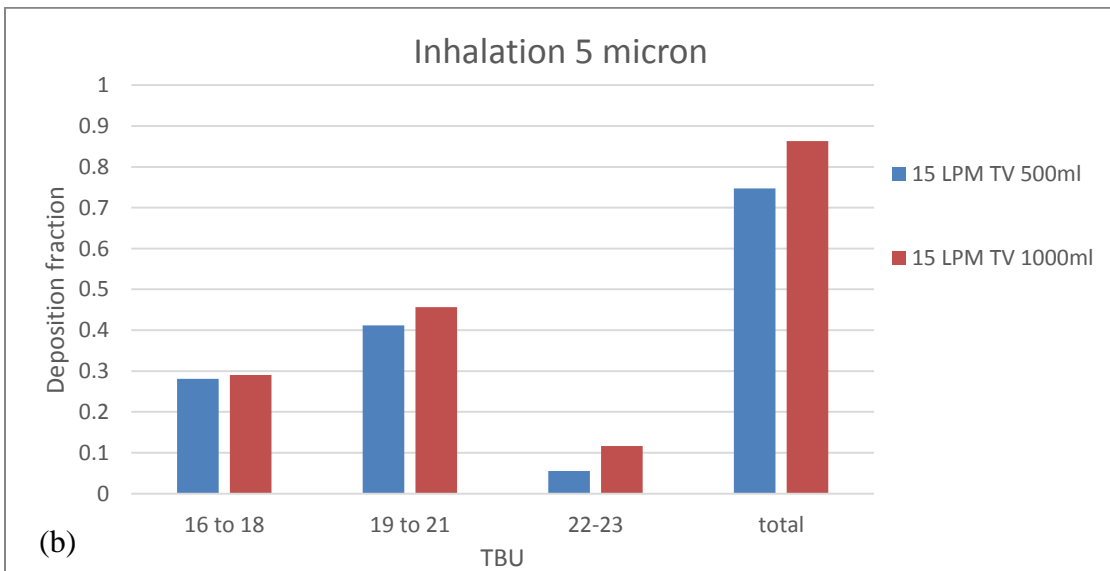
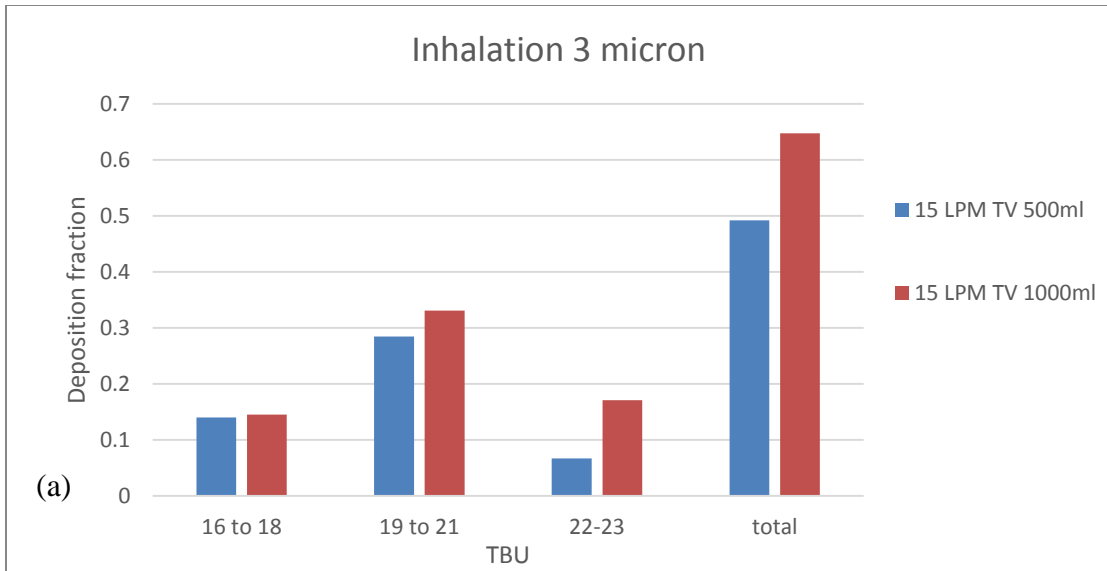


Fig.4.2.12. Particle deposition results for (a) 3 μm and (b) 5 μm case during inhalation phase

The location of the deposited particles (3 μm) in the full alveolar model during inhalation phase with a tidal volume of 1000ml is shown in Fig.4.2.13. The results indicate that majority of the particles are deposited due to gravitational sedimentation.

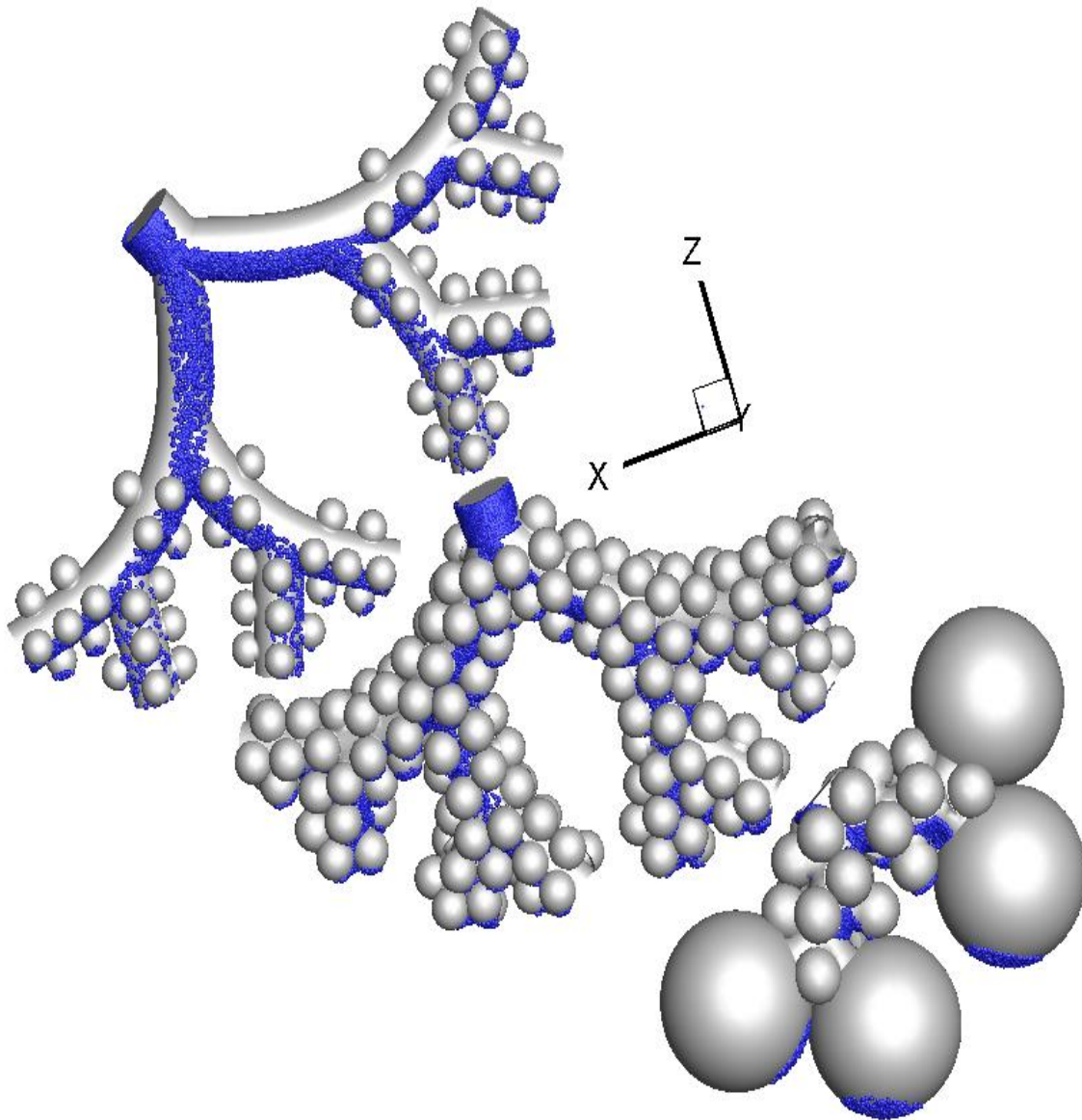


Fig.4.2.13. Location of the deposited particles (3 m) in the full alveolar model during inhalation phase with a tidal volume of 1000ml

Exhalation 15 LPM: The particle deposition results for 3 μm and 5 μm cases during exhalation phase are shown in Fig.4.2.14. As observed during the inhalation phase, the particle deposition is higher in the mid alveolar airways and the proximal alveolar airways. Contrary to the deposition results during inhalation phase, the particle deposition is higher when the inhalation tidal volume is lower. This can be attributed to the large number of suspended particles in the airways. These suspended particles are mostly particles that are being inhaled during the final inhalation phase. Due to the low inhalation flow rate, they reach the mid alveolar airways and during the exhalation phase these particles tend to deposit in the proximal alveolar airways due to gravitational sedimentation.

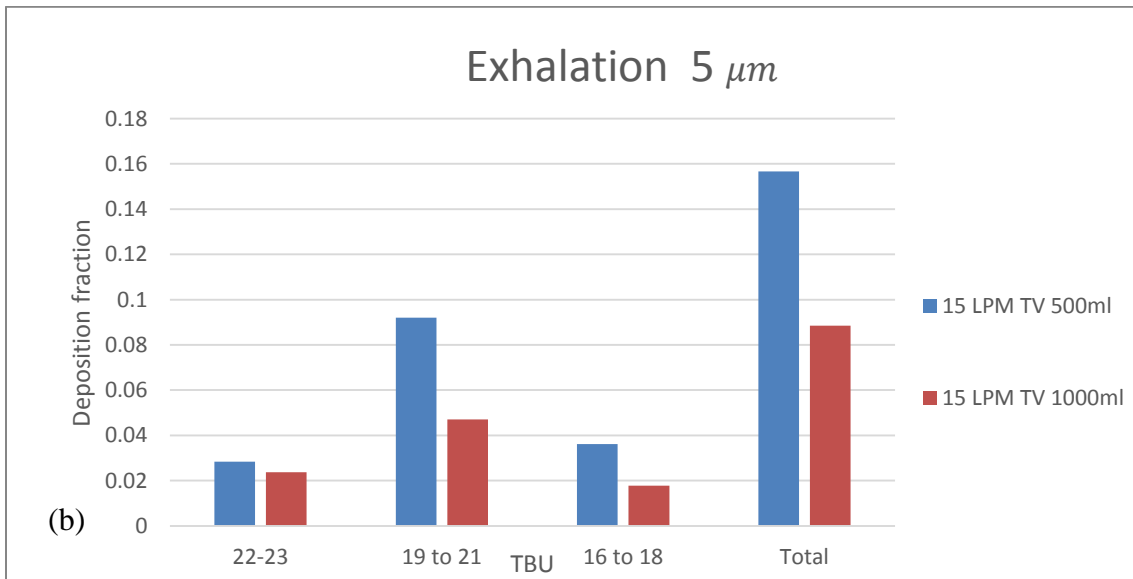
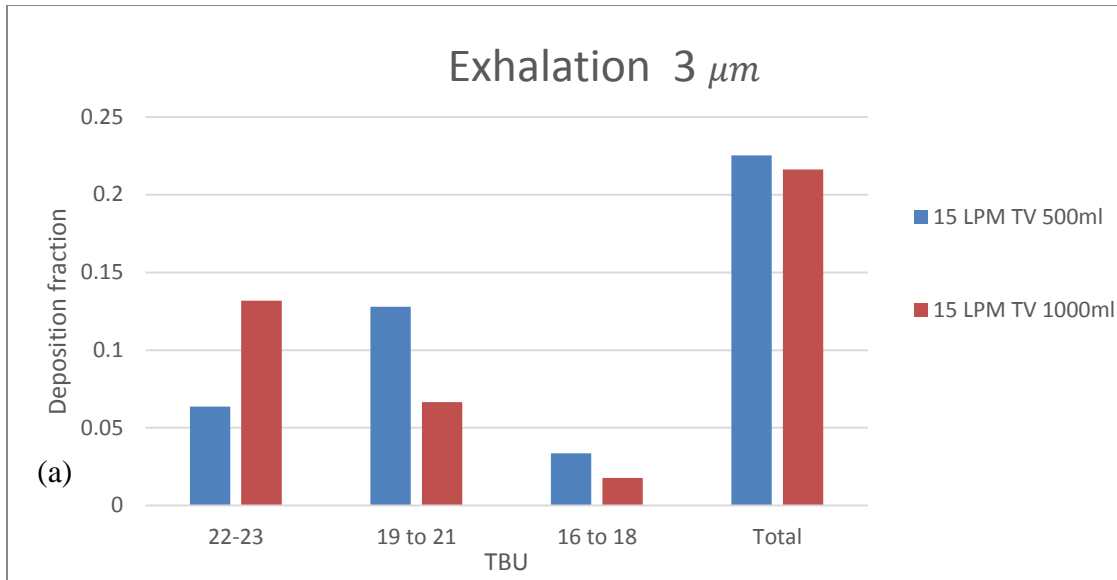


Fig.4.2.14. Particle deposition results for (a) 3 μm and (b) 5 μm case during exhalation phase

4.2.5.3 Total alveolar deposition

The total acinar particle deposition results during a full breathing cycle are plotted in Fig. 4.2.15. The number of particles remained in suspension at the end of the first inhalation cycle is less than 0.5% for inhalation with 500ml tidal volume and 0.1% for inhalation with 1000ml tidal volume. Therefore only one breathing cycle was simulated. It is evident from the results that, an increase in the inhalation tidal volume and/or an increase in particle diameter will result in increased acinar deposition.

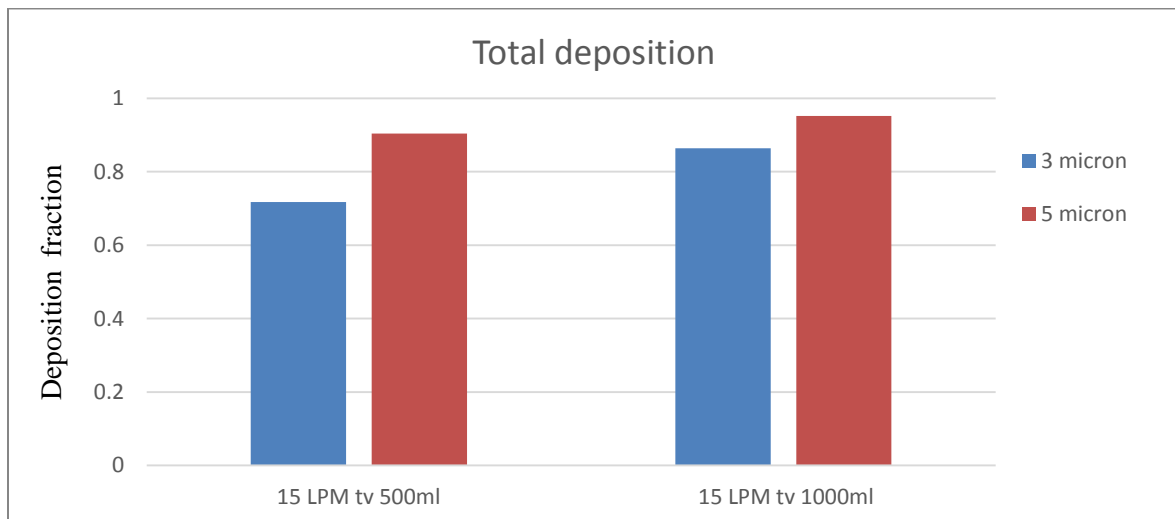


Fig. 4.2.15. Total acinar particle deposition results during a full breathing cycle

4.2.6 Conclusions

A physiologically accurate whole acinar model was developed which can efficiently simulate physiological breathing mechanism and predict alveolar flow pattern and particle deposition. The simulations showed that the alveolar flow pattern depends on the location of the alveoli. The dominating flow mechanism for alveoli present in the proximal lung generations is the recirculating flow. In the mid alveolar lung generations, intensity of the recirculating flow inside the alveolus is decreasing while the radial flow is increasing. In the distal alveoli, the flow pattern is completely radial. The particle simulation results indicate that the particle deposition depend on the inhalation conditions and particle size. The particle deposition rate in the alveolar region increased with increasing inhalation tidal volume and particle diameter. The particle diameters considered for the current study are typical sizes of pharmaceutical pulmonary medicines. As reported in chapter 5.1, the key mechanism for micrometer sized particle deposition in the alveolar lung airways is gravitational sedimentation and the interplay between wall motion and sedimentation significantly increase the deposition. However, it should be noted that these are the deposition results without considering the deposition in the upper airways and the extrathoracic airway, which may filter out many of the micrometer particles before reaching the alveolar region.

The primary objective of this work was to show the modeling framework for a physiologically realistic whole acinar model. In future, the influence of inhalation flow rate and orientation of gravity vector may be analyzed. The limitations of this study includes, the assumption of symmetric alveolar airways and the assumption of the shape and size of the alveoli, There are several studies which have considered polygonal shapes. However, not

many studies have focused on variation of alveolar size with respect to the generation. Hence, future study should focus on adapting the current model to accommodate these limitations.

CHAPTER 5

Whole Lung Airway Model II

5.1 Single-path and two-path models

5.1.1 Introduction

Respiratory drug delivery is becoming an increasingly popular way of administering medicine. It is efficient for treating both pulmonary and systemic pathogenic conditions as discussed in [85, 138, 139]. Respiratory drugs are administered to the lungs with the inhaled air using an inhaler device, as discussed in [140-143]. Scientific measurements to predict the lung dosage and device function are required for new inhaler devices. New or generic drugs have to be bio-equivalent before approval for clinical application. The most common way of measuring the amount of drugs deposited in the lung airways are *in vitro* tests using idealized oral cavity models and assuming that the particles exiting the oral cavity deposit in the lung airways [150-152]. Clearly, these measurements cannot provide detailed total and regional lung deposition/dosage measurements. Alternatively, *in vivo* experiments using radio-nuclide imaging (via gamma scintigraphy and positron emission tomography) and/or pharmacokinetic studies were used [147, 153, 154]. For radionuclide imaging the active therapeutic agents are labeled with a radionuclide before inhalation by the subject. After administration of the radiolabeled drug formulation using the device, the different views of the lung are captured using a gamma camera [147, 155, 156]. In pharmacokinetic measurements, the amount of drugs deposited in the lungs is estimated based on the amount of drugs measured in blood and urinary samples, collected from the subjects after administration of the drugs [153, 157, 158]. There are many limitations for these two measurement techniques; both techniques need human subjects and these techniques involve

either inhalation of radioactive materials or requiring blood and urinary samples during intervals of time. The radionuclide image measurement method is further complicated due to the limited ability to radiolabel drug formulations without varying the aerodynamic properties. However, the gamma scintigraphy image can provide direct image visualization and an approximate whole-lung and regional deposition measurements [138, 154, 159, 160]. In case of the pharmacokinetic measurement method, only an approximate estimate of total lung deposition is possible; thus, without any information regarding the deposition sites. Recently, there has been an effort to combine single-photon-emission-computed-tomography (SPECT) image of deposited radio-labelled drugs with high resolution computed-tomography (CT) scan images of the same subject to accurately estimate the deposition sites [133, 134, 161]. However, due to the limited resolution of airway imaging via CT and SPECT, associated with long processing times, detailed lung anatomical mapping is not possible except for few upper bronchial airways. Considering all these limitations of the experimental and *in vivo* measurement methods, computational analysis has significant advantages as it is safe as well as time and cost efficient [26, 67, 98, 149, 162-164]. Once validated, computer simulations can provide detailed total and regional particle-deposition results which are of interest to toxicologists, health-care providers and inhaler-manufacturers alike [165-167].

Due to the sheer complexity of the lung morphometry, it is unfeasible to model the lung breathing process in its full scale. Hence alternate simplistic models are developed to analyze and predict airflow and particle transfer through the respiratory tract. Most previous works on total lung aerosol deposition have focused on either one-dimensional model or trumpet models. Popular approaches for simulating inhaled particle deposition are the semi-empirical

models [28], ICRP model [77], “trumpet” model [78], deterministic single- and multiple-path models [79, 80, 100], and stochastic multi-path lung models [81, 82]. Hofmann [68] recently reviewed the applicability of these models by comparing the predicted deposition efficiencies of inhaled monodisperse particles with available experimental results. The simplified deposition models are still popular because of their easy implementation and low requirements of computational resources. However, the computed deposition results are not predictive, being based on simple inlet conditions and semi-analytical correlations for the deposition mechanisms [68]. Hence, such models may not be able to predict realistically the drug inhalation conditions from inhaler devices, where inhaler mouth pieces, high momentum flow and dense drug-suspensions may significantly affect the air-particle flow to the lung. As an example, the modeling results by Katz et al. [83] did not provide successful comparison with *in vivo* deposition results, due to the model’s inability to successfully capture the complex secondary flow structures and resultant particle deposition in the extra-thoracic airways. Additionally, processes like drug evaporation/condensation, agglomeration, aerosol atomization and drug-wall interactions cannot be easily incorporated into these simplified models without additional corrections which again require experimental data. While a few reduced whole-lung models have focused on these topics, these models may not be suitable for predicting complex particle dynamics when inhalers are used [101-105]. These limitations can be overcome by employing computational fluid-particle dynamics (CF-PD) techniques, i.e., a modeling approach in which the laminar/turbulent airflow and particle transport/deposition are simulated based on the solution of suitable transport equations [84, 85]. However, the sheer complexity of the human lung, featuring a total of 16 million

complex airways, prohibits full-scale computer simulations of the fluid-particle dynamics for the entire respiratory system [98]. Additionally, realistic airway configurations are currently restricted to the few upper airway generations since lower airway configurations are not easy to reconstruct due to the limited resolution of the scanned images [29]. Nevertheless, even CF-PD simulations covering only mouth/nose to generation 4 are computationally taxing and time consuming. Examples of multiscale hybrid modeling have been provided by several research teams [34, 74, 88, 106]. However, their focus was on applying appropriate boundary conditions, while detailed particle dynamics modeling was not conducted. Additionally, most of the previously reported extensive CF-PD lung models either considered steady-state inhalation conditions [98] or focused on the tracheobronchial airways only [29, 68, 71], or assumed inhalation-phase alone [26]. The objective of this study was to develop a three-dimensional Whole Lung Airway Model (WLAM II) which can realistically simulate airflow through the lung airways under physiological inhalation conditions and predict and particle transport/deposition of inhaled particles in the lung airways.

5.1.2 Model geometry

The sheer complexity of human lung airways prohibits full-scale computer simulations of air-particle flow in the entire respiratory system. Hence, an alternate computer simulation model for lung airflow and particle transport with physiological boundary conditions was developed using a representative whole lung model to predict the particle transport and deposition during breathing. The model geometry consists of subject-specific upper airways (from nose/mouth to, say, generation 3 in 3-D) which are connected to adjusted triple bifurcation

units (TBUs), in series and parallel to cover the remaining generations, based on morphometric measurements of human lung casts [223]. TBUs are used to extend the geometry from upper airway because the influence of bifurcating geometry (carinal ridge) on particle deposition can be better captured (see Fig. 5.1).

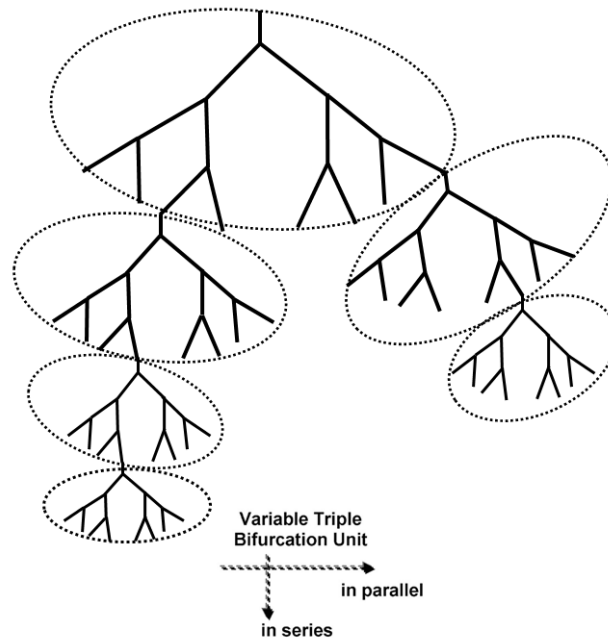


Fig. 5.1. Schematic representation of scaled Triple Bifurcation Unit (TBU) models connected in series and parallel (TBUs are scaled down to match the outlet diameter with the inlet diameter of the successive TBU)

The combined nasal-oral upper airway geometry is shown in Fig. 5.2a. The nasal airway geometry was developed from a magnetic resonance imaging (MRI) scan of a healthy male. The oral airway model was developed by scanning a wax model using NextEngine's Desktop 3D Scanner. The human airway wax replica is the same one as used by [120] for their

experiments. The oral airway consists of oral cavity, oropharynx, and larynx. The tracheobronchial part of the upper airway model has trachea with three generations of bronchial airways. The tracheobronchial part has been trimmed to get a Triple Bifurcation Model (TBU) with eight outlets at generation three. Based on the hydraulic diameter at the tracheobronchial airway outlets, the irregular outlet cross-section has been modified to circular cross-section.

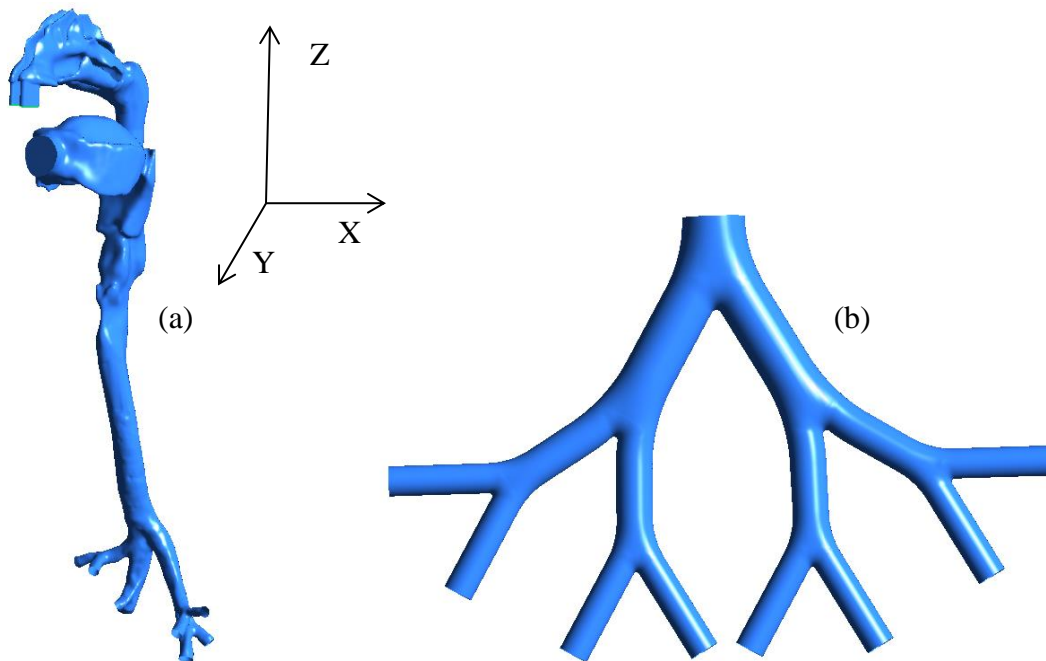


Fig. 5.2. (a) Human nasal-oral upper airway model, (b) representative TBU

Bronchial airway configurations are not easy to reconstruct from scanned images due to the limited resolution. Hence idealized lung geometrical models were developed based on

morphometric measurements of human lung cast. A representative TBU model is shown in Fig. 5.2b. The TBUs were used to represent generation 4 to 15.

The alveolar region of the lung was modeled by attaching spherical alveoli to the TBU units. The alveoli attached TBU units were developed using computer aided design software Solid Works. A cylindrical projection from the lumen was used to anchor the spherical alveolus to the duct. The final alveolus has a $\frac{3}{4}$ spheroid shape. The dimensions of the TBU units and the alveolar cavities were based on the morphometric measurements of [2, 223] Figure 5.3a and 5.3b shows TBUs with alveoli for generation 16-18 and 19-21 respectively. The geometrical dimensions of the TBUs are given in detail in Chapter 4.2. [224].

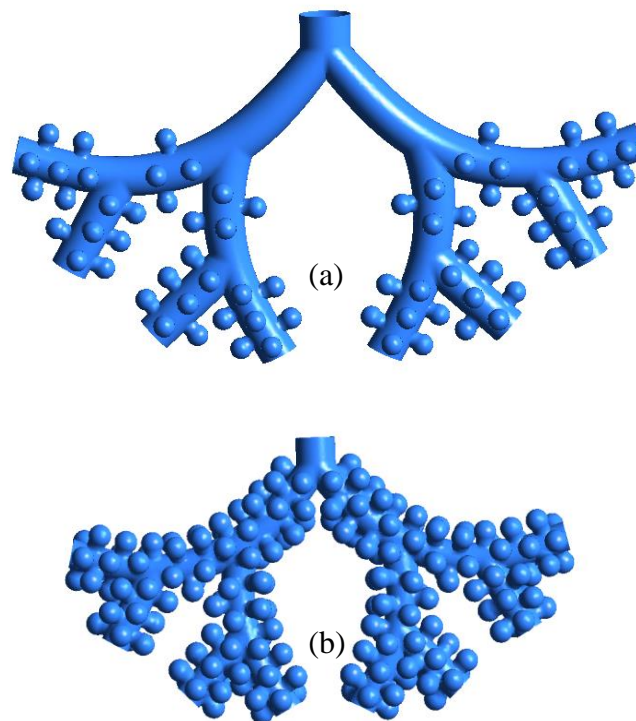


Fig. 5.3. (a) TBU model with alveoli for generation 16-18, (b) TBU model with alveoli for generation 19-21

The last two generations of the lung model were represented using a Double Bifurcation Unit (DBU) with alveoli attached to the first bifurcation geometry and four alveolar sacs attached to the outlet of the second bifurcation, which is formed by cluster of alveoli. The alveolar sac in the whole lung model was modeled using spherical alveolus (Fig. 5.4) which has the same volume as per the morphological data for generation 23 [2].

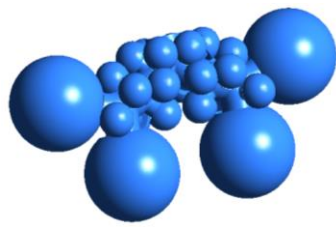


Fig. 5.4. Alveolar sac model for generation 22-23

Single-path whole lung model: In a single-path whole lung model only one outlet of the upper airway model has been extended by attaching TBUs in series (see Fig. 5.5). In order to quantify the average particle deposition in a whole lung model, the outlet which was extended is the median diameter outlet compared to all other outlet diameters at generation three. Hence the attached TBUs have an average diameter and each TBU will be a representative model.

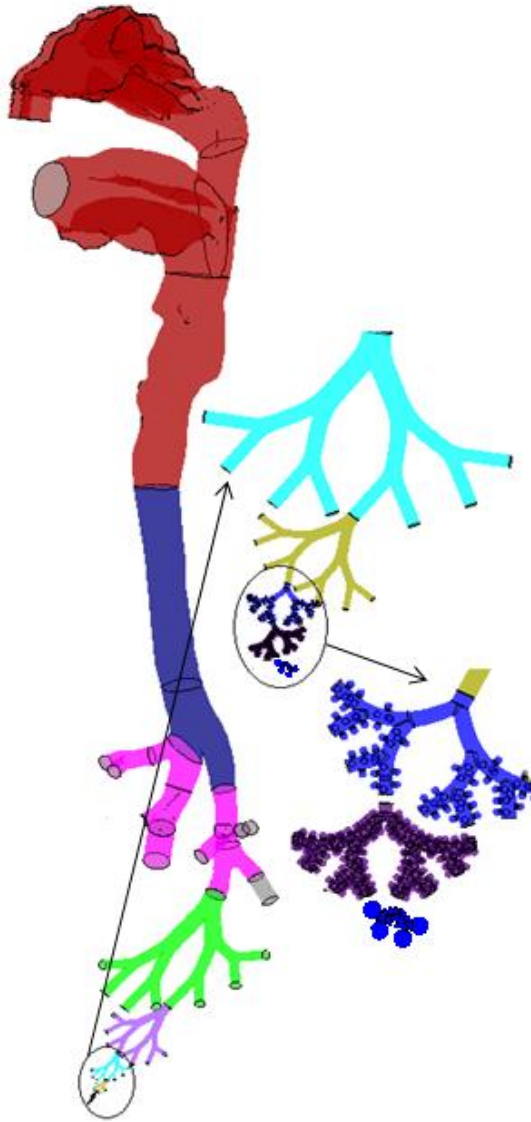


Fig. 5.5. Single-path whole lung model

Dual-path whole lung airway model: In a dual-path whole lung model two outlets of the upper airway model have been extended by attaching TBUs in series (see Fig. 5.6). In order to quantify the average particle deposition in a whole lung model, two outlets which were extended, are the median diameter outlets compared to all other outlet diameters at

generation three in the left and right lung respectively. The right lung path is smaller in dimension than the left lung path. This model can predict the differences in particle deposition in the left and right lungs.

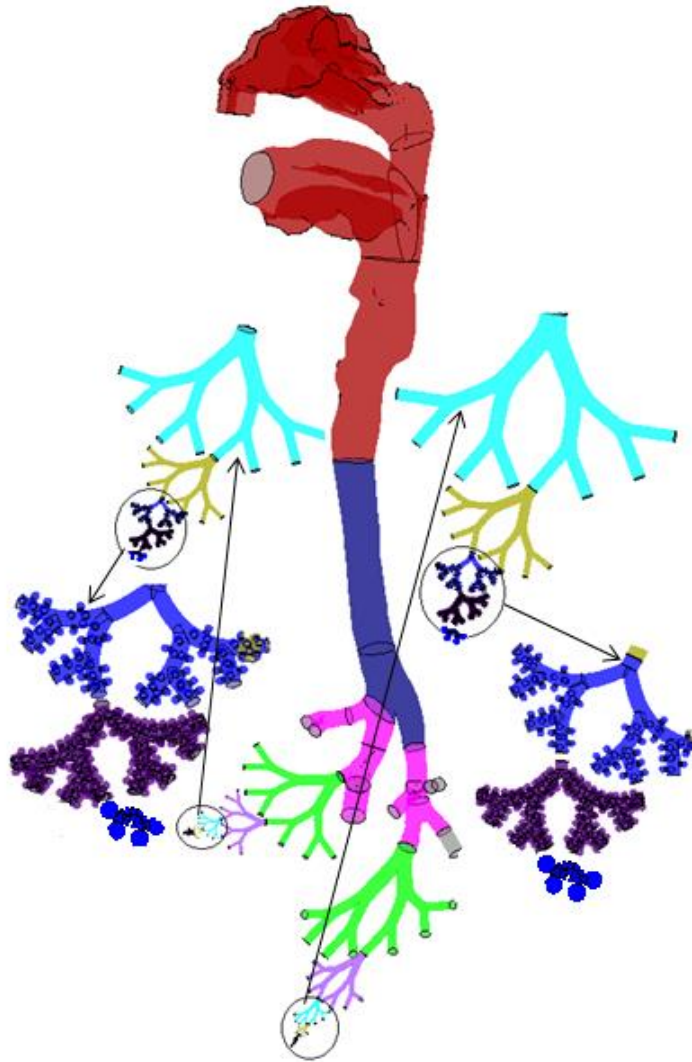


Fig. 5.6. Dual-path whole lung model

5.1.3 Wall deformation and boundary conditions

Assuming that the extrathoracic airways and the conducting airways are rigid and only alveolar airways deform during breathing, the volume flow rate for the whole lung model was maintained due to wall motion of the alveoli in generation 17-21 and alveolar sac representing generation 22-23. The details on alveolar wall deformation and modeling approach are given in chapter 6.

5.1.4 Numerical methods

It is not feasible to model a complete lung with all tracheobronchial airways and acinar airways using the current computational resources. Hence, in this study, a simplified single path and dual path geometrical configuration was used to replicate the whole lung. Only one TBU per generation per path was modeled. Hence, the airways are truncated from generation 3 onwards except for outlets where the TBUs are attached. In order to reduce the computational effort and resources required for simulating the whole lung model, each individual TBU/DBU were simulated independently (divide and conquer approach). For simulating inhalation phase, at the inlet of each TBU/DBU, an opening boundary condition (entrainment) was applied and at the outlet a mass flow rate boundary condition was applied. For the extrathoracic model, the mass flow rates through the outlets were divided based on the ratio of each outlet area to the total outlet area (similar to the Horsfield flow division [10]). This boundary condition will ensure that the physiological breathing mechanism (air sucked in during inspirations and air pushed out during expiration) will be replicated. During

exhalation, the outlets were converted to an inlet boundary and identical mass flow rate boundary condition was applied. The Shear Stress Transport (SST) $k-\omega$ turbulence model was employed to simulate the laminar as well as turbulent flow regimes in the upper lung airways up to generation 6 and a laminar model was used modeling airflow in other lung generations (refer chapter 2 and ANSYS 15.0 CFX-Solver Modeling Guide [91]).

A wall deformation vector (depend on the alveolar TBU/DBU) was applied on the alveoli surface and rest of the airway wall was assumed to be rigid. In order to study the effects of inhalation conditions on alveolar flow pattern, constant oral inhalation flow rates were assumed (refer chapter 6 for inhalation profiles and details). No slip boundary condition was applied at the wall boundaries (duct and alveoli) so that the fluid velocity matches with the wall velocity at the fluid wall interface. A user defined CEL (CFX Expression Language) functions was used to apply the wall deformation vector.

Assuming a dilute particle suspensions, one-way coupling was assumed between the fluid and particle phases. 50,000 particles per second were injected at the oral inlet and particles were assumed to deposit on the walls on contact. A particle independent study was conducted to ensure that the results are independent of the number of particles injected per second. Increasing the number of particles by a factor of 2 showed less than 2% difference in the results. Particles were distributed uniformly at the oral inlet with an initial velocity being the same as the inlet-air velocity. Since the upstream particle distribution has a significant influence on the particle deposition in subsequent generations, the outlet measurements (particle distributions) from the upper TBU were exported at each time step to become the inlet conditions for the next generation TBUs and the process was continued for all TBUs

attached later on. A particle injected into a domain (can be oral-upper airway model or any TBUs) will either deposit or remain suspended in the domain or exit the domain. The particle exited per time step was re-injected into the subsequent TBUs. During exhalation the simulation started from the distal DBU and upwards. The exhalation continued from the end of the inhalation in each domain, so that the suspended particles will be again tracked from their last position. This modeling approach will provide detailed results for the number of particles deposited; remain suspended and exited from the whole lung domain. If the number of particles remain suspended in the domain is more than 2 %, the breathing cycle is repeated. The simulation was stopped when the number of particles remain suspended in the domain was less than 2 %, and the suspended particles were assumed to deposit following the same deposition fraction as in the previous cycle. The remaining particles are assumed to exit after the corresponding cycle.

5.1.5 Experimental data set

Heyder [119] calculated the particle deposition in normal subject lungs for different particle diameters and inhalation conditions. The subjects were asked to breathe through nose and mouth under constant respiratory flow rates without pauses. Table 5.1 lists the experimental deposition results for mouth breathing condition at 15 L/min (LPM). Based on their study, it has been concluded that, the total lung deposition fraction is independent of the subject lung volume. Their results indicate that the particle deposition in lung is governed by time-dependent mechanisms. As the tidal volume increases the total lung deposition increases, indicating deposition is highly influenced by the residence time of particles inside lung

airways. As the residence time increases the deposition increases. From the experimental study it has been concluded that, even though the total residence time for particles in the lung is more at higher tidal volumes, the deposition in the upper tracheobronchial airways is constant. It is because of the constant residence time and flow rate at the upper tracheobronchial airways. But the total lung deposition increases with the tidal volume because of the increase in pulmonary deposition.

Table 5.1. Experimental deposition results from Heyder [119] for mouth breathing condition at 15 L/min (LPM)

Tidal volume	3 μm diameter
500 ml	0.44
1000 ml	0.67

5.1.6 Results and discussion

The whole lung model was used to study two inhalation conditions: inhalation flow rate of 15 LPM with tidal volume 500 ml (inhalation phase 2s followed by 2s exhalation) and inhalation flow rate of 15 LPM with tidal volume 1000 ml (inhalation phase 4s followed by 4s exhalation). The inhalation flow into lung airways was modeled by applying an expanding wall boundary condition on alveoli. A displacement function was created to get required flow rate at the alveolar generations and thereby at the oral inlet.

5.1.6.1 Air flow

Flow fields for the oral-upper airway model for an inhalation flow rate of 15 L/min were simulated. Figure 5.7 shows the flow stream lines which provide a quantitative visualization of the flow behavior, captured by following massless particles released from oral inlets. As the flow proceeds from the oral cavity to the oropharynx, several secondary flow structures including recirculation and flow detachment were noticed because of the change in flow direction. Due to the sudden geometric constriction at the glottis, an asymmetric high-speed laryngeal jet was developed. The laryngeal jet produced a recirculation zone near the anterior wall of the upper trachea. Also the curved geometry of the epiglottis produced secondary vortical structures. Due to the secondary flow structures, the velocity profile in the trachea is skewed towards the anterior part. Once the flow advances in the trachea, the velocity profile is redistributed by the secondary motion, producing a parabolic profile. Flow separation and recirculation was noticed in the bronchial airway bifurcation regions. The flow profile and secondary flow structures in the daughter branches of the bronchial airways were found to vary with the bifurcation angle and daughter tube diameters.

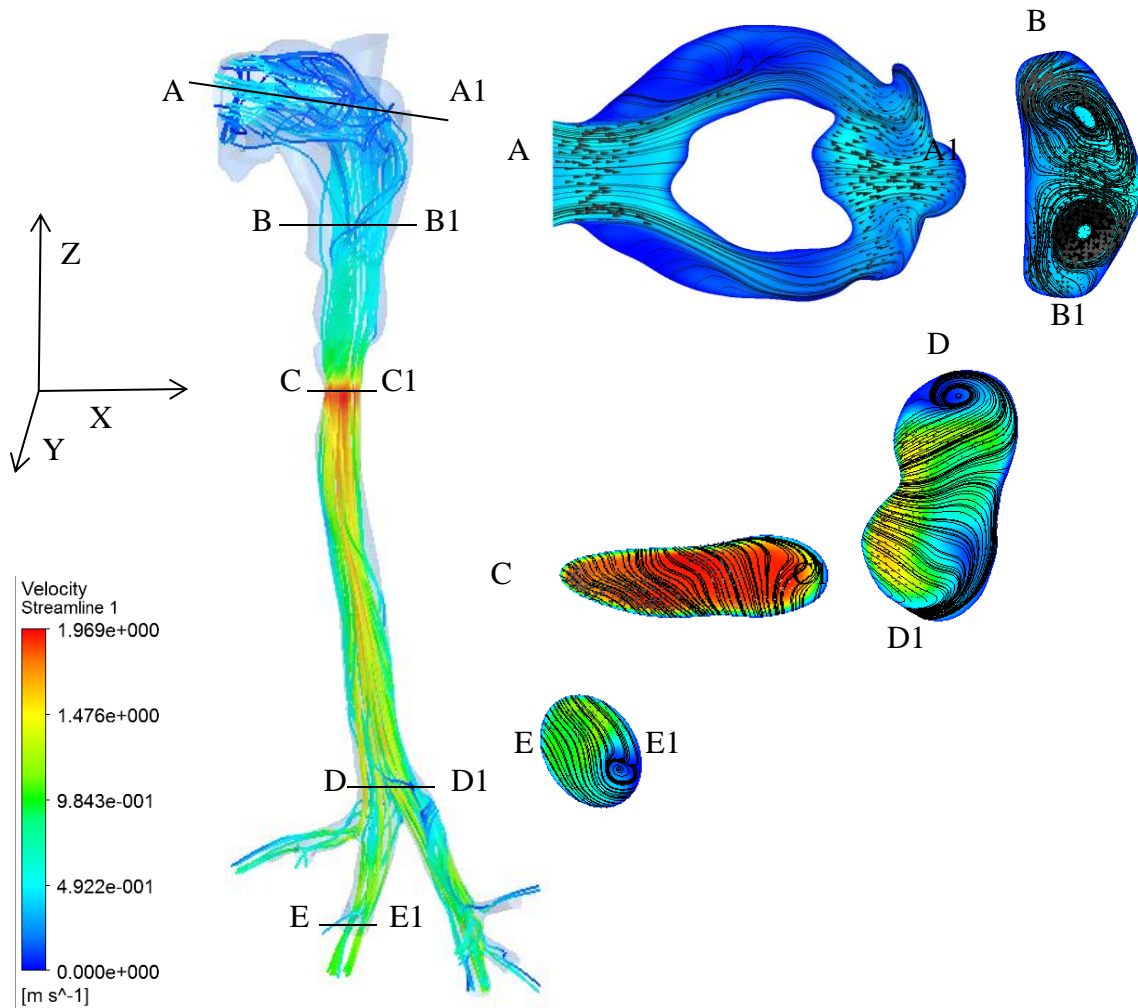


Fig. 5.7. Flow stream lines through the oral-upper airway model for an inhalation flow rate of 15 L/min

For the dual-path whole lung airway model, two outlets of the combined nasal-oral upper airway model (one outlet from right lung lobe and left lung lobe) were selected and the scaled TBUs were connected to these outlets to simulate the particle transport, distribution and deposition in the bronchiolar airways. Figure 5.8 depicts the flow stream lines through the TBUs representing generation 4-15 started from outlet 3 and outlet 7 of the oral-upper

airway model. The inlet condition for this TBU was obtained from respective outlets of the oral-upper airway model. Since the diameters of the bronchiolar airways of the oral-upper airway model were different, the flow rates through each outlet were also different. So the attached TBUs also had different inlet flow rates. This helped in calculating an average deposition data for left and right lung based on different bronchiolar airway diameters. Secondary flow structures were noticed near the vicinity of bronchial bifurcations. The velocity profile changed significantly down the bifurcation. Change of cross section causing adverse pressure gradient and curved geometry drives the fluid towards the inner wall, producing skewed velocity profile with maximum velocity near the inner wall. As the flow proceeds from the bifurcation, fluid from the center line where the velocity is high, move towards the inner wall of the bifurcation. This secondary motion can be attributed to the curvature of the daughter tubes. As the daughter tubes become straight, the secondary motion damps out and the velocity profile changes back to parabolic distribution. Hence the divide and conquer approach for the whole long modeling will not have any influence on the airflow pattern and particle transport.

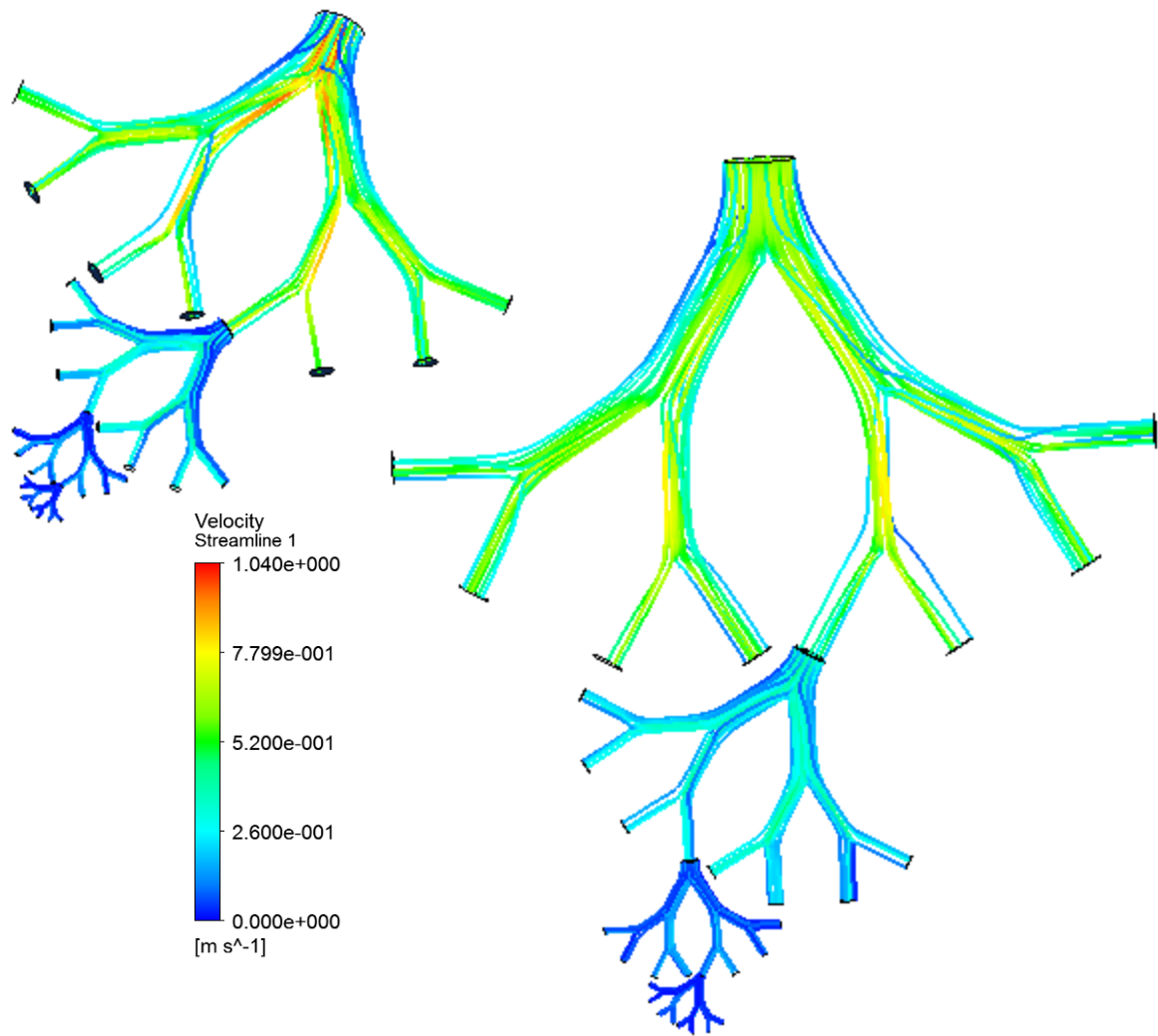


Fig. 5.8. Flow stream lines through the TBUs of the dual-path WLAM for an inhalation flow rate of 15 L/min

5.1.6.2 Whole lung particle transport and deposition

The trajectories of the particle with diameter $3 \mu m$ were simulated using the single- and dual-path whole lung airway model. The gravity was assumed to act in the negative z direction (the axis is shown in Fig.5.1). The particle transport simulation was continued until the number of particles remained in suspension in the domain at the end of the exhalation cycle was less than 2%.

Total and segmental lung deposition: The total and segmental particle deposition results are highly desirable for toxicological studies as well as for impact analyses of administered drug-aerosols. More than 90% of the particle deposition was observed in the bronchoalveolar region of the lung. The total and segmental lung deposition results are compared with the human in vivo deposition results reported by Heyder [119].

15 LPM with tidal volume 500ml: The comparison of the model predicted results with the experimental results are shown in in Fig. 5.9. The results show that the results predicted by a dual-path whole lung model are reasonably accurate than a single-path. It indicates that the model prediction can be improved by adding additional path which will allow improved resolution of particle transport through different lung lobes. Compared to the in vivo total lung deposition results, single-path model prediction were off by 14 % and dual-path by 10%. In another published result by the same group (Heyder [225]), the total lung deposition has shown a standard deviation of 6%, indicating that the current dual-path whole lung model predictions are excellent.

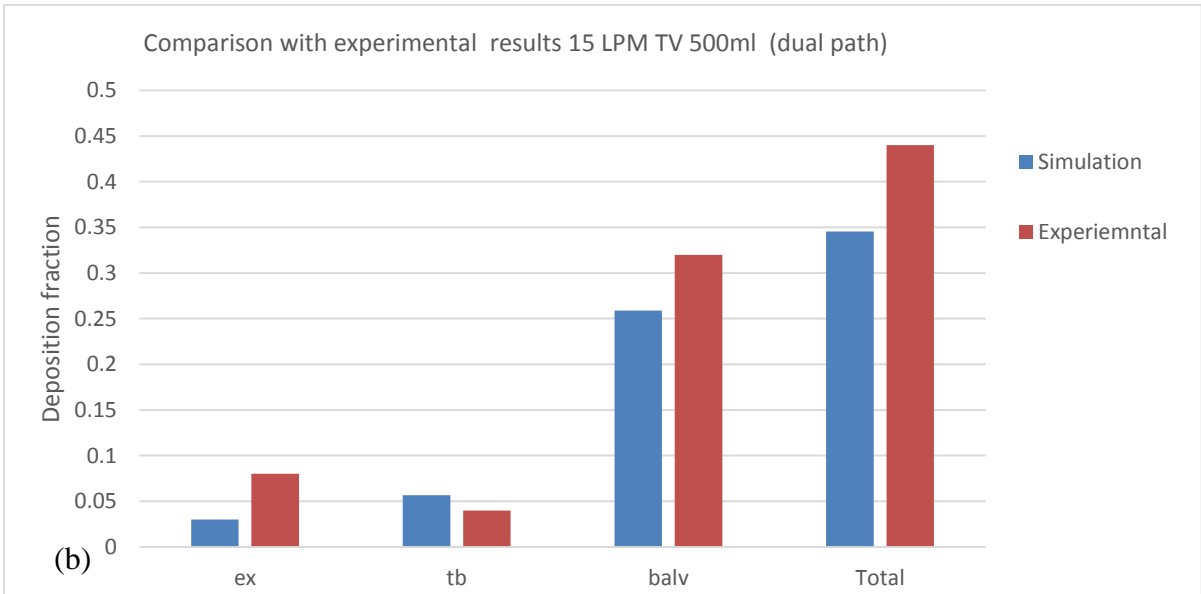
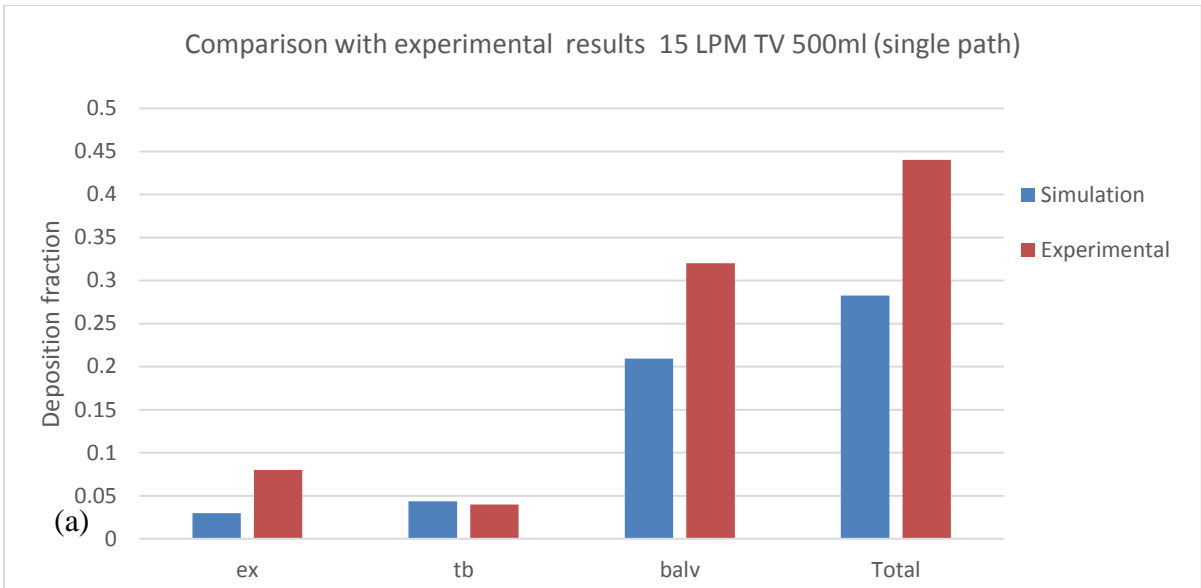


Fig. 5.9. Total and segmental particle deposition results in (a) single- and (b) dual-path whole lung models for an inhalation tidal volume 500ml

15 LPM with tidal volume 1000ml: Similar deposition trend was observed when the inhalation tidal volume was increased to 1000ml. However, the total lung deposition was increased by almost 20%. The comparison of the model predicted results with the experimental results (in Fig. 5.10) shows that the results predicted by a dual-path whole lung model are reasonably accurate. Compared to the in vivo total lung deposition results, single-path model prediction were off by 12 % and dual-path by 7%. This error in model prediction could be because of unresolved flow paths in the upper lung lobes which are positioned against the gravity. Additionally these lung lobes are smaller in dimension compared to the left lung lobe considered for extension. Hence increased particle deposition can be expected in these lung lobes. In another published result by the same group (Heyder [225]), the total lung deposition has shown a standard deviation of 3%, indicating that the current dual-path whole lung model predictions are excellent.

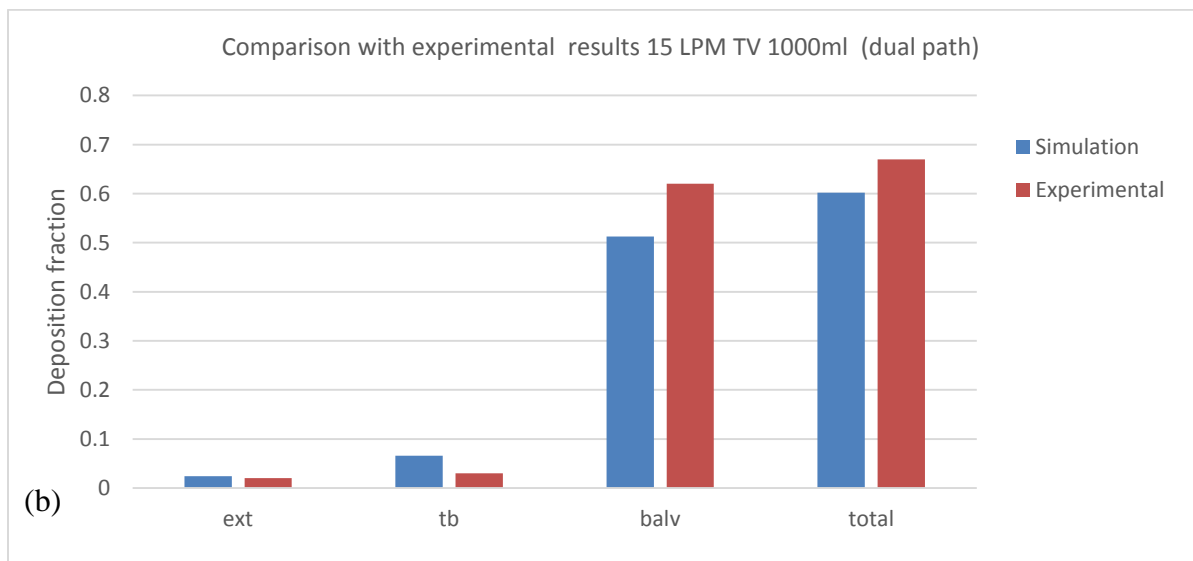
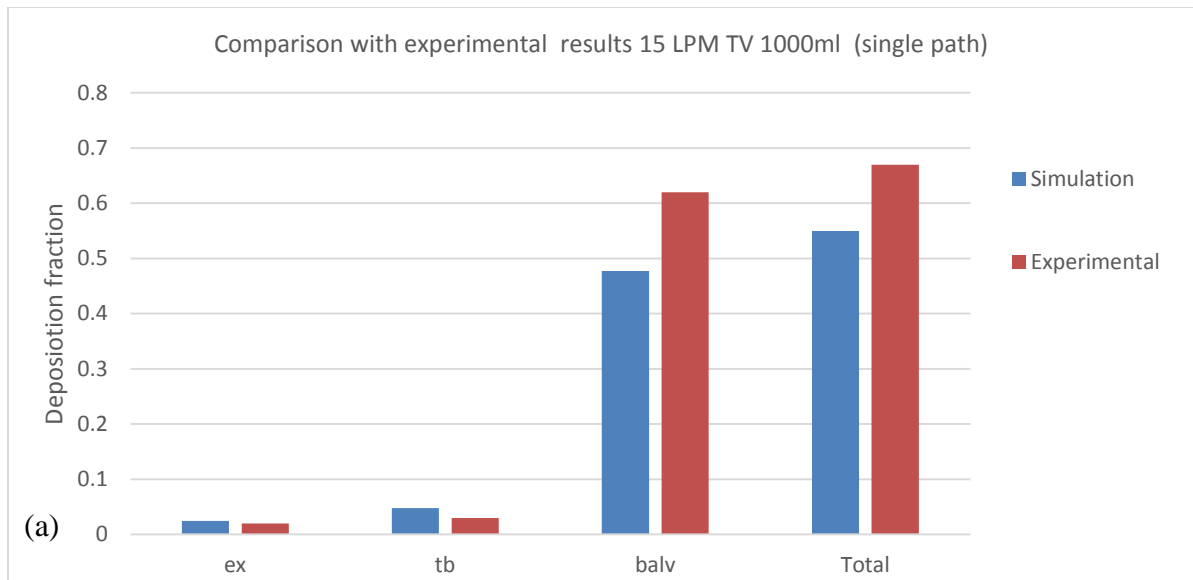


Fig. 5.10. Total and segmental particle deposition results in (a) single- and (b) dual-path whole lung models for an inhalation tidal volume 1000ml

5.1.6.3 Segmental lung deposition results

15 LPM with tidal volume 500ml: For 15 LPM with tidal volume 500 ml, two breathing cycles were simulated to ensure that the number of particles remained in suspension in the domain were below 2%.

During inhalation: The regional deposition results during the inhalation phase in single- and dual-path whole lung models are plotted in Fig. 5.11. The results indicate that the number of particles deposited is higher in the distal alveolar airways compared to other airway generations. However, due to the short inhalation period, only limited number of particles reached the final alveolar DBU model. In the dual-path model higher number of particles was transported to the distal sac model of the left lung than in the right lung. The number of particles deposited in each TBU domain during inhalation cycle 1 is more than that during inhalation cycle 2. The deposition trend in both cycles was similar except for the DBU sac model. In the DBU sac model, more particles were deposited in the second inhalation cycle. This indicates that the suspended particles after the inhalation cycle 1 are carried into the distal lung regions during the subsequent breathing cycles.

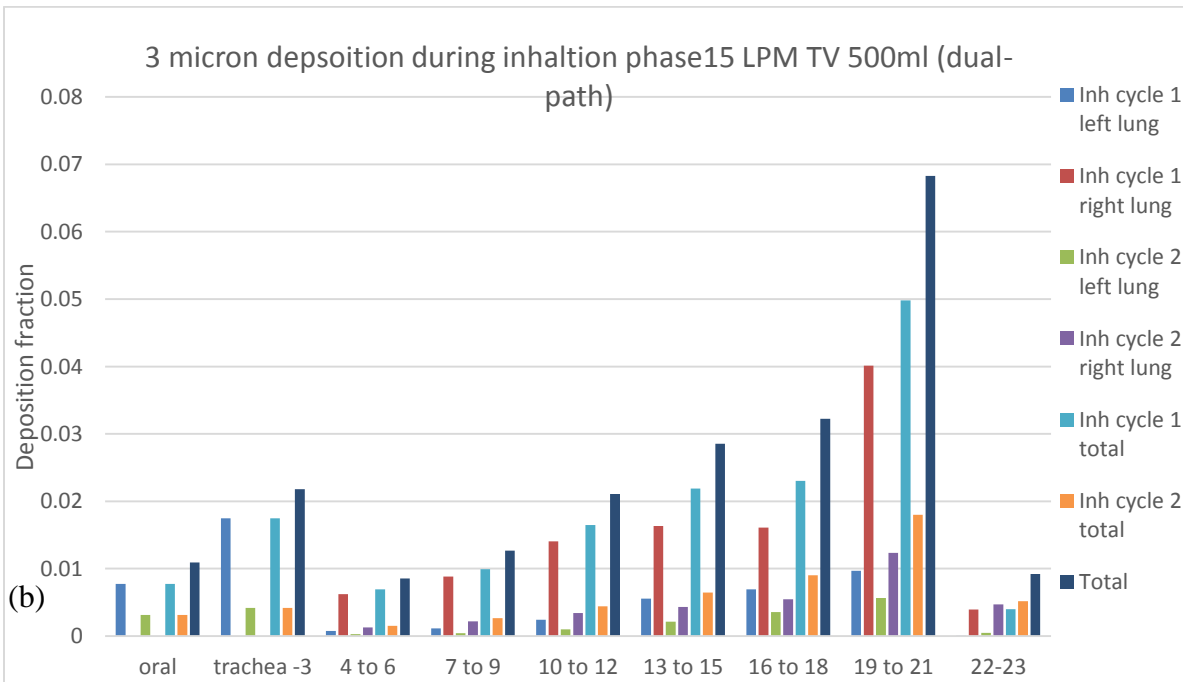
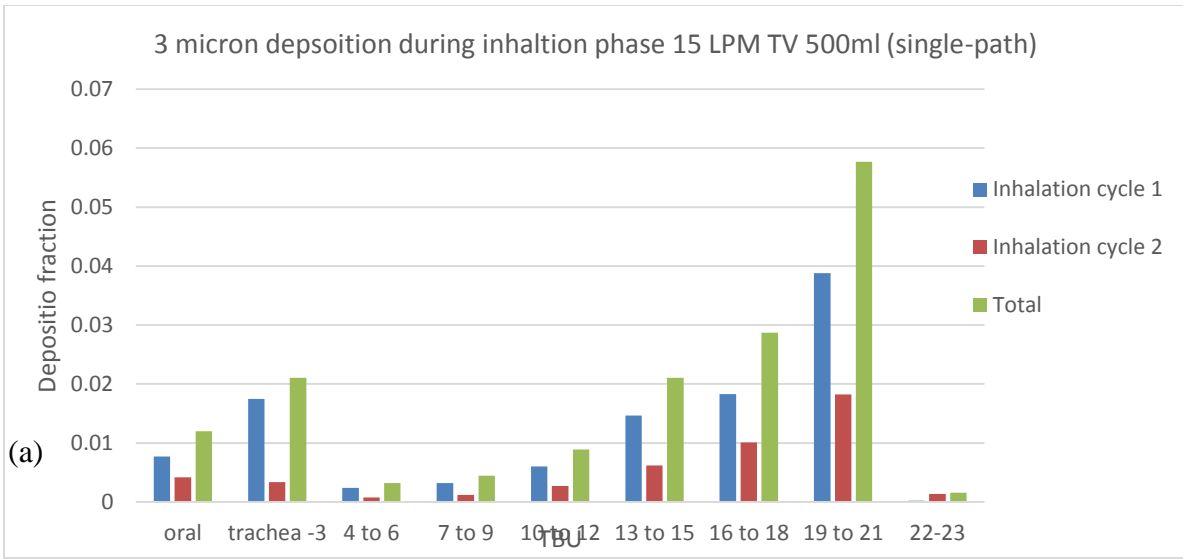


Fig. 5.11. Regional deposition results during the inhalation phase in (a) single- and (b) dual-path whole lung models

During exhalation: The regional deposition results during the exhalation phase in single- and dual-path whole lung models are plotted in Fig. 5.12. The results indicate that the number of particles deposited is higher in the distal alveolar airways compared to other airway generations. The particle deposition in the distal DBU sac model is higher during exhalation cycle 2 than in exhalation cycle 1. It indicates that more numbers of particles have reached these distal alveolar regions during subsequent breathing cycles. The number of particles deposited in each TBU domain during inhalation cycle 1 is more than that during inhalation cycle 2. In the dual-path model higher number of particles was transported to the distal sac model of the left lung than in the right lung. The deposition trend in both cycles was similar except for the DBU sac model. In the DBU sac model, more particles were deposited in the second inhalation cycle.

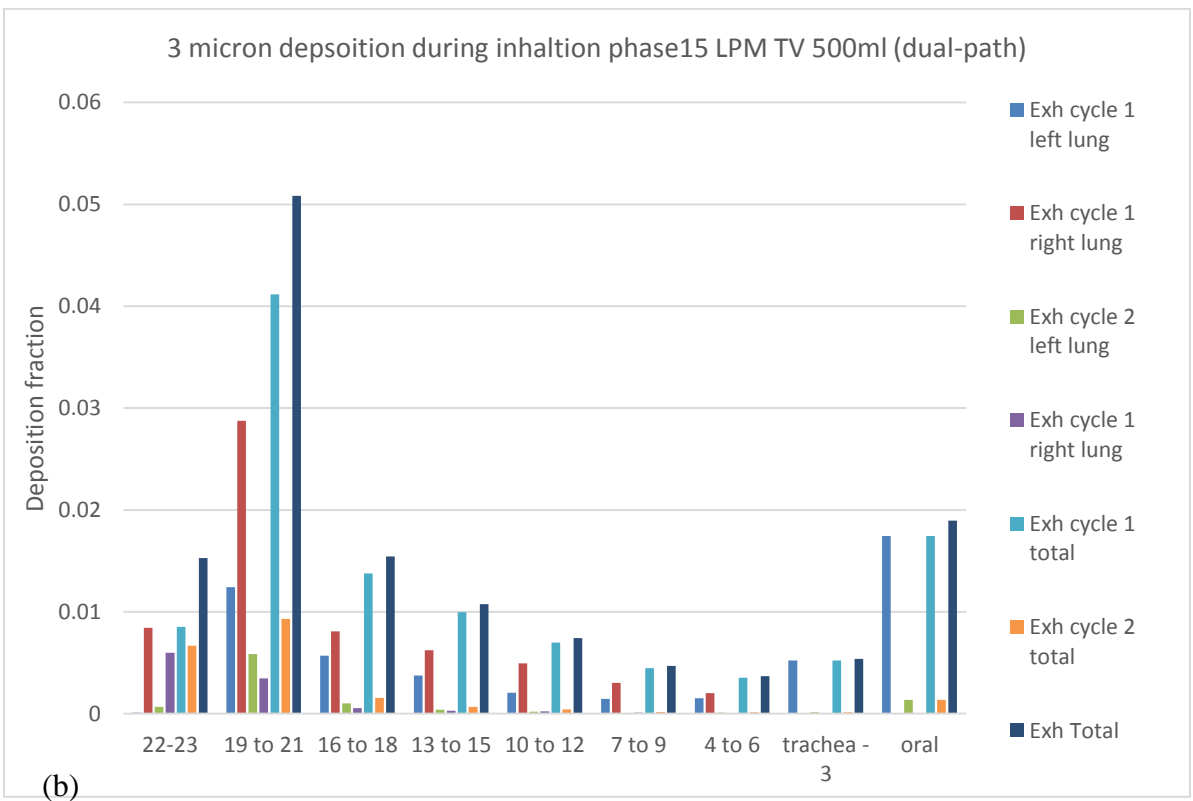
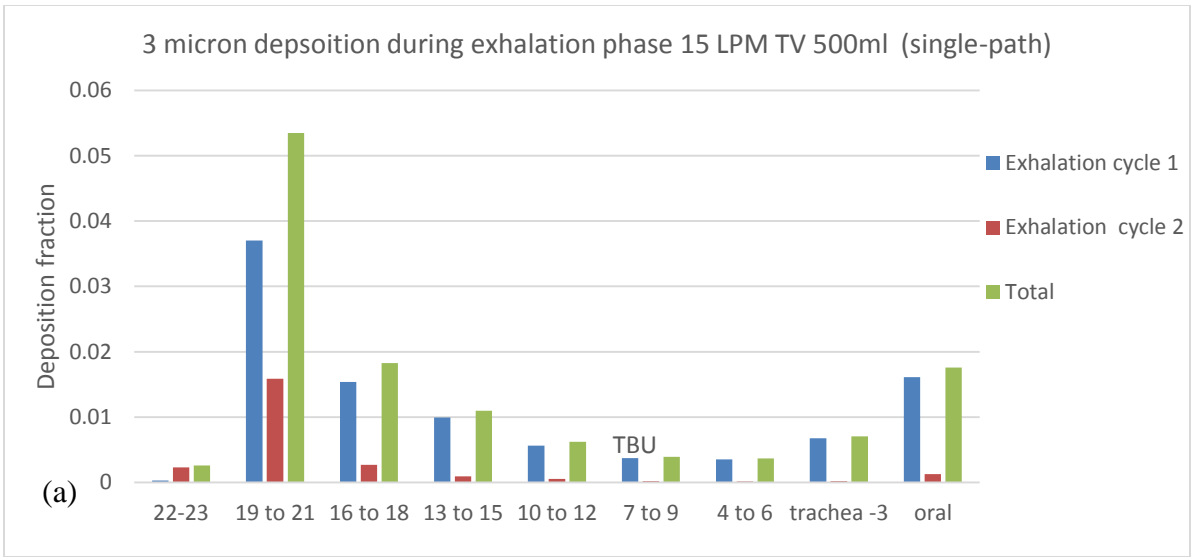


Fig. 5.12. Regional deposition results during the exhalation phase in (a) single- and (b) dual-path whole lung models

15 LPM with tidal volume 1000ml: For 15 LPM with tidal volume 1000 ml, most of the particles exited the lung during the first breathing cycle itself. Hence, only one breathing cycle was simulated, and the number of particles remained in suspension in the domain were below 2% at the end of exhalation.

During inhalation: The regional deposition results during the inhalation phase in single- and dual-path whole lung models are plotted in Fig. 5.13. The results show that as the inhalation tidal volume increases more number of particles are being pulled into the distal lung airways. Due to the increased particle residence time, the deposition increased in the distal alveolar region significantly. The deposition trend is identical to that with inhalation tidal volume 500ml except at the distal DBU sac model where significantly high deposition was noticed. Similarly, the regional deposition is identical in the single-path and dual-path whole lung models except at the distal DBU sac model where significantly high deposition was noticed for the dual-path whole lung model. This indicates that small lung lobes will have higher deposition in the distal alveolar generations.

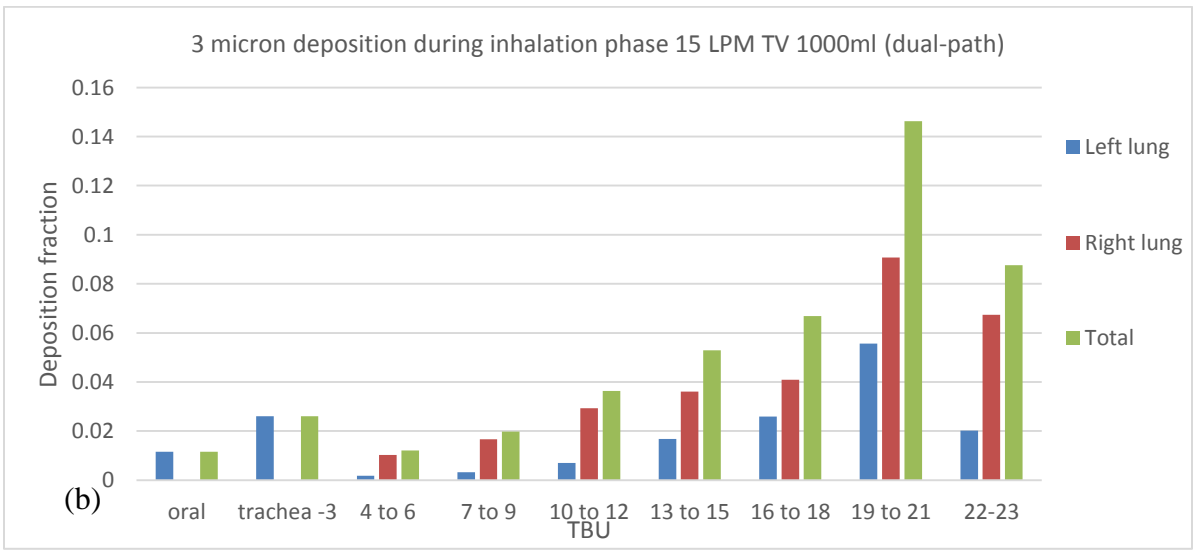
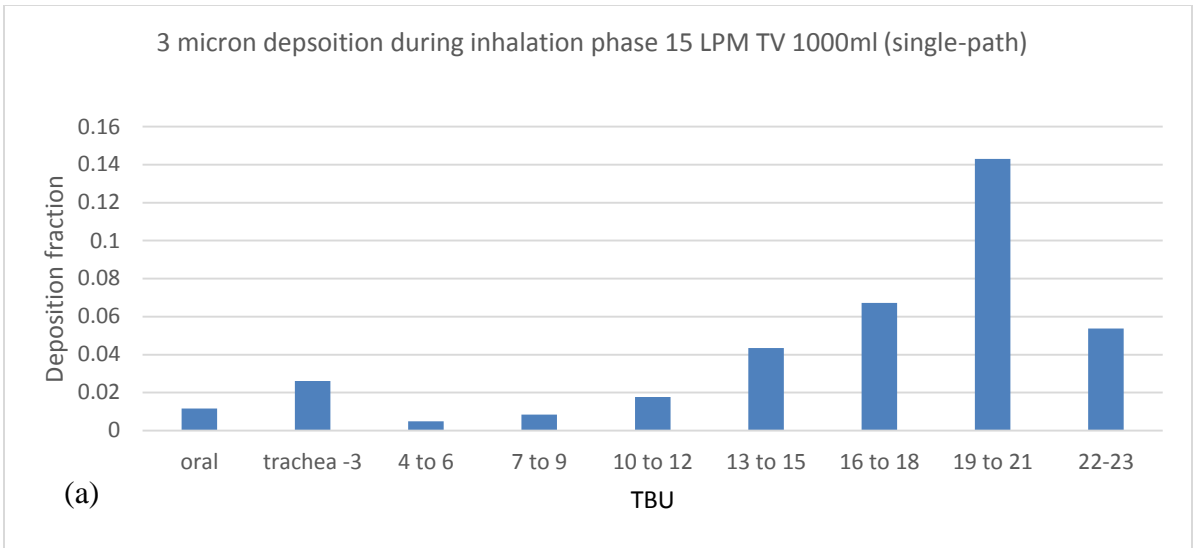


Fig. 5.13. Regional deposition results during the inhalation phase in (a) single- and (b) dual-path whole lung models

During exhalation: The regional deposition results during the exhalation phase in single- and dual-path whole lung models are plotted in Fig. 5.14. Significantly high deposition was noticed in the distal DBU sac model compared to the exhalation with tidal volume 500ml.

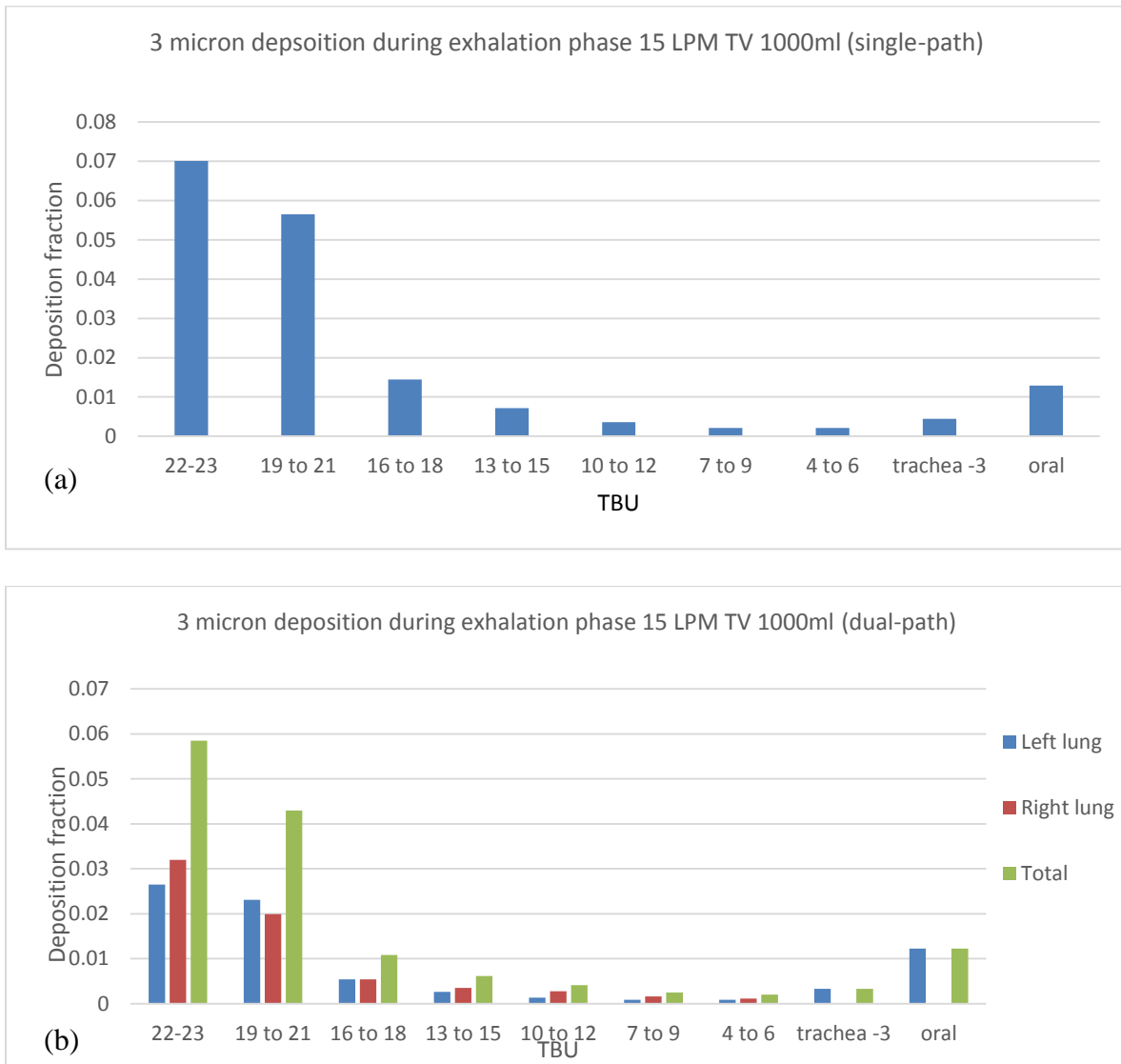


Fig. 5.14. Regional deposition results during the exhalation phase in (a) single- and (b) dual-path whole lung models

5.1.7 Why alveolar sac model and why transient over steady state?

The expansion and contraction of the alveolar sacs causes inhalation of air into lungs. The travel distance of the flow wave front depends on the breathing frequency and flow rate, which means if the frequency is lower; the flow front will get more time to reach the inner lung airways. If the breathing frequency is higher, the inhalation time will be lesser and hence the flow will be exhaled out before reaching the inner lung airways. The particle is transported corresponding to the flow front. Hence the number of particles reaching the inner alveolar sacs will be higher for breathing with long inhalation time. This is better modeled using the alveolar sac model at the peripheral airway generations. If an airway with an outlet was used to model the final generation, the flow would have been let out of the geometry and hence the particles, which is not realistic. Hence alveolar sac model better predicts the particle transport.

In a steady state simulation, the particles are injected without any injection timing. Hence the deposition will be same irrespective of the breathing frequency. Also an alveolar sac model cannot be used under steady state condition.

The following figure explains the particle transport through the alveolar sac model. The particle track is displayed in the DBU sac model for the single-path whole lung model during inhalation with tidal volume 1000ml. The particles reached the generation only after 1.8s, it can be noticed that the particle velocity is very low or the particle residence time is very high in the alveolar generations. At $t = 2s$ only a limited number of particles reached the DBU. As simulation time increases more number of particles reaches the sac wall. It means the inhalation time controls the particle deposition and as the inhalation time increases, the

particle deposition increases. This explains the reason for higher particle deposition under high tidal volume.

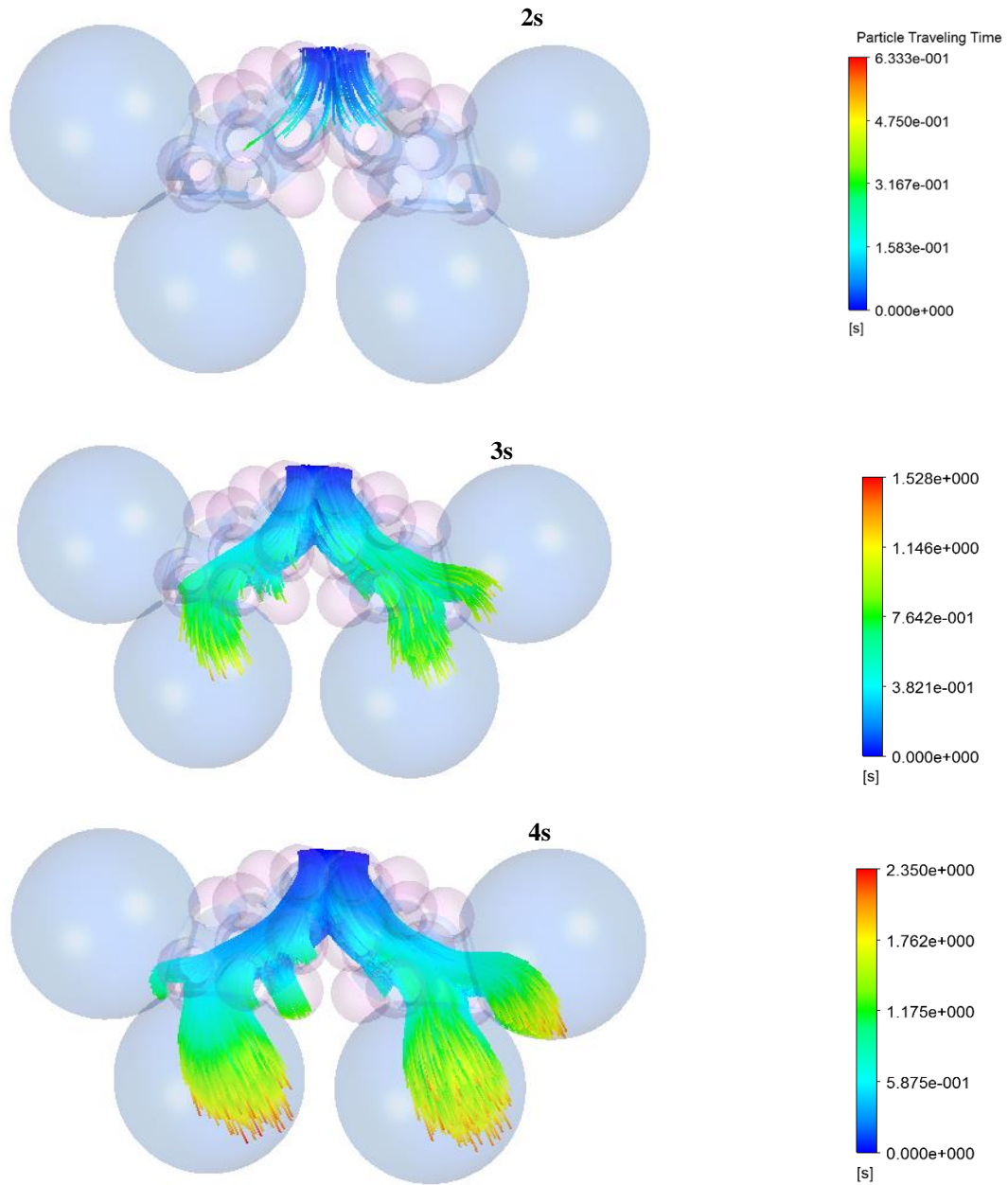


Fig. 5.15. Particle transport in alveolar DBU model at $t= 2s, 3s, 4s$

5.1.8 Limitations of the current model

A major shortcoming of the current numerical study is the approximation of the bronchial and alveolar airways. The lung airway bifurcations were assumed to be symmetrical within a resolved lung path. Lung airways are actually asymmetric and nonplanar, which can influence both fluid flow and particle distribution. Another limitation of the current model is that the displacement function for the alveolar geometries should be predetermined. Also, the influence of breath hold on particle deposition was not considered in this study. Another limitation of the model is that intersubject and intra-subject variability in lung morphometric measurements has not been considered yet. However, the dimensions of the lung airways at the same generation in dual-path whole lung model are different. Hence, the model is incorporating different lung data to represent intra-subject variability.

5.1.9 Future work

The primary objective of this work was to show the modeling framework for a physiologically realistic whole acinar model. In future, the influence of inhalation flow rate and orientation of gravity vector, non-planar lung extensions may be analyzed. In an extension of the dual-path configuration, a five-path WLAM III can be developed; again, with attached TBUs extending from multiple outlets of the upper airway model in order to quantify particle deposition in five lung lobes (see Fig. 5.16). The results from single-path and dual-path study indicate that the accuracy of the model results was improved by incorporating additional lung paths. Hence, CF-PD analyses employing a quintuple –path

WLAM will help to understand the effects of intra-subject variabilities on airflow characteristics and drug aerosol deposition per generation of especially small airways in different lungs and lung lobes.

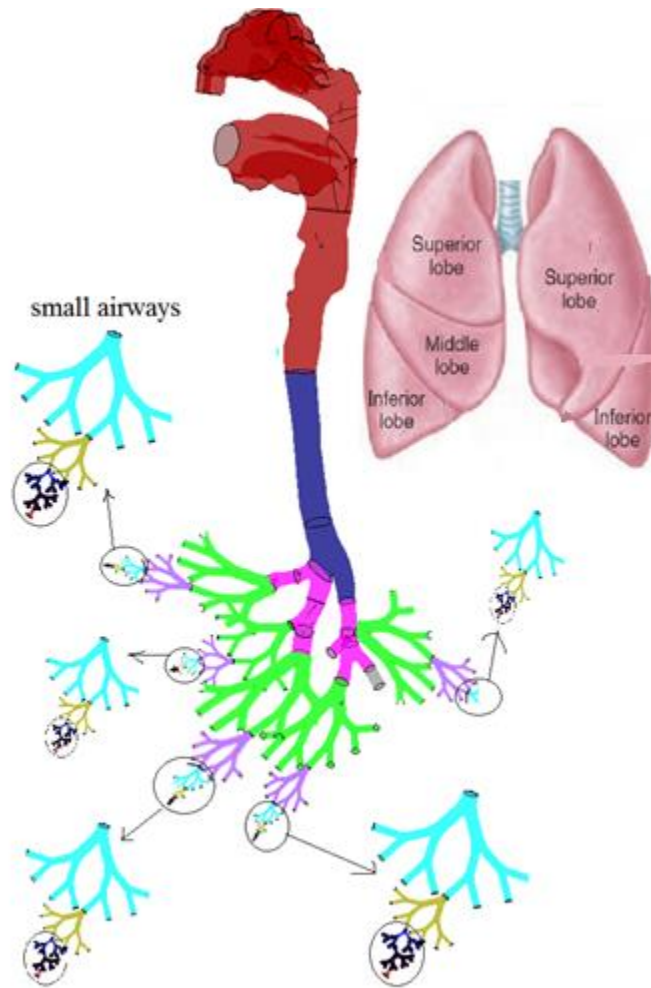


Fig. 5.16. WLAM III (multi-path whole lung model)

5.1.10 Conclusion

In this study, a detailed, physiologically realistic whole lung model (WLAM II) was developed. In WLAM II, a more realistic approximation of the human lung was achieved by using geometric data sets for subject-specific *human upper airways*, typically from nose/mouth to generation three, *with triple bifurcation units* (TBUs) attached to capture a few additional generations. Specifically, the model geometry consists of subject-specific upper airways in 3-D, which are connected to geometrically and flow-rate adjusted TBUs plus the alveolar model in series and parallel - all based on morphometric measurements of human lung casts. So, the TBUs are used to extend the geometry from the 3-D upper airways to simulate the local airflow and hence capture the influence of the bifurcating geometry (carinal ridge) on particle deposition. In this new whole-lung model, the alveolar movement was applied on the alveoli surface to control any given inhalation and exhalation waveform, and hence physiological lung breathing mechanism was captured. The model accounts for lung airway resistances in series and parallel and thereby effectively models the upstream velocity profiles which depend on downstream airway resistances. The airflow and particle transport through the lung airways were successfully simulated and analyzed, using computational fluid-particle dynamics. Total and regional particle depositions were calculated and validated with experimental lung deposition data. These model results indicate that large number of particles is deposited in the distal alveolar airways compared to the upper conducting airways. The model predicted results also indicate that for short inhalation under light breathing conditions, multiple breathing cycles are required to exhale the

particles. These results provide critical insight into aerosol transport and deposition in lung airways.

Chapter 6

Summary

6.1 General conclusions

Epidemiological and pathological studies of occupational and environmental exposures indicate that particulate matter (PM) can cause detrimental effects on human health. Accumulation and retention of toxic particles can result in serious lung diseases, including inflammatory effects and may even lead to lung cancer. Adverse cardiovascular and respiratory problems have been linked to inhalation of high mass concentration of PM. At the same time, respiratory drug delivery is becoming an increasingly popular way of administering medicine. It is efficient for treating both pulmonary and systemic pathogenic conditions. Thus, investigations related to the deposition and removal of inhaled particles are of great importance because mathematical models and associated computer simulations, which can predict realistic particulate lung burden for specific parameters of exposure conditions, can offer valuable assistance in epidemiological, toxicological and pathological inhalation studies and in developing new preventive strategies. This study was conducted to further our understanding and in providing toxicological and pharmacological assessment of inhaled aerosols using two Whole Lung Airway Models.

In this study, a new whole lung-airway model (WLAM I) was introduced. In WLAM I, the actual lung geometry was first represented by a basic 3-D mouth-to-trachea configuration and then all subsequent airways were lumped together, i.e., reduced to an exponentially expanding 1-D conduit. This new whole-lung model combines the advantages of the simplified lung deposition models and the CF-PD model. The diameter for each generation of the 1-D extension can be obtained on a subject-specific basis from the calculated total volume which represents each generation of the individual. The alveolar volume was added

based on the approximate number of alveoli per generation. A wall-displacement boundary condition was applied at the bottom surface of the WLAM I so that any breathing pattern due to the negative alveolar pressure can be reproduced. Specifically, different inhalation/exhalation scenarios (rest, exercise, etc.) were implemented by controlling the mesh displacement to simulate realistic breathing cycles in the WLAM I. Similar to the expansion and contraction of the thoracic cavity, the WLAM I-volume expands and contracts, thereby producing pressure differences resulting in realistic inhalation and exhalation flow waveforms. The WLAM I is able to capture the transient airflow and particle behavior under realistic breathing conditions, providing total as well as regional particle deposition results. By assuming a closed geometry, the model is replicating the human lung action while breathing. The total and regional particle deposition results under transient conditions were compared with measured *in vivo* deposition results. The validated WLAM I was then used to analyze particle transport and deposition in a human respiratory tract configuration when an anti-inflammatory drug was inhaled from a commercial DPI. The drug considered was *curcumin*, which is a polyphenol compound present in *Curcuma longa* plant (commonly known as turmeric) which is largely cultivated in subtropical Asian countries. Recent investigations have shown that *curcumin* possess high therapeutic potential as an antioxidant, anti-inflammatory and anti-cancer agent. More recent studies have reported that curcumin has the therapeutic potential to inhibit lung inflammatory reactions and additionally, *curcumin* has shown to possess potential to reverse steroid resistance in patients with asthma and COPD. The efficacy of the DPI to administer *curcumin* dry powder to lung airways was evaluated in terms of total and regional lung-deposition efficiencies. The model

results provide critical insights regarding drug aerosol transport and deposition in lung airways, where the observations can be used to improve inhaler device design and drug formulation in terms of best physical properties.

In WLAM II, the model geometry consists of subject-specific upper airways in 3-D, which are connected to geometrically and flow-rate adjusted TBUs plus the alveolar model in series - all based on morphometric measurements of human lung casts. So, the TBUs were used to extend the geometry from the 3-D upper airways to simulate the local airflow and hence capture the influence of the bifurcating geometry (carinal ridge) on particle deposition. This model further improves the steady-state model previously reported. In this new WLAM II, the alveolar movement was applied on the alveoli surface to control any given inhalation and exhalation waveform, and hence the lung breathing mechanism is captured. The airflow and particle transport through the lung airways were successfully modeled using computational fluid-particle dynamics. The model results indicate that inhalation flow rate and inhalation period determines the particle trajectories. Results also indicate that for short inhalation under light breathing conditions, multiple breathing cycles are required to exhale the particles. Particle deposition trend is different for inhalation vs. exhalation, and in subsequent cycles. During subsequent cycles, the suspended particles reach the distal airways. The model predictions have excellent agreement with in vivo particle lung deposition results.

These models provide critical insight into aerosol deposition in lung airways. The models can be used in analyzing the toxicological effects of exposure to particulate matters or can be used in estimating pharmacological effects of pulmonary drugs and providing inhaler-design guidelines for improved drug-aerosol targeting.

6.2 Comparison of total lung deposition by WLAM I and WLAM II

Figure 6.1 shows the comparison of total lung deposition prediction by the two models for a $3 \mu\text{m}$ particle under two inhalation conditions. Reasonably accurate agreement was noticed with both model predictions when compared with experimental deposition results from Heyder [119]. However, the WLAM I model is slightly over predicting under slow breathing conditions, while it is under predicting under deep breathing conditions. The trend for WLAM II model predictions is consistent for both inhalation conditions.

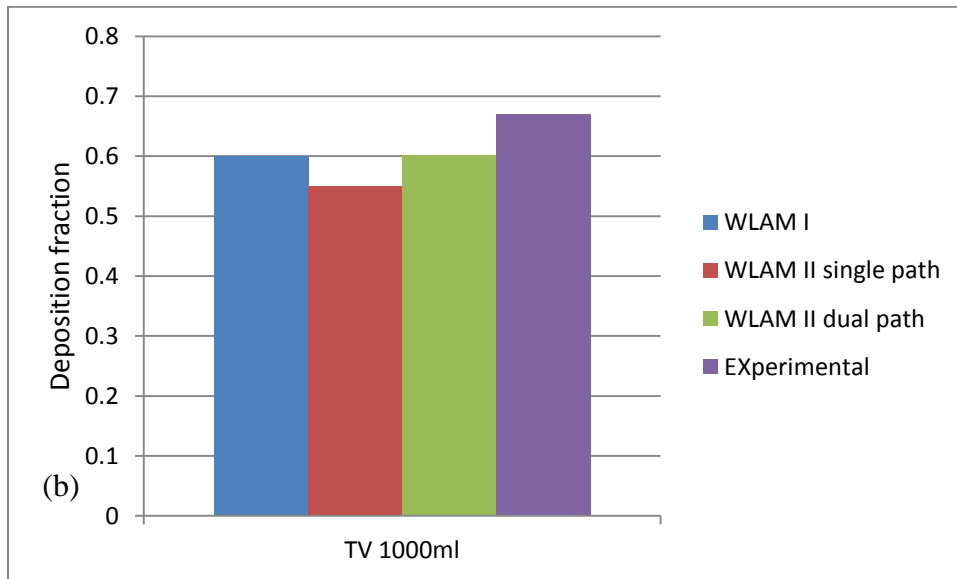
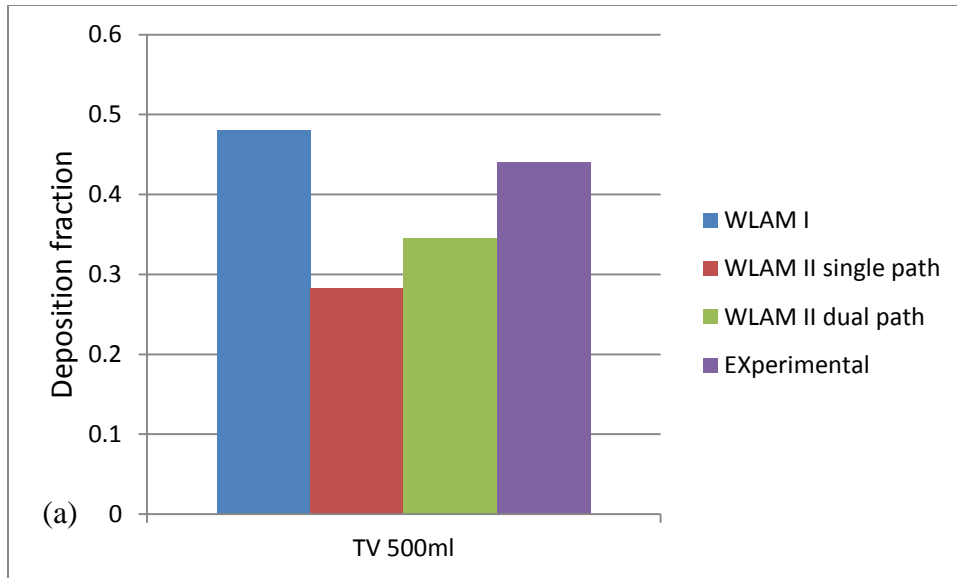


Fig. 6.1 Comparison of total lung deposition prediction by WLAM I and WLAM II with experimental results for (a) TV 500ml and (b) TV 1000ml.

6.3 Computational resource requirement for WLAM I and WLAM II

Run time for a transient simulation for 1s inhalation with particle track on an engineering workstation (Dell computer with 32 GB RAM and four 3.0-GHz Intel Xeon processors) using the two whole-lung models are compared in Table 6.1. As indicated, the computational resource requirement for WLAM I is low compared WLAM II. Increasing the paths of WLAM II resulted in increased computational time.

Table 6.1. Run time comparison between WLAM I and WLAM II

<i>Model</i>	<i>WLAM I</i>	<i>Single-path WLAM II</i>	<i>Dual-path WLAM II</i>
<i>Simulation time</i>	<i>4 hrs.</i>	<i>20 hrs.</i>	<i>27 hrs.</i>

Chapter 7

References

References

- [1] Kleinstreuer, C., and Zhang, Z., 2010, "Airflow and Particle Transport in the Human Respiratory System," *Annu. Rev. Fluid Mech.*, **42**pp. 301-334.
- [2] Weibel, E., 1963, "Morphometry of the human lung," Academic Press, New York, .
- [3] Ochs, M., Nyengaard, J. R., Jung, A., Knudsen, L., Voigt, M., Wahlers, T., Richter, J., and Gundersen, H. J. G., 2004, "The Number of Alveoli in the Human Lung," *American Journal of Respiratory and Critical Care Medicine*, **169**(1), pp. 120-124.
- [4] Malve, M., Perez del Palomar, A., Chandra, S., Lopez-Villalobos, J. L., Mena, A., Finol, E. A., Ginel, A., and Doblare, M., 2011, "FSI Analysis of a Healthy and a Stenotic Human Trachea Under Impedance-Based Boundary Conditions," *J. Biomech. Eng.*, **133**(2), pp. 021001.
- [5] Klein, S. G., Hennen, J., Serchi, T., Blömeke, B., and Gutleb, A. C., 2011, "Potential of Coculture in Vitro Models to Study Inflammatory and Sensitizing Effects of Particles on the Lung," *Toxicology in Vitro*, **25**(8), pp. 1516-1534.
- [6] Yu, C. P., and Dju, C. K., 1982, "A Comparative Study of Aerosol Deposition in Different Lung Models," *The American Industrial Hygiene Association Journal*, **43**(1), pp. 54-65.
- [7] Raabe, O.G., Yeh, H.C., Schum, G.M., 1976, "Tracheobronchial geometry : human, dog, rat, hamster--a compilation of selected data from the project respiratory tract deposition

models," Inhalation Toxicology Research Institute, Lovelace Foundation for Medical Education and Research, Albuquerque, NM., .

[8] Yeh, H., and Schum, G. M., 1980, "Models of Human Lung Airways and their Application to Inhaled Particle Deposition," *Bull. Math. Biol.*, **42**(3), pp. 461-480.

[9] Hansen, J. E., and Ampaya, E. P., 1975, "Human Air Space Shapes, Sizes, Areas, and Volumes," *J. Appl. Physiol.*, **38**(6), pp. 990-995.

[10] Horsfield, K., Dart, G., Olson, D. E., Filley, G. F., and Cumming, G., 1971, "Models of the Human Bronchial Tree." *J. Appl. Physiol.*, **31**(2), pp. 207-217.

[11] Finlay, W.H., 2001, "The Mechanics of Inhaled Pharmaceutical Aerosols," Academic Press, San Diego, .

[12] Kleinstreuer, C., Zhang, Z., Li, Z., Roberts, W. L., and Rojas, C., 2008, "A New Methodology for Targeting Drug-Aerosols in the Human Respiratory System," *Int. J. Heat Mass Transfer*, **51**(23), pp. 5578-5589.

[13] Blackwell, D. L., Lucas, J. W., and Clarke, T. C., 2014, "Summary Health Statistics for US Adults: National Health Interview Survey, 2012." *Vital and Health Statistics.Series 10, Data from the National Health Survey*, (260), pp. 1-161.

[14] Bloom, B., Jones, L., and Freeman, G., 2014, "Summary Health Statistics for Us Children: National Health Interview Survey, 2012." *Vital and Health Statistics.Series 10, Data from the National Health Survey*, (258), pp. 1-88.

- [15] Scichilone, N., Contoli, M., Paleari, D., Pirina, P., Rossi, A., Sanguinetti, C. M., Santus, P., Sofia, M., and Sverzellati, N., 2013, "Assessing and Accessing the Small Airways; Implications for Asthma Management," *Pulm. Pharmacol. Ther.*, **26**(2), pp. 172-179.
- [16] Bateman, E. D., Reddel, H. K., Eriksson, G., Peterson, S., Stlund, O., Sears, M. R., Jenkins, C., Humbert, M., Buhl, R., and Harrison, T. W., 2010, "Overall Asthma Control: The Relationship between Current Control and Future Risk," *J. Allergy Clin. Immunol.*, **125**(3), pp. 608. e6.
- [17] National Heart Lung and Blood Institute, "No Title," National Asthma Education and Prevention Program. Expert Panel Report 3 (EPR3): Guidelines for the Diagnosis and Management of Asthma. National Institutes of Health, US Department of Health and Human Services 2007, .
- [18] Kolanjiyil, A. V., and Kleinstreuer, C., 2016, "Computationally Efficient Analysis of Particle Transport and Deposition in a Human Whole-Lung-Airway Model. Part I: Theory and Model Validation," *Computers in Biology and Medicine*, **79**pp. 193-204.
- [19] Kolanjiyil, A. V., Kleinstreuer, C., and Sadikot, R. T., 2016, "Computationally Efficient Analysis of Particle Transport and Deposition in a Human Whole-Lung-Airway Model. Part II: Dry Powder Inhaler Application," *Computers in Biology and Medicine* (Available Online), .

- [20] Kolanjiyil, A. V., and Kleinstreuer, C., 2013, "Nanoparticle Mass Transfer from Lung Airways to Systemic Regions—Part I: Whole-Lung Aerosol Dynamics," *J. Biomech. Eng.*, **135**(12), pp. 121003.
- [21] Kolanjiyil, A. V., and Kleinstreuer, C., 2013, "Nanoparticle Mass Transfer from Lung Airways to Systemic Regions—Part II: Multi-Compartmental Modeling," *Journal of Biomechanical Engineering*, **135**(12), pp. 121004.
- [22] Kleinstreuer, C., and Zhang, Z., 2009, "An Adjustable Triple-Bifurcation Unit Model for Air-Particle Flow Simulations in Human Tracheobronchial Airways." *ASME J. Biomech. Eng.*, **131**(2), pp. 021007.
- [23] Zhang, Z., and Kleinstreuer, C., 2011, "Laminar- to- turbulent Fluid–nanoparticle Dynamics Simulations: Model Comparisons and Nanoparticle- deposition Applications," *Int. J. Numer. Method Biomed. Eng.*, **27**(12), pp. 1930-1950.
- [24] Feng, Y., and Kleinstreuer, C., 2014, "Micron-Particle Transport, Interactions and Deposition in Triple Lung-Airway Bifurcations using a Novel Modeling Approach," *Journal of Aerosol Science*, **71**pp. 1-15.
- [25] Longest, P. W., Tian, G., Walenga, R. L., and Hindle, M., 2012, "Comparing MDI and DPI Aerosol Deposition using in Vitro Experiments and a New Stochastic Individual Path (SIP) Model of the Conducting Airways," *Pharm. Res.*, **29**(6), pp. 1670-1688.

- [26] Tian, G., Hindle, M., Lee, S., and Longest, P. W., 2015, "Validating CFD Predictions of Pharmaceutical Aerosol Deposition with in Vivo Data," *Pharm. Res.*, **32**(10), pp. 3170-3187.
- [27] Walenga, R. L., Tian, G., Hindle, M., Yelverton, J., Dodson, K., and Longest, P. W., 2014, "Variability in Nose-to-Lung Aerosol Delivery," *J. Aerosol Sci.*, **78**pp. 11-29.
- [28] Finlay, W. H., and Martin, A. R., 2008, "Recent Advances in Predictive Understanding of Respiratory Tract Deposition," *Journal of Aerosol Medicine and Pulmonary Drug Delivery*, **21**(2), pp. 189-206.
- [29] Lin, C., Tawhai, M. H., McLennan, G., and Hoffman, E. A., 2009, "Multiscale Simulation of Gas Flow in Subject-Specific Models of the Human Lung," *IEEE Eng. Med. Biol. Mag.*, **28**(3), pp. 25-33.
- [30] Matida, E. A., Finlay, W. H., Lange, C. F., and Grgic, B., 2004, "Improved Numerical Simulation of Aerosol Deposition in an Idealized Mouth-throat," *J. Aerosol Sci.*, **35**(1), pp. 1-19.
- [31] Tawhai, M. H., Pullan, A. J., and Hunter, P. J., 2000, "Generation of an Anatomically Based Three-Dimensional Model of the Conducting Airways," *Ann. Biomed. Eng.*, **28**(7), pp. 793-802.
- [32] U.S. National Library of Medicine, "Visible Human Project," <http://www.nlm.nih.gov/research/visible/applications.html>, .

- [33] Tawhai, M. H., Nash, M. P., and Hoffman, E. A., 2006, "An Imaging-Based Computational Approach to Model Ventilation Distribution and Soft-Tissue Deformation in the Ovine Lung," *Acad. Radiol.*, **13**(1), pp. 113-120.
- [34] Lin, C., Tawhai, M. H., McLennan, G., and Hoffman, E. A., 2009, "Computational Fluid Dynamics," *IEEE Eng. Med. Biol. Mag.*, **28**(3), pp. 25-33.
- [35] Yin, Y., Choi, J., Hoffman, E. A., Tawhai, M. H., and Lin, C. L., 2010, "Simulation of Pulmonary Air Flow with a Subject-Specific Boundary Condition," *J. Biomech.*, **43**(11), pp. 2159-2163.
- [36] Yin, Y., Hoffman, E. A., and Lin, C., 2009, "Local tissue-weight-based nonrigid registration of lung images with application to regional ventilation," *SPIE Medical Imaging, Anonymous International Society for Optics and Photonics*, pp. 10.
- [37] Yin, Y., Hoffman, E. A., and Lin, C., 2009, "Mass Preserving Nonrigid Registration of CT Lung Images using Cubic B-Spline," *Med. Phys.*, **36**pp. 4213.
- [38] Yin, Y., Choi, J., Hoffman, E. A., Tawhai, M. H., and Lin, C., 2013, "A Multiscale MDCT Image-Based Breathing Lung Model with Time-Varying Regional Ventilation," *Journal of Computational Physics*, **244**pp. 168-192.
- [39] Yin, Y., Hoffman, E. A., Ding, K., Reinhardt, J. M., and Lin, C., 2011, "A Cubic B-Spline-Based Hybrid Registration of Lung CT Images for a Dynamic Airway Geometric Model with Large Deformation," *Phys. Med. Biol.*, **56**(1), pp. 203.

- [40] Wu, G., Wang, Q., Lian, J., 2011, "Medical Image Computing and Computer-Assisted Intervention–MICCAI 2011," Springer, pp. 532-539.
- [41] Wu, G., Wang, Q., Lian, J., and Shen, D., 2013, "Estimating the 4D Respiratory Lung Motion by Spatiotemporal Registration and Super-Resolution Image Reconstruction," *Med. Phys.*, **40**pp. 031710.
- [42] Wall, W. A., and Rabczuk, T., 2008, "Fluid–structure Interaction in Lower Airways of CT- based Lung Geometries," *Int. J. Numer. Methods Fluids*, **57**(5), pp. 653-675.
- [43] Wiechert, L., Metzke, R., and Wall, W. A., 2009, "Modeling the Mechanical Behavior of Lung Tissue at the Microlevel," *J. Eng. Mech.*, **135**(5), pp. 434-438.
- [44] Wall, W. A., Wiechert, L., Comerford, A., and Rausch, S., 2010, "Towards a Comprehensive Computational Model for the Respiratory System," *International Journal for Numerical Methods in Biomedical Engineering*, **26**(7), pp. 807-827.
- [45] Wiechert, L., Comerford, A., Rausch, S., 2011, "Fundamental Medical and Engineering Investigations on Protective Artificial Respiration," Springer, pp. 1-32.
- [46] Yoshihara, L., Ismail, M., and Wall, W.A., 2013, "Computer Models in Biomechanics," Springer, pp. 395-407.
- [47] Balashazy, I., Farkas, A., Szke, I., Hofmann, W., and Sturm, R., 2003, "Simulation of Deposition and Clearance of Inhaled Particles in Central Human Airways," *Radiat. Prot. Dosimet.*, **105**(1-4), pp. 129-132.

- [48] Comer, J. K., Kleinstreuer, C., Hyun, S., and Kim, C. S., 2000, "Aerosol Transport and Deposition in Sequentially Bifurcating Airways," *J. Biomech. Eng.*, **122**(2), pp. 152-158.
- [49] Hofmann, W., Golser, R., and Balashazy, I., 2003, "Inspiratory Deposition Efficiency of Ultrafine Particles in a Human Airway Bifurcation Model," *Aerosol. Sci. Technol.*, **37**(12), pp. 988-994.
- [50] Zhang, Z., and Kleinstreuer, C., 2004, "Airflow Structures and Nano-Particle Deposition in a Human Upper Airway Model," *J. Comput. Phys.*, **198**(1), pp. 178-210.
- [51] Comer, J. K., Kleinstreuer, C., Hyun, S., and Kim, C. S., 2000, "Aerosol Transport and Deposition in Sequentially Bifurcating Airways," *J. Biomech. Eng.*, **122**(2), pp. 152-158.
- [52] Comer, J. K., Kleinstreuer, C., and Zhang, Z., 2001, "Flow Structures and Particle Deposition Patterns in Double-Bifurcation Airway Models. Part 1. Air Flow Fields," *J. Fluid Mech.*, **435**pp. 25-54.
- [53] Zhang, Z., Kleinstreuer, C., and Kim, C. S., 2002, "Cyclic Micron-Size Particle Inhalation and Deposition in a Triple Bifurcation Lung Airway Model," *J. Aerosol Sci.*, **33**(2), pp. 257-281.
- [54] Kleinstreuer, C., and Zhang, Z., 2003, "Laminar-to-Turbulent Fluid-Particle Flows in a Human Airway Model," *Int. J. Multiphase Flow*, **29**(2), pp. 271-289.

- [55] BALSHZY, I., HEISTRACHER, T., and HOFMANN, W., 1996, "Air Flow and Particle Deposition Patterns in Bronchial Airway Bifurcations: The Effect of Different CFD Models and Bifurcation Geometries," *Journal of Aerosol Medicine*, **9**(3), pp. 287-301.
- [56] Stapleton, K., Guentsch, E., Hoskinson, M. K., and Finlay, W. H., 2000, "On the Suitability of $K-\epsilon$ Turbulence Modeling for Aerosol Deposition in the Mouth and Throat: A Comparison with Experiment," *J. Aerosol Sci.*, **31**(6), pp. 739-749.
- [57] Matida, E. A., DeHaan, W. H., Finlay, W. H., and Lange, C. F., 2003, "Simulation of Particle Deposition in an Idealized Mouth with Different Small Diameter Inlets," *Aerosol. Sci. Technol.*, **37**(11), pp. 924-932.
- [58] Heenan, A. F., Matida, E., Pollard, A., and Finlay, W. H., 2003, "Experimental Measurements and Computational Modeling of the Flow Field in an Idealized Human Oropharynx," *Exp. Fluids*, **35**(1), pp. 70-84.
- [59] Koombua, K., Pidaparti, R. M., Longest, P. W., and Ward, K. R., 2008, "Computational Analysis of Fluid Characteristics in Rigid and Flexible Human Respiratory Airway Models," *Engineering Applications of Computational Fluid Mechanics*, **2**(2), pp. 185-194.
- [60] Longest, P. W., Tian, G., Delvadia, R., and Hindle, M., 2012, "Development of a Stochastic Individual Path (SIP) Model for Predicting the Deposition of Pharmaceutical Aerosols: Effects of Turbulence, Polydisperse Aerosol Size, and Evaluation of Multiple Lung Lobes," *Aerosol Science and Technology*, **46**(12), pp. 1271-1285.

- [61] Shi, H., Kleinstreuer, C., and Zhang, Z., 2008, "Dilute Suspension Flow with Nanoparticle Deposition in a Representative Nasal Airway Model," *Phys. Fluids*, **20**(1), pp. 013301.
- [62] Jayaraju, S. T., Brouns, M., Lacor, C., Belkassam, B., and Verbanck, S., 2008, "Large Eddy and Detached Eddy Simulations of Fluid Flow and Particle Deposition in a Human Mouth–throat," *J. Aerosol Sci.*, **39**(10), pp. 862-875.
- [63] Zhang, Z., Kleinstreuer, C., and Feng, Y., 2012, "Vapor Deposition during Cigarette Smoke Inhalation in a Subject-Specific Human Airway Model," *J. Aerosol Sci.*, **53**pp. 40-60.
- [64] Ma, B., and Lutchen, K. R., 2009, "CFD Simulation of Aerosol Deposition in an Anatomically Based Human Large–medium Airway Model," *Ann. Biomed. Eng.*, **37**(2), pp. 271-285.
- [65] Kleinstreuer, C., Zhang, Z., and Donohue, J. F., 2008, "Targeted Drug-Aerosol Delivery in the Human Respiratory System," *Annu.Rev.Biomed.Eng.*, **10**pp. 195-220.
- [66] Rostami, A. A., 2009, "Computational Modeling of Aerosol Deposition in Respiratory Tract: A Review," *Inhal. Toxicol.*, **21**(4), pp. 262-290.
- [67] Kleinstreuer, C., and Zhang, Z., 2010, "Airflow and Particle Transport in the Human Respiratory System," *Annu. Rev. Fluid Mech.*, **42**pp. 301-334.
- [68] Hofmann, W., 2011, "Modelling Inhaled Particle Deposition in the Human Lung—a Review," *J. Aerosol Sci.*, **42**(10), pp. 693-724.

- [69] Jin, H. H., Fan, J. R., Zeng, M. J., and Cen, K. F., 2007, "Large Eddy Simulation of Inhaled Particle Deposition within the Human Upper Respiratory Tract," *J. Aerosol Sci.*, **38**(3), pp. 257-268.
- [70] Zhang, Z., Kleinstreuer, C., Donohue, J. F., and Kim, C. S., 2005, "Comparison of Micro-and Nano-Size Particle Depositions in a Human Upper Airway Model," *J. Aerosol Sci.*, **36**(2), pp. 211-233.
- [71] Zhang, Z., Kleinstreuer, C., and Kim, C. S., 2008, "Airflow and Nanoparticle Deposition in a 16-Generation Tracheobronchial Airway Model," *Ann. Biomed. Eng.*, **36**(12), pp. 2095-2110.
- [72] Nowak, N., Kakade, P. P., and Annapragada, A. V., 2003, "Computational Fluid Dynamics Simulation of Airflow and Aerosol Deposition in Human Lungs," *Ann. Biomed. Eng.*, **31**(4), pp. 374-390.
- [73] Tian, G., Longest, P., Su, G., Walenga, R. L., and Hindle, M., 2011, "Development of a Stochastic Individual Path (SIP) Model for Predicting the Tracheobronchial Deposition of Pharmaceutical Aerosols: Effects of Transient Inhalation and Sampling the Airways," *J. Aerosol Sci.*, **42**(11), pp. 781-799.
- [74] Ma, B., and Lutchen, K. R., 2006, "An Anatomically Based Hybrid Computational Model of the Human Lung and its Application to Low Frequency Oscillatory Mechanics," *Ann. Biomed. Eng.*, **34**(11), pp. 1691-1704.

- [75] Yin, Y., Choi, J., Hoffman, E. A., Tawhai, M. H., and Lin, C., 2010, "Simulation of Pulmonary Air Flow with a Subject-Specific Boundary Condition," *J. Biomech.*, **43**(11), pp. 2159-2163.
- [76] Walters, D. K., and Luke, W. H., 2010, "A Method for Three-Dimensional Navier–Stokes Simulations of Large-Scale Regions of the Human Lung Airway," *ASME J. Fluid Eng.*, **132**(5), pp. 051101.
- [77] ICRP, 1994, "Human Respiratory Tract Model for Radiological Protection," *Ann. ICRP, Publication 66*, **24**pp. 1-3.
- [78] Taulbee, D. B., and Yu, C. P., 1975, "A Theory of Aerosol Deposition in the Human Respiratory Tract," *J. Appl. Physiol.*, **38**(1), pp. 77-85.
- [79] Martonen, T. B., 1982, "Analytical Model of Hygroscopic Particle Behavior in Human Airways," *Bull. Math. Biol.*, **44**(3), pp. 425-442.
- [80] Asgharian, B., Hofmann, W., and Bergmann, R., 2001, "Particle Deposition in a Multiple-Path Model of the Human Lung," *Aerosol. Sci. Technol.*, **34**(4), pp. 332-339.
- [81] Koblinger, L., 1985, "Analysis of Human Lung Morphometric Data for Stochastic Aerosol Deposition Calculations," *Phys. Med. Biol.*, **30**(6), pp. 541.
- [82] Koblinger, L., and Hofmann, W., 1990, "Monte Carlo Modeling of Aerosol Deposition in Human Lungs. Part I: Simulation of Particle Transport in a Stochastic Lung Structure," *J. Aerosol Sci.*, **21**(5), pp. 661-674.

- [83] Katz, I., Pichelin, M., Caillibotte, G., Montesantos, S., Majoral, C., Martonen, T., Fleming, J., Bennett, M., and Conway, J., 2013, "Controlled, Parametric, Individualized, 2D, and 3D Imaging Measurements of Aerosol Deposition in the Respiratory Tract of Healthy Human Subjects: Preliminary Comparisons with Simulations," *Aerosol Science and Technology*, **47**(7), pp. 714-723.
- [84] Kleinstreuer, C., Shi, H., and Zhang, Z., 2007, "Computational Analyses of a Pressurized Metered Dose Inhaler and a New Drug-Aerosol Targeting Methodology," *Journal of Aerosol Medicine*, **20**(3), pp. 294-309.
- [85] Kleinstreuer, C., Feng, Y., and Childress, E., 2014, "Drug-Targeting Methodologies with Applications: A Review," *World Journal of Clinical Cases: WJCC*, **2**(12), pp. 742-756.
- [86] Walenga, R. L., and Longest, P. W., 2016, "Current Inhalers Deliver very Small Doses to the Lower Tracheobronchial Airways: Assessment of Healthy and Constricted Lungs," *J. Pharm. Sci.*, **105**(1), pp. 147-159.
- [87] Tawhai, M. H., and Bates, J. H., 2011, "Multi-Scale Lung Modeling," *J. Appl. Physiol.*, **110**(5), pp. 1466-1472.
- [88] Ismail, M., Comerford, A., and Wall, W. A., 2013, "Coupled and Reduced Dimensional Modeling of Respiratory Mechanics during Spontaneous Breathing," *International Journal for Numerical Methods in Biomedical Engineering*, **29**(11), pp. 1285-1305.

- [89] Longest, P. W., Tian, G., Delvadia, R., and Hindle, M., 2012, "Development of a Stochastic Individual Path (SIP) Model for Predicting the Deposition of Pharmaceutical Aerosols: Effects of Turbulence, Polydisperse Aerosol Size, and Evaluation of Multiple Lung Lobes," *Aerosol Science and Technology*, **46**(12), pp. 1271-1285.
- [90] Longest, P. W., Tian, G., Khajeh-Hosseini-Dalasm, N., and Hindle, M., 2016, "Validating Whole-Airway CFD Predictions of DPI Aerosol Deposition at Multiple Flow Rates," .
- [91] ANSYS 15.0, "CFX-Solver Theory Guide," ANSYS, Inc., .
- [92] Zhang, Z., and Kleinstreuer, C., 2011, "Computational Analysis of Airflow and Nanoparticle Deposition in a Combined Nasal–oral–tracheobronchial Airway Model," *J. Aerosol Sci.*, **42**(3), pp. 174-194.
- [93] Goldberg, M., 2008, "A Systematic Review of the Relation between Long-Term Exposure to Ambient Air Pollution and Chronic Diseases," *Rev. Environ. Health*, **23**(4), pp. 243-298.
- [94] Pope, C. A., Muhlestein, J. B., May, H. T., Renlund, D. G., Anderson, J. L., and Horne, B. D., 2006, "Ischemic Heart Disease Events Triggered by Short-Term Exposure to Fine Particulate Air Pollution," *Circulation*, **114**(23), pp. 2443-2448.
- [95] Schwartz, J., 1993, "Particulate Air Pollution and Chronic Respiratory Disease," *Environ. Res.*, **62**(1), pp. 7-13.

- [96] Geiser, M., and Kreyling, W. G., 2010, "Deposition and Biokinetics of Inhaled Nanoparticles," *Part Fibre Toxicol*, **7**(2), pp. 1-17.
- [97] Seaton, A., Godden, D., MacNee, W., and Donaldson, K., 1995, "Particulate Air Pollution and Acute Health Effects," *The Lancet*, **345**(8943), pp. 176-178.
- [98] Kolanjiyil, A. V., and Kleinstreuer, C., 2013, "Nanoparticle Mass Transfer from Lung Airways to Systemic Regions--Part I: Whole-Lung Aerosol Dynamics," *Journal of Biomechanical Engineering*, **135**(12), pp. 121003.
- [99] Kolanjiyil, A. V., and Kleinstreuer, C., 2013, "Nanoparticle Mass Transfer from Lung Airways to Systemic Regions--Part II: Multi-Compartmental Modeling," *Journal of Biomechanical Engineering*, **135**(12), pp. 121004.
- [100] Choi, J., and Kim, C. S., 2007, "Mathematical Analysis of Particle Deposition in Human Lungs: An Improved Single Path Transport Model," *Inhal. Toxicol.*, **19**(11), pp. 925-939.
- [101] Martonen, T. B., 1982, "Analytical Model of Hygroscopic Particle Behavior in Human Airways," *Bull. Math. Biol.*, **44**(3), pp. 425-442.
- [102] Broday, D. M., and Georgopoulos, P. G., 2001, "Growth and Deposition of Hygroscopic Particulate Matter in the Human Lungs," *Aerosol. Sci. Technol.*, **34**(1), pp. 144-159.

- [103] Asgharian, B., 2004, "A Model of Deposition of Hygroscopic Particles in the Human Lung," *Aerosol Science and Technology*, **38**(9), pp. 938-947.
- [104] Asgharian, B., and Anjilvel, S., 1998, "A Multiple-Path Model of Fiber Deposition in the Rat Lung," *Toxicological Sciences*, **44**(1), pp. 80-86.
- [105] Sturm, R., and Hofmann, W., 2006, "A Computer Program for the Simulation of Fiber Deposition in the Human Respiratory Tract," *Comput. Biol. Med.*, **36**(11), pp. 1252-1267.
- [106] Grandmont, C., Maury, B., and Soualah, A., 2008, "Multiscale modelling of the respiratory track: a theoretical framework," *ESAIM: Proceedings, Anonymous EDP sciences*, **23**, pp. 10-29.
- [107] Huang, J., Sun, H., Liu, C., and Zhang, L., 2013, "Moving Boundary Simulation of Airflow and Micro-Particle Deposition in the Human Extra-Thoracic Airway Under Steady Inspiration. Part I: Airflow," *European Journal of Mechanics / B Fluids*, **37**pp. 29.
- [108] Paiva, M., Lacquet, L. M., and Van Der Linden, L P, 1976, "Gas Transport in a Model Derived from Hansen-Ampaya Anatomical Data of the Human Lung," *J. Appl. Physiol.*, **41**(1), pp. 115-119.
- [109] Paiva, M., 1972, "Computation of the Boundary Conditions for Diffusion in the Human Lung," *Computers and Biomedical Research*, **5**(6), pp. 585-595.
- [110] Paiva, M., and Engel, L. A., 1979, "Pulmonary Interdependence of Gas Transport," *J. Appl. Physiol.*, **47**(2), pp. 296-305.

- [111] Paiva, M., and Engel, L. A., 1981, "The Anatomical Basis for the Sloping N₂ Plateau," *Respir. Physiol.*, **44**(3), pp. 325-337.
- [112] Yu, C. P., 1978, "Exact Analysis of Aerosol Deposition during Steady Breathing," *Powder Technol.*, **21**(1), pp. 55-62.
- [113] Darquenne, C., and Paiva, M., 1994, "One-Dimensional Simulation of Aerosol Transport and Deposition in the Human Lung," *J. Appl. Physiol.*, **77**(6), pp. 2889-2898.
- [114] Sarangapani, R., and Wexler, A. S., 1999, "Modeling Aerosol Bolus Dispersion in Human Airways," *J. Aerosol Sci.*, **30**(10), pp. 1345-1362.
- [115] Longest, P. W., and Vinchurkar, S., 2009, "Inertial Deposition of Aerosols in Bifurcating Models during Steady Expiratory Flow," *J. Aerosol Sci.*, **40**(4), pp. 370-378.
- [116] Sarangapani, R., and Wexler, A. S., 2000, "The Role of Dispersion in Particle Deposition in Human Airways," *Toxicological Sciences*, **54**(1), pp. 229-236.
- [117] Vaish, M., and Kleinstreuer, C., 2015, "A Lagrangian Approach for Calculating Microsphere Deposition in a One-Dimensional Lung-Airway Model," *J. Biomech. Eng.*, **137**(9), pp. 094502.
- [118] Kolanjiyil, A. V., 2016, "Whole-Lung Airflow and Particle Transport/Deposition Modeling and Simulation," (doctoral dissertation) North Carolina State University, Raleigh, NC, USA.

- [119] Heyder, J., Gebhart, J., Rudolf, G., Schiller, C. F., and Stahlhofen, W., 1986, "Deposition of Particles in the Human Respiratory Tract in the Size Range 0.005–15 Mm," *J. Aerosol Sci.*, **17**(5), pp. 811-825.
- [120] Cheng, Y., Zhou, Y., and Chen, B. T., 1999, "Particle Deposition in a Cast of Human Oral Airways," *Aerosol. Sci. Technol.*, **31**(4), pp. 286-300.
- [121] Grgic, B., Finlay, W. H., Burnell, P., and Heenan, A. F., 2004, "In Vitro Intersubject and Intrasubject Deposition Measurements in Realistic Mouth–throat Geometries," *J. Aerosol Sci.*, **35**(8), pp. 1025-1040.
- [122] Zhou, Y., and Cheng, Y., 2005, "Particle Deposition in a Cast of Human Tracheobronchial Airways," *Aerosol Science and Technology*, **39**(6), pp. 492-500.
- [123] Zhang, Y., and Finlay, W. H., 2005, "Experimental Measurements of Particle Deposition in Three Proximal Lung Bifurcation Models with an Idealized Mouth-Throat," *Journal of Aerosol Medicine*, **18**(4), pp. 460-473.
- [124] Lizal, F., Belka, M., Adam, J., Jedelsky, J., and Jicha, M., 2015, "A Method for in Vitro Regional Aerosol Deposition Measurement in a Model of the Human Tracheobronchial Tree by the Positron Emission Tomography," *Proceedings of the Institution of Mechanical Engineers. Part H, Journal of Engineering in Medicine*, **229**(10), pp. 750-757.

- [125] Chan, T. L., and Lippmann, M., 1980, "Experimental Measurements and Empirical Modelling of the Regional Deposition of Inhaled Particles in Humans," *The American Industrial Hygiene Association Journal*, **41**(6), pp. 399-409.
- [126] Stahlhofen, W., Rudolf, G., and James, A. C., 1989, "Intercomparison of Experimental Regional Aerosol Deposition Data," *Journal of Aerosol Medicine*, **2**(3), pp. 285-308.
- [127] Kim, C. S., and Hu, S. C., 2006, "Total Respiratory Tract Deposition of Fine Micrometer-Sized Particles in Healthy Adults: Empirical Equations for Sex and Breathing Pattern," *J. Appl. Physiol.* (1985), **101**(2), pp. 401-412.
- [128] Emmett, P. C., Aitken, R. J., and Hannan, W. J., 1982, "Measurements of the Total and Regional Deposition of Inhaled Particles in the Human Respiratory Tract," *J. Aerosol Sci.*, **13**(6), pp. 549-560.
- [129] Lippmann, M., 1977, "Regional Deposition of Particles in the Human Respiratory Tract," *Comprehensive Physiology*, pp. 213-232.
- [130] Foord, N., Black, A., and Walsh, M., 1978, "Regional Deposition of 2.5–7.5 Mm Diameter Inhaled Particles in Healthy Male Non-Smokers," *J. Aerosol Sci.*, **9**(4), pp. 343-357.
- [131] Yu, C. P., Diu, C. K., and Soong, T. T., 1981, "Statistical Analysis of Aerosol Deposition in Nose and Mouth," *The American Industrial Hygiene Association Journal*, **42**(10), pp. 726-733.

[132] Devi, S. K., Panchagnula, M. V., and Alladi, M., 2016, "Designing Aerosol Size Distribution to Minimize Inter-Subject Variability of Alveolar Deposition," *J. Aerosol Sci.*, **101**pp. 144-155.

[133] Fleming, J., Conway, J., Majoral, C., Tossici-Bolt, L., Katz, I., Caillibotte, G., Perchet, D., Pichelin, M., Muellinger, B., and Martonen, T., 2011, "The use of Combined Single Photon Emission Computed Tomography and X-Ray Computed Tomography to Assess the Fate of Inhaled Aerosol," *Journal of Aerosol Medicine and Pulmonary Drug Delivery*, **24**(1), pp. 49-60.

[134] Majoral, C., Fleming, J., Conway, J., Katz, I., Tossici-Bolt, L., Pichelin, M., Montesantos, S., and Caillibotte, G., 2014, "Controlled, Parametric, Individualized, 2D and 3D Imaging Measurements of Aerosol Deposition in the Respiratory Tract of Healthy Human Volunteers: In Vivo Data Analysis," *Journal of Aerosol Medicine and Pulmonary Drug Delivery*, **27**(5), pp. 349-362.

[135] Feng, Y., and Kleinstreuer, C., 2013, "Analysis of Non-Spherical Particle Transport in Complex Internal Shear Flows," *Physics of Fluids (1994-Present)*, **25**(9), pp. 091904.

[136] Feng, Y., Kleinstreuer, C., and Rostami, A., 2015, "Evaporation and Condensation of Multicomponent Electronic Cigarette Droplets and Conventional Cigarette Smoke Particles in an Idealized G3–G6 Triple Bifurcating Unit," *J. Aerosol Sci.*, **80**pp. 58-74.

- [137] Longest, P. W., and Xi, J., 2008, "Condensational Growth may Contribute to the Enhanced Deposition of Cigarette Smoke Particles in the Upper Respiratory Tract," *Aerosol Science and Technology*, **42**(8), pp. 579-602.
- [138] Newman, S. P., and Chan, H., 2008, "In Vitro/in Vivo Comparisons in Pulmonary Drug Delivery," *Journal of Aerosol Medicine and Pulmonary Drug Delivery*, **21**(1), pp. 77-84.
- [139] Dolovich, M. B., and Dhand, R., 2011, "Aerosol Drug Delivery: Developments in Device Design and Clinical Use," *The Lancet*, **377**(9770), pp. 1032-1045.
- [140] Martin, A. R., and Finlay, W. H., 2015, "Nebulizers for Drug Delivery to the Lungs," *Expert Opinion on Drug Delivery*, **12**(6), pp. 889-900.
- [141] Sanchis, J., Corrigan, C., Levy, M. L., and Viejo, J. L., 2013, "Inhaler Devices—from Theory to Practice," *Respir. Med.*, **107**(4), pp. 495-502.
- [142] Yang, M. Y., Chan, J. G. Y., and Chan, H., 2014, "Pulmonary Drug Delivery by Powder Aerosols," *J. Controlled Release*, **193**pp. 228-240.
- [143] D Brocklebank, F Ram, J Wright, and P Barry, 2002, "Comparison of the Effectiveness of Inhaler Devices in Asthma and Chronic Obstructive Airways Disease: A Systematic Review of the Literature," *British Journal of Clinical Governance*, **7**(2), pp. 125.
- [144] Newman, S. P., and Busse, W. W., 2002, "Evolution of Dry Powder Inhaler Design, Formulation, and Performance," *Respir. Med.*, **96**(5), pp. 293-304.

- [145] Islam, N., and Cleary, M. J., 2012, "Developing an Efficient and Reliable Dry Powder Inhaler for Pulmonary Drug Delivery—a Review for Multidisciplinary Researchers," *Med. Eng. Phys.*, **34**(4), pp. 409-427.
- [146] Berkenfeld, K., Lamprecht, A., and McConville, J. T., 2015, "Devices for Dry Powder Drug Delivery to the Lung," *AAPS PharmSciTech*, **16**(3), pp. 479-490.
- [147] Newman, S. P., Pitcairn, G. R., Hirst, P. H., Bacon, R. E., O'Keefe, E., Reiners, M., and Hermann, R., 2000, "Scintigraphic Comparison of Budesonide Deposition from Two Dry Powder Inhalers," *European Respiratory Journal*, **16**(1), pp. 178-183.
- [148] Fenton, C., Keating, G. M., and Plosker, G. L., 2003, "Novolizer®: A Multidose Dry Powder Inhaler," *Drugs*, **63**(22), pp. 2437-2445.
- [149] Longest, P. W., Tian, G., Walenga, R. L., and Hindle, M., 2012, "Comparing MDI and DPI Aerosol Deposition using in Vitro Experiments and a New Stochastic Individual Path (SIP) Model of the Conducting Airways," *Pharm. Res.*, **29**(6), pp. 1670-1688.
- [150] Delvadia, R. R., Longest, P. W., and Byron, P. R., 2012, "In Vitro Tests for Aerosol Deposition. I: Scaling a Physical Model of the Upper Airways to Predict Drug Deposition Variation in Normal Humans," *Journal of Aerosol Medicine and Pulmonary Drug Delivery*, **25**(1), pp. 32-40.

- [151] DeHaan, W. H., and Finlay, W. H., 2001, "In Vitro Monodisperse Aerosol Deposition in a Mouth and Throat with Six Different Inhalation Devices," *Journal of Aerosol Medicine*, **14**(3), pp. 361-367.
- [152] DeHaan, W. H., and Finlay, W. H., 2004, "Predicting Extrathoracic Deposition from Dry Powder Inhalers," *J. Aerosol Sci.*, **35**(3), pp. 309-331.
- [153] Newman, S., Steed, K., Hooper, G., Källén, A., and Borgström, L., 1995, "Comparison of Gamma Scintigraphy and a Pharmacokinetic Technique for Assessing Pulmonary Deposition of Terbutaline Sulphate Delivered by Pressurized Metered Dose Inhaler," *Pharm. Res.*, **12**(2), pp. 231-236.
- [154] Hirst, P. H., Bacon, R. E., Pitcairn, G. R., Silvasti, M., and Newman, S. P., 2001, "A Comparison of the Lung Deposition of Budesonide from Easyhaler®, Turbuhaler® and pMDI Plus Spacer in Asthmatic Patients," *Respir. Med.*, **95**(9), pp. 720-727.
- [155] Biddiscombe, M. F., Melchor, R., Mak, V., Marriott, R. J., Taylor, A. J., Short, M. D., and Spiro, S. G., 1993, "The Lung Deposition of Salbutamol, Directly Labelled with Technetium-99m, Delivered by Pressurised Metered Dose and Dry Powder Inhalers," *Int. J. Pharm.*, **91**(2), pp. 111-121.
- [156] Usmani, O. S., Biddiscombe, M. F., and Barnes, P. J., 2005, "Regional Lung Deposition and Bronchodilator Response as a Function of B₂-Agonist Particle Size," *American Journal of Respiratory and Critical Care Medicine*, **172**(12), pp. 1497-1504.

- [157] Srichana, T., Suedee, R., Muanpanarai, D., and Tanmanee, N., 2005, "The Study of in Vitro–in Vivo Correlation: Pharmacokinetics and Pharmacodynamics of Albuterol Dry Powder Inhalers," *J. Pharm. Sci.*, **94**(1), pp. 220-230.
- [158] Srichana, T., Suedee, R., Tanmanee, N., Muanpanarai, D., and Marriott, C., 2007, "The Correlation of Urinary Levels of Albuterol and its Metabolites Isomers Following Inhalation from a Dry Powder Inhaler and in Vitro Particle Size Characterisation," *Pulm. Pharmacol. Ther.*, **20**(1), pp. 36-45.
- [159] Fleming, J. S., Conway, J. H., Bolt, L., and Holgate, S. T., 2003, "A Comparison of Planar Scintigraphy and SPECT Measurement of Total Lung Deposition of Inhaled Aerosol," *Journal of Aerosol Medicine*, **16**(1), pp. 9-19.
- [160] Fleming, J. S., Epps, B. P., Conway, J. H., and Martonen, T. B., 2006, "Comparison of SPECT Aerosol Deposition Data with a Human Respiratory Tract Model," *Journal of Aerosol Medicine*, **19**(3), pp. 268-278.
- [161] Fleming, J., Conway, J., Majoral, C., Katz, I., Caillibotte, G., Pichelin, M., Montesantos, S., and Bennett, M., 2015, "Controlled, Parametric, Individualized, 2-D and 3-D Imaging Measurements of Aerosol Deposition in the Respiratory Tract of Asthmatic Human Subjects for Model Validation," *Journal of Aerosol Medicine and Pulmonary Drug Delivery*, **28**(6), pp. 432-451.
- [162] Tian, G., Hindle, M., and Longest, P. W., 2014, "Targeted Lung Delivery of Nasally Administered Aerosols," *Aerosol Science and Technology*, **48**(4), pp. 434-449.

- [163] Coates, M. S., Chan, H., Fletcher, D. F., and Chiou, H., 2007, "Influence of Mouthpiece Geometry on the Aerosol Delivery Performance of a Dry Powder Inhaler," *Pharm. Res.*, **24**(8), pp. 1450-1456.
- [164] Tong, Z. B., Zheng, B., Yang, R. Y., Yu, A. B., and Chan, H., 2013, "CFD-DEM Investigation of the Dispersion Mechanisms in Commercial Dry Powder Inhalers," *Powder Technol.*, **240**pp. 19-24.
- [165] Rahimi-Gorji, M., Gorji, T. B., and Gorji-Bandpy, M., 2016, "Details of Regional Particle Deposition and Airflow Structures in a Realistic Model of Human Tracheobronchial Airways: Two-Phase Flow Simulation," *Comput. Biol. Med.*, **74**pp. 1-17.
- [166] Lambert, A. R., O'shaughnessy, P. T., Tawhai, M. H., Hoffman, E. A., and Lin, C., 2011, "Regional Deposition of Particles in an Image-Based Airway Model: Large-Eddy Simulation and Left-Right Lung Ventilation Asymmetry," *Aerosol Science and Technology*, **45**(1), pp. 11-25.
- [167] Ruzycki, C. A., Javaheri, E., and Finlay, W. H., 2013, "The use of Computational Fluid Dynamics in Inhaler Design," *Expert Opinion on Drug Delivery*, **10**(3), pp. 307-323.
- [168] Cheng, Y. S., 2014, "Mechanisms of Pharmaceutical Aerosol Deposition in the Respiratory Tract," *AAPS PharmSciTech*, **15**(3), pp. 630-640.

- [169] Hu, L., Kong, D., Hu, Q., Gao, N., and Pang, S., 2015, "Evaluation of High-Performance Curcumin Nanocrystals for Pulmonary Drug Delivery both in Vitro and in Vivo," *Nanoscale Research Letters*, **10**(1), pp. 1-9.
- [170] Mehta, H. J., Patel, V., and Sadikot, R. T., 2014, "Curcumin and Lung Cancer—a Review," *Targeted Oncology*, **9**(4), pp. 295-310.
- [171] McClure, R., Yanagisawa, D., Stec, D., Abdollahian, D., Koktysh, D., Xhillari, D., Jaeger, R., Stanwood, G., Chekmenev, E., and Tooyama, I., 2015, "Inhalable Curcumin: Offering the Potential for Translation to Imaging and Treatment of Alzheimer's Disease," *J. Alzheimer's Dis.*, **44**(1), pp. 283-295.
- [172] Wang, W., Zhu, R., Xie, Q., Li, A., Xiao, Y., Li, K., Liu, H., Cui, D., Chen, Y., and Wang, S., 2012, "Enhanced Bioavailability and Efficiency of Curcumin for the Treatment of Asthma by its Formulation in Solid Lipid Nanoparticles," *Int J Nanomedicine*, **7**pp. 3667-3677.
- [173] Lee, W., Loo, C., Young, P. M., Traini, D., Mason, R. S., and Rohanizadeh, R., 2014, "Recent Advances in Curcumin Nanoformulation for Cancer Therapy," *Expert Opinion on Drug Delivery*, **11**(8), pp. 1183-1201.
- [174] Yuan, Z., Syed, M. A., Panchal, D., Rogers, D., Joo, M., and Sadikot, R. T., 2012, "Curcumin Mediated Epigenetic Modulation Inhibits TREM-1 Expression in Response to Lipopolysaccharide," *Int. J. Biochem. Cell Biol.*, **44**(11), pp. 2032-2043.

- [175] Meja, K. K., Rajendrasozhan, S., Adenuga, D., Biswas, S. K., Sundar, I. K., Spooner, G., Marwick, J. A., Chakravarty, P., Fletcher, D., and Whittaker, P., 2008, "Curcumin Restores Corticosteroid Function in Monocytes Exposed to Oxidants by Maintaining HDAC2," *American Journal of Respiratory Cell and Molecular Biology*, **39**(3), pp. 312-323.
- [176] Biswas, S. K., McClure, D., Jimenez, L. A., Megson, I. L., and Rahman, I., 2005, "Curcumin Induces Glutathione Biosynthesis and Inhibits NF- κ B Activation and Interleukin-8 Release in Alveolar Epithelial Cells: Mechanism of Free Radical Scavenging Activity," *Antioxidants & Redox Signaling*, **7**(1-2), pp. 32-41.
- [177] Barnes, P. J., 2013, "Corticosteroid Resistance in Patients with Asthma and Chronic Obstructive Pulmonary Disease," *J. Allergy Clin. Immunol.*, **131**(3), pp. 636-645.
- [178] Helson, L., 2013, "Curcumin (Diferuloylmethane) Delivery Methods: A Review," *Biofactors*, **39**(1), pp. 21-26.
- [179] Byron, P. R., Hindle, M., Lange, C. F., Longest, P. W., McRobbie, D., Oldham, M. J., Olsson, B., Thiel, C. G., Wachtel, H., and Finlay, W. H., 2010, "In Vivo-in Vitro Correlations: Predicting Pulmonary Drug Deposition from Pharmaceutical Aerosols," *Journal of Aerosol Medicine and Pulmonary Drug Delivery*, **23 Suppl 2**(S2), pp. S59.
- [180] Olsson, B., Borgström, L., Lundbäck, H., and Svensson, M., 2013, "Validation of a General in Vitro Approach for Prediction of Total Lung Deposition in Healthy Adults for Pharmaceutical Inhalation Products," *Journal of Aerosol Medicine and Pulmonary Drug Delivery*, **26**(6), pp. 355-369.

- [181] Fadl, A., Wang, J., Zhang, Z., and Cheng, Y. S., 2007, "Effects of MDI Spray Angle on Aerosol Penetration Efficiency through an Oral Airway Cast," *J. Aerosol Sci.*, **38**(8), pp. 853-864.
- [182] Delvadia, R. R., Longest, P. W., Hindle, M., and Byron, P. R., 2013, "In Vitro Tests for Aerosol Deposition. III: Effect of Inhaler Insertion Angle on Aerosol Deposition," *Journal of Aerosol Medicine and Pulmonary Drug Delivery*, **26**(3), pp. 145-156.
- [183] Zeman, K. L., and Bennett, W. D., 2006, "Growth of the Small Airways and Alveoli from Childhood to the Adult Lung Measured by Aerosol-Derived Airway Morphometry," *J. Appl. Physiol.*, **100**(3), pp. 965-971.
- [184] Sznitman, J., Heimsch, F., Heimsch, T., Rusch, D., and Rosgen, T., 2007, "Three-Dimensional Convective Alveolar Flow Induced by Rhythmic Breathing Motion of the Pulmonary Acinus," *ASME J. Biomech. Eng.*, **129**(5), pp. 658-665.
- [185] Oakes, J. M., Hofemeier, P., Vignon-Clementel, I. E., and Sznitman, J., 2015, "Aerosols in Healthy and Emphysematous in Silico Pulmonary Acinar Rat Models," *J. Biomech.*, .
- [186] Sznitman, J., 2013, "Respiratory Microflows in the Pulmonary Acinus," *J. Biomech.*, **46**(2), pp. 284-298.
- [187] Rubenfeld, G. D., and Herridge, M. S., 2007, "Epidemiology and Outcomes of Acute Lung Injury," *CHEST Journal*, **131**(2), pp. 554-562.

- [188] Sznitman, J., Heimsch, T., Wildhaber, J. H., Tsuda, A., and Rosgen, T., 2009, "Respiratory Flow Phenomena and Gravitational Deposition in a Three-Dimensional Space-Filling Model of the Pulmonary Acinar Tree," *J. Biomech. Eng.*, **131**(3), pp. 031010.
- [189] Harding Jr, E. M., and Robinson, R. J., 2010, "Flow in a Terminal Alveolar Sac Model with Expanding Walls using Computational Fluid Dynamics," *Inhal. Toxicol.*, **22**(8), pp. 669-678.
- [190] Haefeli-Bleuer, B., and Weibel, E. R., 1988, "Morphometry of the Human Pulmonary Acinus," *Anat. Rec.*, **220**(4), pp. 401-414.
- [191] Sznitman, J., Sutter, R., Altorfer, D., Stampanoni, M., Rösger, T., and Schittny, J. C., 2010, "Visualization of Respiratory Flows from 3D Reconstructed Alveolar Airspaces using X-Ray Tomographic Microscopy," *J. Visualization*, **13**(4), pp. 337-345.
- [192] Hofemeier, P., and Sznitman, J., 2014, "Role of Alveolar Topology on Acinar Flows and Convective Mixing," *J. Biomech. Eng.*, **136**(6), pp. 061007.
- [193] Sznitman, J., Heimsch, T., Wildhaber, J. H., Tsuda, A., and Rosgen, T., 2009, "Respiratory Flow Phenomena and Gravitational Deposition in a Three-Dimensional Space-Filling Model of the Pulmonary Acinar Tree," *ASME J. Biomech. Eng.*, **131**(3), pp. 031010.
- [194] Vasilescu, D. M., Gao, Z., Saha, P. K., Yin, L., Wang, G., Haefeli-Bleuer, B., Ochs, M., Weibel, E. R., and Hoffman, E. A., 2012, "Assessment of Morphometry of Pulmonary

Acini in Mouse Lungs by Nondestructive Imaging using Multiscale Microcomputed Tomography," Proceedings of the National Academy of Sciences, **109**(42), pp. 17105-17110.

[195] Vasilescu, D. M., Klinge, C., Knudsen, L., Yin, L., Wang, G., Weibel, E. R., Ochs, M., and Hoffman, E. A., 2013, "Stereological Assessment of Mouse Lung Parenchyma Via Nondestructive, Multiscale Micro-CT Imaging Validated by Light Microscopic Histology," J. Appl. Physiol., **114**(6), pp. 716-724.

[196] Heyder, J., Blanchard, J. D., Feldman, H. A., and Brain, J. D., 1988, "Convective Mixing in Human Respiratory Tract: Estimates with Aerosol Boli," J. Appl. Physiol., **64**(3), pp. 1273-1278.

[197] Tsuda, A., Henry, F. S., and Butler, J. P., 1995, "Chaotic Mixing of Alveolated Duct Flow in Rhythmically Expanding Pulmonary Acinus," J. Appl. Physiol., **79**(3), pp. 1055-1063.

[198] Tsuda, A., Rogers, R. A., Hydon, P. E., and Butler, J. P., 2002, "Chaotic Mixing Deep in the Lung," Proceedings of the National Academy of Sciences, **99**(15), pp. 10173-10178.

[199] Haber, S., and Tsuda, A., 1998, "The Effect of Flow Generated by a Rhythmically Expanding Pulmonary Acinus on Aerosol Dynamics," J. Aerosol Sci., **29**(3), pp. 309-322.

[200] Haber, S., Yitzhak, D., and Tsuda, A., 2003, "Gravitational Deposition in a Rhythmically Expanding and Contracting Alveolus," J. Appl. Physiol., **95**(2), pp. 657-671.

[201] Henry, F. S., Butler, J. P., and Tsuda, A., 2002, "Kinematically Irreversible Acinar Flow: A Departure from Classical Dispersive Aerosol Transport Theories," *J. Appl. Physiol.*, **92**(2), pp. 835-845.

[202] Darquenne, C., and Paiva, M., 1996, "Two-and Three-Dimensional Simulations of Aerosol Transport and Deposition in Alveolar Zone of Human Lung," *J. Appl. Physiol.*, **80**(4), pp. 1401-1414.

[203] Harrington, L., Prisk, G. K., and Darquenne, C., 2006, "Importance of the Bifurcation Zone and Branch Orientation in Simulated Aerosol Deposition in the Alveolar Zone of the Human Lung," *J. Aerosol Sci.*, **37**(1), pp. 37-62.

[204] Darquenne, C., Harrington, L., and Prisk, G. K., 2009, "Alveolar Duct Expansion Greatly Enhances Aerosol Deposition: A Three-Dimensional Computational Fluid Dynamics Study," *Philosophical Transactions of the Royal Society of London A: Mathematical, Physical and Engineering Sciences*, **367**(1896), pp. 2333-2346.

[205] Darquenne, C., 2001, "A Realistic Two-Dimensional Model of Aerosol Transport and Deposition in the Alveolar Zone of the Human Lung," *J. Aerosol Sci.*, **32**(10), pp. 1161-1174.

[206] Darquenne, C., 2002, "Heterogeneity of Aerosol Deposition in a Two-Dimensional Model of Human Alveolated Ducts," *J. Aerosol Sci.*, **33**(9), pp. 1261-1278.

- [207] Sznitman, J., Schmuki, S., Sutter, R., Tsuda, A., and Rosgen, T., 2007, "CFD Investigation of Respiratory Flows in a Space-Filling Pulmonary Acinus Model," *Modelling in Medicine and Biology VII, WIT Transactions on Biomedicine and Health*, **12**pp. 147-156.
- [208] Oakes, J. M., Day, S., Weinstein, S. J., and Robinson, R. J., 2010, "Flow Field Analysis in Expanding Healthy and Emphysematous Alveolar Models using Particle Image Velocimetry." *J. Biomech. Eng.*, **132**(2), pp. 021008.
- [209] Berg, E. J., Weisman, J. L., Oldham, M. J., and Robinson, R. J., 2010, "Flow Field Analysis in a Compliant Acinus Replica Model using Particle Image Velocimetry (PIV)," *J. Biomech.*, **43**(6), pp. 1039-1047.
- [210] Hofemeier, P., and Sznitman, J., 2016, "The Role of Anisotropic Expansion for Pulmonary Acinar Aerosol Deposition," *J. Biomech.*, **49**(14), pp. 3543-3548.
- [211] Kumar, H., Tawhai, M. H., Hoffman, E. A., and Lin, C., 2011, "Steady Streaming: A Key Mixing Mechanism in Low-Reynolds-Number Acinar Flows," *Physics of Fluids (1994-Present)*, **23**(4), pp. 041902.
- [212] Kumar, H., Tawhai, M. H., Hoffman, E. A., and Lin, C., 2009, "The Effects of Geometry on Airflow in the Acinar Region of the Human Lung," *J. Biomech.*, **42**(11), pp. 1635-1642.
- [213] Ma, B., and Darquenne, C., 2011, "Aerosol Deposition Characteristics in Distal Acinar Airways Under Cyclic Breathing Conditions," *J. Appl. Physiol.*, **110**(5), pp. 1271-1282.

- [214] Fishler, R., Mulligan, M. K., and Sznitman, J., 2013, "Acinus-on-a-Chip: A Microfluidic Platform for Pulmonary Acinar Flows," *J. Biomech.*, **46**(16), pp. 2817-2823.
- [215] Tenenbaum-Katan, J., Fishler, R., Rothen-Rutishauser, B., 2015, "Microfluidic in Vitro Platforms of Pulmonary Alveolar Physiology," 6th European Conference of the International Federation for Medical and Biological Engineering, Anonymous Springer, pp. 777-780.
- [216] Fishler, R., Hofemeier, P., Etzion, Y., Dubowski, Y., and Sznitman, J., 2015, "Particle Dynamics and Deposition in True-Scale Pulmonary Acinar Models," *Scientific Reports*, **5**.
- [217] Fishler, R., Ostrovski, Y., Lu, C., and Sznitman, J., 2016, "Streamline Crossing: An Essential Mechanism for Aerosol Dispersion in the Pulmonary Acinus," *J. Biomech.*, .
- [218] Chantal Darquenne, Mark D Hoover, and Robert F Phalen, 2016, "Inhaled Aerosol Dosimetry: Some Current Research Needs," *Journal of Aerosol Science*, **99**pp. 1-5.
- [219] Chantal Darquenne, Mark D Hoover, and Robert F Phalen, 2016, "Inhaled Aerosol Dosimetry: Some Current Research Needs," *Journal of Aerosol Science*, **99**pp. 1-5.
- [220] Tsuda, A., Henry, F. S., and Butler, J. P., 2013, "Particle Transport and Deposition: Basic Physics of Particle Kinetics," *Comprehensive Physiology*, **3**(4), pp. 1437.
- [221] Haber, S., Yitzhak, D., and Tsuda, A., 2003, "Gravitational Deposition in a Rhythmically Expanding and Contracting Alveolus," *J. Appl. Physiol.*, **95**(2), pp. 657-671.

[222] Khajeh-Hosseini-Dalasm, N., and Longest, P. W., 2015, "Deposition of Particles in the Alveolar Airways: Inhalation and Breath-Hold with Pharmaceutical Aerosols," *J. Aerosol Sci.*, **79**pp. 15-30.

[223] Weibel, E. R., 2009, "What Makes a Good Lung," *Swiss Med. Wkly.*, **139**(27-28), pp. 375-386.

[224] Kolanjiyil, A. V., 2013, "Deposited Nanomaterial Mass Transfer from Lung Airways to Systemic Regions," North Carolina State University.

[225] Heyder, J., Armbruster, L., Gebhart, J., Grein, E., and Stahlhofen, W., 1975, "Total Deposition of Aerosol Particles in the Human Respiratory Tract for Nose and Mouth Breathing," *J. Aerosol Sci.*, **6**(5), pp. 311-328.

Appendix

The following pages present the copyright permissions to reprint text and/or figures within this work.

Permission for Figure 1.2

12/8/2016

RightsLink Printable License

ELSEVIER LICENSE TERMS AND CONDITIONS

Dec 08, 2016

This Agreement between Arun V Kolanjiyil (you) and Elsevier ("Elsevier") consists of your license details and the terms and conditions provided by Elsevier and Copyright Clearance Center

License Number	4004351227499
License date	Dec 08, 2016
Licensed Content Publisher	Elsevier
Licensed Content Publication	Toxicology in Vitro
Licensed Content Title	Potential of coculture in vitro models to study inflammatory and sensitizing effects of particles on the lung
Licensed Content Author	Sebastian G. Klein, Jenny Hennen, Tommaso Serchi, Brunhilde Blömeke, Arno C. Gutleb
Licensed Content Date	December 2011
Licensed Content Volume Number	25
Licensed Content Issue Number	8
Licensed Content Pages	19
Start Page	1516
End Page	1534
Type of Use	reuse in a thesis/dissertation
Portion	figures/tables/illustrations
Number of figures/tables/illustrations	1
Format	both print and electronic
Are you the author of this Elsevier article?	No
Will you be translating?	No
Order reference number	
Original figure numbers	Figure 1
Title of your thesis/dissertation	Whole-Lung Airflow and Particle Transport/Deposition Modeling
Expected completion date	Jan 2017
Estimated size (number of pages)	200
Elsevier VAT number	GB 494 6272 12
Requestor Location	Arun V Kolanjiyil 911 Oval Dr 3rd floor EB III Depart. of Mechanical and Aerospace Eng RALEIGH, NC 27695 United States Attn: Arun V Kolanjiyil
Total	0.00 USD

<https://s100.copyright.com/AppDispatchServlet>

1/8

INTRODUCTION

1. The publisher for this copyrighted material is Elsevier. By clicking "accept" in connection with completing this licensing transaction, you agree that the following terms and conditions apply to this transaction (along with the Billing and Payment terms and conditions established by Copyright Clearance Center Inc. ("CCC"), at the time that you opened your Rightslink account and that are available at any time <http://myaccount.copyright.com>

GENERAL TERMS

2. Elsevier hereby grants you permission to reproduce the aforementioned material subject to the terms and conditions indicated.
3. Acknowledgement: If any part of the material to be used (for example, figures) has appeared in our publication with credit or acknowledgement to another source, permission must also be sought from that source. If such permission is not obtained then that material may not be included in your publication/copies. Suitable acknowledgement to the source must be made, either as a footnote or in a reference list at the end of your publication, as follows:
 "Reprinted from Publication title [Vedition number] Author(s), Title of article / title of chapter Pages No., Copyright (Year), with permission from Elsevier [OR APPLICABLE SOCIETY COPYRIGHT OWNER]." Also Lancet special credit - "Reprinted from The Lancet, Number Author(s), Title of article, Pages No., Copyright (Year), with permission from Elsevier
4. Reproduction of this material is confined to the purpose and/or media for which permission is hereby given.
5. Altering/Modifying Material: Not Permitted. However figures and illustrations may be altered/adapted minimally to serve your work. Any other abbreviations, additions, deletions and/or any other alterations shall be made only with prior written authorization of Elsevier Ltd. (Please contact Elsevier at permissions@elsevier.com). No modifications can be made to any Lancet figures/tables and they must be reproduced in full.
6. If the permission fee for the requested use of our material is waived in this instance, please be advised that your future requests for Elsevier materials may attract a fee.
7. Reservation of Rights: Publisher reserves all rights not specifically granted in the combination of (i) the license details provided by you and accepted in the course of this licensing transaction, (ii) these terms and conditions and (iii) CCC's Billing and Payment terms and conditions.
8. License Contingent Upon Payment: While you may exercise the rights licensed immediately upon issuance of the license at the end of the licensing process for the transaction, provided that you have disclosed complete and accurate details of your proposed use, no license is final unless and until full payment is received from you (either by publisher or by CCC) as provided in CCC's Billing and Payment terms and conditions. If full payment is not received on a timely basis, then any license preliminarily granted shall be deemed automatically revoked and shall be void as if never granted. Further in the event that you breach any of these terms and conditions or any of CCC's Billing and Payment terms and conditions, the license is automatically revoked and shall be void as if never granted. Use of materials as described in a revoked license, as well as any use of the materials beyond the scope of an unrevoked license, may constitute copyright infringement and publisher reserves the right to take any and all action to protect its copyright in the materials.
9. Warranties: Publisher makes no representations or warranties with respect to the licensed material.
10. Indemnity: We hereby indemnify and agree to hold harmless publisher and CCC, and their respective officers, directors, employees and agents, from and against any and all claims arising out of your use of the licensed material other than as specifically authorized pursuant to this license.

11. **No Transfer of License:** This license is personal to you and may not be sublicensed, assigned, or transferred by you to any other person without publisher's written permission.
12. **No Amendment Except in Writing:** This license may not be amended except in a writing signed by both parties (or in the case of publisher CCC on publisher's behalf).
13. **Objection to Contrary Terms:** Publisher hereby objects to any terms contained in any purchase order, acknowledgment, check endorsement or other writing prepared by you, which terms are inconsistent with these terms and conditions or CCC's Billing and Payment terms and conditions. These terms and conditions, together with CCC's Billing and Payment terms and conditions (which are incorporated herein), comprise the entire agreement between you and publisher (and CCC) concerning this licensing transaction. In the event of any conflict between your obligations established by these terms and conditions and those established by CCC's Billing and Payment terms and conditions, these terms and conditions shall control.
14. **Revocation:** Elsevier or Copyright Clearance Center may deny the permissions described in this License at their sole discretion, for any reason or no reason, with a full refund payable to you. Notice of such denial will be made using the contact information provided by you. Failure to receive such notice will not alter or invalidate the denial. In no event will Elsevier or Copyright Clearance Center be responsible or liable for any costs, expenses or damage incurred by you as a result of a denial of your permission request, other than a refund of the amount(s) paid by you to Elsevier and/or Copyright Clearance Center for denied permissions.

LIMITED LICENSE

The following terms and conditions apply only to specific license types:

15. **Translation:** This permission is granted for non-exclusive ~~worldwide~~ **English** rights only unless your license was granted for translation rights. If you licensed translation rights you may only translate this content into the languages you requested. A professional translator must perform all translations and reproduce the content word for word preserving the integrity of the article.
16. **Posting licensed content on any Website:** The following terms and conditions apply as follows: Licensing material from an Elsevier journal: All content posted to the web site must maintain the copyright information line on the bottom of each image; A ~~hyper~~ **hyper** must be included to the Homepage of the journal from which you are licensing at <http://www.sciencedirect.com/science/journal/xxxx> or the Elsevier homepage for books at <http://www.elsevier.com>. Central Storage: This license does not include permission for a scanned version of the material to be stored in a central repository such as that provided by Heron/XanEdu. Licensing material from an Elsevier book: A ~~hyper~~ **hyper** link must be included to the Elsevier homepage at <http://www.elsevier.com>. All content posted to the web site must maintain the copyright information line on the bottom of each image.

Posting licensed content on Electronic reserve: In addition to the above the following clauses are applicable: The web site must be password-protected and made available only to bona fide students registered on a relevant course. This permission is granted for 1 year ~~only~~ **only** may obtain a new license for future website posting.

17. **For journal author** the following clauses are applicable in addition to the above:

Preprints:

A preprint is an author's own write-up of research results and analysis, it has not been peer reviewed, nor has it had any other value added to it by a publisher (such as formatting, copyright, technical enhancement etc.).

Authors can share their preprints anywhere at any time. Preprints should not be added to or enhanced in any way in order to appear more like, or to substitute ~~for~~ **for** final versions of articles

however authors can update their preprints on arXiv or RePEc with their Accepted Author Manuscript (see below).

If accepted for publication, we encourage authors to link from the preprint to their formal publication via its DOI. Millions of researchers have access to the formal publications on ScienceDirect, and so links will help users to find, access, cite and use the best available version. Please note that Cell Press, The Lancet and some society-owned have different preprint policies. Information on these policies is available on the journal homepage.

Accepted Author Manuscripts: An accepted author manuscript is the manuscript of an article that has been accepted for publication and which typically includes author incorporated changes suggested during submission, peer review and editor/author communications.

Authors can share their accepted author manuscript:

- immediately
 - o via their non-commercial person homepage or blog
 - o by updating a preprint in arXiv or RePEc with the accepted manuscript
 - o via their research institute or institutional repository for internal institutional uses or as part of an invitation-only research collaboration work-group
 - o directly by providing copies to their students or to research collaborators for their personal use
 - o for private scholarly sharing as part of an invitation-only work group on commercial sites with which Elsevier has an agreement
- after the embargo period
 - o via non-commercial hosting platforms such as their institutional repository
 - o via commercial sites with which Elsevier has an agreement

In all cases accepted manuscripts should:

- link to the formal publication via its DOI
- bear a CC-BY-NC-ND license - this is easy to do
- if aggregated with other manuscripts, for example in a repository or other site, be shared in alignment with our hosting policy not be added to or enhanced in any way to appear more like, or to substitute for the published journal article.

Published journal article (PJA): A published journal article (PJA) is the definitive final record of published research that appears or will appear in the journal and embodies all value-adding publishing activities including peer review co-ordination, copy-editing, formatting, (if relevant) pagination and online enrichment.

Policies for sharing publishing journal articles for subscription and gold open access articles:

Subscription Articles: If you are an author please share a link to your article rather than the full-text. Millions of researchers have access to the formal publications on ScienceDirect, and so links will help your users to find, access, cite, and use the best available version.

Theses and dissertations which contain embedded PJAs as part of the formal submission can be posted publicly by the awarding institution with DOI links back to the formal publications on ScienceDirect.

If you are affiliated with a library that subscribes to ScienceDirect you have additional private sharing rights for others' research accessed under that agreement. This includes use for classroom teaching and internal training at the institution (including use in course packs and courseware programs), and inclusion of the article for grant funding purposes.

Gold Open Access Articles: May be shared according to the author selected end-user license and should contain [CrossMark logo](#) the end user license, and a DOI link to the formal publication on ScienceDirect.

Please refer to Elsevier's [posting policy](#) for further information.

18. **For book authors** the following clauses are applicable in addition to the above. Authors are permitted to place a brief summary of their work online **only** are not allowed to download and post the published electronic version of your chapter **nor** may you scan the printed edition to create an electronic version.

Posting to a repository: Authors are permitted to post a summary of their chapter only in their institution's repository

19. **Thesis/Dissertation:** If your license is for use in a thesis/dissertation your thesis may be submitted to your institution in either print or electronic form. Should your thesis be published commercially please reapply for permission. These requirements include permission for the Library and Archives of Canada to supply single copies, on demand, of the complete thesis and include permission for Proquest/UMI to supply single copies, on demand, of the complete thesis. Should your thesis be published commercially please reapply for permission. Theses and dissertations which contain embedded PJAs as part of the formal submission can be posted publicly by the awarding institution with DOI links back to the formal publications on ScienceDirect.

Elsevier Open Access Terms and Conditions

You can publish open access with Elsevier in hundreds of open access journals or in nearly 2000 established subscription journals that support open access publishing. Permitted third party re-use of these open access articles is defined by the author's choice of Creative Commons user license. See our [open access license policy](#) for more information.

Terms & Conditions applicable to all Open Access articles published with Elsevier:

Any reuse of the article must not represent the author as endorsing the adaptation of the article nor should the article be modified in such a way as to damage the author's honour or reputation. If any changes have been made, such changes must be clearly indicated.

The author(s) must be appropriately credited and we ask that you include the end user license and a DOI link to the formal publication on ScienceDirect.

If any part of the material to be used (for example, figures) has appeared in our publication with credit or acknowledgement to another source it is the responsibility of the user to ensure their reuse complies with the terms and conditions determined by the rights holder

Additional Terms & Conditions applicable to each Creative Commons user license:

CC BY: The CC-BY license allows users to copy to create extracts, abstracts and new works from the Article, to alter and revise the Article and to make commercial use of the Article (including reuse and/or resale of the Article by commercial entities), provided the user gives appropriate credit (with a link to the formal publication through the relevant DOI), provides a link to the license, indicates if changes were made and the licensor is not represented as endorsing the use made of the work. The full details of the license are available <http://creativecommons.org/licenses/by/4.0>

CC BY NC SA: The CC BY-NC-SA license allows users to copy to create extracts, abstracts and new works from the Article, to alter and revise the Article, provided this is not done for commercial purposes, and that the user gives appropriate credit (with a link to the formal publication through the relevant DOI), provides a link to the license, indicates if changes were made and the licensor is not represented as endorsing the use made of the work. Further new works must be made available on the same conditions. The full details of the license are available at <http://creativecommons.org/licenses/by-nc-sa/4.0>

CC BY NC ND: The CC BY-NC-ND license allows users to copy and distribute the Article, provided this is not done for commercial purposes and further does not permit distribution of the

Article if it is changed or edited in any way and provided the user gives appropriate credit (with a link to the formal publication through the relevant DOI), provides a link to the license, and that the licensor is not represented as endorsing the use made of the work. The full details of the license are available at <http://creativecommons.org/licenses/by-nc-nd/4.0>. Any commercial reuse of Open Access articles published with a CC BY NC SA or CC BY NC ND license requires permission from Elsevier and will be subject to a fee.

Commercial reuse includes:

- Associating advertising with the full text of the Article
- Charging fees for document delivery or access
- Article aggregation
- Systematic distribution via e-mail lists or share buttons

Posting or linking by commercial companies for use by customers of those companies.

20. Other Conditions

v1.9

Questions? customercare@copyright.com or +1-855-239-3415 (toll free in the US) or +1-978-646-2777.

Permission for Chapter 3.1

1/3/2017

RightsLink Printable License

ELSEVIER LICENSE TERMS AND CONDITIONS

Jan 03, 2017

This Agreement between Arun V Kolanjiyil (你) and Elsevier ("Elsevier") consists of your license details and the terms and conditions provided by Elsevier and Copyright Clearance Center

License Number	4021160351953
License date	Jan 03, 2017
Licensed Content Publisher	Elsevier
Licensed Content Publication	Computers in Biology and Medicine
Licensed Content Title	Computationally efficient analysis of particle transport and deposition in a human whole-lung-airway model. Part I: Theory and model validation
Licensed Content Author	Arun V. Kolanjiyil, Clement Kleinstreuer
Licensed Content Date	1 December 2016
Licensed Content Volume Number	79
Licensed Content Issue Number	n/a
Licensed Content Pages	12
Start Page	193
End Page	204
Type of Use	reuse in a thesis/dissertation
Intended publisher of new work	other
Portion	full article
Format	electronic
Are you the author of this Elsevier article?	Yes
Will you be translating?	No
Order reference number	
Title of your thesis/dissertation	Whole-Lung Airflow and Particle Transport/Deposition Modeling
Expected completion date	Jan 2017
Estimated size (number of pages)	200
Elsevier VAT number	GB 494 6272 12
Requestor Location	Arun V Kolanjiyil 911 Oval Dr 3rd floor EB III Depart. of Mechanical and Aerospace Eng RALEIGH, NC 27695 United States Attn: Arun V Kolanjiyil
Total	0.00 USD
Terms and Conditions	

<https://s100.copyright.com/AppDispatchServlet>

1/8

INTRODUCTION

1. The publisher for this copyrighted material is Elsevier. By clicking "accept" in connection with completing this licensing transaction, you agree that the following terms and conditions apply to this transaction (along with the Billing and Payment terms and conditions established by Copyright Clearance Center Inc. ("CCC"), at the time that you opened your Rightslink account and that are available at any time <http://myaccount.copyright.com>

GENERAL TERMS

2. Elsevier hereby grants you permission to reproduce the aforementioned material subject to the terms and conditions indicated.
3. Acknowledgement: If any part of the material to be used (for example, figures) has appeared in our publication with credit or acknowledgement to another source, permission must also be sought from that source. If such permission is not obtained then that material may not be included in your publication/copies. Suitable acknowledgement to the source must be made, either as a footnote or in a reference list at the end of your publication, as follows:
 "Reprinted from Publication title/Section number Author(s), Title of article / title of chapter Pages No., Copyright (Year), with permission from Elsevier [OR APPLICABLE SOCIETY COPYRIGHT OWNER]." Also Lancet special credit - "Reprinted from The Lancet, Number Author(s), Title of article, Pages No., Copyright (Year), with permission from Elsevier
4. Reproduction of this material is confined to the purpose and/or media for which permission is hereby given.
5. Altering/Modifying Material: Not Permitted. However figures and illustrations may be altered/adapted minimally to serve your work. Any other abbreviations, additions, deletions and/or any other alterations shall be made only with prior written authorization of Elsevier Ltd. (Please contact Elsevier at permissions@elsevier.com). No modifications can be made to any Lancet figures/tables and they must be reproduced in full.
6. If the permission fee for the requested use of our material is waived in this instance, please be advised that your future requests for Elsevier materials may attract a fee.
7. Reservation of Rights: Publisher reserves all rights not specifically granted in the combination of (i) the license details provided by you and accepted in the course of this licensing transaction, (ii) these terms and conditions and (iii) CCC's Billing and Payment terms and conditions.
8. License Contingent Upon Payment: While you may exercise the rights licensed immediately upon issuance of the license at the end of the licensing process for the transaction, provided that you have disclosed complete and accurate details of your proposed use, no license is final until full payment is received from you (either by publisher or by CCC) as provided in CCC's Billing and Payment terms and conditions. If full payment is not received on a timely basis, then any license preliminarily granted shall be deemed automatically revoked and shall be void as if never granted. Further in the event that you breach any of these terms and conditions or any of CCC's Billing and Payment terms and conditions, the license is automatically revoked and shall be void as if never granted. Use of materials as described in a revoked license, as well as any use of the materials beyond the scope of an unrevoked license, may constitute copyright infringement and publisher reserves the right to take any and all action to protect its copyright in the materials.
9. Warranties: Publisher makes no representations or warranties with respect to the licensed material.
10. Indemnity: You hereby indemnify and agree to hold harmless publisher and CCC, and their respective officers, directors, employees and agents, from and against any and all claims arising out of your use of the licensed material other than as specifically authorized pursuant to this license.
11. No Transfer of License: This license is personal to you and may not be sublicensed, assigned, or transferred by you to any other person without publisher's written permission.

12. **No Amendment Except in Writing:** This license may not be amended except in a writing signed by both parties (or in the case of publication by CCC on publisher's behalf).

13. **Objection to Contrary Terms:** Publisher hereby objects to any terms contained in any purchase order, acknowledgment, check endorsement or other writing prepared by you, which terms are inconsistent with these terms and conditions or CCC's Billing and Payment terms and conditions. These terms and conditions, together with CCC's Billing and Payment terms and conditions (which are incorporated herein), comprise the entire agreement between you and publisher (and CCC) concerning this licensing transaction. In the event of any conflict between your obligations established by these terms and conditions and those established by CCC's Billing and Payment terms and conditions, these terms and conditions shall control.

14. **Revocation:** Elsevier or Copyright Clearance Center may deny the permissions described in this License at their sole discretion, for any reason or no reason, with a full refund payable to you.

Notice of such denial will be made using the contact information provided by you. Failure to receive such notice will not alter or invalidate the denial. In no event will Elsevier or Copyright Clearance Center be responsible or liable for any costs, expenses or damage incurred by you as a result of a denial of your permission request, other than a refund of the amount(s) paid by you to Elsevier and/or Copyright Clearance Center for denied permissions.

LIMITED LICENSE

The following terms and conditions apply only to specific license types:

15. **Translation** This permission is granted for non-exclusive ~~worldwide~~ **English** rights only unless your license was granted for translation rights. If you licensed translation rights you may only translate this content into the languages you requested. A professional translator must perform all translations and reproduce the content word for word preserving the integrity of the article.

16. **Posting licensed content on any Website:** The following terms and conditions apply as follows: Licensing material from an Elsevier journal: All content posted to the web site must maintain the copyright information line on the bottom of each image; A ~~hyper~~ **hyper** must be included to the Homepage of the journal from which you are licensing at <http://www.sciencedirect.com/science/journal/xxxx> or the Elsevier homepage for books at <http://www.elsevier.com>; Central Storage: This license does not include permission for a scanned version of the material to be stored in a central repository such as that provided by Heron/XanEdu. Licensing material from an Elsevier book: A ~~hyper~~ **hyper** link must be included to the Elsevier homepage at <http://www.elsevier.com>. All content posted to the web site must maintain the copyright information line on the bottom of each image.

Posting licensed content on Electronic reserve: In addition to the above the following clauses are applicable: The web site must be password-protected and made available only to bona fide students registered on a relevant course. This permission is granted for 1 year ~~only~~ **only** may obtain a new license for future website posting.

17. **For journal authors** the following clauses are applicable in addition to the above:

Preprints:

A preprint is an author's own write-up of research results and analysis, it has not been peer reviewed, nor has it had any other value added to it by a publisher (such as formatting, copyright, technical enhancement etc.).

Authors can share their preprints anywhere at any time. Preprints should not be added to or enhanced in any way in order to appear more like, or to substitute ~~for~~ **for** the final versions of articles however authors can update their preprints on arXiv or RePEc with their Accepted Author Manuscript (see below).

If accepted for publication, we encourage authors to link from the preprint to their formal publication via its DOI. Millions of researchers have access to the formal publications on ScienceDirect, and so links will help users to find, access, cite and use the best available version. Please note that Cell Press, The Lancet and some society-owned have different preprint policies. Information on these policies is available on the journal homepage.

Accepted Author Manuscripts An accepted author manuscript is the manuscript of an article that has been accepted for publication and which typically includes author incorporated changes suggested during submission, peer review and editor/author communications.

Authors can share their accepted author manuscript:

- immediately
 - o via their non-commercial person homepage or blog
 - o by updating a preprint in arXiv or RePEc with the accepted manuscript
 - o via their research institute or institutional repository for internal institutional uses or as part of an invitation-only research collaboration work-group
 - o directly by providing copies to their students or to research collaborators for their personal use
 - o for private scholarly sharing as part of an invitation-only work group on commercial sites with which Elsevier has an agreement
- after the embargo period
 - o via non-commercial hosting platforms such as their institutional repository
 - o via commercial sites with which Elsevier has an agreement

In all cases accepted manuscripts should:

- link to the formal publication via its DOI
- bear a CC-BY-NC-ND license - this is easy to do
- if aggregated with other manuscripts, for example in a repository or other site, be shared in alignment with our hosting policy not be added to or enhanced in any way to appear more like, or to substitute for the published journal article.

Published journal article (PJA): A published journal article (PJA) is the definitive final record of published research that appears or will appear in the journal and embodies all value-adding publishing activities including peer review co-ordination, copy-editing, formatting, (if relevant) pagination and online enrichment.

Policies for sharing publishing journal articles differ for subscription and gold open access articles:

Subscription Articles: If you are an author please share a link to your article rather than the full-text. Millions of researchers have access to the formal publications on ScienceDirect, and so links will help your users to find, access, cite, and use the best available version.

Theses and dissertations which contain embedded PJAs as part of the formal submission can be posted publicly by the awarding institution with DOI links back to the formal publications on ScienceDirect.

If you are affiliated with a library that subscribes to ScienceDirect you have additional private sharing rights for others' research accessed under that agreement. This includes use for classroom teaching and internal training at the institution (including use in course packs and courseware programs), and inclusion of the article for grant funding purposes.

Gold Open Access Articles: May be shared according to the author selected end-user license and should contain [CrossMark logo](#) the end user license, and a DOI link to the formal publication on ScienceDirect.

post the published electronic version of your chapter or may you scan the printed edition to create an electronic version
Posting to a repository: Authors are permitted to post a summary of their chapter only in their institution's repository

19. Thesis/Dissertation: If your license is for use in a thesis/dissertation your thesis may be submitted to your institution in either print or electronic form. Should your thesis be published commercially please reapply for permission. These requirements include permission for the Library and Archives of Canada to supply single copies, on demand, of the complete thesis and include permission for Proquest/UMI to supply single copies, on demand, of the complete thesis. Should your thesis be published commercially please reapply for permission. Theses and dissertations which contain embedded PJAs as part of the formal submission can be posted publicly by the awarding institution with DOI links back to the formal publications on ScienceDirect.

Elsevier Open Access Terms and Conditions

You can publish open access with Elsevier in hundreds of open access journals or in nearly 2000 established subscription journals that support open access publishing. Permitted third party re-use of these open access articles is defined by the author's choice of Creative Commons user license. See our [open access license policy](#) for more information.

Terms & Conditions applicable to all Open Access articles published with Elsevier:

Any reuse of the article must not represent the author as endorsing the adaptation of the article nor should the article be modified in such a way as to damage the author's honour or reputation. If any changes have been made, such changes must be clearly indicated.

The author(s) must be appropriately credited and we ask that you include the end user license and a DOI link to the formal publication on ScienceDirect.

If any part of the material to be used (for example, figures) has appeared in our publication with credit or acknowledgement to another source it is the responsibility of the user to ensure their reuse complies with the terms and conditions determined by the rights holder

Additional Terms & Conditions applicable to each Creative Commons user license:

CC BY: The CC-BY license allows users to copy to create extracts, abstracts and new works from the Article, to alter and revise the Article and to make commercial use of the Article (including reuse and/or resale of the Article by commercial entities), provided the user gives appropriate credit (with a link to the formal publication through the relevant DOI), provides a link to the license, indicates if changes were made and the licensor is not represented as endorsing the use made of the work. The full details of the license are available at <http://creativecommons.org/licenses/by/4.0>

CC BY NC SA: The CC BYNC-SA license allows users to copy to create extracts, abstracts and new works from the Article, to alter and revise the Article, provided this is not done for commercial purposes, and that the user gives appropriate credit (with a link to the formal publication through the relevant DOI), provides a link to the license, indicates if changes were made and the licensor is not represented as endorsing the use made of the work. Further new works must be made available on the same conditions. The full details of the license are available at <http://creativecommons.org/licenses/by-nc-sa/4.0>

CC BY NC ND: The CC BYNC-ND license allows users to copy and distribute the Article, provided this is not done for commercial purposes and further does not permit distribution of the Article if it is changed or edited in any way and provided the user gives appropriate credit (with a link to the formal publication through the relevant DOI), provides a link to the license, and that the licensor is not represented as endorsing the use made of the work. The full details of the license are

available at <http://creativecommons.org/licenses/by-nc-nd/4.0> Any commercial reuse of Open Access articles published with a CC BY NC SA or CC BY NC ND license requires permission from Elsevier and will be subject to a fee.

Commercial reuse includes:

- Associating advertising with the full text of the Article
- Charging fees for document delivery or access
- Article aggregation
- Systematic distribution via e-mail lists or share buttons

Posting or linking by commercial companies for use by customers of those companies.

20. Other Conditions

v1.9

Questions? customercare@copyright.com or +1-855-239-3415 (toll free in the US) or +1-978-646-2777.

Permission for Figure 3.2.1

1/3/2017

RightsLink Printable License

SPRINGER LICENSE TERMS AND CONDITIONS

Jan 03, 2017

This Agreement between Arun V Kolanjiyil (NY) and Springer ("Springer") consists of your license details and the terms and conditions provided by Springer and Copyright Clearance Center

License Number	4021160134424
License date	Jan 03, 2017
Licensed Content Publisher	Springer
Licensed Content Publication	Drugs
Licensed Content Title	Novolizer®
Licensed Content Author	Caroline Fenton
Licensed Content Date	Jan 1, 2003
Licensed Content Volume Number	63
Licensed Content Issue Number	22
Type of Use	Thesis/Dissertation
Portion	Figures/tables/illustrations
Number of figures/tables/illustrations	1
Author of this Springer article	No
Order reference number	
Original figure numbers	figure 1
Title of your thesis / dissertation	Whole-Lung Airflow and Particle Transport/Deposition Modeling
Expected completion date	Jan 2017
Estimated size(pages)	200
Requestor Location	Arun V Kolanjiyil 911 Oval Dr 3rd floor EB III Depart. of Mechanical and Aerospace Eng RALEIGH, NC 27695 United States Attn: Arun V Kolanjiyil
Billing Type	Invoice
Billing Address	Arun V Kolanjiyil 911 Oval Dr 3rd floor EB III Depart. of Mechanical and Aerospace Eng RALEIGH, NC 27695 United States Attn: Arun V Kolanjiyil
Total	0.00 USD
Terms and Conditions	

<https://s100.copyright.com/AppDispatchServlet>

1/4

Introduction

The publisher for this copyrighted material is Springer. By clicking "accept" in connection with completing this licensing transaction, you agree that the following terms and conditions apply to this transaction (along with the Billing and Payment terms and conditions established by Copyright Clearance Center Inc. ("CCC"), at the time that you opened your Rightslink account and that are available at any time <http://myaccount.copyright.com>

Limited License

With reference to your request to reuse material on which Springer controls the copyright, permission is granted for the use indicated in your enquiry under the following conditions:

- Licenses are for one-time use only with a maximum distribution equal to the number stated in your request.
- Springer material represents original material which does not carry references to other sources. If the material in question appears with a credit to another source, this permission is not valid and authorization has to be obtained from the original copyright holder
- This permission
 - is non-exclusive
 - is only valid if no personal rights, trademarks, or competitive products are infringed.
 - explicitly excludes the right for derivatives.
- Springer does not supply original artwork or content.
- According to the format which you have selected, the following conditions apply accordingly:
 - **Print and Electronic:** This License include use in electronic form provided it is password protected, on intranet, or CD-Rom/DVD or E-book/E-journal. It may not be republished in electronic open access.
 - **Print:** This License excludes use in electronic form.
 - **Electronic:** This License only pertains to use in electronic form provided it is password protected, on intranet, or CD-Rom/DVD or E-book/E-journal. It may not be republished in electronic open access.

For any electronic use not mentioned, please contact Springer at permissions.springer@spi-global.com.

- Although Springer controls the copyright to the material and is entitled to negotiate on rights, this license is only valid subject to courtesy information to the author (address is given in the article/chapter).
- If you are an STM Signatory or your work will be published by an STM Signatory and you are requesting to reuse figures/tables/illustrations or single text extracts, permission is granted according to STM Permissions Guideline <http://www.stm-assoc.org/permissions-guidelines/>

For any electronic use not mentioned in the Guidelines, please contact Springer at permissions.springer@spi-global.com if you request to reuse more content than stipulated in the STM Permissions Guidelines, you will be charged a permission fee for the excess content.

Permission is valid upon payment of the fee as indicated in the licensing process. If permission is granted free of charge on this occasion, that does not prejudice any rights we might have together for reproduction of our copyrighted material in the future.

-If your request is for reuse in a Thesis, permission is granted free of charge under the following conditions:

This license is valid for one-time use only for the purpose of defending your thesis and with a maximum of 100 extra copies in paper if the thesis is going to be published, permission needs to be reobtained.

- includes use in an electronic form, provided it is an authorized version of the thesis on his/her own website and his/her university repository including UMI (according to the definition on the

Sherpa website: <http://www.sherpa.ac.uk/romeo/>;

- is subject to courtesy information to the co-author or corresponding author

Geographic Rights: Scope

Licenses may be exercised anywhere in the world.

Altering/Modifying Material: Not Permitted

Figures, tables, and illustrations may be altered minimally to serve your work. You may not alter or modify text in any manner. Abbreviations, additions, deletions and/or any other alterations shall be made only with prior written authorization of the author(s).

Reservation of Rights

Springer reserves all rights not specifically granted in the combination of (i) the license details provided by you and accepted in the course of this licensing transaction and (ii) these terms and conditions and (iii) CCC's Billing and Payment terms and conditions.

License Contingent on Payment

While you may exercise the rights licensed immediately upon issuance of the license at the end of the licensing process for the transaction, provided that you have disclosed complete and accurate details of your proposed use, no license is finally effective unless and until full payment is received from you (either by Springer or by CCC) as provided in CCC's Billing and Payment terms and conditions. If full payment is not received by the date due, then any license preliminarily granted shall be deemed automatically revoked and shall be void as if never granted. Further, in the event that you breach any of these terms and conditions or any of CCC's Billing and Payment terms and conditions, the license is automatically revoked and shall be void as if never granted. Further, the use of materials as described in a revoked license, as well as any use of the materials beyond the scope of an unrevoked license, may constitute copyright infringement and Springer reserves the right to take any and all action to protect its copyright in the materials.

Copyright Notice: Disclaimer

You must include the following copyright and permission notice in connection with any reproduction of the licensed material:

"Springer book/journal title, chapter/article title, volume, year of publication, page, name(s) of author(s), (original copyright notice as given in the publication in which the material was originally published) "With permission of Springer"

In case of use of a graph or illustration, the caption of the graph or illustration must be included, as it is indicated in the original publication.

Warranties: None

Springer makes no representations or warranties with respect to the licensed material and adopts on its own behalf the limitations and disclaimers established by CCC on its behalf in its Billing and Payment terms and conditions for this licensing transaction.

Indemnity

You hereby indemnify and agree to hold harmless Springer and CCC, and their respective officers, directors, employees and agents, from and against any and all claims arising out of your use of the licensed material other than as specifically authorized pursuant to this license.

No Transfer of License

This license is personal to you and may not be sublicensed, assigned, or transferred by you without Springer's written permission.

No Amendment Except in Writing

This license may not be amended except in a writing signed by both parties in the case of Springer by CCC on Springer's behalf.

Objection to Contrary Terms

Springer hereby objects to any terms contained in any purchase order. In acknowledgment, check

endorsement or other writing prepared by you, which terms are inconsistent with these terms and conditions or CCC's Billing and Payment terms and conditions. These terms and conditions, together with CCC's Billing and Payment terms and conditions (which are incorporated herein), comprise the entire agreement between you and Springer (and CCC) concerning this licensing transaction. In the event of any conflict between your obligations established by these terms and conditions and those established by CCC's Billing and Payment terms and conditions, these terms and conditions shall control.

Jurisdiction

All disputes that may arise in connection with this present License, or the breach thereof, shall be settled exclusively by arbitration, to be held in the Federal Republic of Germany in accordance with German law

Other conditions:

V 12AUG2015

Questions? customercare@copyright.com or +1-855-239-3415 (toll free in the US) or +1-978-646-2777.

Permission for Chapter 3.2

ELSEVIER LICENSE TERMS AND CONDITIONS

Jan 06, 2017

This Agreement between Arun V Kolanjiyil ("You") and Elsevier ("Elsevier") consists of your license details and the terms and conditions provided by Elsevier and Copyright Clearance Center.

License Number	4023150628451
License date	Jan 03, 2017
Licensed Content Publisher	Elsevier
Licensed Content Publication	Computers in Biology and Medicine
Licensed Content Title	Computationally efficient analysis of particle transport and deposition in a human whole-lung-airway model. Part II: Dry powder inhaler application
Licensed Content Author	Arun V. Kolanjiyil,Clement Kleinstreuer,Ruxana T. Sadikot
Licensed Content Date	Available online 3 November 2016
Licensed Content Volume Number	n/a
Licensed Content Issue Number	n/a
Licensed Content Pages	1
Start Page	
End Page	
Type of Use	reuse in a thesis/dissertation
Portion	full article
Format	electronic
Are you the author of this Elsevier article?	Yes
Will you be translating?	No
Order reference number	
Title of your thesis/dissertation	Whole-Lung Airflow and Particle Transport/Deposition Modeling
Expected completion date	Jan 2017
Estimated size (number of pages)	200
Elsevier VAT number	GB 494 6272 12
Requestor Location	Arun V Kolanjiyil 911 Oval Dr 3rd floor EB III Depart. of Mechanical and Aerospace Eng RALEIGH, NC 27695 United States Attn: Arun V Kolanjiyil
Billing Type	Invoice
Billing Address	Arun V Kolanjiyil 911 Oval Dr 3rd floor EB III Depart. of Mechanical and Aerospace Eng RALEIGH, NC 27695 United States

Attn: Arun V Kolanjiyil
0.00 USD

Total

[Terms and Conditions](#)

INTRODUCTION

1. The publisher for this copyrighted material is Elsevier. By clicking "accept" in connection with completing this licensing transaction, you agree that the following terms and conditions apply to this transaction (along with the Billing and Payment terms and conditions established by Copyright Clearance Center, Inc. ("CCC"), at the time that you opened your Rightslink account and that are available at any time at <http://myaccount.copyright.com>).

GENERAL TERMS

2. Elsevier hereby grants you permission to reproduce the aforementioned material subject to the terms and conditions indicated.

3. Acknowledgement: If any part of the material to be used (for example, figures) has appeared in our publication with credit or acknowledgement to another source, permission must also be sought from that source. If such permission is not obtained then that material may not be included in your publication/copies. Suitable acknowledgement to the source must be made, either as a footnote or in a reference list at the end of your publication, as follows:

"Reprinted from Publication title, Vol /edition number, Author(s), Title of article / title of chapter, Pages No., Copyright (Year), with permission from Elsevier [OR APPLICABLE SOCIETY COPYRIGHT OWNER]." Also Lancet special credit - "Reprinted from The Lancet, Vol. number, Author(s), Title of article, Pages No., Copyright (Year), with permission from Elsevier."

4. Reproduction of this material is confined to the purpose and/or media for which permission is hereby given.

5. Altering/Modifying Material: Not Permitted. However figures and illustrations may be altered/adapted minimally to serve your work. Any other abbreviations, additions, deletions and/or any other alterations shall be made only with prior written authorization of Elsevier Ltd. (Please contact Elsevier at permissions@elsevier.com). No modifications can be made to any Lancet figures/tables and they must be reproduced in full.

6. If the permission fee for the requested use of our material is waived in this instance, please be advised that your future requests for Elsevier materials may attract a fee.

7. Reservation of Rights: Publisher reserves all rights not specifically granted in the combination of (i) the license details provided by you and accepted in the course of this licensing transaction, (ii) these terms and conditions and (iii) CCC's Billing and Payment terms and conditions.

8. License Contingent Upon Payment: While you may exercise the rights licensed immediately upon issuance of the license at the end of the licensing process for the transaction, provided that you have disclosed complete and accurate details of your proposed use, no license is finally effective unless and until full payment is received from you (either by publisher or by CCC) as provided in CCC's Billing and Payment terms and conditions. If full payment is not received on a timely basis, then any license preliminarily granted shall be deemed automatically revoked and shall be void as if never granted. Further, in the event that you breach any of these terms and conditions or any of CCC's Billing and Payment terms and conditions, the license is automatically revoked and shall be void as if never granted. Use of materials as described in a revoked license, as well as any use of the materials beyond the scope of an unrevoked license, may constitute copyright infringement and publisher reserves the right to take any and all action to protect its copyright in the materials.

9. Warranties: Publisher makes no representations or warranties with respect to the licensed material.

10. Indemnity: You hereby indemnify and agree to hold harmless publisher and CCC, and their respective officers, directors, employees and agents, from and against any and all claims arising out of your use of the licensed material other than as specifically authorized pursuant to this license.

11. No Transfer of License: This license is personal to you and may not be sublicensed, assigned, or transferred by you to any other person without publisher's written permission.

12. No Amendment Except in Writing: This license may not be amended except in a writing signed by both parties (or, in the case of publisher, by CCC on publisher's behalf).

13. Objection to Contrary Terms: Publisher hereby objects to any terms contained in any purchase order, acknowledgment, check endorsement or other writing prepared by you, which terms are inconsistent with these terms and conditions or CCC's Billing and Payment terms and conditions. These terms and conditions, together with CCC's Billing and Payment terms and conditions (which are incorporated herein), comprise the entire agreement between you and publisher (and CCC) concerning this licensing transaction. In the event of any conflict between your obligations established by these terms and conditions and those established by CCC's Billing and Payment terms and conditions, these terms and conditions shall control.

14. Revocation: Elsevier or Copyright Clearance Center may deny the permissions described in this License at their sole discretion, for any reason or no reason, with a full refund payable to you. Notice of such denial will be made using the contact information provided by you. Failure to receive such notice will not alter or invalidate the denial. In no event will Elsevier or Copyright Clearance Center be responsible or liable for any costs, expenses or damage incurred by you as a result of a denial of your permission request, other than a refund of the amount(s) paid by you to Elsevier and/or Copyright Clearance Center for denied permissions.

LIMITED LICENSE

The following terms and conditions apply only to specific license types:

15. **Translation:** This permission is granted for non-exclusive world English rights only unless your license was granted for translation rights. If you licensed translation rights you may only translate this content into the languages you requested. A professional translator must perform all translations and reproduce the content word for word preserving the integrity of the article.

16. **Posting licensed content on any Website:** The following terms and conditions apply as follows: Licensing material from an Elsevier journal: All content posted to the web site must maintain the copyright information line on the bottom of each image; A hyper-text must be included to the Homepage of the journal from which you are licensing at <http://www.sciencedirect.com/science/journal/xxxx> or the Elsevier homepage for books at <http://www.elsevier.com>; Central Storage: This license does not include permission for a scanned version of the material to be stored in a central repository such as that provided by Heron/XanEdu. Licensing material from an Elsevier book: A hyper-text link must be included to the Elsevier homepage at <http://www.elsevier.com>. All content posted to the web site must maintain the copyright information line on the bottom of each image.

Posting licensed content on Electronic reserve: In addition to the above the following clauses are applicable: The web site must be password-protected and made available only to bona fide students registered on a relevant course. This permission is granted for 1 year only. You may obtain a new license for future website posting.

17. **For journal authors:** the following clauses are applicable in addition to the above:

Preprints:

A preprint is an author's own write-up of research results and analysis, it has not been peer-reviewed, nor has it had any other value added to it by a publisher (such as formatting, copyright, technical enhancement etc.).

Authors can share their preprints anywhere at any time. Preprints should not be added to or enhanced in any way in order to appear more like, or to substitute for, the final versions of articles however authors can update their preprints on arXiv or RePEc with their Accepted Author Manuscript (see below).

If accepted for publication, we encourage authors to link from the preprint to their formal publication via its DOI. Millions of researchers have access to the formal publications on ScienceDirect, and so links will help users to find, access, cite and use the best available version. Please note that Cell Press, The Lancet and some society-owned have different preprint policies.

Information on these policies is available on the journal homepage.

Accepted Author Manuscripts: An accepted author manuscript is the manuscript of an article that has been accepted for publication and which typically includes author-incorporated changes suggested during submission, peer review and editor-author communications.

Authors can share their accepted author manuscript:

- immediately
 - via their non-commercial person homepage or blog
 - by updating a preprint in arXiv or RePEc with the accepted manuscript
 - via their research institute or institutional repository for internal institutional uses or as part of an invitation-only research collaboration work-group
 - directly by providing copies to their students or to research collaborators for their personal use
 - for private scholarly sharing as part of an invitation-only work group on commercial sites with which Elsevier has an agreement
- after the embargo period
 - via non-commercial hosting platforms such as their institutional repository
 - via commercial sites with which Elsevier has an agreement

In all cases accepted manuscripts should:

- link to the formal publication via its DOI
- bear a CC-BY-NC-ND license - this is easy to do
- if aggregated with other manuscripts, for example in a repository or other site, be shared in alignment with our hosting policy not be added to or enhanced in any way to appear more like, or to substitute for, the published journal article.

Published journal article (JPA): A published journal article (PJA) is the definitive final record of published research that appears or will appear in the journal and embodies all value-adding publishing activities including peer review co-ordination, copy-editing, formatting, (if relevant) pagination and online enrichment.

Policies for sharing publishing journal articles differ for subscription and gold open access articles:

Subscription Articles: If you are an author, please share a link to your article rather than the full-text. Millions of researchers have access to the formal publications on ScienceDirect, and so links will help your users to find, access, cite, and use the best available version.

Theses and dissertations which contain embedded PJAs as part of the formal submission can be posted publicly by the awarding institution with DOI links back to the formal publications on ScienceDirect.

If you are affiliated with a library that subscribes to ScienceDirect you have additional private sharing rights for others' research accessed under that agreement. This includes use for classroom teaching and internal training at the institution (including use in

course packs and courseware programs), and inclusion of the article for grant funding purposes.

Gold Open Access Articles: May be shared according to the author-selected end-user license and should contain a [CrossMark logo](#), the end user license, and a DOI link to the formal publication on ScienceDirect.

Please refer to Elsevier's [posting policy](#) for further information.

18. For book authors the following clauses are applicable in addition to the above: Authors are permitted to place a brief summary of their work online only. You are not allowed to download and post the published electronic version of your chapter, nor may you scan the printed edition to create an electronic version. Posting to a repository: Authors are permitted to post a summary of their chapter only in their institution's repository.

19. **Thesis/Dissertation:** If your license is for use in a thesis/dissertation your thesis may be submitted to your institution in either print or electronic form. Should your thesis be published commercially, please reapply for permission. These requirements include permission for the Library and Archives of Canada to supply single copies, on demand, of the complete thesis and include permission for Proquest/UMI to supply single copies, on demand, of the complete thesis. Should your thesis be published commercially, please reapply for permission. Theses and dissertations which contain embedded PJAs as part of the formal submission can be posted publicly by the awarding institution with DOI links back to the formal publications on ScienceDirect.

Elsevier Open Access Terms and Conditions

You can publish open access with Elsevier in hundreds of open access journals or in nearly 2000 established subscription journals that support open access publishing. Permitted third party re-use of these open access articles is defined by the author's choice of Creative Commons user license. See our [open access license policy](#) for more information.

Terms & Conditions applicable to all Open Access articles published with Elsevier:

Any reuse of the article must not represent the author as endorsing the adaptation of the article nor should the article be modified in such a way as to damage the author's honour or reputation. If any changes have been made, such changes must be clearly indicated.

The author(s) must be appropriately credited and we ask that you include the end user license and a DOI link to the formal publication on ScienceDirect.

If any part of the material to be used (for example, figures) has appeared in our publication with credit or acknowledgement to another source it is the responsibility of the user to ensure their reuse complies with the terms and conditions determined by the rights holder.

Additional Terms & Conditions applicable to each Creative Commons user license:

CC BY: The CC-BY license allows users to copy, to create extracts, abstracts and new works from the Article, to alter and revise the Article and to make commercial use of the Article (including reuse and/or resale of the Article by commercial entities), provided the user gives appropriate credit (with a link to the formal publication through the relevant DOI), provides a link to the license, indicates if changes were made and the licensor is not represented as endorsing the use made of the work. The full details of the license are available at <http://creativecommons.org/licenses/by/4.0>.

CC BY NC SA: The CC BY-NC-SA license allows users to copy, to create extracts, abstracts and new works from the Article, to alter and revise the Article, provided this is not done for commercial purposes, and that the user gives appropriate credit (with a link to the formal publication through the relevant DOI), provides a link to the license, indicates if changes were made and the licensor is not represented as endorsing the use made of the work. Further, any new works must be made available on the same conditions. The full details of the license are available at <http://creativecommons.org/licenses/by-nc-sa/4.0>.

CC BY NC ND: The CC BY-NC-ND license allows users to copy and distribute the Article, provided this is not done for commercial purposes and further does not permit distribution of the Article if it is changed or edited in any way, and provided the user gives appropriate credit (with a link to the formal publication through the relevant DOI), provides a link to the license, and that the licensor is not represented as endorsing the use made of the work. The full details of the license are available at <http://creativecommons.org/licenses/by-nc-nd/4.0>. Any commercial reuse of Open Access articles published with a CC BY NC SA or CC BY NC ND license requires permission from Elsevier and will be subject to a fee.

Commercial reuse includes:

- Associating advertising with the full text of the Article
- Charging fees for document delivery or access
- Article aggregation
- Systematic distribution via e-mail lists or share buttons

Posting or linking by commercial companies for use by customers of those companies.

20. **Other Conditions:**

v1.9

Questions? customercare@copyright.com or +1-855-239-3415 (toll free in the US) or +1-978-646-2777.